The Dissertation Committee for Hong Sun
certifies that this is the approved version of the following dissertation:

Performance Prediction of Cavitating Propulsors using a Viscous/Inviscid Interaction Method

Committee:

Spyros A. Kinnas, Supervisor

Howard M. Liljestrand

Ben R. Hodges

Ronald L. Panton

David G. Bogard

Hanseong Lee

Performance Prediction of Cavitating Propulsors using a Viscous/Inviscid Interaction Method

by

Hong Sun, B.S.; M.S.

DISSERTATION

Presented to the Faculty of the Graduate School of
The University of Texas at Austin
in Partial Fulfillment
of the Requirements
for the Degree of

DOCTOR OF PHILOSOPHY

THE UNIVERSITY OF TEXAS AT AUSTIN
August 2008

Dedicated to the memory of my father.

Acknowledgments

Many people deserve acknowledgment for their contributions, encouragement and support during my study at the University of Texas at Austin. I first and foremost would like to thank my supervisor, Professor Spyros A. Kinnas, for his great guidance and continuous support. I have benefited a lot from his invaluable inputs and suggestions. His endeavor, wisdom, enthusiasm and patience as a teacher and researcher always inspire me to do my best in my research and future career.

I would also like to express my deepest gratitude to all those who served on my dissertation committee: Professors David G. Bogard, Ben R. Hodges, Howard M. Liljestrand, Ronald L. Panton, and Dr. Hanseong Lee. They unconditionally offered me their advice and encouragement. Specially, Dr. Hanseong Lee generously helped and guided me through the course of the project with his knowledge and experience.

I also want to take this chance to thank Prof. Justin E. Kerwin (Department of Mechanical Engineering, Massachusetts Institute of Technology) and Dr. William M. Milewski (Applied Physics, Inc.) for exchange of information and for the suggestions during the course of this work.

I am very grateful to my friends in the Computation Hydrodynamics Laboratory for their help, ideas and encouragements. I really enjoyed sharing my life with them these years. I would also like to thank all the staff at the Offshore Technology Research Center (OTRC) and the Department of CAEE for their friendship and assistance.

Words fail to express my sincere thanks and appreciation to my family. Without their love and support, I would never have made it this far. Special thanks to my husband for his consideration and constant support during those years of study.

Finally, I would like to thank all of the individuals and organizations who supported me in this work. They include Phase IV and Phase V Members of the “Consortium on Cavitation Performance of High Speed Propulsors”: AB Volvo Penta, Sweden, American Bureau of Shipping, USA, Daewoo Shipbuilding and Marine Engineering Co. Ltd., Korea, Kawasaki Heavy Industries Ltd., Japan, Naval Surface Warfare Center Carderock Division and Office of Naval Research (contracts N00014-04-1-0287 and N00014-07-1-0616), USA, Rolls-Royce Marine AS, Norway, Rolls-Royce Marine AB, Sweden, Samsung Heavy Industries Co. Ltd., Korea, SSPA AB, Sweden, VA Tech Escher Wyss GMBH, Germany, Wärtsilä Propulsion AS, Norway, Wärtsilä Propulsion BV, The Netherlands, Wärtsilä Lips Defense S.A.S., France and Wärtsilä Propulsion CME Zhenjiang Propeller Co. Ltd., P. R. China. Thanks to their representatives for their interests, quick response, advice and help to my research work. Special thanks go to Mr. Thad Michael (Naval Surface Warfare Center Carderock Division) for sending the water-jet geometry and for his feedback and suggestions on the water-jet model and the corresponding code. Partial support of this work was also provided by Office of Naval Research under the NNR-NE (National Naval Responsibility - Naval Engineering) program, through Florida Atlantic University (TRD67).

Performance Prediction of Cavitating Propulsors using a Viscous/Inviscid Interaction Method

Publication No. ____________________

Hong Sun, Ph.D.
The University of Texas at Austin, 2008

Supervisor: Spyros A. Kinnas

A viscous/inviscid interaction method for predicting the effect of viscosity on the performance of wetted and cavitating propulsors is presented. The emphasis is placed on steady wetted and cavitating propulsor flows. A three-dimensional low order potential based boundary element method is strongly coupled with a two dimensional integral boundary layer analysis method based on the strip theory assumption. The influence of viscosity on the outer inviscid flow is modeled through the wall transpiration model by distributing "blowing" sources on the propulsor blade and trailing wake surfaces. The boundary layer edge velocities are expressed as the sum of the inviscid edge velocity and a correction which depends only on the boundary layer variables. The influence of outer potential flow on the inner boundary layer flow is considered through the edge velocities. In the case of sheet cavitation, a "thin" cavity approach is employed and the viscous/inviscid interaction method is applied on the blade surface underneath the cavity. On the cavity surface, the friction force coefficient is forced to be zero.

Numerical predictions by the present viscous/inviscid interaction method are presented for open, ducted, and water-jet propulsors. For water-jet propulsors, the flow is solved in an iterative manner by solving the rotor and stator problems separately and by considering the time-averaged effects of one component on the other. Predicted forces, pressure distributions, and boundary layer variables are compared with those predicted by other numerical methods and experimental measurements.

Table of Contents

List of Tables

List of Figures

Nomenclature

Latin Symbols

C_τ	shear stress coefficient, $C_\tau = \tau_{max}/\rho_e U_e^2$
C_f	skin-friction coefficient, $C_f = \tau_{wall}/0.5\rho_e U_e^2$
C_D	dissipation coefficient, $C_D = (1/\rho_e U_e^3)\int \tau \frac{\partial U}{\partial \eta} d\eta$
C_p	pressure coefficient, $C_p = (P - P_o)/(\frac{1}{2}\rho n^2 D^2)$ for propellers or $C_p = (P - P_o)/(\frac{1}{2}\rho U_\infty^2)$ for hydrofoils
D	propeller diameter, $D = 2R$
f_{max}/C	maximum camber to chord ratio
F_{nD}	Froude number based on V_s, $F_{nD} = V_s/\sqrt{gD}$
F_r	Froude number based on n, $F_r = n^2 D/g$
g	gravitational acceleration
G	Green's function
h	cavity thickness over the blade surface
h_w	cavity thickness over the wake surface
H	shape factor, $H = \delta^*/\theta$
H^*	kinetic energy shape parameter, $H^* = \theta^*/\theta$
H^{**}	density shape parameter, $H^{**} = \delta^{**}/\theta$
H_k	kinematic shape parameter, $\frac{\int[1-(U/U_e)]d\eta}{\int(U/U_e)[1-(U/U_e)]d\eta}$
J_s	advance ratio based on V_s, $J_s = V_s/nD$
K_{Fx}, K_{Fy}, K_{Fz}	dynamic blade force coefficients in ship fixed coordinates

K_{Mx}, K_{My}, K_{Mz}	dynamic blade moment coefficients in ship fixed coordinates
K_Q	torque coefficient, $K_Q = Q/\rho n^2 D^5$
K_T	thrust coefficient, $K_T = T/\rho n^2 D^4$
l	cavity length
M_e	boundary layer edge Mach number
n	propeller rotational frequency (revolution/second)
$\tilde{n}$	transition disturbance amplification variable
P	pressure
P_{atm}	atmospheric pressure
P_o	pressure far Upstream, at the propeller shaft
P_v	vapor pressure of water
$\vec{q}$	total velocity
$\vec{q}_t$	total cavity velocity
$\vec{q}_{in}$	local inflow velocity (in the propeller fixed system)
$\vec{q}_w$	wake inflow velocity (in the ship fixed system)
Q	propeller torque
r	radius of propeller blade section
R	propeller radius
Re_θ	momentum thickness Reynolds number, $Re_\theta = \rho_e U_e \theta/\mu_e$
Re_C	strip Reynolds number, $Re_C = U_r C/\nu$, based on the reference velocity U_r and the chord length C at $r/R = 0.7$

$\vec{s}, \vec{v}, \vec{n}$	non-orthogonal unit vectors along the local grid directions
S_C	cavitating surface, $S_C = S_{CB} + S_{CW}$
S_{CB}	cavitating portion of blade surface
S_{CW}	cavitating portion of wake surface
S_∞	infinite boundary surface for foil entry problem
S_{WB}	wetted portion of blade, hub and duct surfaces
S_W	wake surface
t	time
T	propeller thrust
t_{max}/C	maximum thickness to chord ratio
U_e	boundary layer edge velocity
U_r	reference velocity, $U_r = \sqrt{V_s^2 + (0.7\pi n D)^2}$
U_τ	wall shear velocity, $U_\tau = \sqrt{\tau_{wall}/\rho}$
u_*	friction velocity at the wall
$\vec{V}$	velocity of 2-D surface-piercing hydrofoil
V_s	advance speed of propeller, or inflow speed for 3-D hydrofoil
x, y, z	propeller fixed coordinates
x_s, y_s, z_s	ship fixed coordinates
y^+	non-dimensional wall distance, $y^+ = \frac{u_* y}{\nu}$

Greek Symbols

α	angle of attack for 3-D hydrofoil
δ^*	displacement thickness, $\delta^* = \int [1 - (\rho U / \rho_e U_e)] d\eta$
δ^{**}	density thickness, $\delta^{**} = \int (U/U_e)[1 - (\rho/\rho_e)] d\eta$
$\Delta\phi_{TE}$	potential jump at the trailing edge of propulsor blade
$\Delta\phi_W$	potential jump across the trailing wake sheet of the propulsor blade or the duct
Δt	time step size
$\Delta\theta$	blade angle increment, $\Delta\theta = \omega \Delta t$
η_p	propeller efficiency, $\eta_p = \frac{K_T}{K_Q} \frac{J_s}{2\pi}$
Γ	non-dimensionalized circulation $\Gamma = \Delta\phi_{TE} / 2\pi R \sqrt{V_s^2 + (0.7 n \pi D)^2}$ for rotating propulsor
Γ_s	non-dimensionalized circulation $\Gamma_s = \Delta\phi_{TE} / 2\pi R V_s$ for rudder or stator
λ	ratio of full-scale diameter to model-scale diameter
μ_e	boundary layer edge viscosity
ν	kinematic viscosity of water
ω	propeller angular velocity
ϕ	perturbation potential
Φ	total potential
ψ	angle between $\vec{s}$ and $\vec{v}$
ρ	fluid density
ρ_e	fluid density at the boundary layer edge
σ_n	cavitation number based on n, $\sigma_n = (P_o - P_v)/(0.5 \rho n^2 D^2)$

σ_v	cavitation number based on V_s, $\sigma_v = (P_o - P_v)/(0.5\rho V_s^2)$
τ	shear stress
θ	momentum thickness, $\theta = \int (\rho U/\rho_e U_e)[1 - (U/U_e)] d\eta$
θ^*	kinetic energy thickness, $\theta^* = \int (\rho U/\rho_e U_e)[1 - (U^2/U_e^2)] d\eta$
ξ, η	steam-wise and span-wise coordinate along propulsor blade strip or thin shear layer coordinate

Superscripts

$+$	upper cavity, separated region, or wake surface
$-$	lower cavity, separated region, or wake surface

Acronyms

2-D	two dimensional
3-D	three dimensional
BEM	Boundary Element Method
CFD	Computational Fluid Dynamics
CPU	central processing unit (time)
DTMB	David Taylor Model Basin
DTRC	David Taylor Research Center
ITTC	International Towing Tank Conference
MIT	Massachusetts Institute of Technology
NACA	National Advisory Committee for Aeronautics
ONR	Office of Naval Research
VII	Viscous/Inviscid Interaction
VLM	Vortex-Lattice Method

Computer Program Names

CAV2D-BL	2-D viscous/inviscid interaction method for wetted, partially and super cavitating hydrofoil flows (2-D BEM coupled with XFOIL)
FLUENT	a commercial Computational Fluid Dynamics software
MPUF-3A	cavitating propeller potential flow solver based on VLM
PCPAN	2-D BEM solver for partially cavitating hydrofoil flow
PROPCAV	cavitating propeller potential flow solver based on BEM
SCPAN	2-D BEM solver for super-cavitating hydrofoil flow
U^2NCLE	Unsteady, Unstructured Navier Stokes Solver developed at the Mississippi State University
XFOIL	2-D integral boundary layer analysis code

Chapter 1

Introduction

1.1 Background

There has been an increasing demand for high-speed marine vehicles in both commercial and navy applications in recent decades. In consequence, marine propulsors are designed with more and more complex geometries to meet the requirements that are related to performance (high efficiency), comfort (low noise and vibration levels), safety and economic operation (less erosion). As demonstrations of this trend, ducted propellers, podded propulsors and water-jet pumps have become more and more common in contemporary designs. The complexity of the geometric characteristics of modern propulsors has introduced very complicated flows around the propulsor and has created a lot of challenges to those dealing with ship propulsor design and analysis. The predominant problems and challenges are caused by hydrodynamic *cavitation* and *viscosity*.

Hydrodynamic *cavitation* is the formation of vapor pockets within a moving fluid at low-pressure regions where the liquid has been accelerated to high velocities, such as in the operation of pumps, impellers, water turbines and marine propellers. In ship hydrodynamics, marine propulsors often experience different types of cavitation: sheet, bubble, cloud, hub vortex and tip vortex cavitation. They can occur either alone or together, depending on the inflow wake field, the propulsor geometry, and the operating conditions. A summary of formation and characteristics of these cavity patterns can be found in [Lee 2002]. These different patterns of cavitation are the main causes of the detrimental effects on ship performance, such as thrust breakdown, blade surface material erosion, vibrations and noise. Therefore, the design of modern propulsors with good cavity properties is a challenging task and requires accurate and efficient computational tools to predict the cavitating performance of propulsors. The present work addresses the simulation of *sheet* cavitation, which forms on the propulsor blade surface and remains attached to it, like a thin vapor bubble. Studies on sheet cavitation are important because sheet cavity is a very common type of cavity on marine propulsors, and can affect both the radiated pressure field and the formation of cloud cavitation [Lee 2002].

Viscosity is an internal property of a real fluid that offers resistance to flow. For propulsor flows, viscosity can affect not only the pressure distributions on propulsor blades, resulting in changes of thrust/torque forces and efficiency of the propulsor, but also the process of cavitation inception, development and decay. For conventional designs of marine propulsors, the effect of viscosity was often considered through empirical corrections to potential flow methods. However, as the types of modern propulsors become increasingly complicated and the flow around propulsors becomes more complex, the effects of viscosity are significant and can not be accurately predicted by empirical viscous corrections. For example, in ducted propeller flows, the viscous effects are dominant in the gap flow region between the propeller tip and the duct inner surface, and modeling of the viscous gap flow must be implemented [Gu 2006]. In podded propulsor flows, the aft propeller is subject to the boundary layer flow developed along the pod and the viscous wake field behind the strut. Viscous flow solvers are needed to evaluate the complex inflow wake profile to the aft propeller [Kinnas et al. 2006]. For water-jets, the flow is even more complex and multi-featured. The inflow profile to the water-jet rotor is greatly affected by the boundary layers developed along the hull and the casing; the gap flows between the rotor (or stator) blade tip and the casing are fully viscous; and the flow among the rotating and stationary components are very complicated because of their interactions with each other. The focus of this dissertation is on the viscous effects inherent with the wetted (non-cavitating) and sheet cavitating flows over the propulsor blades.

Simulation methods currently used to study ship propulsor flows can be divided into three major groups:

1. **Potential flow methods**, which include lifting line, lifting surface, and boundary element methods. The effects of viscosity are included in the potential methods by making empirical corrections to the pitch angles of the propulsor blade and by approximating the friction forces on the blades using a constant friction coefficient [Kerwin and Lee 1978]. The potential methods are very fast, accurate and efficient in performance analysis of conventional propulsor designs [Kerwin and Lee 1978; Lee 1987]. Moreover, this group of methods are very successful in performance prediction of cavitating propulsor flows without or with the existence of sheet cavitation [Lee 1979; Fine 1992; Young

2002; Lee 2002; Gu 2006]. However, for modern propulsor design, the potential methods are inadequate to accurately predict the effects of viscosity.

2. **Viscous flow solvers**, which include the Reynolds Averaged Navier-Stokes (RANS) solvers or Large Eddy Simulation (LES)[1]. This group of methods solves the time dependent, 2-D or 3-D viscous flows around the propulsors directly. The viscous solvers have gained more attention from researchers and designers in recent years because of their advantage of general applicability, and capability of providing a large amount of information of the flow without ignoring a lot of the physics. However, in spite of the increasing speed and memory size of modern computers, the application of viscous solvers to propulsor flows is still limited because of the excessive demand on computer resources and the large effort required for input preparation and post processing [Stanier 2002; Watanabe et al. 2003; Ebert et al. 2003; Rhee et al. 2005; Sanchez-Caja et al. 2006; Brewton et al. 2006]. In addition, the application of the viscous flow solvers to cavitating flows has not been fully established.

3. **Viscous/inviscid interaction (VII) methods**, which couple the potential flow solver with a boundary layer analysis code to provide a composite solution of the overall flow in two or three dimensions. The theoretical foundation for the viscous/inviscid interaction method is based on Prandtl's boundary layer concept. In high Reynolds number flows, the flow field can be divided into two regions: an outer flow where the flow is essentially inviscid, and an inner

---

[1] To the author's knowledge, no Direct Numerical Simulation (DNS) on propeller has been published.

thin boundary layer region along the body and the wake which can be approximated by the boundary layer equations. The effect of the boundary layer is to displace the outer inviscid flow away from the body by an amount equal to the displacement thickness. The outer inviscid flow in turn affects the viscous boundary layer flow solution through the pressure field at the edge of the boundary layer. Since the simulation method for each flow region uses a simplified model, the overall computational requirement is significantly less than that required by the viscous solvers. The application of the viscous/inviscid interaction method has been very successful in aerodynamic flows. In ship hydrodynamics, however, most of the applications of this method have been limited to modeling of flows under non-cavitating conditions.

Propulsor design requires fast, accurate and robust analysis methods which allow for more detailed optimization and thus are more suitable for routine design work. Thus, the viscous/inviscid interaction method is chosen in this dissertation to study the cavitating performance of ship propulsors.

1.2 Motivation

The motivation for this study is to develop a viscous/inviscid interaction method which is able to accurately predict the effects of viscosity on performance of cavitating propulsors. The emphasis is placed on the modeling of *sheet* cavitating flows around open, ducted propellers and inside water-jets.

1.3 Viscous/Inviscid Interaction

Researchers have performed extensive studies on the viscous/inviscid interaction methods since the mid 20th century and developed various coupling schemes for the interaction between the viscous boundary-layer flow and the external inviscid flow. To this end, there are mainly *five* developed coupling schemes that are applied in 2-D and 3-D viscous/inviscid interaction. The five coupling schemes are direct, fully-inverse, semi-inverse, quasi-simultaneous and fully-simultaneous schemes. The first three belong to *weak* coupling schemes which combine the solutions to the inviscid and viscous regions in an iterative manner. Quasi-simultaneous and fully-simultaneous methods are *strong* coupling schemes which solve the two regions of flows at the same time. Detailed description and explanation of the five coupling schemes can be found in the review paper by Lock & Williams [Lock and Williams 1987].

The relative merits of the *strong* and the *weak* coupling schemes are discussed here for their applications in both 2-D and 3-D flows. The direct coupling scheme is successful in attached flows, but breaks down when non-physical singularity develops in 2-D or 3-D separated flows. For 2-D flows, this singularity, named Goldstein singularity, is related to the vanishing wall shear stresses [Wigton and Holt 1981]. In 3-D flows, these singularities are formed by focusing of the characteristic lines of the system equations [Cousteix and Houdeville 1981]. The occurrence of the 2-D and 3-D singularities can be avoided by using the inverse coupling scheme with prescribed wall transpiration velocities [Catherall and Mangler 1966]. However, the inverse scheme (also the direct scheme) has difficulty in simulating flows where the interaction between the viscous and inviscid regions is strong. The semi-inverse method proposed by Lazareff & LeBalleur [Lazareff and LeBalleur 1986] has overcome this problem by using a multi-zone-marching technique to combine the inviscid and viscous regions. The drawback of the semi-inverse scheme is that the update procedure, which was used to match the inviscid and viscous solutions, is very time consuming. The *strong* coupling schemes, such as the quasi-simultaneous method by Veldman [Veldman 1981] and the fully simultaneous algorithm by Drela [Drela 1985, 1989], avoid the use of an update procedure and improve the convergence rate by solving the inviscid and viscous regions simultaneously. In particular, the fully simultaneous coupling scheme has proved to be the most robust and efficient method for 2-D separated flows [Drela 1989].

The weak and strong coupling methods have achieved different degrees of success in 2-D flows. However, in 3-D flows, their applications are still limited due to the complexity of the 3-D boundary layer equations. According to Cousteix & Houdeville [Cousteix and Houdeville 1981], the steady integral boundary layer equations for 2-D problems can simply be given by a set of ordinary differential equations. However, the 3-D steady integral boundary layer is described by three non-linear partial differential equations which are fully hyperbolic, corresponding to 2-D unsteady problem. Moreover, for 3-D unsteady flows over rotating body, Coriolis and centrifugal forces, and forces due to the unsteadiness of translating or rotating frame of reference also need to be considered in the 3-D integral boundary layer equations. Detailed reviews of the studies on 3-D integral boundary layer analysis can be referred to Mughal's work [Mughal 1992, 1998]. Although the *strong* coupling schemes are the most promising choices for 3-D viscous/inviscid interactions, the computational cost for coupling the system of 3-D inviscid and integral boundary layer equations is expensive even for flows over simple geometries, such as wings or ducts [Nishida 1996; Milewski 1997a; Coenen 2001].

Application of The VII Method in Propulsor Flows

For the application of the viscous/inviscid interaction methods in wetted (non-cavitating) propulsor flows, Coney first developed a direct coupling scheme for 2-D hydrofoil flows [Coney 1989]. This coupling scheme was later extended to wetted propeller flows by coupling a 3-D boundary element method with a 2-D integral boundary layer solver based on the strip theory assumption. Since Coney's direct coupling scheme failed to deal with separated flows, Hufford [Hufford 1992] developed a strongly coupled scheme for 2-D wetted hydrofoil flows, by coupling a panel method with Drela's integral boundary layer analysis code (XFOIL) [Drela 1989]. This method worked successfully and was extended to wetted propeller flows, by coupling a 3-D panel method with XFOIL along constant radius strips of propeller blade [Hufford 1992; Hufford et al. 1994]. Hufford's method was stable in separated flow, but did not take into account the boundary layer effects of neighboring strips and on the other blades. In order to include these effects, Black developed an iterative stripwise coupled method, which strongly coupled a 3-D lifting surface method with XFOIL along equivalent 2-D strips, and then iterated the stripwise viscous calculations with the outer flow to capture the effects of neighboring and intra-blade boundary layer strips [Black 1997]. For the coupling of 3-D inviscid solver with 3-D integral boundary layer analysis, as mentioned above, Milewski developed a fully simultaneous viscous/inviscid interaction scheme for 3-D wetted hydrofoil and duct flows [Milewski 1997a]. Unfortunately, solving the 3-D integral boundary layer equations requires a large amount of computer resources.

For cavitating propulsor flows, the applications of the viscous/inviscid interaction methods are limited to 2-D *sheet* cavitation. Villeneuve extended Hufford's 2-D viscous/inviscid interaction method to partially cavitating hydrofoils by using the "thin" cavity assumption [Villeneuve 1993]. The "thin" cavity assumption is that both the cavity height and the boundary layer thickness are assumed to be small compared to the foil thickness, and the panels representing the cavity are assumed to be located on the foil surface underneath the cavity. This method was later improved to treat flow around 2-D partially and super cavitating hydrofoils using a fully non-linear cavity approach [Kinnas et al. 1994; Brewer and Kinnas 1997]. In the fully non-linear cavity approach, the boundary layer thickness is still assumed to be small, but the cavity thickness is not necessarily small compared to the foil thickness. The viscous cavitating problem is solved on top of the combined non-linear cavity and foil surfaces. The current versions of these codes are named PCPAN/XFOIL (for partial cavitating) and SCPAN/XFOIL (for super cavitating), respectively. The drawbacks of the two codes are that they can only predict back side cavities, and can not do cavity detachment search, *i.e.* the cavity detachment point has to be known a priori. For 3-D cavitating flows, Salvatore *et al.* developed a weakly coupled method to include the viscosity effects for 3-D cavitating hydrofoils, and then extended this method to cavitating open propeller flows [Salvatore and Esposito 2001a; Salvatore et al. 2003]. They obtained reasonable results for 3-D hydrofoil flows, but the viscosity effects on cavitating propeller flows was questionable because the flow was not affected by viscosity.

1.4 Objective

The objective of this dissertation is to strongly couple an existing 3-D boundary element method (named PROPCAV) with Drela's 2-D integral boundary layer analysis (XFOIL) to investigate the effects of viscosity on performance prediction of open, ducted propellers and water-jets, with the presence of sheet cavitation.

1.5 Organization

This dissertation is organized into seven chapters.

Chapter 1 contains background, motivation and objectives of this study. A literature review on the viscous/inviscid interaction methods is also provided.

Chapter 2 presents the assumptions, formulation and numerical implementation for the proposed viscous/inviscid interaction method, which couples a 3-D low order potential based boundary element method with a 2-D integral boundary layer analysis.

In Chapter 3, the developed 3-D viscous/inviscid interaction method is applied to 2-D cavitating hydrofoil problems, and verified with a previously developed 2-D viscous/inviscid interaction method.

In Chapter 4, the present method is applied to investigate the effects of viscosity on steady wetted and/or cavitating flows over single component propulsors. Validation and verification of the results with experimental measurements and a commercial software FLUENT are addressed in the cases of wetted rudder, duct, and single propeller flows.

In Chapter 5, the developed viscous/inviscid method is used to simulate flow around ducted propellers. A short review of previous work, convergence and verification studies, and comparisons with experimental measurements are presented.

Chapter 6 presents previous work, assumptions, methodology, numerical implementation, verification and validation studies for water-jet flows.

Chapter 7 presents the discussions, conclusions, contributions of this dissertation, and recommendations for future research.

Chapter 2

Methodology

This chapter presents the proposed viscous/inviscid coupling method for the performance prediction of cavitating propulsors. The flow outside the boundary layer of the propulsor is modeled as incompressible, inviscid flow. A low order potential based boundary element method is applied to solve the boundary value problem. The viscous flow inside the boundary layer is solved by using a 2-D integral boundary layer analysis code. By applying a strip theory assumption [Coney 1989], the 3-D inviscid flow model and the 2-D integral boundary layer analysis are strongly coupled through a wall transpiration model.

2.1 The Inviscid Flow Model

This section presents the low order potential based boundary element method without considering the effect of viscous boundary layer. This method has proved to be very successful in the applications to cavitating propulsor flows [Young 2002; Lee 2002]. The most recent version (under the name PROPCAV) is able to consider partially cavitating, super cavitating, and surface-piercing propellers [Young and Kinnas 2003a], ducted propellers [Lee and Kinnas 2006], tunnel effects [Lee and Kinnas 2005a], tip vortex cavitation and unsteady wake alignment [Lee and Kinnas

2004]. The following sections summarize the governing equations and boundary conditions in the case of open and ducted propellers for the sake of explanation.

2.1.1 Problem Description

As shown in Figure 2.1, a propeller which rotates at an angular velocity $\vec{\omega}$ is subject to a general inflow wake, $\vec{q}_w(x_s, y_s, z_s)$, which is assumed to be the effective wake [1] and includes the interaction between the inflow vorticity and the propeller. The inflow wake is usually expressed in terms of the ship fixed coordinate system (x_s, y_s, z_s). Since this problem is more easily to be solved in the blade fixed coordinates system (x, y, z), which rotates with the propeller, the inflow velocity $\vec{q}_{in}$ with respect to the propeller can be expressed as the sum of the inflow wake velocity, $\vec{q}_w$, and the propeller's angular velocity $\vec{\omega}$, at a given location $\vec{x}$:

$$\vec{q}_{in}(x, y, z, t) = \vec{q}_w(x, r, \theta_B - \omega t) + \vec{\omega} \times \vec{x} \tag{2.1}$$

where $r = \sqrt{y^2 + z^2}$, $\theta_B = \arctan(z/y)$, and $\vec{x} = (x, y, z)$.

With the assumption that the resulting flow is incompressible, inviscid and irrotational, the total velocity $\vec{q}(x, y, z, t)$ at any point in the fluid domain can be expressed as follows :

$$\vec{q}(x, y, z, t) = \vec{q}_{in}(x, y, z, t) + \nabla\phi(x, y, z, t) \tag{2.2}$$

where $\phi(x, y, z, t)$ is the perturbation potential, which satisfies the Laplace's equa-

---

[1] The effective wake can be evaluated via coupling of the present method with an Euler solver [Choi and Kinnas 2003] or a viscous flow solver [Warren et al. 2000].

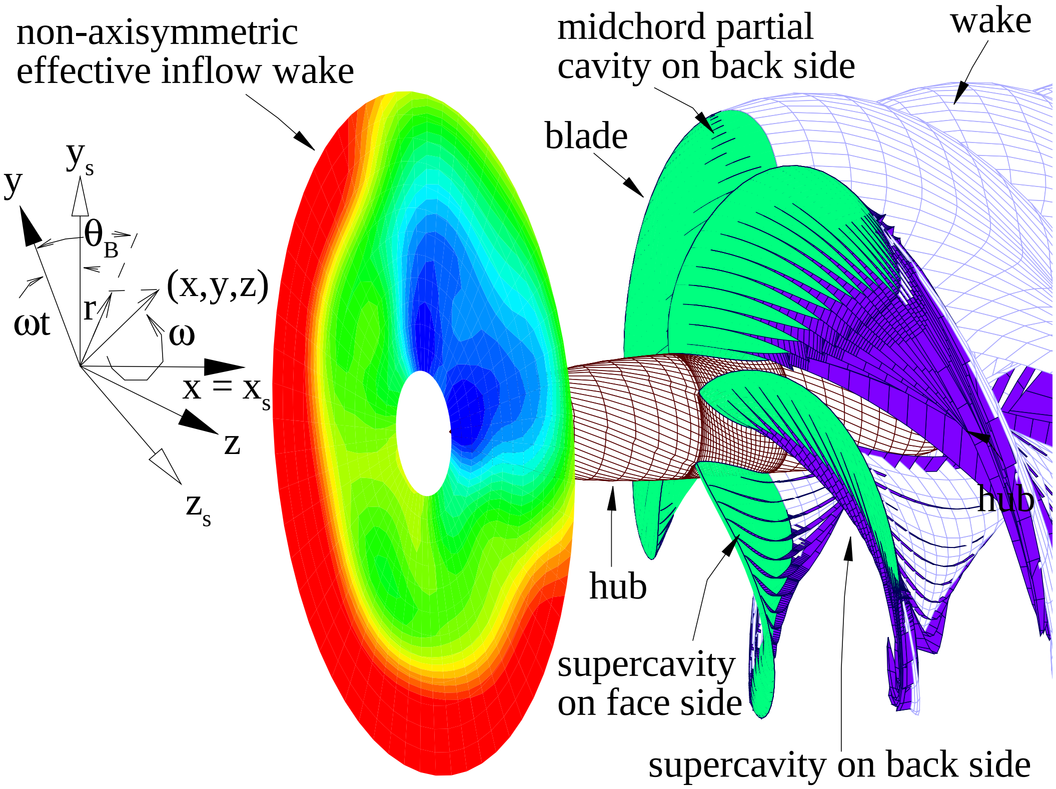

Figure 2.1: Propeller subjected to a general inflow wake. The blade fixed (x, y, z) and ship fixed (x_s, y_s, z_s) coordinate systems are shown. Taken from [Young 2002].

tion, *i.e.* the governing equation for incompressible potential flow:

$$\nabla^2 \phi = 0 \tag{2.3}$$

The Green's third identity is next applied to solve the Laplace's equation for the perturbation potential in the flow field.

2.1.2 Governing Equation

The perturbation potential, $\phi(x, y, z, t)$, at any point $p(x, y, z)$ located either on the wetted body (blade, hub or duct) surfaces, $S_{WB}(t)$ or on the cavity surface $S_C(t)$, must satisfy Green's third identity:

$$\begin{aligned} 2\pi\phi(\vec{x}, t) &= \int_{S_{WB}(t) \cup S_C(t)} \left[\phi_q(\vec{x}, t) \frac{\partial G(p; q)}{\partial n_q(t)} - G(p; q) \frac{\partial \phi_q(\vec{x}, t)}{\partial n_q(t)} \right] dS \\ &+ \int_{S_{W(t)}} \Delta\phi_W(\vec{x}, t) \frac{\partial G(p; q)}{\partial n_q(t)} dS \end{aligned} \tag{2.4}$$

where the subscripts, q and p, correspond to the variable point and the field point, respectively. $G(p; q) = 1/R(p; q)$ is the Green's function with $R(p; q)$ being the distance between field point p and the variable point q. $\vec{n}_q$ is the unit vector normal to the integration surface, with the positive direction pointing into the fluid domain. $S_W(t)$ is the trailing wake sheet of the propulsor blade or duct. $\Delta\phi_W$ is the potential jump either across the blade trailing wake sheet or the duct trailing wake sheet.

Equation (2.4) implies that the solution potential $\phi_p(\vec{x}, t)$ on the blade, cavity and duct surfaces can be expressed by distributing sources and dipoles over the blade, hub, duct and cavity surfaces, and dipoles only on the trailing wake surfaces behind the propulsor blade or duct.

2.1.3 Boundary Conditions

In order to uniquely determine the solution of Equation (2.4), appropriate boundary conditions have to be applied on the exact flow boundary. It should be pointed out that the kinematic and dynamic boundary conditions for the cavity surface are applied on the approximate flow boundary, which coincides with the blade surface beneath the cavity. The reason for using the approximate flow boundary is that the cavity surface is unknown and to be determined as part of the solution, while performing a fully non-linear analysis for 3-D cavitating flows is prohibitively expensive due to the requirement of repaneling on the cavity surface and recalculation of the dipole and source influence coefficients [Fine 1992].

The boundary conditions applied on the blade, duct, cavity and the trailing wake surfaces are as follows:

1. The flow on the wetted blade, hub, and duct surfaces is tangent to the wetted body surfaces.

$$\frac{\partial \phi}{\partial n} = -\vec{q}_{in}(x, y, z, t) \cdot \vec{n}$$

2. Kutta condition, which implies that the fluid velocities at the blade and duct trailing edge are finite.

$$|\nabla \phi| < \infty \qquad \text{at blade and duct trailing edge}$$

At the duct trailing edge, an extension of Morino's steady Kutta condition is applied. At the blade trailing edge, an iterative pressure Kutta condition is applied to ensure that the pressure on the suction and pressure sides are equal [Kerwin et al. 1987; Kinnas and Hsin 1992].

3. The dynamic boundary condition on cavitating blade and wake surfaces requires that the pressure everywhere on the cavity surface is constant and equal to the vapor pressure, P_v. By applying the Bernoulli's equation in the propeller fixed coordinate system, the total velocity, $\vec{q_t}$, on the cavity surface can be expressed as follows:

   $$|\vec{q_t}|^2 = n^2 D^2 \sigma_n + |\vec{q_{in}}|^2 + \omega^2 r^2 - 2 g y_s - 2\frac{\partial \phi}{\partial t}$$

   where r is the distance from the axis of rotation. g is the acceleration of gravity and y_s the vertical distance from the horizontal plane through the axis of rotation. n and D are the blade rotational frequency and the propeller diameter, respectively. The cavitation number, σ_n is defined as follows:

   $$\sigma_n = \frac{P_o - P_v}{\frac{1}{2}\rho n^2 D^2}$$

   P_o is the pressure far upstream on the shaft axis, and ρ is the fluid density.

   The total velocity $\vec{q_t}$ also can be expressed in terms of the directional derivatives of the perturbation potential and the inflow components at the non-orthogonal coordinate system:

   $$\vec{q_t} = \left(\frac{\partial \phi}{\partial n} + U_n\right)\vec{n} + \frac{(\frac{\partial \phi}{\partial s} + U_s)\left[\vec{s} - (\vec{s}\cdot\vec{v})\vec{v}\right] + (\frac{\partial \phi}{\partial v} + U_v)\left[\vec{v} - (\vec{s}\cdot\vec{v})\vec{s}\right]}{||\vec{s}\times\vec{v}||^2}$$

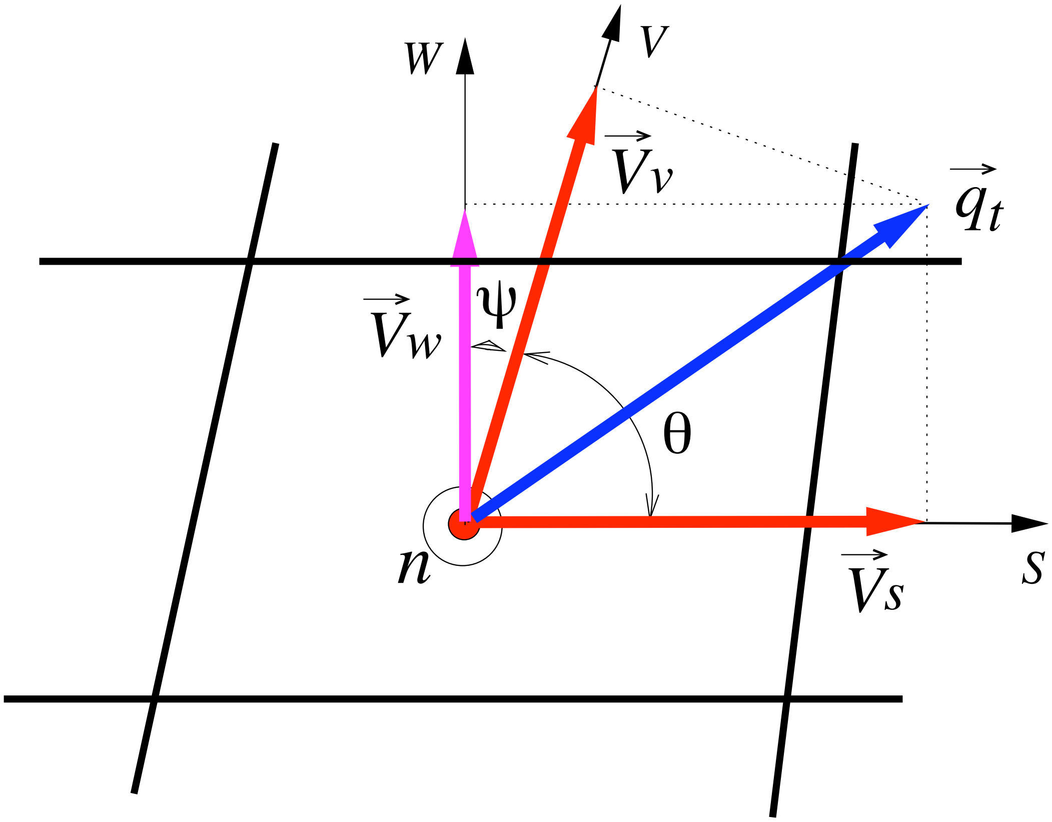

Figure 2.2: Local coordinate system on blade, hub, and duct panel. Taken from [Lee 2002].

As shown in Figure 2.2, $\vec{s}$ and $\vec{v}$ are the unit vectors corresponding to the coordinates s (chordwise) and v (spanwise). $\vec{n}$ is the unit normal vector to the cavity. U_s, U_v and U_n are the inflow velocities along (s, v, n) directions. Combining the equations for $\vec{q}_t$, $\frac{\partial \phi}{\partial s}$ can be expressed as follows:

$$\frac{\partial \phi}{\partial s} = -U_s + \left(\frac{\partial \phi}{\partial v} + U_v\right)\cos\theta + + \sin\theta\sqrt{|\vec{q}_t|^2 - \left(\frac{\partial \phi}{\partial v} + U_v\right)^2}$$

where θ is the angle between s and v, and defined as $\cos\theta = \vec{s}\cdot\vec{v}$. A Dirichlet type of boundary condition on ϕ can be derived by integrating the equation for $\frac{\partial \phi}{\partial s}$. Finally, the equation for the perturbation potential on the cavity over blade surface is

$$\begin{aligned} \phi(s, v, t) &= \phi(0, v, t) + \int_0^s \left[-U_s + \left(\frac{\partial \phi}{\partial v} + U_v\right)\cos\theta\right. \\ &+ \left.\sin\theta\sqrt{|\vec{q}_t|^2 - \left(\frac{\partial \phi}{\partial v} + U_v\right)^2}\right] ds \end{aligned}$$

and, on the super cavity over wake surface is

$$\phi^+(s, u, t) = \phi(s_{TE}, u, t) + \int_{s_{TE}}^{s} \left[-U_s + \sqrt{|\vec{q}_t|^2 - (V_u^+)^2}\right] ds$$

The potential $\phi(0, v, t)$ corresponds to the potential value at the cavity leading edge, and can be extrapolated in terms of the unknown potentials of wetted parts in front of the cavity detachment location. $s = s_{TE}$ denotes the blade trailing edge. The variable u in the equation for $\phi^+(s, u, t)$ corresponds to the directional derivative normal to (s, n) plane on wake surface, and the superscript, $+$, represents the upper side of the wake sheet. The equations for the potential on cavity includes the unknown functions, $\frac{\partial\phi}{\partial v}$ and $\frac{\partial\phi}{\partial t}$, and those terms are determined in an iterative manner.

4. Kinematic boundary condition on cavity surface requires that the substantial derivative of the cavity surface has to be vanished.

$$\left(\frac{\partial}{\partial t}+\vec{q}_t\cdot\nabla\right)[n-h(s,v,t)]=0$$

where h is the cavity thickness normal to the blade surface.

Once the boundary value problem is solved, the kinematic condition is utilized to determine the position of the cavity surface. The partial differential equation for the cavity thickness is as follows:

$$\frac{\partial h}{\partial s}\left[V_s-\cos\psi V_v\right]+\frac{\partial h}{\partial v}\left[V_v-\cos\psi V_s\right]=\left[V_n-\frac{\partial h}{\partial t}\right]\sin^2\psi$$

where

$$V_s=\frac{\partial\phi}{\partial s}+U_s,\quad V_v=\frac{\partial\phi}{\partial v}+U_v,\quad V_n=\frac{\partial\phi}{\partial n}+U_n$$

The cavity height normal to the blade surface can be determined by solving the above partial differential equation. Similarly, the cavity height on wake surface, h_w, when the supercavity occurs, can be determined:

$$\frac{\partial h_w}{\partial s}|\vec{q}_t|=q_w(t)-\frac{\partial h_w}{\partial t}$$

where the strength of the cavity source on wake surface, $q_w(t)$ is

$$q_w(t)=\frac{\partial\phi^+}{\partial n}-\frac{\partial\phi^-}{\partial n}$$

5. The cavity closure condition implies that the cavity has to be close at the cavity trailing edge. Since the extent of the unsteady cavity is unknown and has to be determined as part of the solution, a split-panel technique and a Newton-Raphson iterative method are applied to find the correct cavity extent which satisfies the cavity closure condition at the given cavitation number [Fine 1992; Kinnas and Fine 1993b].

6. The cavity detachment locations are determined iteratively by satisfying the Villat-Brillouin smooth detachment conditions, as described in [Young 2002].

The solutions, ϕ on the wetted surface and $\frac{\partial \phi}{\partial n}$ on cavity surface, of a boundary value problem for cavitating open or ducted propeller can then be determined by solving Equation (2.4) together with the boundary conditions described above.

Evaluation of Perturbation Potential in The Wake

Once the boundary value problem is solved by using Equation (2.4) together with the boundary conditions, the induced potentials on the wake surface ϕ_w can be calculated by using Green's formulation,

$$\begin{aligned} \phi_w(\vec{x},t) &= \frac{1}{4\pi}\int_{S_{WB}(t)\cup S_C(t)} \left[\phi_q(\vec{x},t)\frac{\partial G(p;q)}{\partial n_q(t)} - G(p;q)\frac{\partial \phi_q(\vec{x},t)}{\partial n_q(t)}\right] dS \\ &+ \frac{1}{4\pi}\int_{S_{W(t)}} \Delta\phi_W(\vec{x},t)\frac{\partial G(p;q)}{\partial n_q(t)} dS \end{aligned} \tag{2.5}$$

2.1.4 Empirical Viscous Pitch Correction

In the past, since the solutions for propeller blade boundary layers were not evaluated, the influence of blade boundary layer on propeller performance was approximated by applying empirical corrections to the potential flow solutions. Kerwin & Lee [Kerwin and Lee 1978] proposed a viscous pitch correction according to Brockett's work on 2-D sections [Brockett 1966], where the influence of the boundary layer on blade section lift was approximated by reducing the pitch angle of each blade section by the amount:

$$\Delta\alpha = 1.9454\frac{t_{max}}{c}\left|\frac{f_{max}}{c}\right| \tag{2.6}$$

where $\Delta\alpha$ is in radians. c is the chord length of each blade section. t_{max}/c is the maximum thickness-chord ratio, and f_{max}/c is the maximum camber-chord ratio.

2.2 The 2-D Integral Boundary Layer Analysis

According to Jessup's work [Jessup 1989], the viscous flow in the boundary layer of the propulsor blade can be assumed to develop only along the stream-wise direction. The growth of the boundary layer in the cross flow direction is negligible. In this study, Drela's 2-D integral boundary layer analysis code (XFOIL) is used to solve the boundary layer flow along the stream-wise direction [Drela 1989]. XFOIL employs a two-equation lagged dissipation integral method including the treatment of laminar and turbulent boundary layers, and is able to represent accurately flows with limited separation regions. The prediction of transition is based on an e^9-type amplification formulation. Detailed information of the solution method can be found in [Drela 1989]. The boundary layer equations are summarized here for the sake of completeness.

For a given distribution of the boundary layer edge velocities U_e, the boundary layer parameters can be determined by solving the momentum integral equation (2.7) and the kinetic energy shape factor equation (2.8) with a third closure equation (2.9) or (2.10).

Momentum Equation

$$\frac{d\theta}{ds} + (2+H)\frac{\theta}{U_e}\frac{dU_e}{ds} = \frac{Cf}{2} \tag{2.7}$$

Kinetic Energy Equation

$$\theta\frac{dH^*}{ds} + \left[2H^{**} + H^*(1-H)\right]\frac{\theta}{U_e}\frac{dU_e}{ds} = 2C_D - H^*\frac{C_f}{2} \tag{2.8}$$

Turbulent Closure

$$\frac{\delta}{C_\tau}\frac{dC_\tau}{ds} = 5.6\left[C_{\tau EQ}^{1/2} - C_\tau^{1/2}\right] + 2\delta \times \left\{\frac{4}{3\delta^*}\left[\frac{C_f}{2} - \left(\frac{H_k-1}{6.7H_k}\right)^2\right] - \frac{1}{U_e}\frac{dU_e}{ds}\right\} \tag{2.9}$$

Equation (2.9) is the rate equation for the maximum shear stress coefficient C_τ, and is used when the viscous flow has transitioned to turbulent flow. In laminar regions, a rate equation (2.10), which models the growth of the the amplitude $\tilde{n}$ of the most amplified Tollmien-Schlichting wave, is used instead.

Laminar Closure

$$\frac{d\tilde{n}}{ds} = \frac{d\tilde{n}(H_k)}{dR_{e\theta}}\frac{dR_{e\theta}(H_k,\theta)}{ds} \tag{2.10}$$

The empirical relation $d\tilde{n}(H_k)/dR_{e\theta}$ is a correlation of spatial growth rates computed from solutions to Orr-Sommerfield equation, and $dR_{e\theta}(H_k,\theta)/ds$ is obtained from the properties of Falkner-Scan profile family. The transition point is defined by the location where $\tilde{n}$ reaches a user specified critical value $\tilde{n}_{crit}$. The parameter in practice is used to represent the background disturbance level.

Equation (2.7) and Equation (2.8) represent momentum conservation and kinetic energy along the stream-wise direction. s is the stream-wise coordinate, $\delta^* = \int(1 - \frac{u}{U_e})dz$ is the displacement thickness, and $\theta = \int \frac{u}{U_e}(1 - \frac{u}{U_e})dz$ is the momentum thickness, where z is the vertical distance normal to the blade. $C_f = \frac{\tau_{wall}}{0.5\rho U_e^2}$ is the friction coefficient, and $C_f = 0$ is enforced in the wake. Definition of the momentum thickness shape factor H, the kinetic energy shape factor $H^\star$, the density shape factor $H^{\star\star}$, the dissipation coefficient C_D, the shear stress coefficient $C_{\tau EQ}$, the kinematic shape factor H_k and the momentum thickness Reynolds number $R_{e\theta}$ can be found in Appendix A.

Three primary variables are chosen for the above boundary layer governing equations: the mass defect m, the momentum thickness θ, and the amplitude growth rate $\tilde{n}$ for the laminar regions or the square root of the maximum shear stress coefficient $C_\tau^{1/2}$. The mass defect m is defined as the product of the edge velocity U_e and the mass displacement thickness δ^*,

$$m = U_e \delta^* \tag{2.11}$$

For laminar flow, Equations (2.7) and (2.8) are closed with Equation (2.10) to solve for m, θ and $\tilde{n}$. For turbulent flow, Equations (2.7), (2.8) and (2.9) are solved for m, θ and C_τ.

2.3 The Viscous/Inviscid Flow Coupling

The coupling of the outer inviscid flow and inner boundary layer flow over the propulsor blade is based on the strip theory assumption [Coney 1989; Hufford 1992]. The developed boundary layers are assumed to be two dimensional along strips of the propulsor blade, and the boundary layer in the cross flow direction is ignored. According to [Groves and Chang 1984; Jessup 1989], these strips can be assumed to be along the constant radial direction of the propulsor blade.

The 3-D inviscid model (PROPCAV) and the 2-D integral boundary layer analysis (XFOIL) are strongly coupled along these blade strips through the wall transpiration model. In the wall transpiration model, “blowing” sources which represent the viscosity effects are added to the panels on the blade, sheet cavity and wake surfaces. The effect of these “blowing” sources is to displace the potential flow away from the body, and to create a component of velocity normal to the body [Lighthill 1958; Nishida and Drela 1995].

Strength of the “blowing” source $\hat{\sigma}$ is related to the rate of growth of the boundary layer, and defined as:

$$\hat{\sigma} = \frac{dm}{ds} = \frac{d(U_e \delta^*)}{ds} \tag{2.12}$$

where s is the local coordinate along each constant radial strip, U_e is the velocity at the edge of the viscous boundary layer, and δ^* is the displacement thickness.

2.3.1 Modified Green's Formulation

The outer flow, including the viscous boundary layer effects, can be represented by adding the "blowing" sources to the Green's third identity, Equation (2.4):

$$\begin{aligned}
2\pi\phi(\vec{x},t) &= \int_{S_{WB}(t)\cup S_C(t)} \left[\phi_q(\vec{x},t)\frac{\partial G(p;q)}{\partial n_q(t)} - G(p;q)\frac{\partial \phi_q(\vec{x},t)}{\partial n_q(t)}\right] dS \\
&+ \int_{S_{W(t)}} \Delta\phi_W(\vec{x},t)\frac{\partial G(p;q)}{\partial n_q(t)} dS \\
&- \int_{S_{WB}(t)\cup S_C(t)\cup S_W(t)} \hat{\sigma}(p;q)\frac{\partial \phi_q(\vec{x},t)}{\partial n_q(t)} dS \qquad (2.13)
\end{aligned}$$

Both the perturbation potential ϕ and the "blowing" source strength $\hat{\sigma}$ in Equation 2.13 are unknown and to be solved by coupling the potential and boundary layer equations.

2.3.2 The Coupling Algorithm

The integral boundary layer equations are coupled with the inviscid solution through the edge velocity of the boundary layer at each blade strip. According to [Drela 1989], the edge velocity can be expressed in terms of the known inviscid component and a correction involving the unknown blowing sources through the mass defect:

$$U_e = U_e^{inv} + \Im\{m\} = U_e^{inv} + \Im\{U_e\delta^*\} \qquad (2.14)$$

where U_e is velocity at the edge of the boundary layer along each blade strip, U_e^{inv} is the inviscid component of the edge velocity, $m = U_e\delta^*$ is the mass defect term, and $\Im$ is a geometry dependent operator defined in Appendix B.

Equation (2.14) gives the solution to the potential flow for any distribution of mass defect on the blade and wake. The system of equations is elliptic in nature because of the global influence of the mass defect m on the edge velocities U_e. The solution can be found using a Newton iterative solver [Drela 1989]. For a given distribution of U_e, the mass defect term m and the momentum thickness θ can be determined from the boundary layer equations (Equation (2.7) to (2.10)). In the first iteration, the edge velocity distribution from the inviscid solution U_e^{inv} is set as the given U_e to solve the boundary layer equations. Once the mass defect term m is solved, U_e will be updated via Equation (2.14), and then the boundary layer equations are solved again. This process iterates until convergence is achieved.

For the calculation of the geometry dependent operator $\Im$, Hufford used the 3-D influence coefficients of dipoles and sources along each blade strip but ignored the effects of blowing sources on neighboring strips and on the other blades [Hufford 1992]. This method failed to predict the correct solution for flow over infinite 3-D hydrofoil. Moreover, it greatly depends on the panel discretization. In this dissertation, the calculation of $\Im$ uses the 2-D section formed along the panel centroid of each blade strip. This is based on the simplification of $\Im$ for 3-D flows when the cross flow is very small and can be ignored [Milewski 1997a].

Reynolds Number

Following [Hufford 1992], the input Reynolds number to the present viscous/inviscid interaction method (PROPCAV/XFOIL) is defined based on propeller diameter,

$$Re_D = \frac{V_s D}{\nu} \tag{2.15}$$

where V_s is the ship speed or speed of the inflow of a water tunnel, D is the propeller diameter, and ν is the kinematic viscosity of water.

In the boundary layer calculation, XFOIL uses a strip Reynolds number, which is defined as,

$$Re_C = \frac{V_r C}{\nu} \tag{2.16}$$

where C is the chord length at each blade strip, and the velocity V_r is defined by

$$V_r = \sqrt{V_s^2 + (2\pi n r)^2} \tag{2.17}$$

n is the rotational speed in revolution per second, and r is the radius of the strip. The strip Reynolds number can be represented by the input Reynolds number,

$$Re_C = Re_D \left[\frac{C}{D} \frac{1}{J_s} \sqrt{J_s^2 + \pi^2 \left(\frac{r}{R} \right)^2} \right] \tag{2.18}$$

where J_s is the advance coefficient defined by $J_s = \frac{V_s}{nD}$ and $R = D/2$ is the maximum radius of the propeller.

Chapter 3

2-D Cavitating Hydrofoils

In this chapter, the developed viscous/inviscid interaction method (PROPCAV/XFOIL) is applied to model steady flows over 2-D cavitating hydrofoils. Results from the present method are verified with a previously developed 2-D viscous/inviscid interaction method. In addition, two approaches, the "thin" cavity approach and the non-linear cavity approach, for the coupling of the inviscid cavity model and the boundary layer analysis on top of cavity surface are presented and compared.

3.1 The 2-D Viscous/Inviscid Interaction Method

In this section, previously developed 2-D viscous/inviscid interaction methods for 2-D steady flows over cavitating hydrofoils by [Kinnas et al. 1994] are reviewed. Two approaches for 2-D viscous cavity model, the *"thin" cavity* approach and the *non-linear cavity* approach, are summarized.

In both approaches, the complex two phase flow near the cavity surface is ignored, and the fluid/vapor interface is treated as a constant pressure free-streamline. The viscous flow in the vicinity of the cavity is assumed to be confined to a thin boundary layer, and the friction coefficient everywhere on the cavity surface is forced to be zero.

$$C_f = 0, \qquad\qquad on\ the\ cavity\ surface \tag{3.1}$$

3.1.1 "Thin" Cavity Approach

In the "thin" cavity approach, both the cavity and the boundary layer displacement thickness are assumed to be "small", as shown in Figure 3.1. The inviscid cavity model is based on a linear cavity theory, in which the dynamic and kinematic boundary conditions are applied on the hydrofoil surface underneath the cavity. It should be pointed out that the panels representing the cavity are also assumed to be located on the hydrofoil surface. The dynamic boundary condition on the cavity is simplified by satisfying the condition that the velocity tangent to the hydrofoil is constant, instead of requiring that the total velocity on the cavity surface is constant. For the viscous cavity model, the integral boundary layer equations (Equation 2.7 to 2.10) are solved along the hydrofoil surface, and the effect of cavity is represented through the cavity sources $\hat{\sigma}^c$.

$$\hat{\sigma}^c = \frac{d(U_e h)}{ds} \tag{3.2}$$

where h is the cavity thickness, s is the acr-length along the foil and wake surface. The effects of the cavity sources are incorporated into the edge velocity equation (2.14) as follows:

$$U_e = U_e^{inv} + \Im\{U_e \delta^*\} + \Im\{U_e h\} \tag{3.3}$$

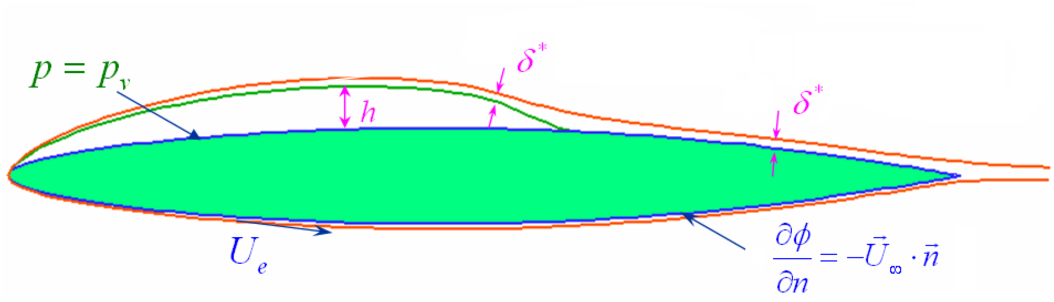

Figure 3.1: The thin cavity approach.

The geometry dependent operator $\Im$ is calculated using the geometry information of the hydrofoil.

3.1.2 Non-linear Cavity Approach

In this approach, the inviscid cavity flow model is based on a fully non-linear boundary element method by [Kinnas and Fine 1991]. For given cavity extent or cavitation number, the cavity shape is determined in an iterative manner until both the dynamic and the kinematic boundary conditions are satisfied on the exact cavity surface. The cavity thickness in this case is not necessarily small. The boundary layer displacement thickness though, is still assumed to be small. The viscous boundary conditions are then applied on the “compound” foil surface, *i.e.* the combined non-linear cavity and foil surface, as shown in Figure 3.2. The integral boundary layer equations are integrated along the combined non-linear cavity and foil surface,

$$U_e = U_e^{inv} + \Im\{U_e \delta^*\} \tag{3.4}$$

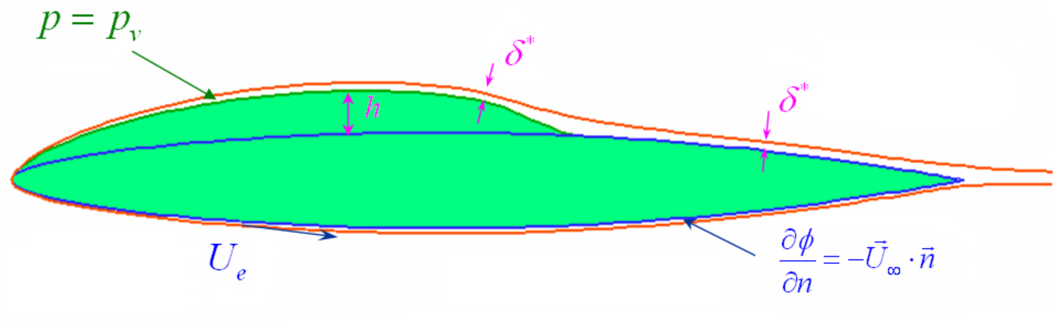

Figure 3.2: The non-linear cavity approach.

Here, the geometry dependent operator $\Im$ is calculated using the “compound” foil geometry.

The most recent version of the non-linear cavity approach, PCPAN/XFOIL, has been validated with experimental measurements [Brewer and Kinnas 1997] and with a commercial code FLUENT [Kinnas et al. 2003]. It needs to be pointed out that the cavity shape by the linear cavity theory is given as the initial guess of the cavity geometry in the non-linear inviscid model. Therefore, the 1st iteration from the non-linear cavity approach should be the same as the “thin” cavity approach.

3.2 PROPCAV/XFOIL in 2-D Applications

This section presents the application of the developed viscous/inviscid interaction method, PROPCAV/XFOIL, to 2-D cavitating hydrofoil problems. The 3-D inviscid cavity model (PROPCAV) was modified to solve unsteady 2-D cavitating hydrofoil problem, and re-named as PROPCAV-2D [Lee 2007].

Figure 3.3 shows a sketch of how to modify PROPCAV for 2-D applications.

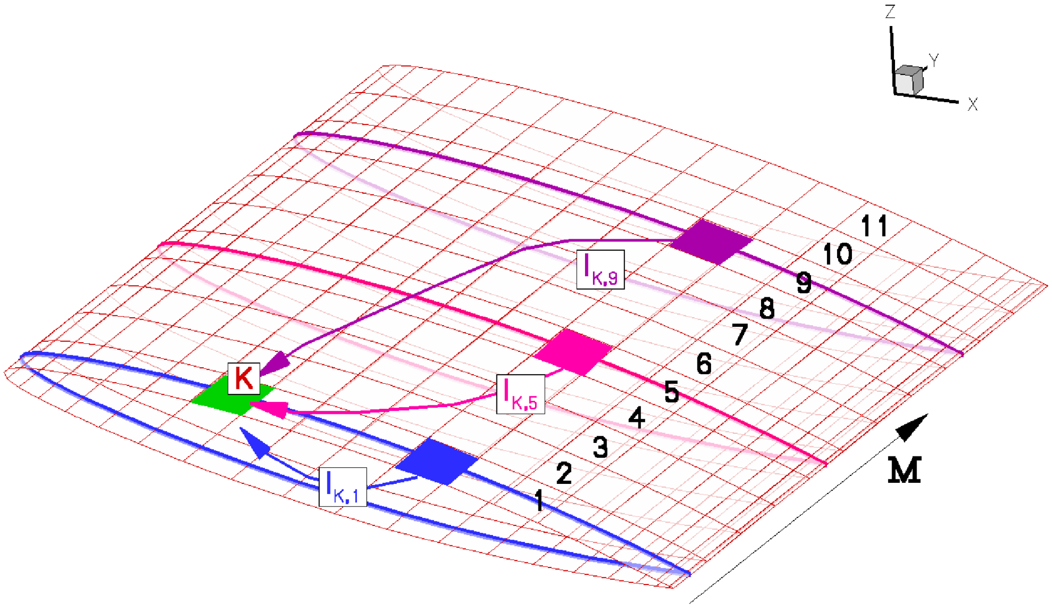

Figure 3.3: Modification of PROPCAV for 2-D cavitating hydrofoil problem, created by H. Lee (2004).

A dummy 3-D hydrofoil is created with all blade sections being the same as the 2-D hydrofoil geometry. $I_{K,M}$ denotes the 2-D dipole or source influence coefficients calculated along each hydrofoil section, where K is the panel index in chord-wise direction, and M is the blade strip index along span-wise direction. To set up the matrices for the system equations, the 3-D influence coefficients in PROPCAV are replaced by 2-D influence coefficients $I_{K,M}$, and $I_{K,1} = I_{K,2} = \ldots = I_{K,MR}$, where MR is the total number of strips on the 3-D dummy foil. The Green's formulation, Equation (2.4), is solved only at one strip ($M = 1$), and then the solutions of $M = 1$ are applied to the other strips $M = 2, \ldots, MR$.

Compared with previously developed 2-D inviscid cavity models [Kinnas and Fine 1991], PROPCAV-2D has the advantage of being able to search cavity detachment point and predict both back and face side cavities for unsteady cavitating hydrofoil. The disadvantage is that the dynamic and kinematic boundary conditions are applied on the foil surface underneath the cavity, and the coupling of PROPCAV-2D and XFOIL at each blade section is indeed a thin cavity approach.

3.3 Results

In this section, the inviscid cavity solutions for two sample foil geometries are studied by using both the "thin" cavity approach (PROPCAV-2D) and the non-linear cavity approach (PCPAN non-linear).

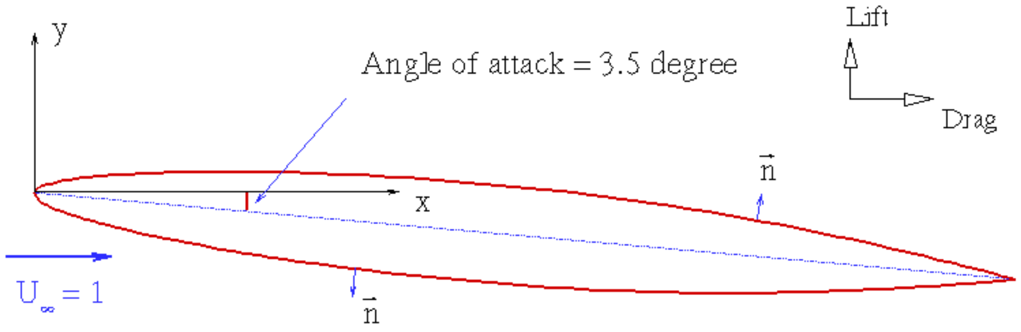

Figure 3.4: The geometry of sample foil 1.

3.3.1 Sample Case 1

Figure 3.4 shows the geometry of a symmetric foil, named sample foil 1. It is with NACA66 thickness distribution, with the maximum thickness to chord length ratio $t_{max}/C = 0.10$, and the chord length is $C = 1.0$. The inflow velocity is non-dimensionalized and $U_\infty = 1.0$. The foil is placed at an angle of attack of $\alpha = 3.5^o$. The cavitation number is $\sigma = 0.90$, where $\sigma = \frac{P_o - P_v}{\frac{1}{2}\rho U_\infty^2}$. ρ is the density of the fluid. P_o is the pressure far upstream, and P_v is the vapor pressure.

Figure 3.5 compares the inviscid cavity shapes at $\sigma = 0.90$ from both the “thin” cavity approach (PROPCAV-2D) and the fully non-linear cavity approach (PCPAN non-linear). For the same cavitation number, the “thin” cavity approach predicts slightly longer cavity than the non-linear cavity approach. Figure 3.6 shows the inviscid cavitating pressure distributions on the sample foil surface from both approaches, where Cp is defined as $Cp = \frac{P - P_o}{0.5\rho U_\infty^2}$.

It is known that, if the predicted cavity shape is correct, the *inviscid wetted pressure* calculated on the “compound” foil surface (combined foil + cavity surface)

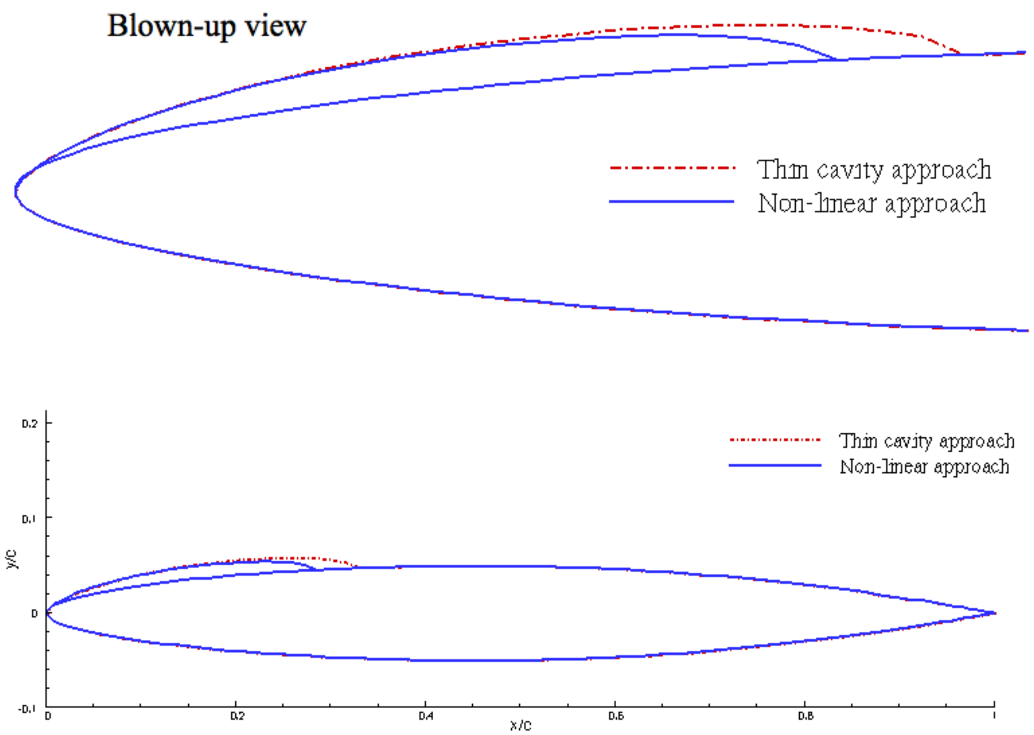

Figure 3.5: Comparison of the cavity shapes using the “thin” cavity approach (PROPCAV-2D) and the non-linear cavity approach (PCPAN non-linear). Sample Foil 1, $\sigma = 0.90$.

will recover the *inviscid cavitating pressure* on the foil. The non-linear cavity approach (PCPAN non linear), as expected, predicts the correct cavity shape, and the inviscid wetted pressure on the "compound" foil surface recovers the inviscid cavitating pressure on the foil, as shown in Figure 3.7. For the "thin" cavity approach, Figure 3.8 shows that there are some differences between the wetted pressure on the "compound" foil and the inviscid cavitating pressure on the foil. The zone name "PCPAN 1st iteration" in Figure 3.8 denotes the first iteration of the non-linear inviscid cavity approach. As discussed in [Kinnas et al. 1994], the inviscid solution from the "thin" cavity approach (PROPCAV-2D) should be the same as that from the first iteration of the non-linear inviscid cavity approach (PCPAN 1st iteration). Figure 3.8 proves that PROPCAV-2D produces the same solution as that from the first iteration of the 2-D inviscid model (PCPAN 1st iteration).

The discrepancy between the "thin" cavity approach and the non-linear cavity approach enlarges when the cavity is extremely thick. For general propulsor flows, the differences between the two approaches are acceptable. Sample Run 2 in the following section shows that the differences can be negligible when the predicted cavity is very thin.

3.3.2 Sample Case 2

A 2-D hydrofoil with a general shape is considered, as shown in Figure 3.9. The foil is of NACA66 thickness distribution with $t_{max}/C = 0.10$, and of $a = 0.8$ camber distribution with $f_{max}/C = 0.06$. The flow is uniform and at an angle of attack of $\alpha = 0.0^o$. The cavitation number is $\sigma = 0.82$.

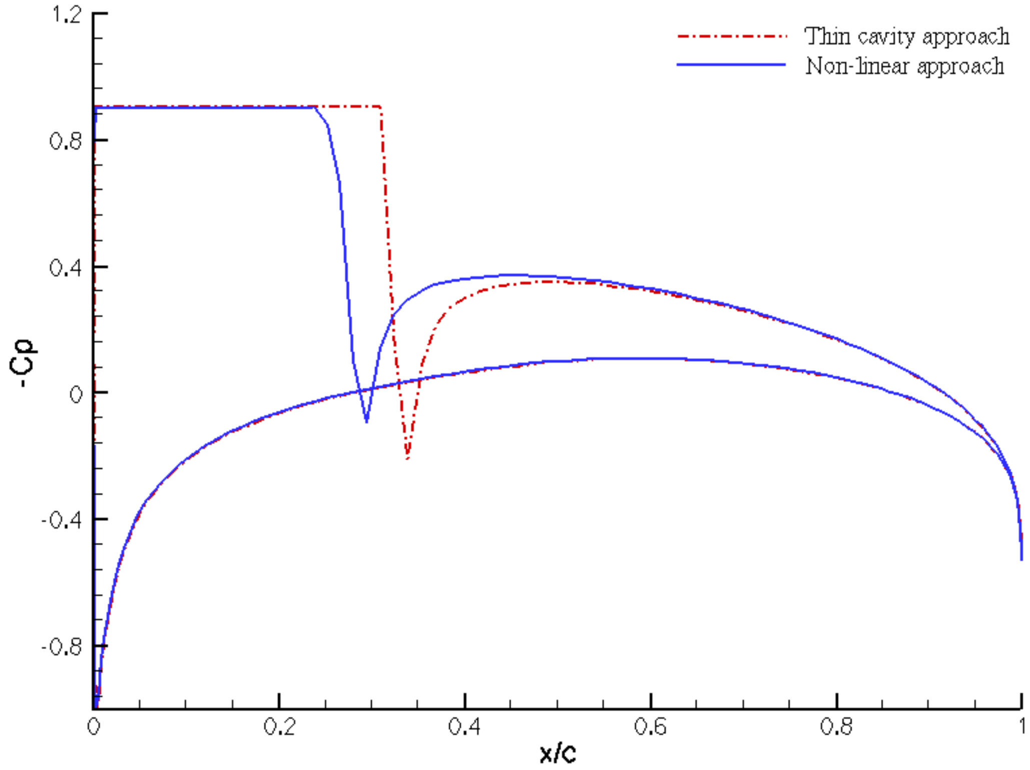

Figure 3.6: Comparison of the inviscid cavitating pressure using the thin cavity approach (PROPCAV-2D) and the non-linear approach (PCPAN non-linear). Sample Foil 1, $\sigma = 0.90$.

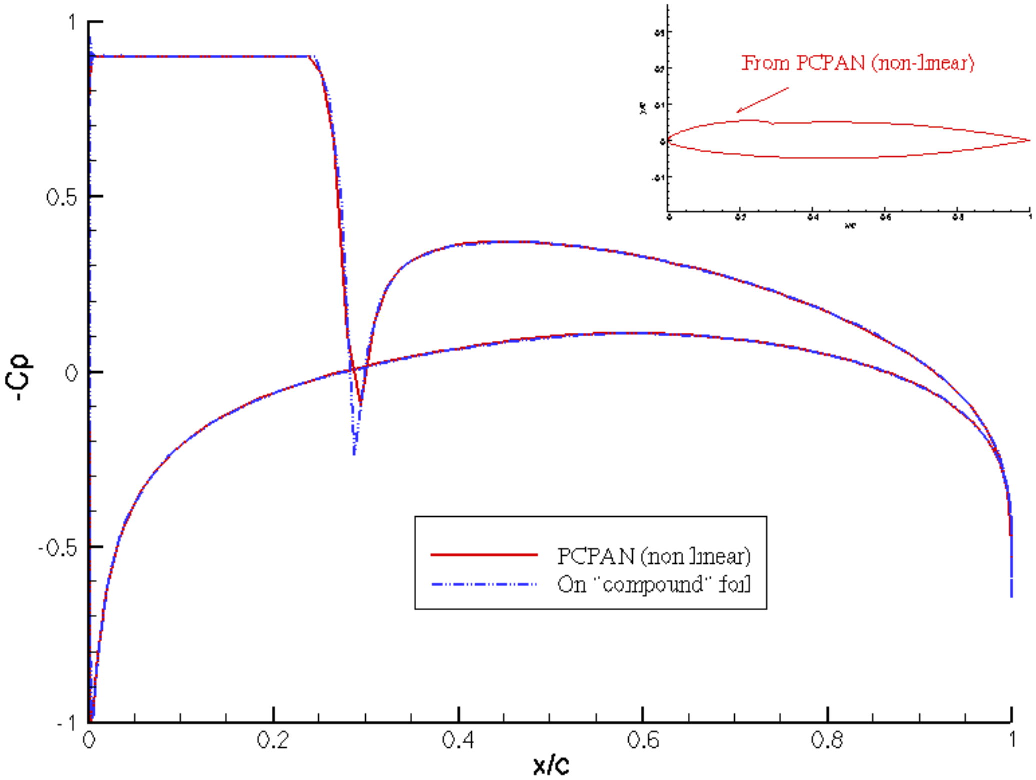

Figure 3.7: Inviscid wetted pressures on “compound” foil vs. inviscid cavitating pressure on the foil, by non-linear approach (PCPAN). Sample Foil 1.

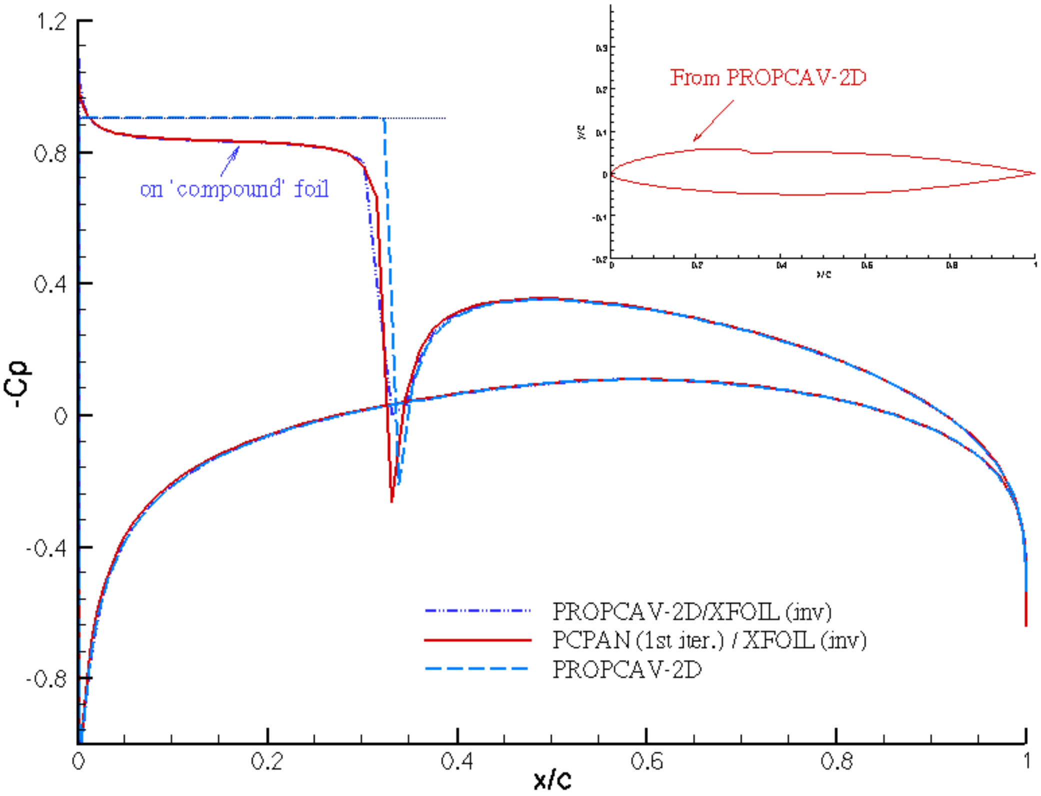

Figure 3.8: Inviscid wetted pressures on "compound" foil vs. inviscid cavitating pressure on the foil, by "thin" cavity approach (PROPCAV-2D and PCPAN 1st iteration). Sample Foil 1.

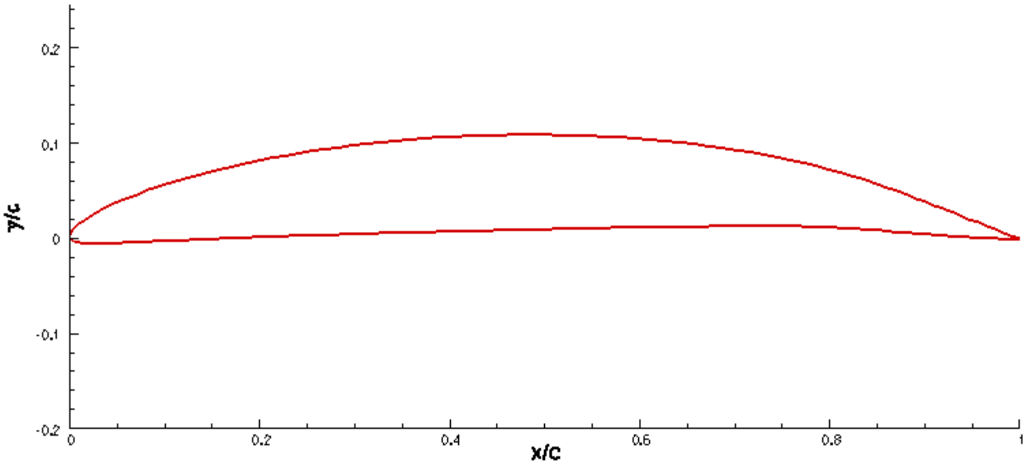

Figure 3.9: Foil geometry and run conditions for sample foil 2.

Figure 3.10 shows the cavity shapes, which detach from the mid chord, by the "thin" cavity approach and the non-linear approach. As expected, the differences between the two approaches are negligible. Figure 3.11 depicts the inviscid cavitating pressure distributions on the foil surface from both approaches.

3.4 Viscous Effects on Cavity

In this section, the effect of viscosity on cavitation is investigated by using the 2-D viscous/inviscid interaction method and a commercial software FLUENT. Since the non-linear cavity approach predicts the correct cavity shape, results from PCPAN (non-linear) XFOIL are addressed here to analyze the inviscid and viscous solutions and verified with the viscous model of FLUENT.

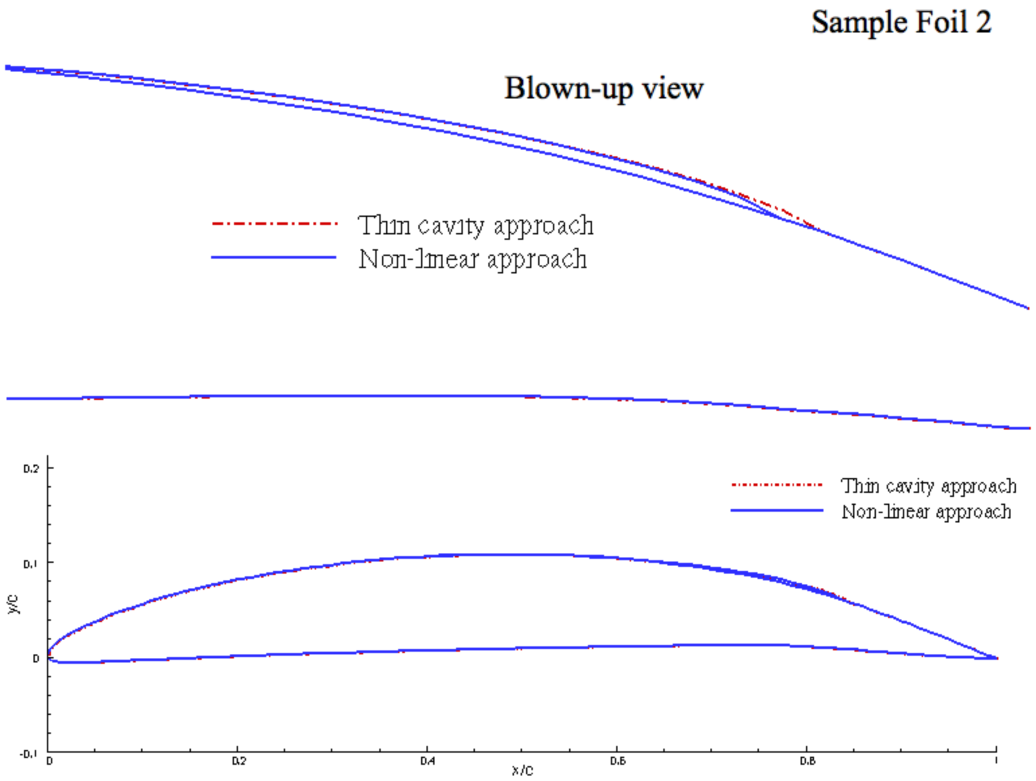

Figure 3.10: Comparison of the cavity shapes using thin cavity and non-linear approach. Sample Foil 2, $\sigma = 0.82$.

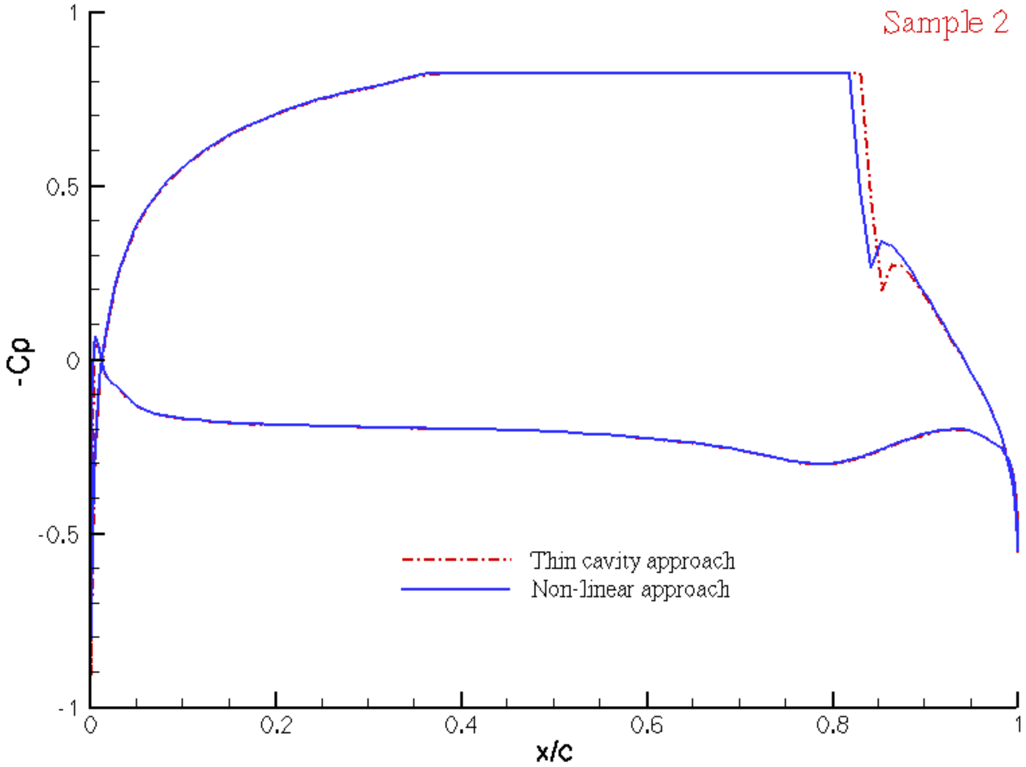

Figure 3.11: Comparison of the inviscid cavitating pressure using thin cavity and non-linear approach. Sample Foil 2, $\sigma = 0.82$.

2-D Viscous/Iniscid Interaction

The foil geometry and run conditions in Sample Run 1 are used for the test in this section. The flow Reynolds number is $Re = 1.0 \times 10^6$, where $Re = U_\infty C/\nu$. C is the foil chord length and ν is the kinematic viscosity of water. The flow turbulence level is equal to 1%. Forced transition at the foil leading edge is applied on both the pressure and suction sides of the hydrofoil. The convergence criterion for the integral boundary layer analysis is $1.0e-5$. It takes less than 1.0 minute to finish both the inviscid and viscous analysis on a SUN BLADE 2000 ($2 \times$ 1.2GHz, 8G RAM) workstation.

Figure 3.12 compares the inviscid and viscous cavitating pressure distributions on the foil surface calculated from the non-linear cavity approach. The cavity length is fixed at $l = 0.30$ for both the inviscid and viscous runs. The viscous pressure on the cavity surface, denoted by PCPAN/XFOIL (viscous), is nearly constant but not fully flat. The reason is that the dynamic boundary condition, which requires a constant total velocity on the cavity, is not fully satisfied. In addition, it is noted that the viscous pressure on the face side is affected by the dynamic boundary condition on the cavity, as also observed in the previous work [Kinnas et al. 1994; Brewer and Kinnas 1997]. Theoretically, the viscous pressure on the face side should not be affected; and the reason for that is still under investigation. The correction scheme presented in [Kinnas et al. 1994] is applied to correct the dynamic boundary condition, and flat pressure distribution over the cavity was obtained, as denoted by PCPAN non-linear(corrected) in Figure 3.12. The cavity shapes before and after applying the correction scheme are shown in Figure 3.13.

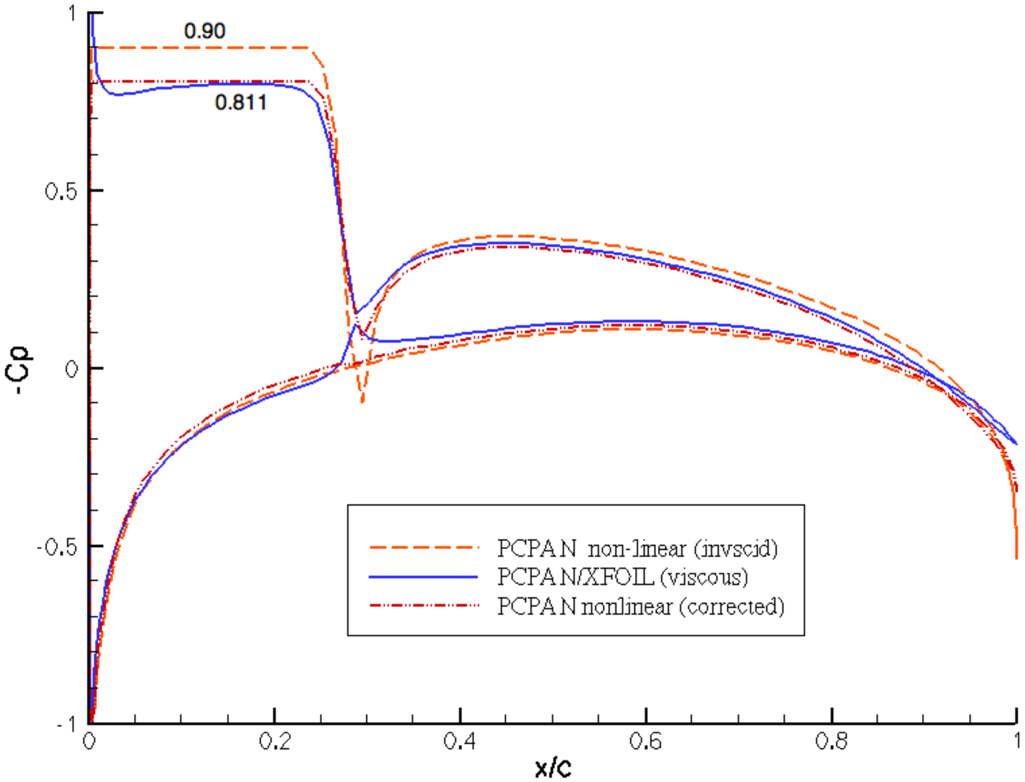

Figure 3.12: Comparison of inviscid and viscous cavitating pressure using the nonlinear approach, PCPAN(non linear)/XFOIL. Sample Foil 1. Fixed cavity length, $l = 0.30$.

The correction has almost no effects on the predicted cavity shape.

Figure 3.12 indicates that, in the case of given cavity length, viscosity decrease the pressure magnitude on the cavity, and thus “decreases” the cavitation number. The cavity shapes in Figure 3.13 actually correspond to the real viscous flow at the “real” cavitation number $\sigma = 0.811$. Alternatively, for the same cavitation number, the predicted cavity when including viscosity effect will have smaller extent and volume than that from the inviscid solution, as illustrated in Figure 3.14.

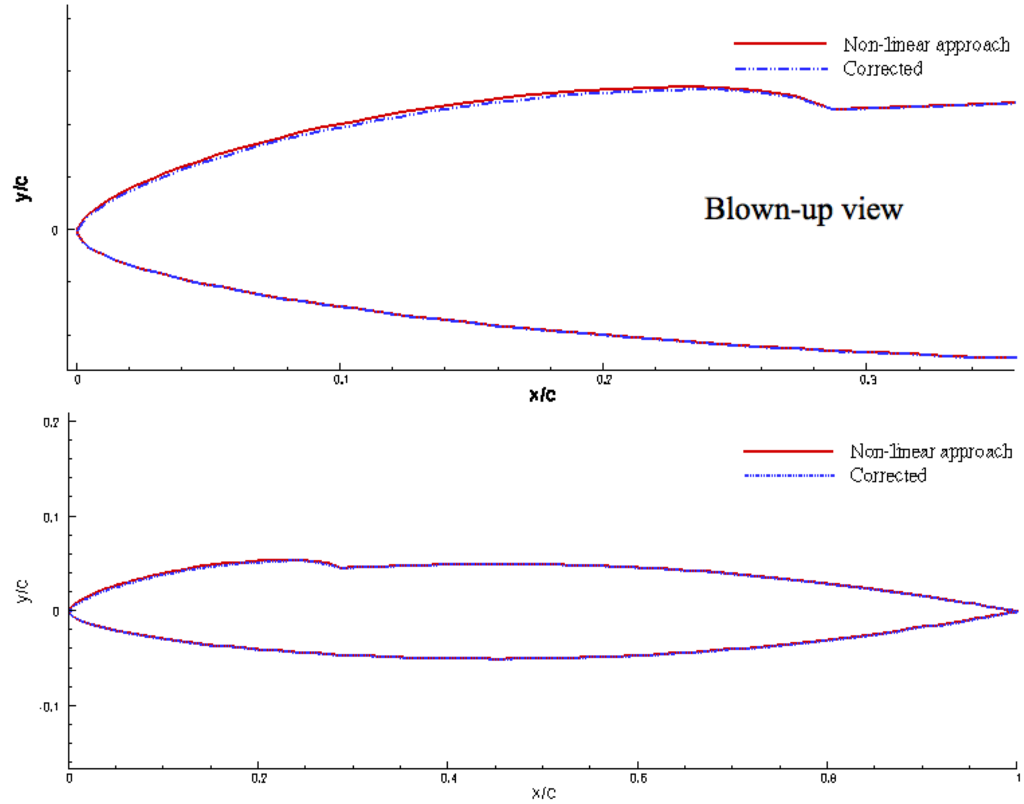

Figure 3.13: Comparison of cavity shapes before and after applying correction. Sample Foil 1. Cavity length, $l = 0.30$, “actual” cavitation number $\sigma = 0.811$.

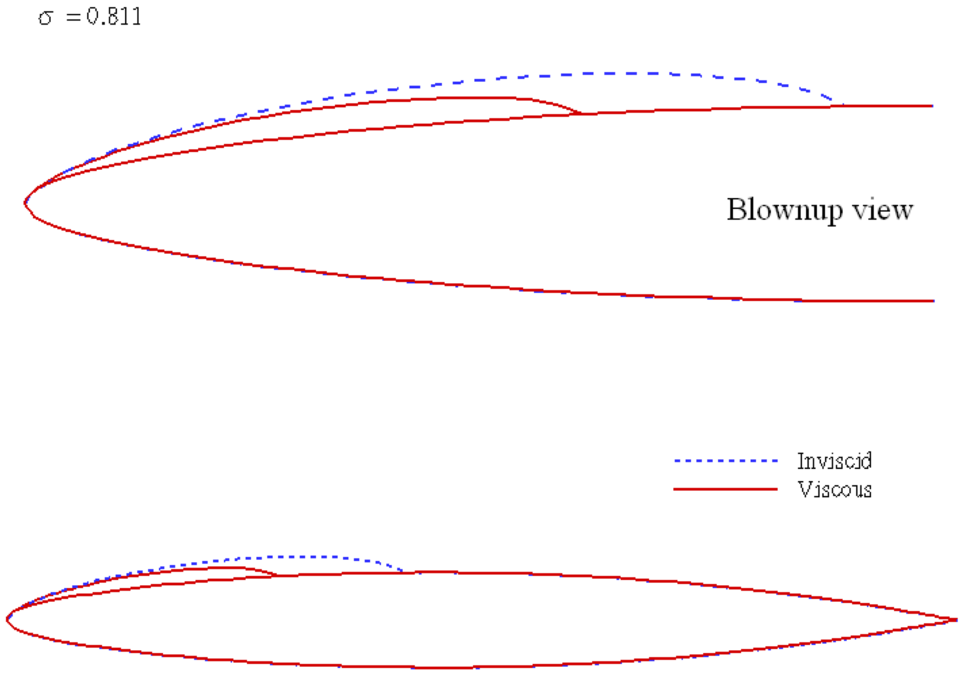

Figure 3.14: Comparison of inviscid and viscous cavity shapes for $\sigma = 0.811$. Sample Foil 1.

Verification with FLUENT

In order to verify the viscous solution from the viscous/inviscid interaction method, a commercial RANS solver FLUENT is applied to model the viscous flow around the “compound” foil, of which the geometry is from PCPAN(nonlinear)/XFOIL. On the cavity surface, the friction coefficient is set as zero, $C_f = 0$.

Figure 3.15 shows the flow domain and the boundary conditions fed into FLUENT. The flow Reynolds number is 1.0×10^6. The flow turbulence level is set as 1%. The Spalart-Allmaras (S-A) model is chosen to solve this problem. On the foil surface, non-slip wall boundary condition is applied. On the cavity surface, slip boundary condition is applied instead to obtain zero friction force on the cavity surface. Figure 3.16 shows the blown-up view of the mesh around the leading edge and trailing edge of the cavity and the foil. There are totally $199,968$ cells and $110,724$ nodes in the flow domain. It takes 5314 iterations for the flow to reach a convergence of continuity at $1.0e-5$. The total run time is about 8 hours using a SUN BLADE 2000 (2 × 1.2GHz, 8G RAM) workstation.

The Spalart-Allmaras model requires that the non-dimensional wall distance y^+ to be equal to 1 for a wall bounded flow. y^+ is defined as $y^+ = \frac{u_* y}{\nu}$, where u_* is the friction velocity at the nearest wall, and y is the nearest wall and ν is the kinematic viscosity of the fluid. Figure 3.17 shows the y^+ distribution on the foil and cavity surface. Noted that y^+ is equal to zero on the cavity surface because of the slip boundary condition there. On the foil surface, the requirement that the y^+ value should be very close to 1 for the Spalart-Allmaras model is satisfied.

Table 3.1: Comparison of lift and drag forces between PCPAN/XFOIL and FLUENT (viscous, cavitating).

Force	PCPAN/XFOIL	FLUENT
C_L^{vis}	0.3692	0.3744
C_D	0.0174	0.0159

Figure 3.18 compares the viscous cavitating pressure using PCPAN (non linear)/XFOIL and FLUENT S-A model. The comparison is pretty good except that FLUENT S-A model has difficulties in predicting correct pressure at the stagnation point. Table 3.1 gives the viscous lift and drag forces from PCPAN (non-linear)/XFOIL and FLUENT S-A model. The difference in lift force between the two models is very small and under 1.5%, but the difference in drag force is about 10% due to the differences in the evaluated pressures at the leading edge and trailing edge of the cavity and foil.

3.5 Summary

The 3-D inviscid model (PROPCAV) has been modified to predict flow around 2-D cavitating hydrofoil, under a new name of PROPCAV-2D. PROPCAV-2D was coupled with the 2-D integral boundary layer analysis code XFOIL by using a “thin” cavity approach. PROPCAV-2D/XFOIL was verified with a previously developed 2-D viscous/inviscid interaction method (PCPAN/XFOIL), which uses a non-linear cavity approach. The differences between the “thin” cavity approach and the non-linear cavity approach were found to be acceptable. The viscous solution

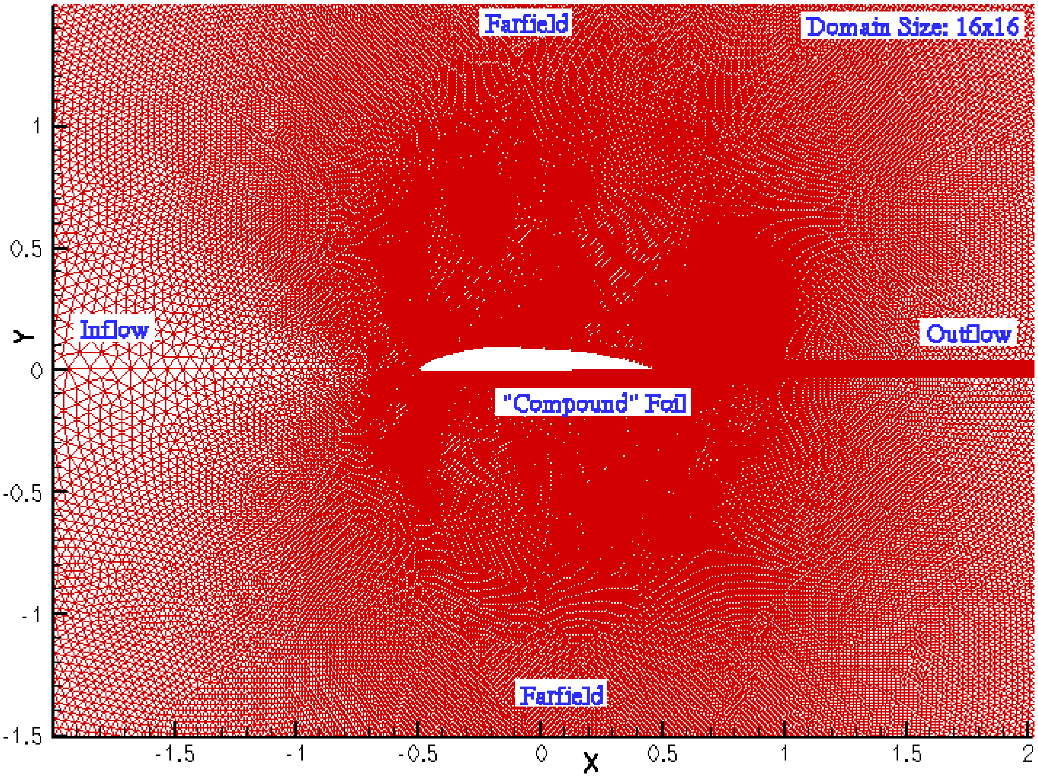

Figure 3.15: Flow domain and boundary conditions of 2-D FLUENT run.

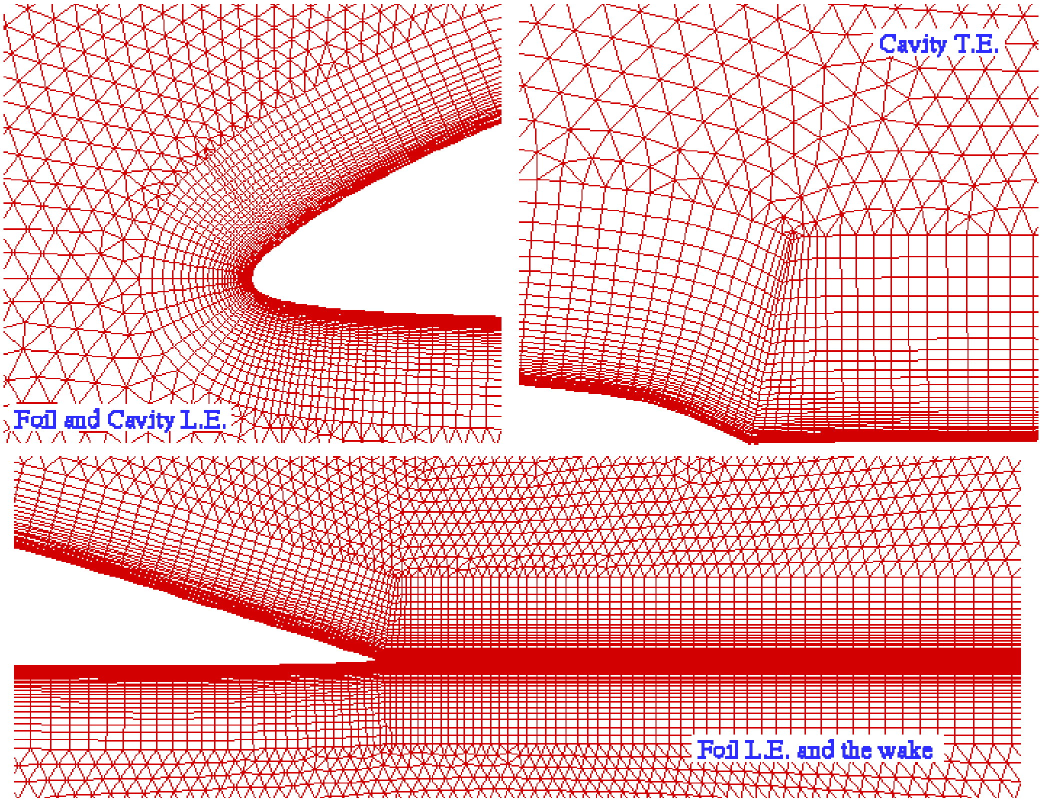

Figure 3.16: Blown-up view of the mesh around the foil and cavity leading and trailing edges. FLUENT run.

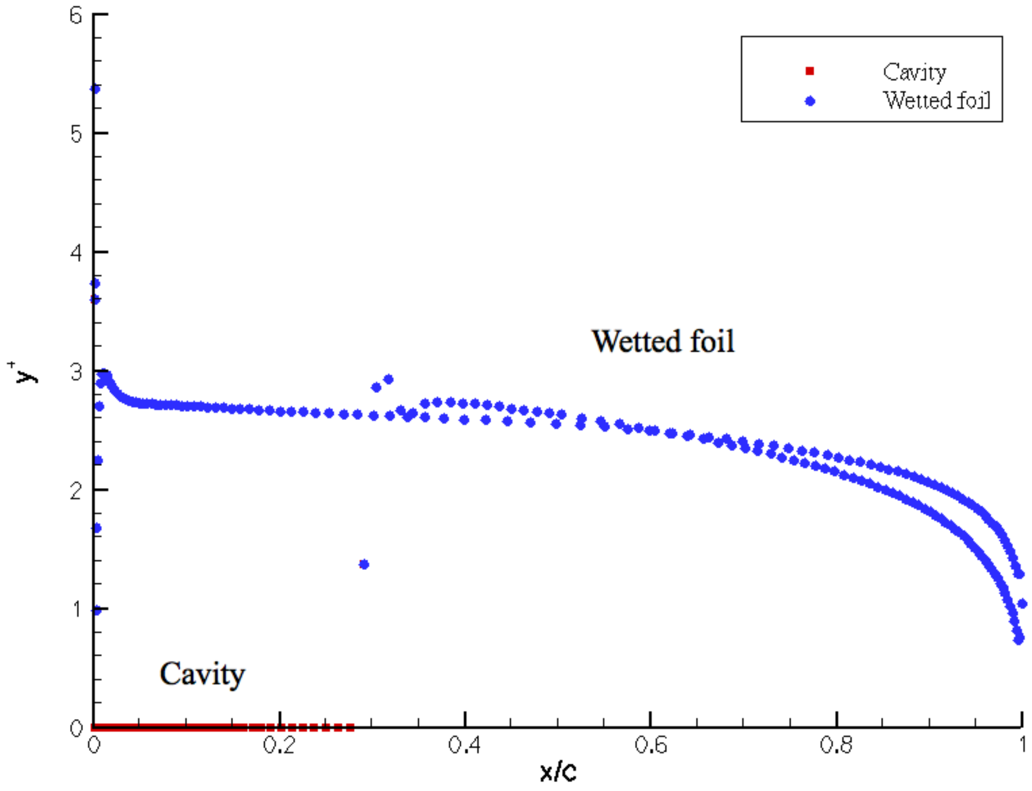

Figure 3.17: Plot of y^+ distributions on the foil and cavity for the FLUENT run.

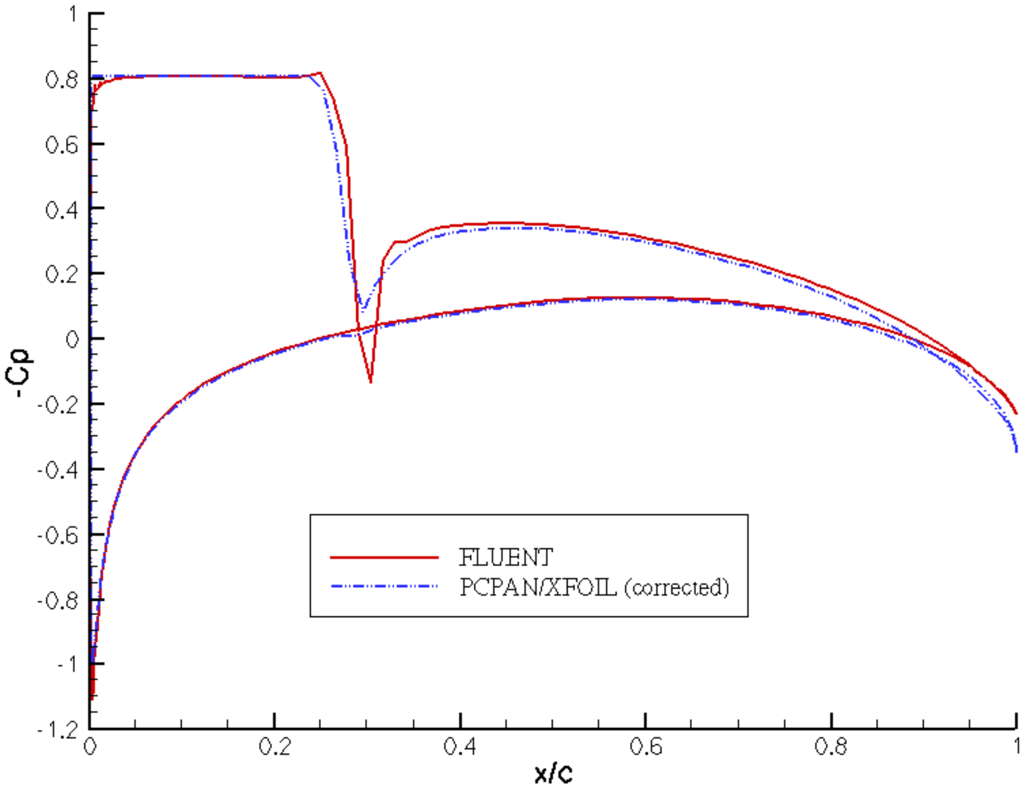

Figure 3.18: Comparison of the viscous pressures on the foil and cavity surefaces using the present method (PCPAN non-linear/XFOIL) and the FLUENT Spalart-Allmaras model (applied on the foil and cavity predicted by the present method).

from the non-linear cavity approach was verified by using the commercial solver FLUENT. The results compared well. It is obvious that the required CPU time for the present VII method is far less than the viscous model of FLUENT.

In 3-D inviscid propulsor flow problem, as presented in Chapter 2, the cavitating kinematic and dynamic boundary conditions are applied on the approximated flow boundary which is the blade surface underneath the cavity, to avoid re-paneling and re-calculation of influence coefficients. Therefore, the present viscous/inviscid interaction method, PROPCAV/XFOIL, applies the "thin" cavity approach to predict the cavitating performance of propulsor flows. The studies in this chapter indicate that the present method is able to predict, in a computationally efficient manner, the effects of viscosity on sheet cavitation. Viscosity not only changed the forces on the foil, but also affected the characteristics of cavity. It was shown that, for fixed cavity extent, viscosity decreased the pressure distribution on the cavity, *that is*, the cavity extent corresponded to a smaller cavitation number. That means, in the case that the cavitation number is known, the extent and size of the viscous cavity will be smaller than that predicted by the inviscid model.

Chapter 4

Viscous Flow around Rudders and Single Component Propulsors

In this chapter, the developed viscous/inviscid interaction method is used to investigate steady viscous flows around rudder, bare duct, and open propeller under wetted and/or cavitating conditions. Coupling of the inviscid and viscous modeling is applied on strips of the propulsor blade. Results from the present method are compared with those from a commercial CFD software (FLUENT) and experimental measurements.

4.1 Steady Wetted Rudder Flow

In this section, the steady viscous flow around a non-cavitating 3-D rudder is studied by using PROPCAV/XFOIL and the Reynolds Stress turbulent model (RSM) of FLUENT. Pressure distributions and lift forces predicted by the two models are compared.

Rudder Geometry and Run Conditions

The rudder is symmetric with respect to its mid span, with NACA66 thickness distribution and $a = 0.8$ camber mean line at each section. The maximum

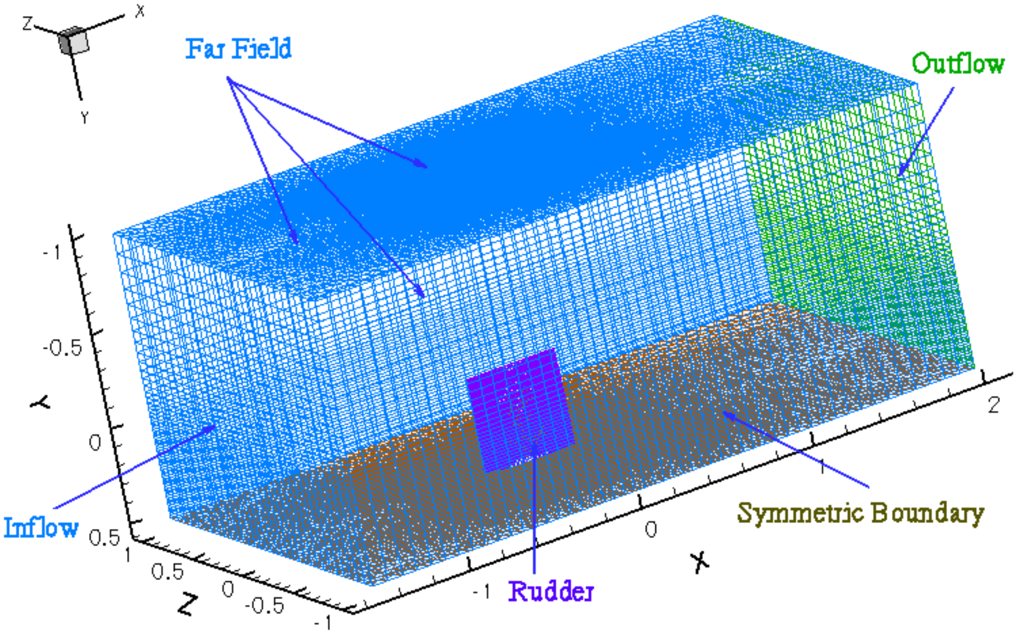

Figure 4.1: Flow domain and boundary conditions used in FLUENT for the 3-D rudder run.

camber-chord ratio f_{max}/C is zero everywhere on the rudder. Over the span, the thickness distribution is parabolic, and the maximum thickness-chord ratio is located at the rudder mid span, with $t_{max}/C = 0.16$. At both ends, the rudder thickness is forced to be zero in order to minimize the cross flow. Figure 4.1 shows half of the rudder geometry. There is no skew and no rake, but with pitch distribution. Figure 4.2 shows the twist angles distributed along the span of the rudder. The rudder length is of $L = 1.0$.

The inflow to the rudder is uniform $U_\infty = 1$. The hydrostatic effect is not considered in this case, and Froude number is set to $Fr = 9999$. Figure 4.3

shows the circulation distribution over the rudder span. Γ_s is defined as $\Gamma_s = \Delta\phi_{TE}/2\pi R U_\infty$, where $\Delta\phi_{TE}$ is the potential jump at the trailing edge of the rudder, R is the section location on the rudder span. It is observed that the circulation slope at both ends are finite, and thus the cross flow effect is reduced. For the viscous run, the Reynolds number, $Re = \frac{U_\infty L}{\nu}$, based on the length of the rudder, $L = 1.0$, is equal to 1.0×10^6. ν is the kinematic viscosity of water. The flow disturbance level is set to 1% in both models. The convergence criterion for PROPCAV/XFOIL is $1.0e-5$. The total run time for PROPCAV/XFOIL is less than 1.0 minute on a SUN BLADE 2000 (2 × 1.2GHz, 8G RAM) workstation.

The computational domain and boundary conditions used in the Reynolds Stress turbulent model (RSM) of FLUENT are shown in Figure 4.1. Since the rudder is symmetric, only a half of the rudder geometry is used to save computational time. Non-slip wall boundary condition is applied on the rudder surface, and symmetric boundary condition is applied on the rudder middle plane. There are totally $1,604,400$ cells and $824,847$ nodes in the flow domain. It takes 509 iterations for the flow to converge, and the total run time is about 1.0 hour using the paralleled version of FLUENT on a cluster with 16 CPUs of AMD Opteron (1.6GHz & 2G RAM per CPU).

Results

The pressure coefficient Cp on the rudder is defined as $Cp = \frac{P-P_0}{\frac{1}{2}\rho U_\infty^2}$, where P_0 is the pressure far upstream, and $U_\infty = 1$ for uniform inflow. Figure 4.4 compares the inviscid wetted pressure distributions on the rudder at three different lo-

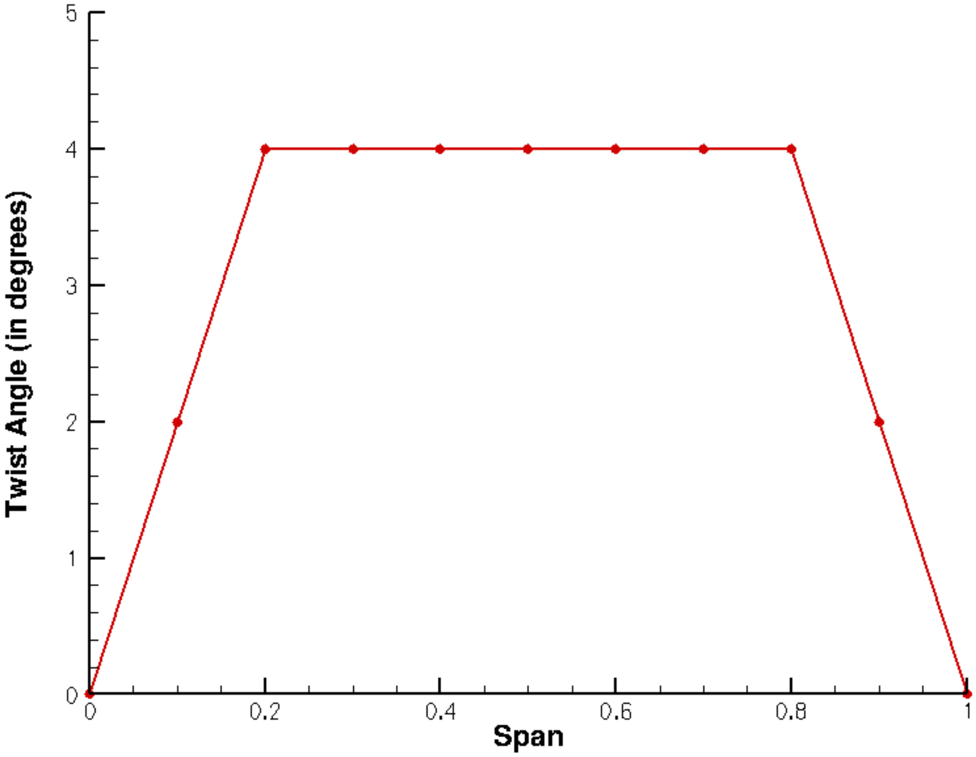

Figure 4.2: Distribution of twist angle along the span of the rudder.

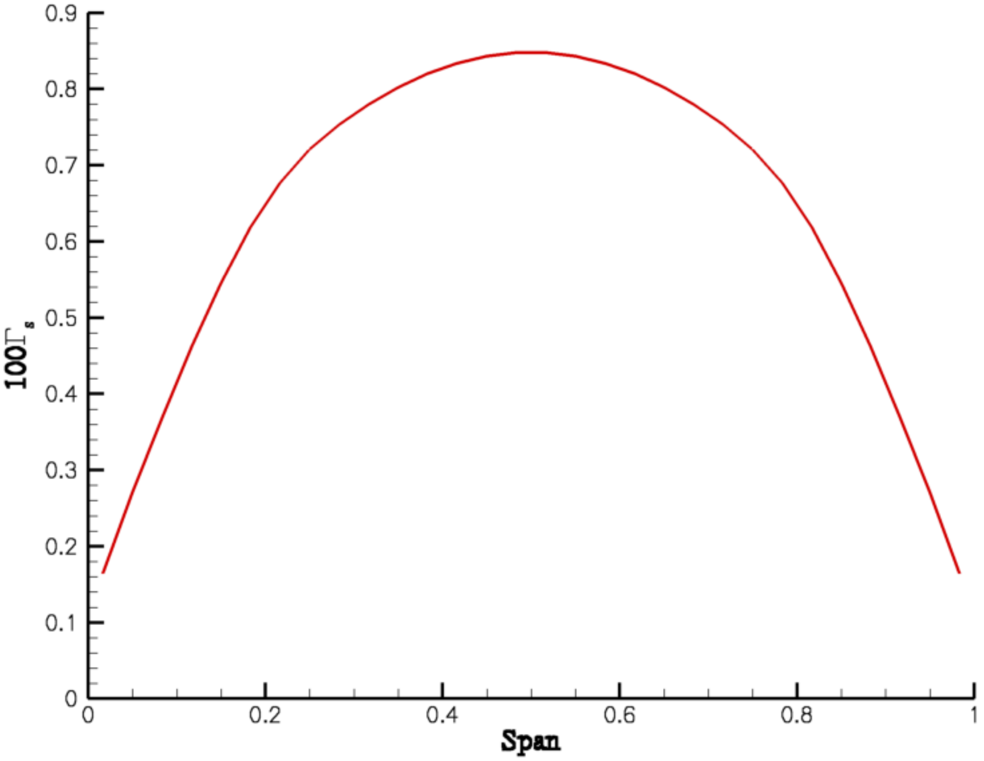

Figure 4.3: Circulation distribution over the rudder span.

Table 4.1: Comparison of inviscid and viscous lift forces on the rudder between PROPCAV/XFOIL and FLUENT RSM model.

Force	PROPCAV/XFOIL	FLUENT RSM
C_L^{inv}	0.157	0.168
C_L^{vis}	0.145	0.161

cations $r/R = 0.05, 0.25$ and 0.483 between PROPCAV and FLUENT inviscid model. The results compare very well with each other. Figure 4.5 shows the non-dimensional wall distance y^+ distribution on the rudder surface, which satisfies the requirement of $30 < y^+ < 300$ for the wall functions for the RSM model. Figure 4.6 compares the viscous wetted pressure distributions between PROPCAV/XFOIL and FLUENT RSM model. Results from the two methods agree well with each other except slight differences at the rudder trailing edge. Table 4.1 gives the inviscid and viscous lift forces predicted by PROPCAV/XFOIL and FLUENT RSM model. There are about 7% differences in the inviscid lift and 10% differences in the viscous lift forces. It is somewhat surprising that the lift forces from the two methods do not compare as well as the pressure distributions. The reason for the discrepancies is probably due to different schemes of integration and/or interpolation used in the two methods.

4.2 Steady Wetted Duct Flow

In this section, the present method (PROPCAV/XFOIL) is applied to investigate the steady wetted flow around a bare duct, DTMB Duct II, which is an

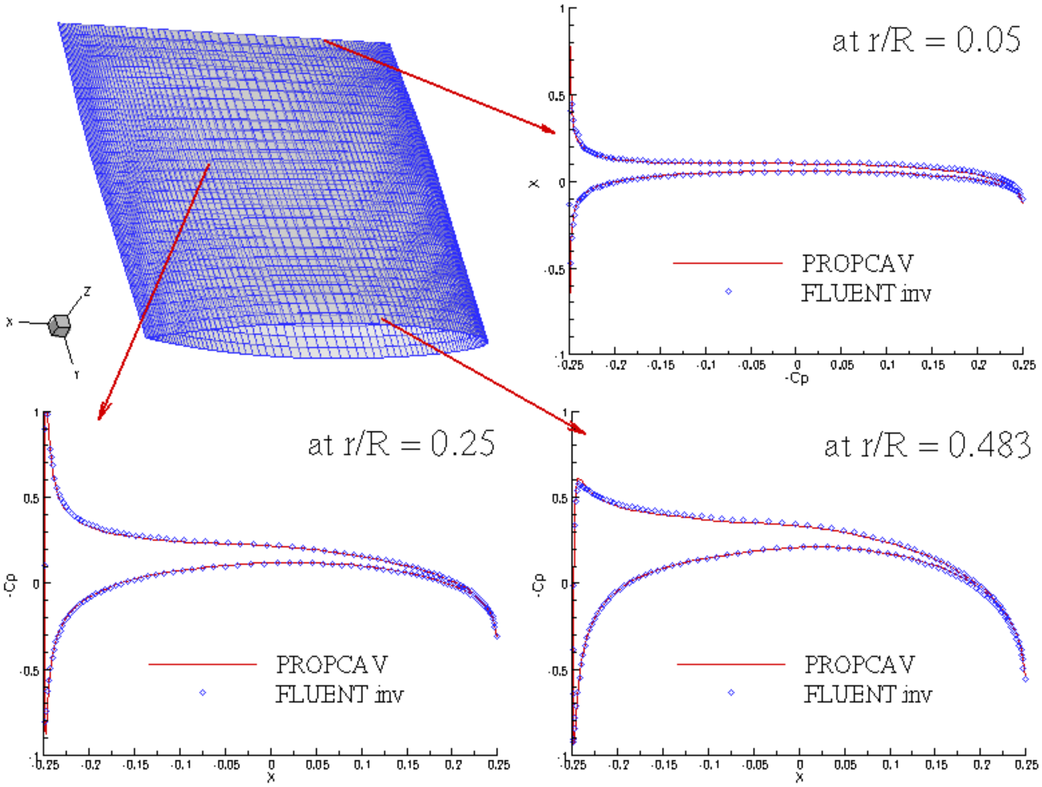

Figure 4.4: Comparison of inviscid wetted pressure distributions on the rudder between PROPCAV (inviscid) and FLUENT inviscid model.

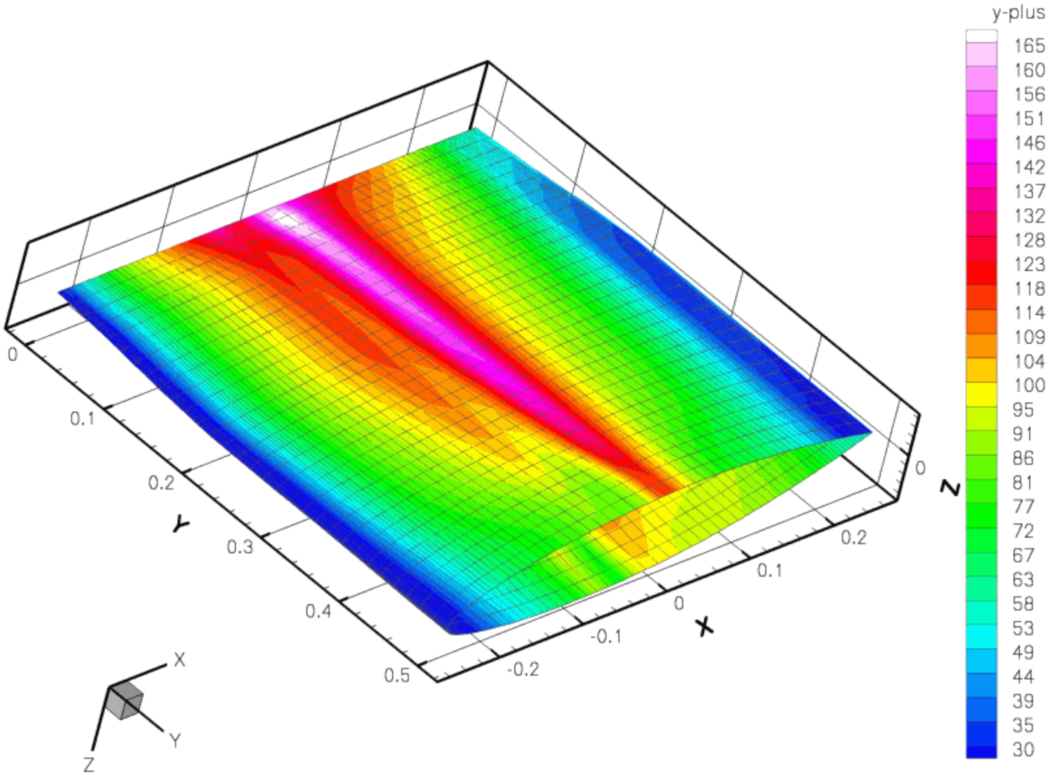

Figure 4.5: y^+ distributions on the rudder surface, FLUENT RSM model.

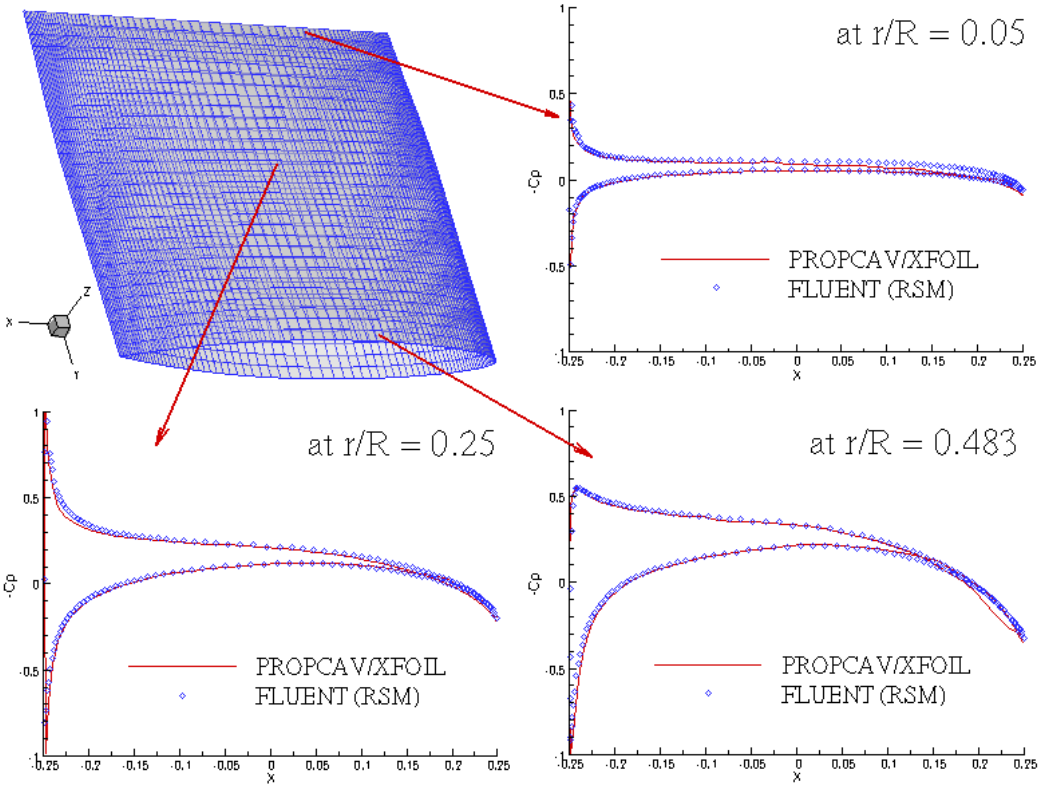

Figure 4.6: Comparison of viscous wetted pressure distributions on the rudder between PROPCAV/XFOIL and FLUENT RSM model.

axisymmetric duct. The predicted pressure distribution are compared with the experimental measurements by [Morgan and Caster 1965].

Duct Geometry and Run Conditions

Figure 4.7 shows the geometry of the DTMB Duct II. The section of the duct is of NACA66 Modified thickness form, with the maximum thickness-chord ratio $t_{max}/C = 0.10$, and of NACA $a = 0.8$ mean camber distribution, with the maximum camber-chord ratio $f_{max}/C = 0.04$. The chord-diameter ratio is $C/D = 0.8$, where C is the chord of the duct section and D is the diameter of the duct taken at the leading edge of the duct. The duct section is placed at zero degree angle of attack. As shown in Figure 4.7, the discretization on the duct used in PROPCAV/XFOIL is of 60 panels in the chordwise direction with cosine spacing, and 150 panels in the circumferential direction with uniform spacing.

The DTMB Duct II is subject to uniform inflow. The hydrostatic effect is also neglected, with Froude number $Fr = 9999$. The flow Reynolds number, $Re_D = \frac{U_\infty D}{\nu}$, based on the duct diameter D is equal to 2.06×10^6. The flow turbulence level is 1%. Forced transition at 5% chord length from the leading edge is applied on both the inner and outer surfaces of the duct in the calculation in accordance with the experiment results. The convergence criterion for the 2-D integral boundary layer analysis is $1.0e - 5$. It takes less than 1.0 minute to finish both the inviscid and viscous analysis of the steady wetted duct flow on a SUN BLADE 2000 (2 × 1.2GHz, 8G RAM) workstation.

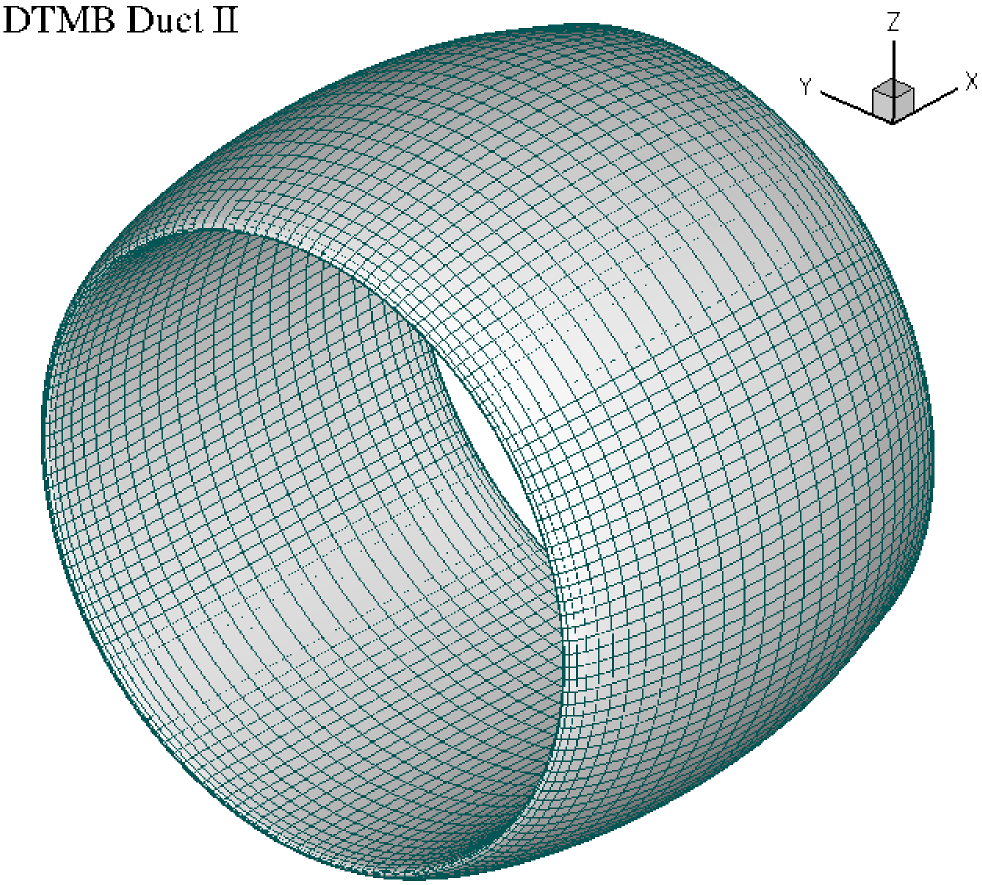

Figure 4.7: Paneled geometry of the DTMB Duct II, viewed from upstream.

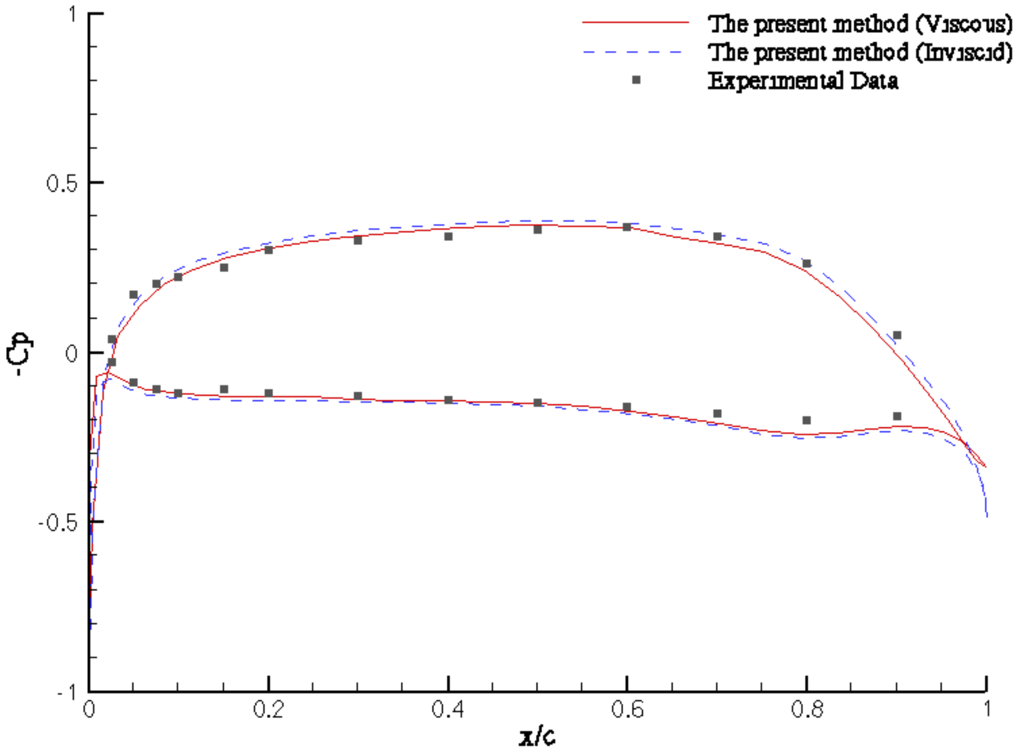

Figure 4.8: Predicted viscous and inviscid pressure distributions on the DTMB Duct II, comparison with the experiment measurement [Morgan and Caster 1965].

Results

The definition of the pressure coefficient on the duct Cp is the same as that of the rudder case. Figure 4.8 shows the predicted inviscid and viscous pressure distributions on the duct compared with the experimental data. The pressure magnitude is decreased due to the effect of viscosity, and the viscous solution from the present method agrees better with the measured pressure by Morgan & Caster [Morgan and Caster 1965].

4.3 Steady Wetted and Cavitating Propeller Flow

This section presents the steady wetted and cavitating flows around a screw propeller DTRC 4119 by using the developed viscous/inviscid interaction method. The 2-D integral boundary layer analysis is performed along the constant radius strips of the propeller blade. The cavity effects are represented by using cavity sources and cavitating velocities which are evaluated on the blade surface underneath the cavity. Numerical results from the present method are compared with Jessup's experimental measurements [Jessup 1989] in the case of wetted flow. Preliminary studies of cavitating flow are also presented.

Figure 4.9 shows the paneled geometry of the propeller DTRC 4119, which is a three-bladed propeller and the geometrical characteristics of which are given in [Jessup 1989]. The discretization on the propeller blade is of 60 panels in the chordwise direction with cosine spacing, and 20 panels in the spanwise direction with uniform spacing. The inflow wake to the propeller is uniform, with the hydrostatic effect ignored, $Fr = 9999.0$. The propeller is tested at different advance ratios, with J_s ranging from 0.5 to 1.1. For the viscous runs, the strip Reynolds number, $Re_C = U_r C/\nu$, at radius $r/R = 0.7$ is constant and equal to 1.0×10^6. $U_r = \sqrt{V_s^2 + (0.7\pi n D)^2}$ is the reference velocity and C is the chord length at $r/R = 0.7$. The flow turbulence level is about 1% according to the experiment. The convergence criterion for PROPCAV/XFOIL is set to $1.0e-5$. In general, it takes less than 1.0 minute to finish the coupling run on a cluster using 1 CPU of AMD Opteron (1.6GHz & 2G RAM per CPU).

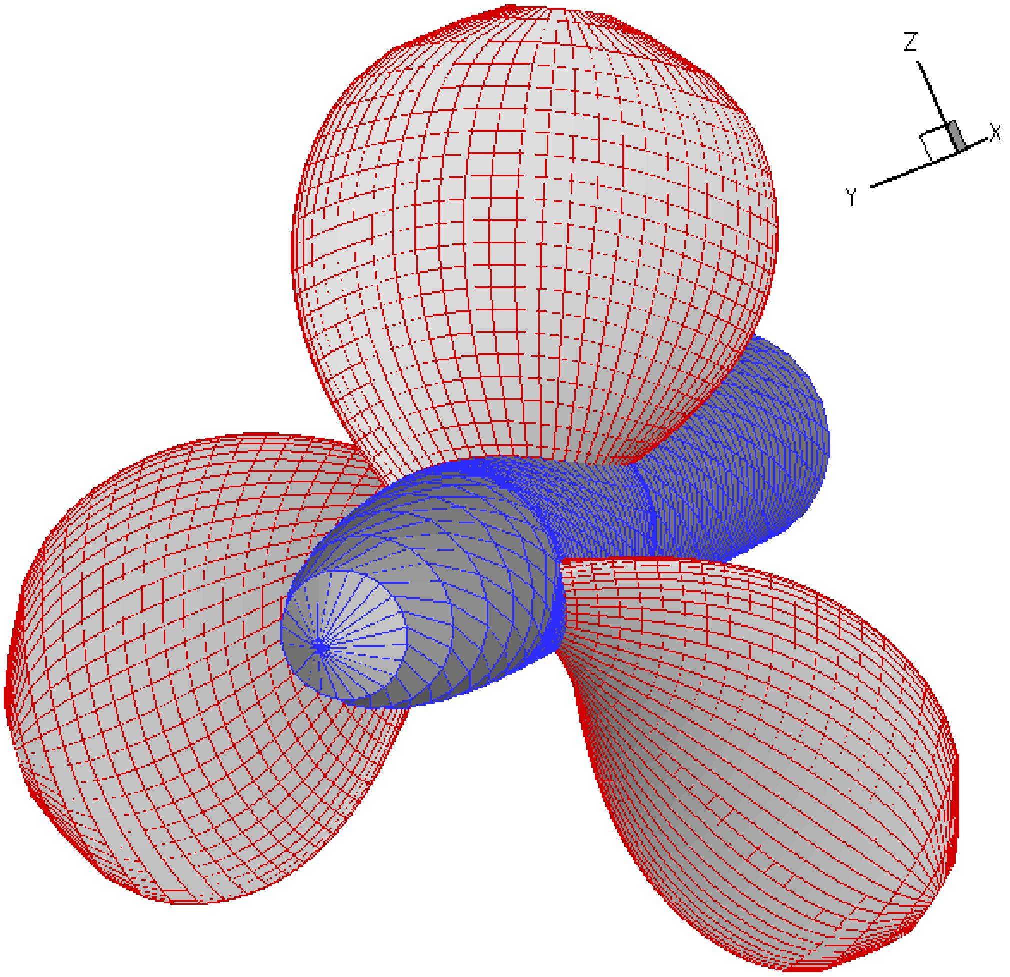

Figure 4.9: Paneled geometry of Propeller DTRC4119.

4.3.1 Fully Wetted Flow

Figure 4.10 compares the predicted inviscid and viscous thrust K_T and torque forces K_Q by PROPCAV/XFOIL at different advance ratios with the measured [Jessup 1989]. The legend, PROPCAV(Inviscid + correction), denotes the viscous blade forces by applying empirical viscous correction to the inviscid solution. A constant friction coefficient $C_f = 0.0035$ (ITTC 1957) is applied everywhere on the blades. It is apparent that the inviscid model, PROPCAV (inviscid), over-predicts the thrust force and under-predicts the torque force. Moreover, the predicted viscous thrust and torque forces by the present viscous/inviscid interaction method, PROPCAV/XFOIL, have better correlation with Jessup's measurements than those predicted by applying empirical viscous corrections.

Validation Results at $J_s = 0.833$

This section presents the comparisons of boundary layer parameters between the predicted by PROPCAV/XFOIL and the measured, at advance ratio $J_s = 0.833$, for both smooth and tripped conditions that are used in [Jessup 1989]. The strip Reynolds number, $Re_C = U_r C/\nu$, is 1.0×10^6. The predicted wetted pressure distributions at different blade strips for smooth condition are also compared with the experimental data.

For the tripped condition, forced transition at $x/c = 0.05$ on both the suction and pressure sides of the blade is used in PROPCAV/XFOIL according to the experiment setup, where c is the chord length at each strip. Figure 4.11 shows the predicted and the measured displacement thickness on the pressure and suction

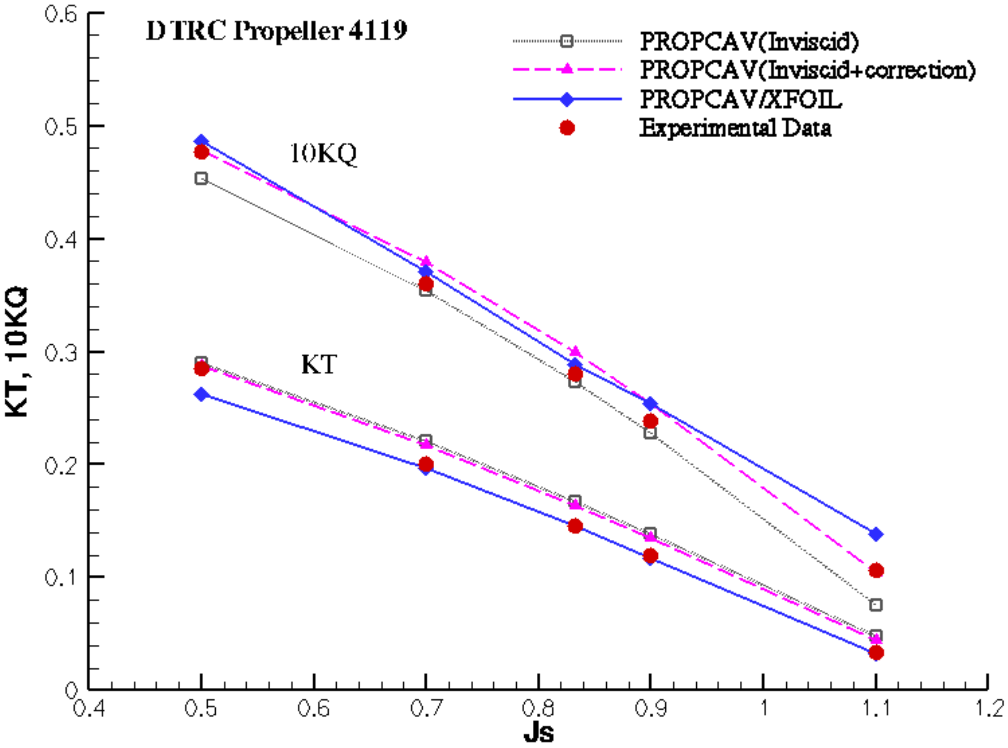

Figure 4.10: Comparison of the predicted wetted blade forces vs. advance ratio J_s by the present method with the measured [Jessup 1989], Propeller DTRC 4119.

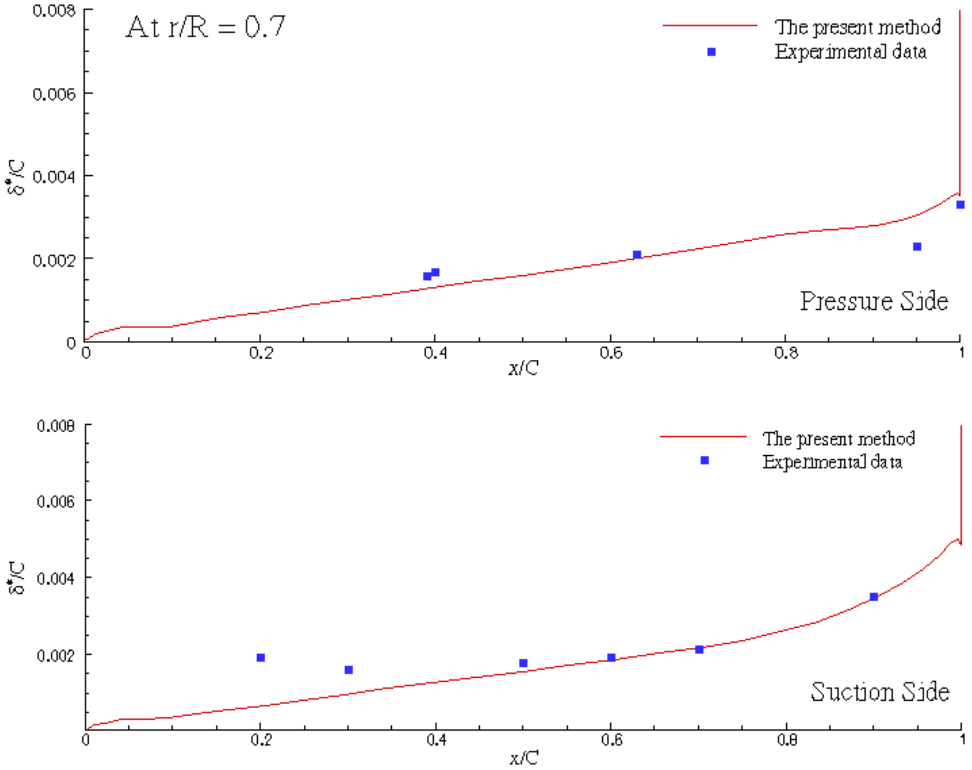

Figure 4.11: The displacement thickness on the pressure and suction sides at strip $r/R = 0.7$ for the tripped condition. $J_s = 0.833$, wetted, Propeller DTRC 4119.

sides at strip $r/R = 0.7$. The comparisons are very good except that the experimental data close to the leading edge on the suction side look questionable. Figure 4.12 compares the section drag coefficient at different strips between PROPCAV/XFOIL and the experiments. The section drag coefficient is defined as $C_D = 2\theta_\infty/c$, where θ_∞ is the momentum thickness at far downstream. x/R denotes that the As shown, the section drag by the present method agrees well with the experimental measurements.

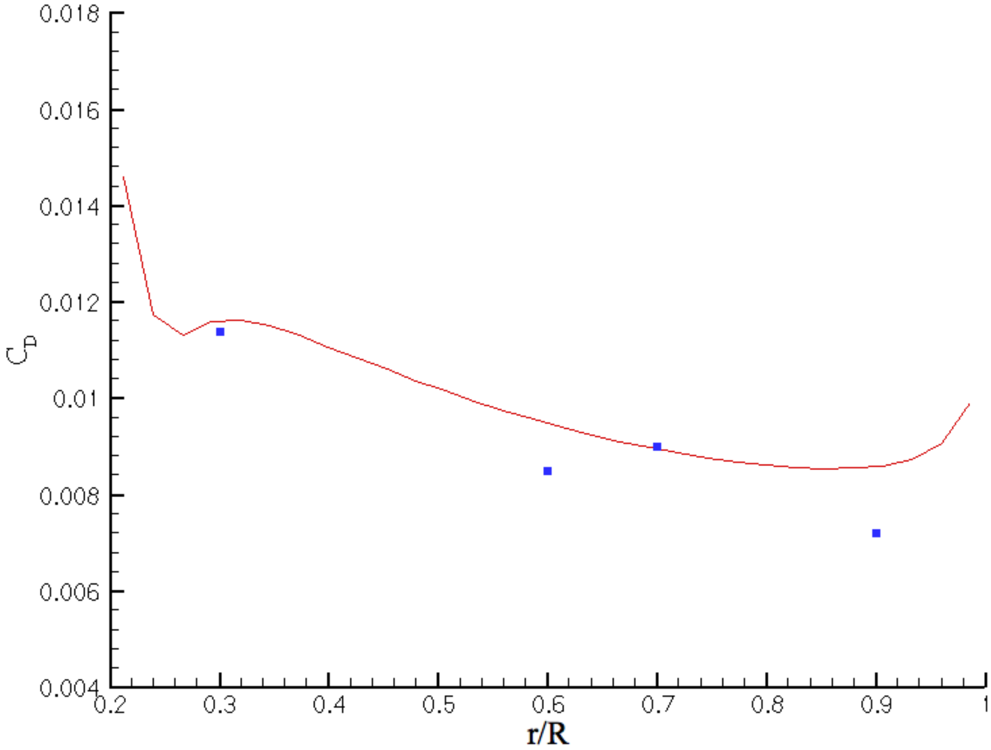

Figure 4.12: The section drag at strip $r/R = 0.7$ for the tripped condition. $J_s = 0.833$, wetted, Propeller DTRC 4119.

For smooth condition, a free transition is set on the pressure side and a forced transition at $x/c = 0.5$ is specified on the suction side in the boundary layer analysis according to the measurements. Figure 4.13 shows the comparisons of the displacement thickness on the pressure and suction sides at strip $r/R = 0.7$. Results by the present method compare very well with the experiment. Figure 4.14 compares the section drag coefficients for this condition. The differences between the numerical solution and the measurements are most probably because that the predicted transition locations are not exactly the same as in the experiment for all strips.

Table 4.2 compares the thrust and torque coefficients predicted by PROPCAV/XFOIL with those from open water test [Jessup 1989]. PROPCAV (inv) denotes the inviscid solution from PROPCAV. PROPCAV/XFOIL (smooth) denotes the viscous results for the smooth condition, and PROPCAV/XFOIL (tripped) is for the tripped condition. As expected, the forces by PROPCAV/XFOIL (smooth) are the closest to the measurements where the flow was not tripped. In addition, it is apparent that, with increasing viscosity, the thrust force is reduced and the torque force is increases by a larger amount.

Figure 4.15 to 4.17 show the comparisons of the viscous pressure distributions $-Cp_{exp}$ from the present method with the experimental measurements. Cp_{exp} is defined as $Cp_{exp} = 1.0 - \frac{V^2}{U_\infty^2}$, where V is the magnitude of the total velocity on blade, $U_\infty = 1$ corresponds to the uniform inflow wake to the propeller. There are big differences between the predicted and measurements at strip $r/R = 0.3$. It is most probably due to the hub effect, the flow is more complicated and the assump-

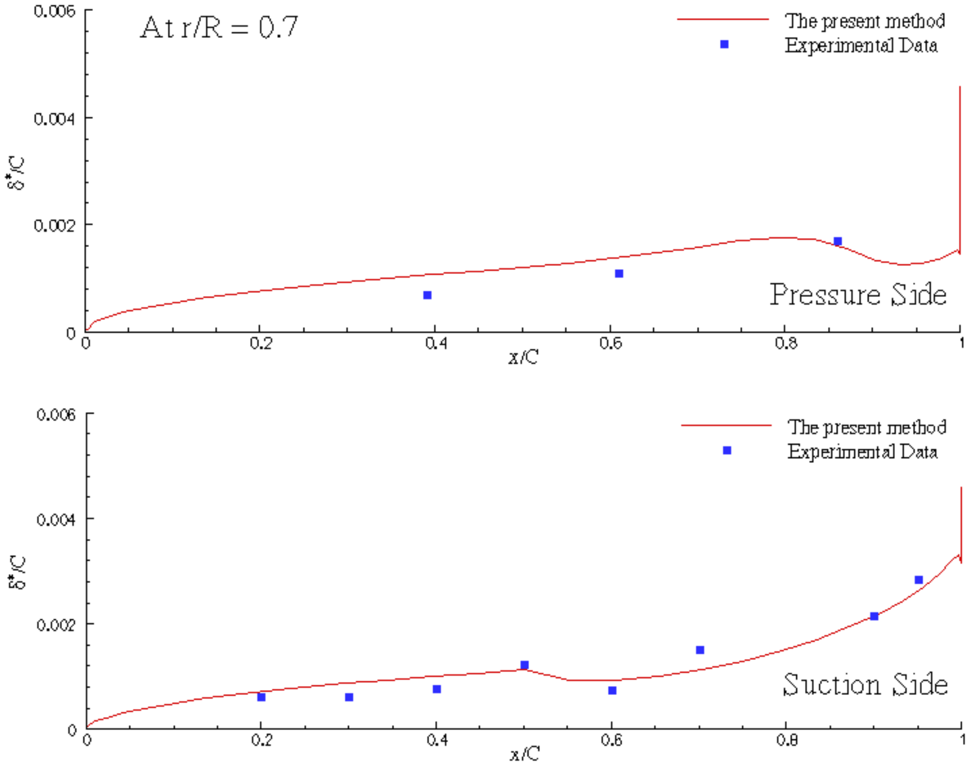

Figure 4.13: The displacement thickness on the pressure and suction sides at strip $r/R = 0.7$ for the smooth condition. $J_s = 0.833$, wetted, Propeller DTRC 4119.

Table 4.2: Comparison of wetted thrust and torque forces between PROPCAV/XFOIL and experimental measurements for $J_s = 0.833$, Propeller DTRC 4119.

Force	KT	$10KQ$
PROPCAV(inv)	0.1619	0.2631
PROPCAV/XFOIL(smooth)	0.1439	0.2990
PROPCAV/XFOIL(tripped)	0.1338	0.3112
Experiment	0.146	0.280

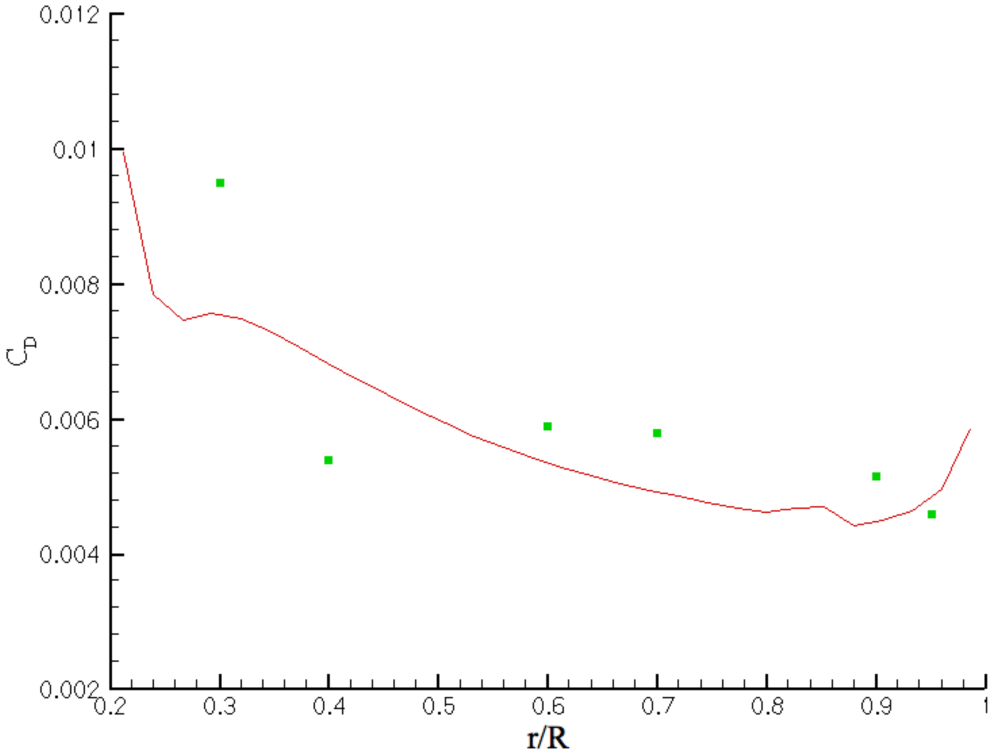

Figure 4.14: The section drag at strip $r/R = 0.7$ for the smooth condition. $J_s = 0.833$, wetted, Propeller DTRC 4119.

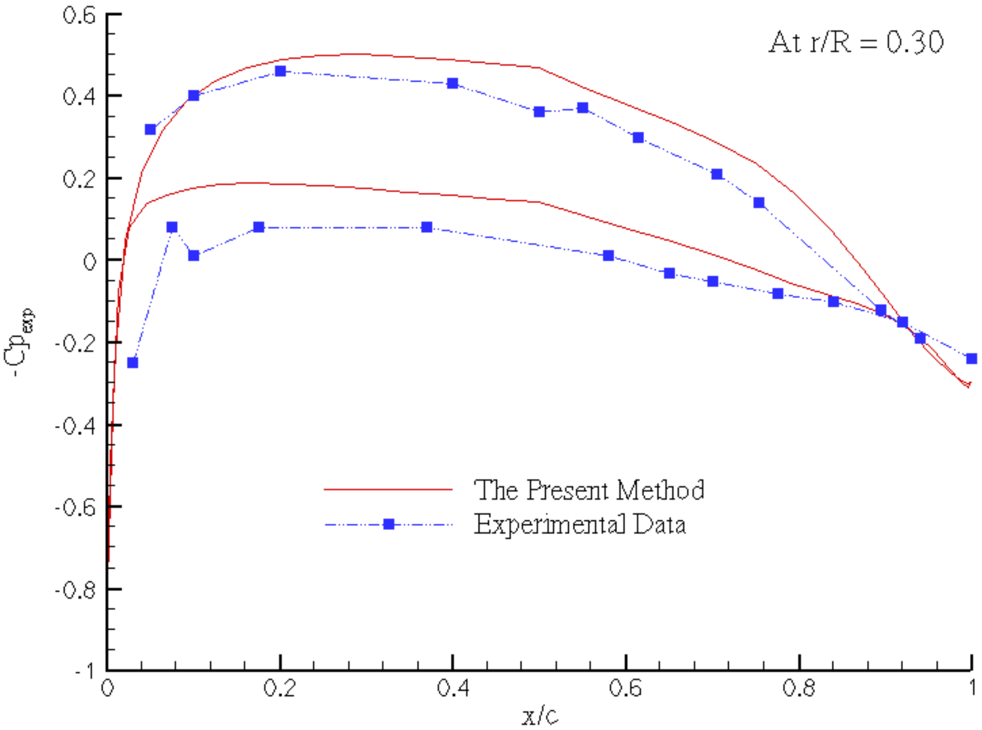

Figure 4.15: Comparison of viscous pressures at strip $r/R = 0.3$ (smooth). $J_s = 0.833$, wetted, Propeller DTRC 4119.

tion of 2-D developed boundary layer is not valid along this strip. Comparisons at strips $r/R = 0.7$ and $r/R = 0.9$ are reasonably good except at the blade trailing edge.

Figure 4.18 plots the distributions of shape factor H at all blade strips predicted by PROPCAV/XFOIL, where H is defined as $H = \delta^*/\theta$. $H \geq 2.8$ indicates turbulent flow separation. As shown in the figure, the flow is separated on the suction side close to the blade trailing edge only at the root of the propeller.

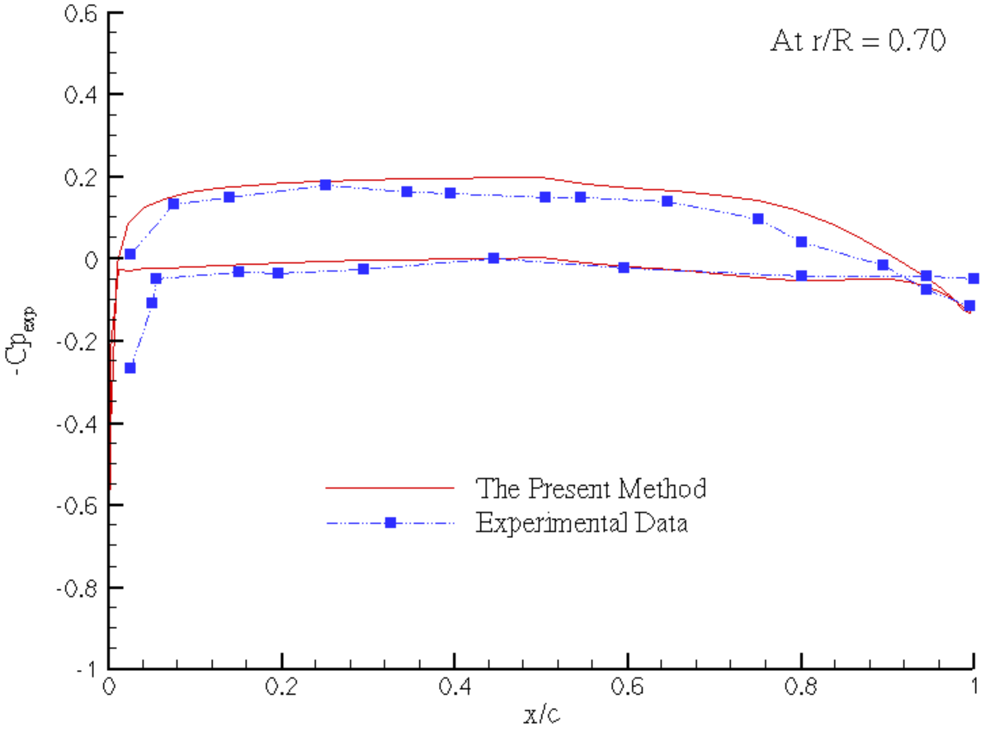

Figure 4.16: Comparison of viscous pressures at strip $r/R = 0.7$ (smooth). $J_s = 0.833$, wetted, Propeller DTRC 4119.

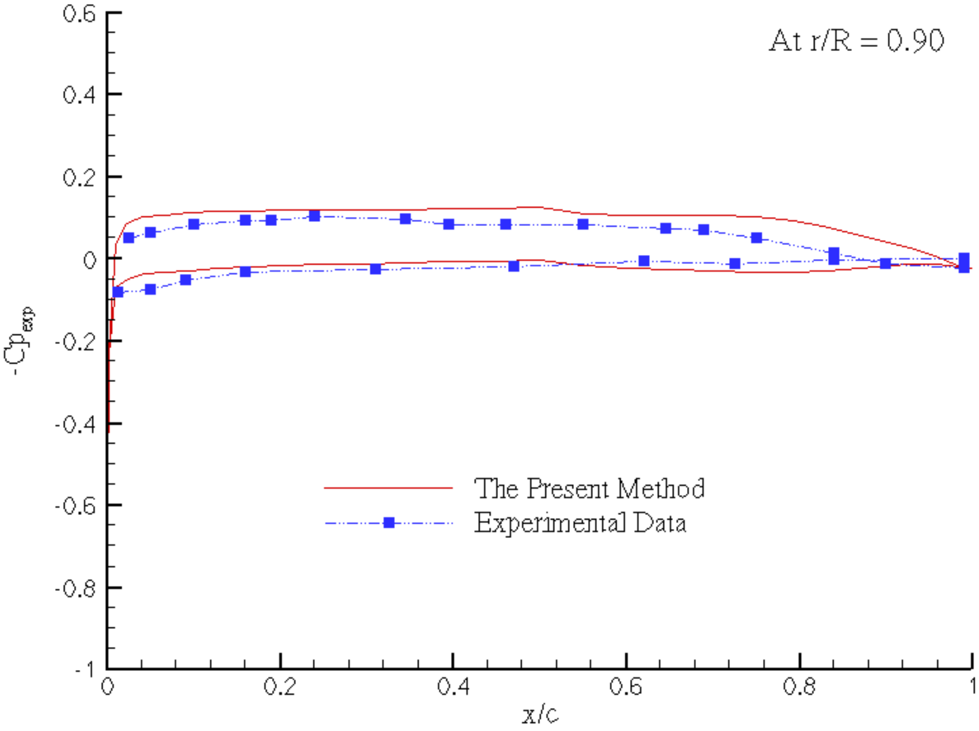

Figure 4.17: Comparison of viscous pressures at strip $r/R = 0.9$ (smooth). $J_s = 0.833$, wetted, Propeller DTRC 4119.

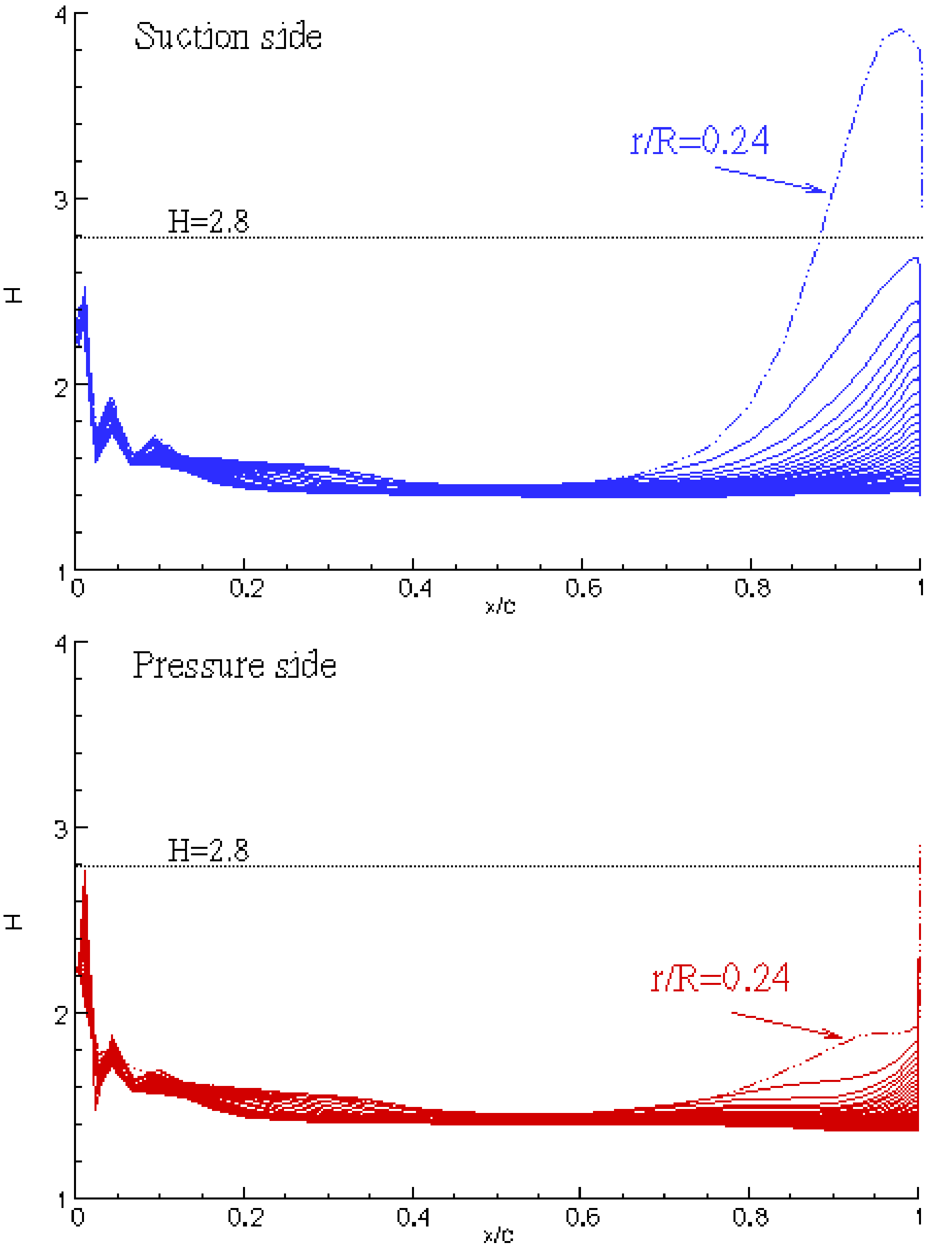

Figure 4.18: Shape factor on the pressure and suction sides predicted by PROP-CAV/XFOIL. $J_s = 0.833$, wetted, Propeller DTRC 4119.

4.3.2 Cavitating Flow

For the cavitating run, the propeller is tested at cavitation number $\sigma_n = 1.02$ for $J_s = 0.833$. σ_n is defined as $\sigma_n = (P_o - P_v)/(0.5\rho n^2 D^2)$, where P_o is the pressure far upstream at the depth of the propeller shaft, P_v is the vapor pressure, n is the propeller rotational frequency (rev/s) and D is the propeller diameter. The other run conditions are the same as the wetted flow. It takes about 10 minutes to finish both the inviscid and viscous analysis of the steady cavitating flow on a cluster using 1 CPU of AMD Opteron (1.6GHz & 2G RAM per CPU). Figure 4.19 shows the inviscid cavity patterns on the propeller blade from the present method. The propeller is partially cavitating and most of the cavities start from the mid-chord.

Figure 4.20 to Figure 4.24 show comparisons of the inviscid and viscous pressure distributions on the propeller blade under cavitating conditions. The inviscid and viscous pressures for wetted conditions are also plotted for reference. It needs to be noticed that the pressure coefficient Cp on the propeller is defined as,

$$Cp = \frac{P - P_0}{0.5\rho n^2 D^2}$$

where P_0 is the pressure far upstream, n is the propeller rotation frequency (rev/s), and D is the diameter of the propeller. The present method is able to predict the effect of viscosity on cavitating propeller flows by evaluating the viscous cavitating pressures on the cavity. Similar to the 2-D cavitating hydrofoil problem, viscosity reduces the pressures on both the foil and cavity surfaces. Therefore, the inviscid cavity patterns in Figure 4.19 actually correspond to a smaller cavitation number.

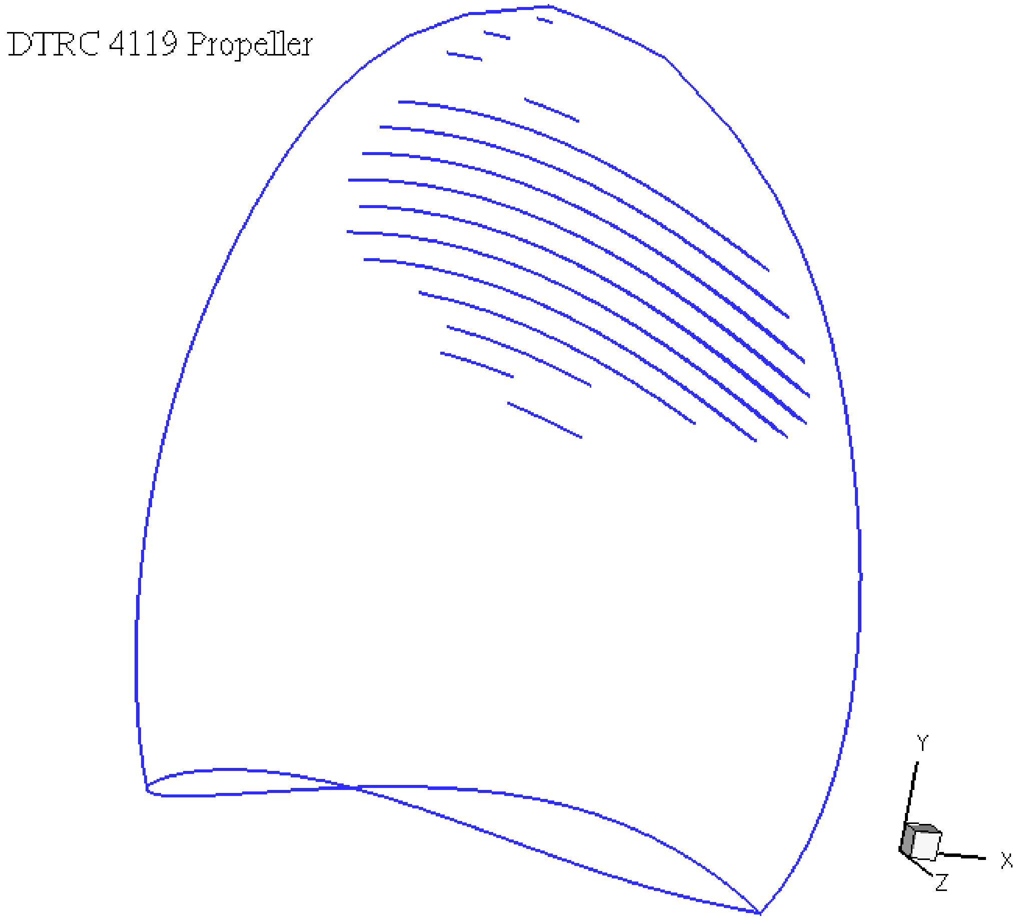

Figure 4.19: Cavity patterns on Propeller DTRC4119, at $\sigma_n = 1.02$, $J_s = 0.833$.

Figure 4.25 shows the predicted shape factors at all strips for the cavitating case. Same as the wetted flow, there is no separation happened except at the propeller root $r/R = 0.24$.

4.4 Summary

The present viscous/inviscid interaction method was applied to predict wetted and/or cavitating flows around a 3-D rudder, a bare duct and an open propeller. Numerical results by the present method were in good agreement with FLUENT turbulent model and experimental measurements. These studies proved that viscosity changes the pressure distributions and thus the thrust (or lift) forces and the torque (or drag) forces on the propulsor. Additionally, based on the studies carried out in Chapter 3, the effects of viscosity are also expected to affect the extent and volume of the cavity.

The cavity prediction including the effects of viscosity, for a given cavitation number, were not conducted during the course of the study. It will need additional work to include the effects of “blowing” sources into the boundary value problem, and to modify the cavity detachment criterion since viscosity plays an important role in the detachment of cavities [Arakeri and Acosta 1973; Arakeri 1975; Franc and Michel 1985], both of which will require implementation of iterative procedures.

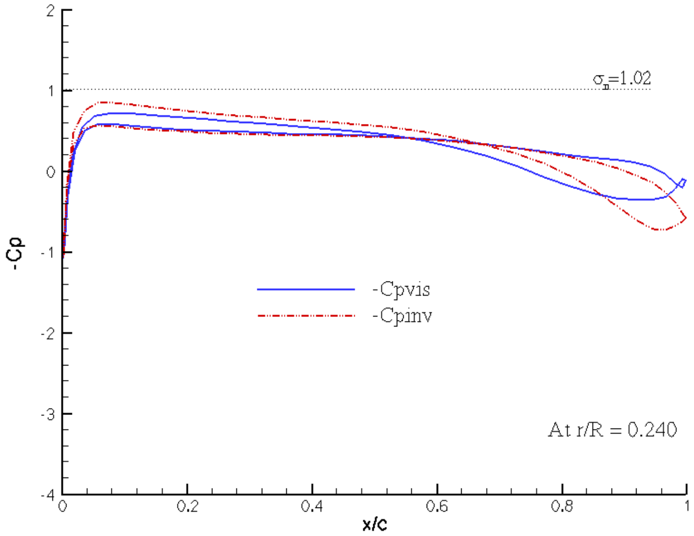

(a) wetted

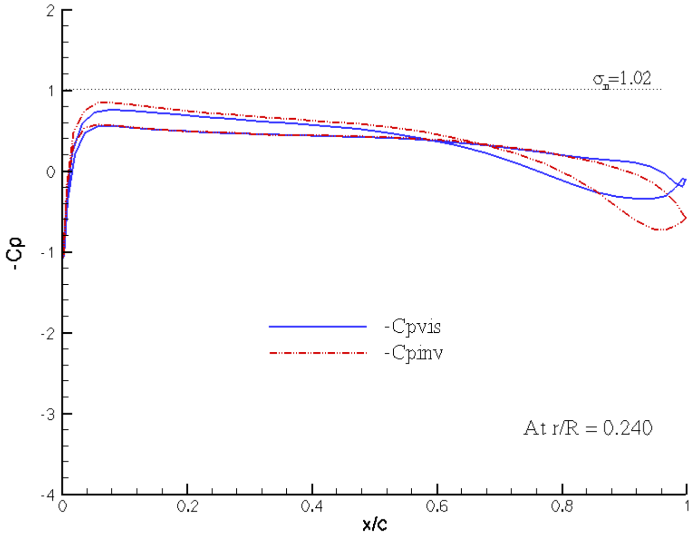

(b) cavitating, $\sigma_n = 1.02$

Figure 4.20: Comparison of inviscid and viscous pressure distributions at strip $r/R = 0.24$, $J_s = 0.833$, Propeller DTRC 4119.

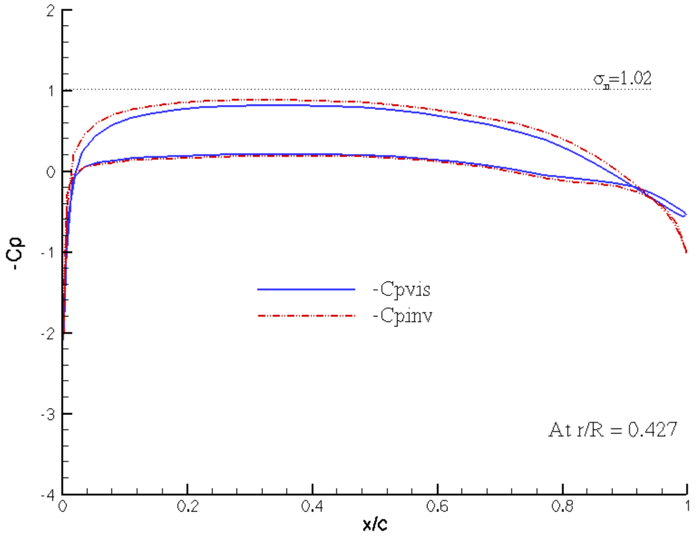

(a) wetted

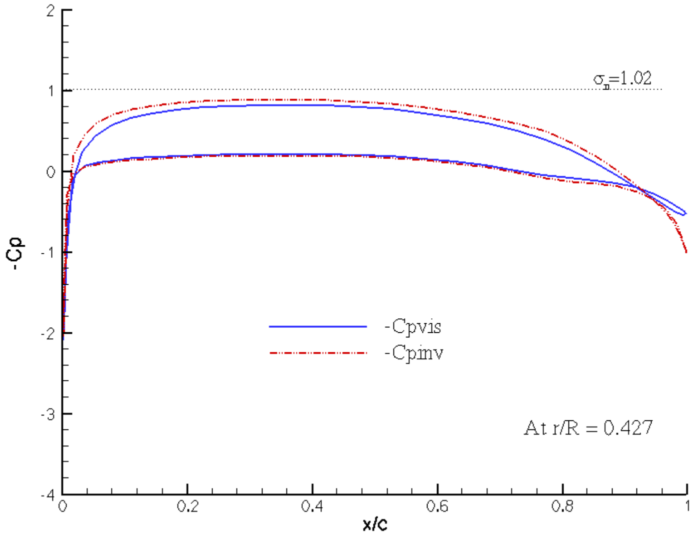

(b) cavitating, $\sigma_n = 1.02$

Figure 4.21: Comparison of inviscid and viscous pressure distributions at strip $r/R = 0.427$, $J_s = 0.833$, Propeller DTRC 4119.

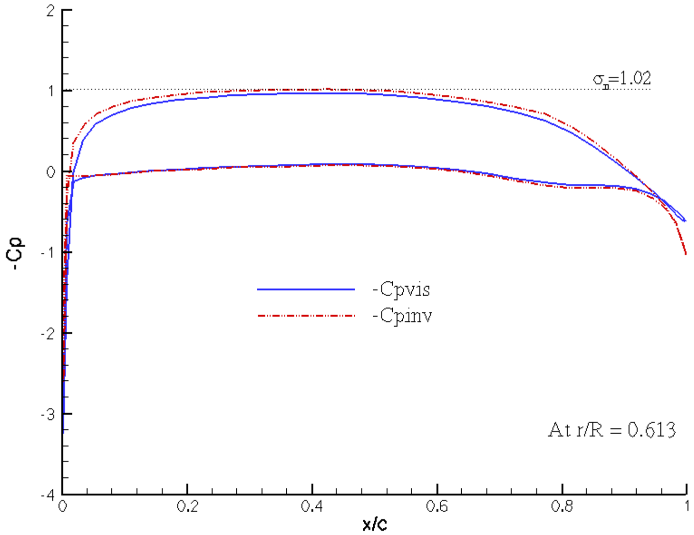

(a) wetted

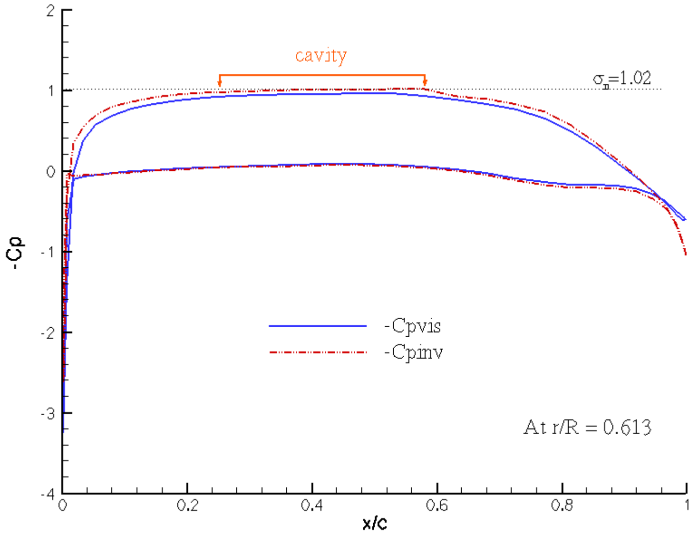

(b) cavitating, $\sigma_n = 1.02$

Figure 4.22: Comparison of inviscid and viscous pressure distributions at strip $r/R = 0.613$, $J_s = 0.833$, Propeller DTRC 4119.

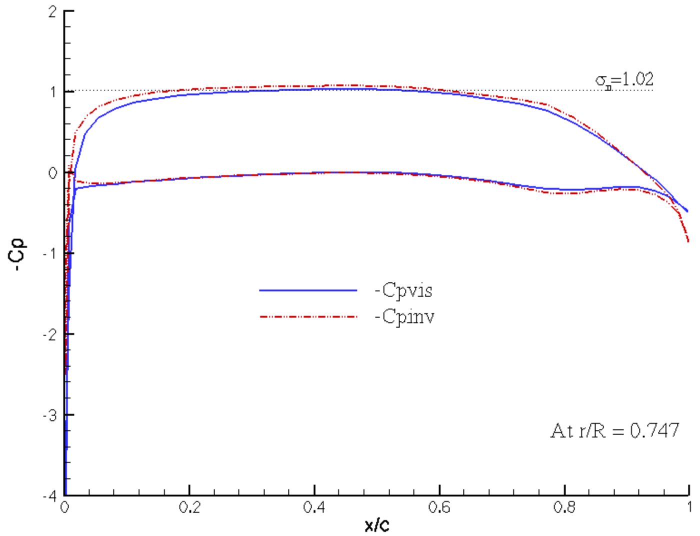

(a) wetted

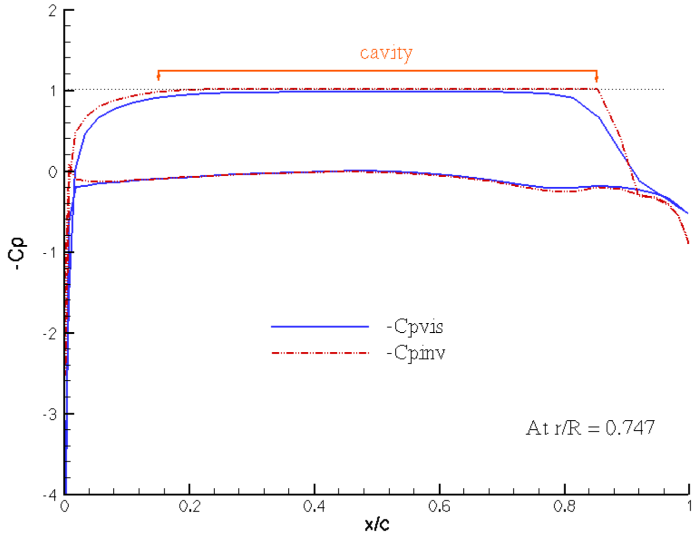

(b) cavitating, $\sigma_n = 1.02$

Figure 4.23: Comparison of inviscid and viscous pressure distributions at strip $r/R = 0.747$, $J_s = 0.833$, Propeller DTRC 4119.

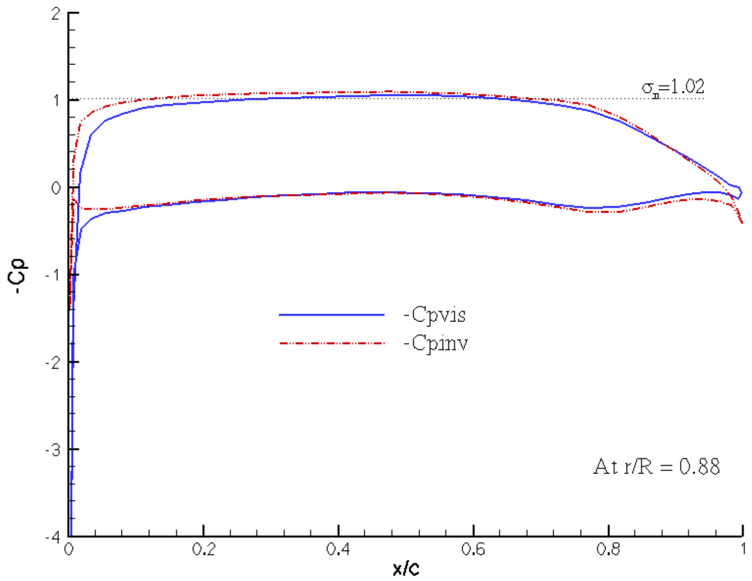

(a) wetted

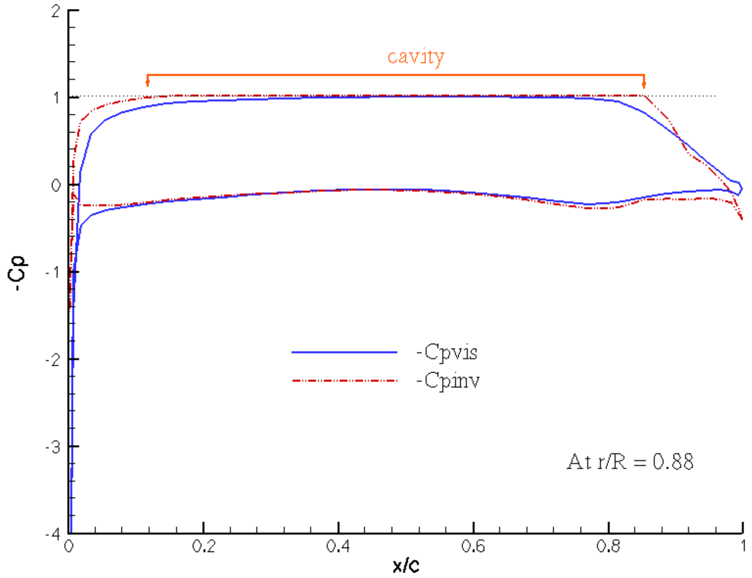

(b) cavitating, $\sigma_n = 1.02$

Figure 4.24: Comparison of inviscid and viscous pressure distributions at strip $r/R = 0.88$, $J_s = 0.833$, Propeller DTRC 4119.

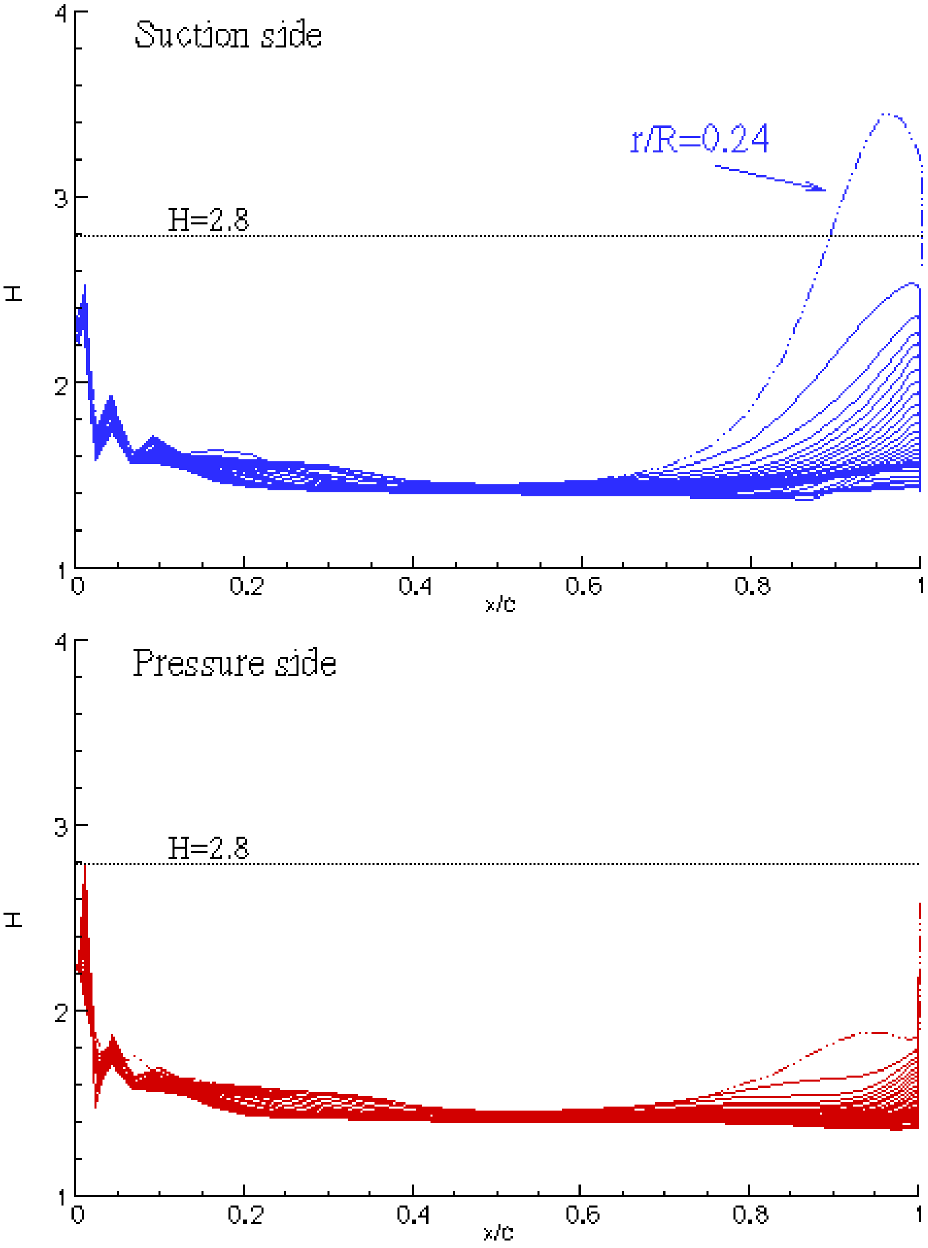

Figure 4.25: Shape factor on the pressure and suction sides (cavitating) predicted by PROPCAV/XFOIL, $J_s = 0.833$, $\sigma_n = 1.02$, Propeller DTRC 4119.

Chapter 5

Viscous Flow around Ducted Propellers

Ducted propellers have been increasingly used in marine vehicles in recent years because of their attractive advantages over open propellers: better steerability, high efficiency, and good cavitation performance. In this chapter, the present viscous/inviscid interaction method is used to investigate steady, viscous flows around ducted propeller under wetted and cavitating conditions. Results by the present method are validated with experimental measurements.

5.1 Previous Work

Flow around a ducted propeller is generally considered in an iterative manner by coupling different numerical methods to account for the interactive effects between propeller and duct [Gu 2006; Lee and Kinnas 2006]. In early 70s and 80s, [Glover and Ryan 1973] and [Gibson and Lewis 1973] coupled the surface vorticity method with a lifting line method or an actuator disk model, and Falcão de Campos [1983] coupled an Euler solver with an actuator disk model. Later, to improve the representation of the duct and propeller geometries, lifting surface and boundary element methods were combined to analyze the flow around ducted propellers [Van Houten 1986; Kerwin et al. 1987; Kinnas et al. 1991; Hughes et al. 1992].

In their work, the propeller was represented by a lifting surface method and the duct by a boundary element method. Since the interactions between the ducted propeller and the upstream vortices are dismissed in the nominal inflow wake, [Kinnas et al. 2004, 2005b] developed a coupled axi-symmetric Euler solver based on finite volume method and a potential solver based on lifting surface method to improve the effective inflow wake prediction to the ducted propeller. Then, the effects of the small gap region (between the propeller tip and the duct inner surface) were considered in the coupled method by using the orifice equation model proposed by [Kerwin et al. 1987] or a tip leakage vortex model [Kinnas et al. 2005a; Gu 2006].

Researchers also performed studies on the viscous flow around ducted propeller. [Kerwin et al. 1994, 1997] and Warren et al. [2000] coupled a RANS (Reynolds-Averaged Navier-Stokes) solver with a lifting surface method (potential solver) to include the viscous effects on the duct and hub walls. [Sanchez-Caja et al. 2000] applied the $k - \epsilon$ turbulence model to a RANS solver to simulate the incompressible viscous flow around a ducted propeller. In [Abdel-Maksoud and Heinke 2002], the SST (Shear-Stress Transport) model of the RANS solver was utilized to investigate the scale effects on ducted propellers. [Brewer et al. 2003] simulated the viscous gap flow and the tip leakage vortex cavitation inception by using a 3-D, unstructured, unsteady Navier-Stokes with an artificial compressibility term. [Hsiao and Chahine 2004] conducted studies on the cavitation inception in the presence of two interacting vortices, the tip leakage vortex and the trailing edge vortex, by combing their unsteady RANS solver with bubble dynamic models.

In this study, the potential based boundary element method (PROPCAV) described in Chapter 2 is applied to predict the unsteady performance of cavitating ducted propellers. PROPCAV solves the boundary value problem for both duct and propeller at the same time, and inherently includes the interactions between the propeller and the duct [Lee and Kinnas 2006]. The viscosity effects on the ducted propeller flow are considered by coupling PROPCAV with the 2-D integral boundary layer analysis (XFOIL) on the duct and the propeller blades.

5.2 Problem Description

Dyne conducted systematic experiments to investigate wetted and cavitating performance of ducted propellers in a cavitation tunnel [Dyne 1973]. One of Dyne's configuration, P1452 propeller with D15 duct, is chosen for this work to validate the present viscous/inviscid interaction method. In this section, the geometry information of the ducted propeller and the run conditions are described.

Figure 5.1 shows the geometry of the P1452 propeller and the D15 duct. Propeller P1452 is a four-bladed propeller. The propeller blade section is of NACA66 thickness form, and of NACA $a = 0.8$ camber mean line. The hub ratio is equal to $R_{hub}/R = 0.26$. R_{hub} is the hub radius, and R is the propeller radius and equal to one half of the propeller diameter D. For the D15 duct, the profile angle is 9.2^o, and the maximum camber-chord ratio is $f_{max}/C = 0.06$ with C is the chord length of the duct. The gap size between the duct inner surface and the blade tip is 1.09% of the propeller radius R.

The inflow wake to Dyne's ducted propeller is uniform, and the hydrostatic effect is ignored ($Fr = 9999.0$). The flow Reynolds number, $Re_D = V_s D/\nu$, based

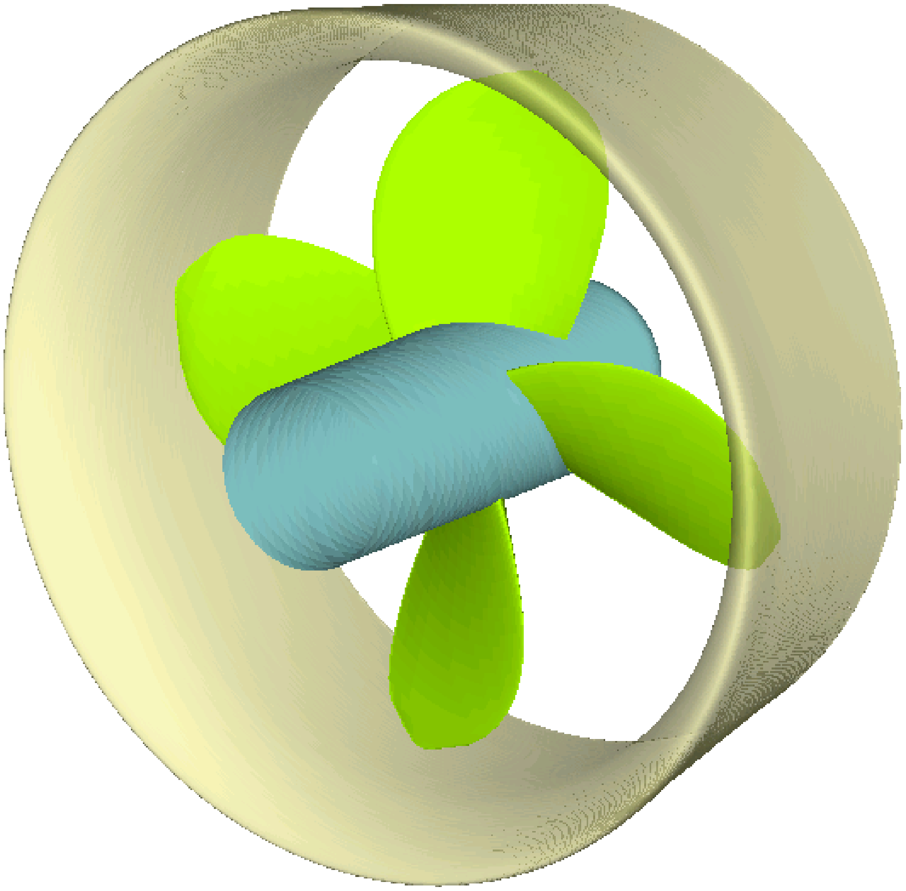

Figure 5.1: Geometry of P1452 propeller and D15 duct.

on the propeller diameter D is 1.15×10^6 at the high advance ratios and 0.67×10^6 at the low advance ratio. V_s is the ship speed, and ν is the kinematic viscosity. The flow turbulence level is set to 1%. The convergence criterion for the integral boundary layer analysis is $1.0e-5$. Results from the present method are compared with the measurements under conditions of $\sigma_v = 5$ and $\sigma_v = 20$ at different advance ratios J_s. The cavitation number σ_v is defined based on the ship speed:

$$\sigma_v = \frac{P_0 - P_v}{\frac{1}{2}\rho V_s^2} \tag{5.1}$$

where V_s is the ship speed. P_0 is the far upstream pressure on the shaft axis, and P_v is the vapor pressure. ρ is the water density.

5.3 Results

According to Dyne's measurements [Dyne 1973], for $\sigma_v = 20$, the flow was fully wetted and there was no cavitation for a range of J_s values from 0.4 to 0.7; for $\sigma_v = 5$, both partial and super cavities were observed. In the following two sections, viscous flows around the wetted and cavitating ducted propellers predicted by the viscous/inviscid interaction method are presented and compared to the Dyne's measurements.

5.3.1 Fully Wetted Flows

The convergence of the present method is first studied by looking at the inviscid solutions on the propeller blades and on the duct surface for advance ratio

$J_s = 0.5$. The predicted wetted blade forces on the propeller and on the duct are then compared with the experimental data at different advance ratios.

Convergence Studies

Figure 5.2 presents the dependence of inviscid wetted circulation distributions on blade with number of panels on each blade in the chord-wise and span-wise directions. The circulation Γ is defined as $\Gamma = \Delta\phi/2\pi R\sqrt{V_s^2 + (0.7n\pi D)^2}$, where $\Delta\phi$ is the potential jump across the blade trailing wake at each radius. V_s is the ship speed and n is the propeller rotational frequency. The convergence of the results is good and 60×20 panels on the blade was used for other convergence studies.

Figure 5.3 shows the convergence of inviscid wetted circulation distributions with the panel size of trailing wake. Four different angle increments, $\Delta\theta = 3^o, 6^o, 9^o$ and 15^o for the wake geometry are used. Figure 5.4 compares the trailing wake geometries for $\Delta\theta = 6^o$ and $\Delta\theta = 15^o$. The convergence of the results is almost not affected by the panel size on wake, and $\Delta\theta = 6^o$ is used for the following studies.

Figure 5.5 presents the dependence of wetted circulation distributions on blade with number of panels on duct in the chord-wise and circumferential directions. It should be pointed out that the number of panels in the circumferential direction denotes only the discretization on the duct surface between two adjacent blade rows. As shown in Figure 5.5 (b), at least 20 panels in the circumferential direction on duct is required to achieve converged results.

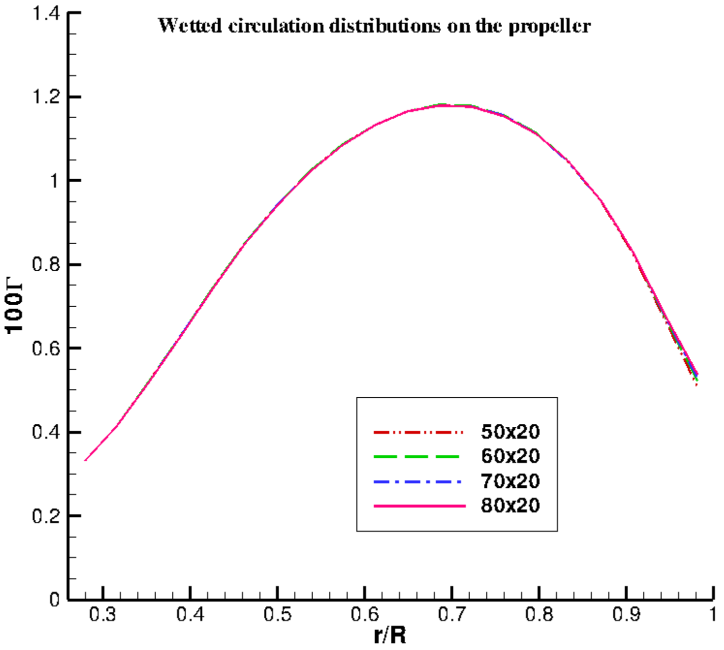

(a) Chord-wise

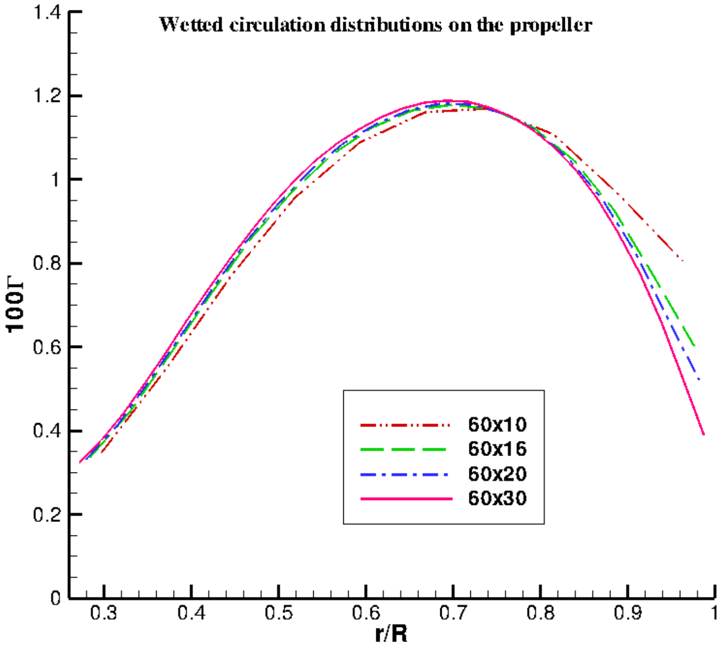

(b) Span-wise

Figure 5.2: Convergence of inviscid wetted circulation distributions on propeller blade with number of panels on *blade* at $J_s = 0.5$.

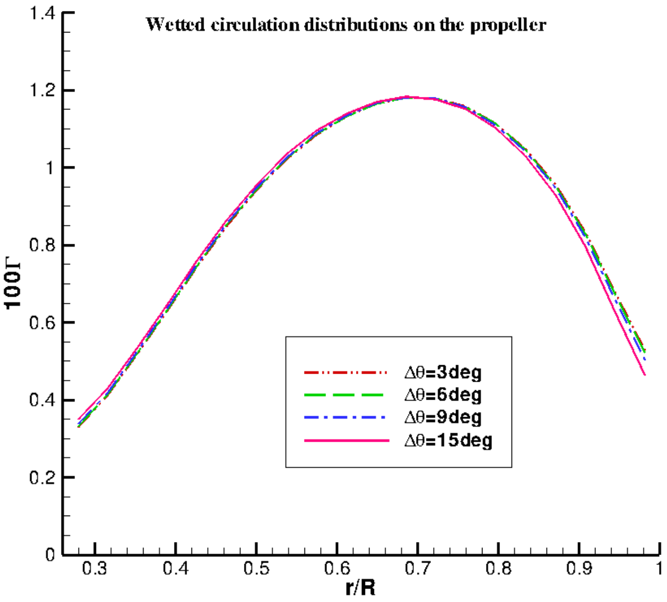

Figure 5.3: Convergence of inviscid wetted circulation distributions on propeller blade with panel size of trailing wake at $J_s = 0.5$.

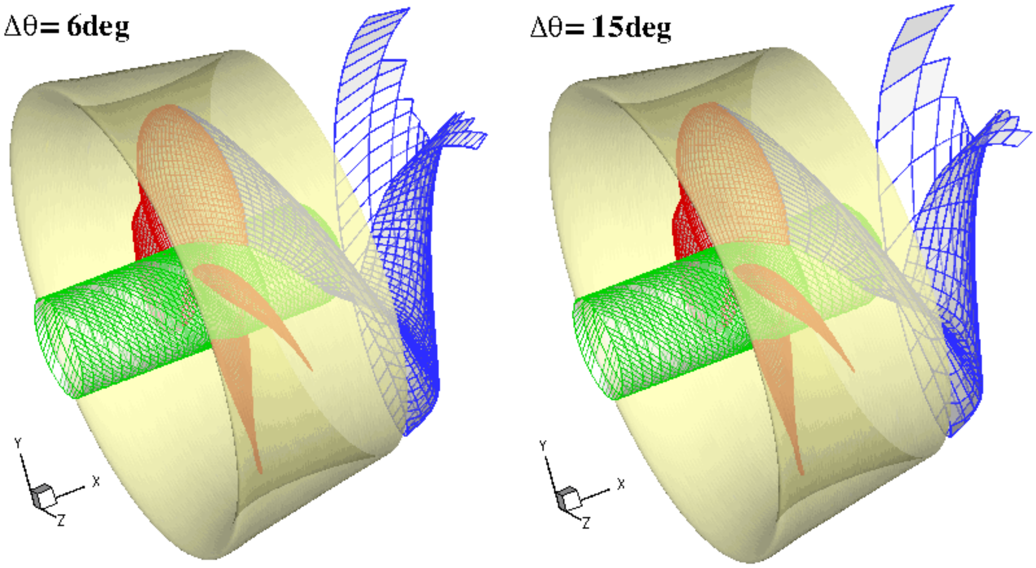

Figure 5.4: Comparison of trailing wake geometries for $\Delta\theta = 6^o$ and $\Delta\theta = 15^o$.

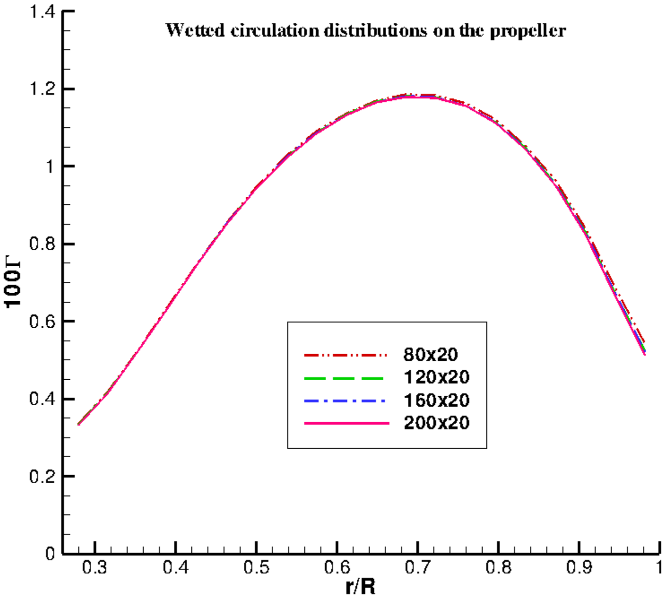

(a) Chord-wise

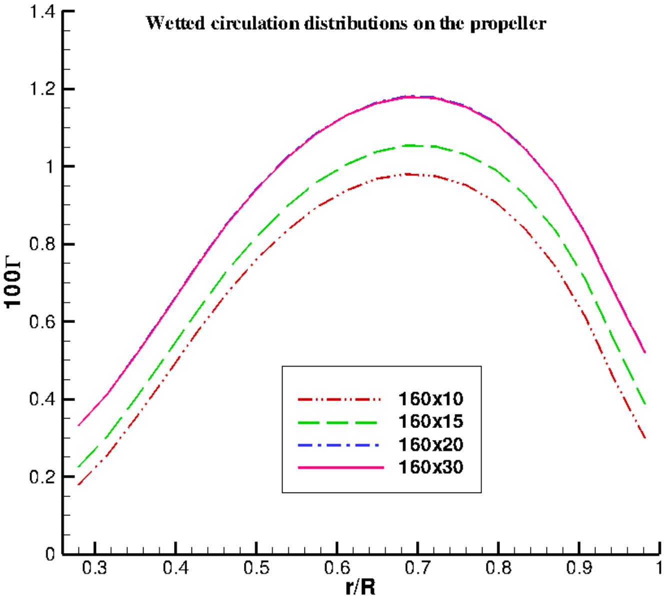

(b) Circumferential (No. of panels between blades)

Figure 5.5: Convergence of inviscid wetted circulation distributions on propeller blade with number of panels on *duct* at $J_s = 0.5$.

Results

At cavitation number $\sigma_v = 20$, for J_s values varying from 0.4 to 0.7, there is no cavitation detected by PROPCAV (inviscid) and the flows are fully wetted. For the PROPCAV/XFOIL runs, it generally takes about 3.0 minutes to finish both the inviscid and viscous analysis for this case on a cluster with 1 CPU of AMD Opteron (1.6GHz & 2G RAM per CPU).

Figure 5.6 compares the inviscid and viscous thrust and torque forces at different advance ratios J_s by the present method with the measurements [Dyne 1973]. K_{TD} denotes the thrust force generated by the duct. $(K_T)_{Total}$ is the total thrust force, *that is*, the sum of the thrust forces on the duct and the propeller. K_Q denotes the torque force on the propeller. The legend, PROPCAV (Inviscid+correction), denotes the forces predicted by applying empirical viscous corrections to the inviscid solution. It is obvious that the predicted viscous thrust and torque forces by PROPCAV/XFOIL agree better with the measured than using empirical viscous corrections. It should be pointed out that the viscosity effect on duct flow is simulated only by using empirical viscous corrections. Viscous analysis of the flow over the duct using XFOIL crashed because of the complicated flow in the tip gap region between the propeller tip and duct inner surface. As shown in Figure 5.7, the pressure peak on the duct inner surface results in divergence of the boundary layer analysis.

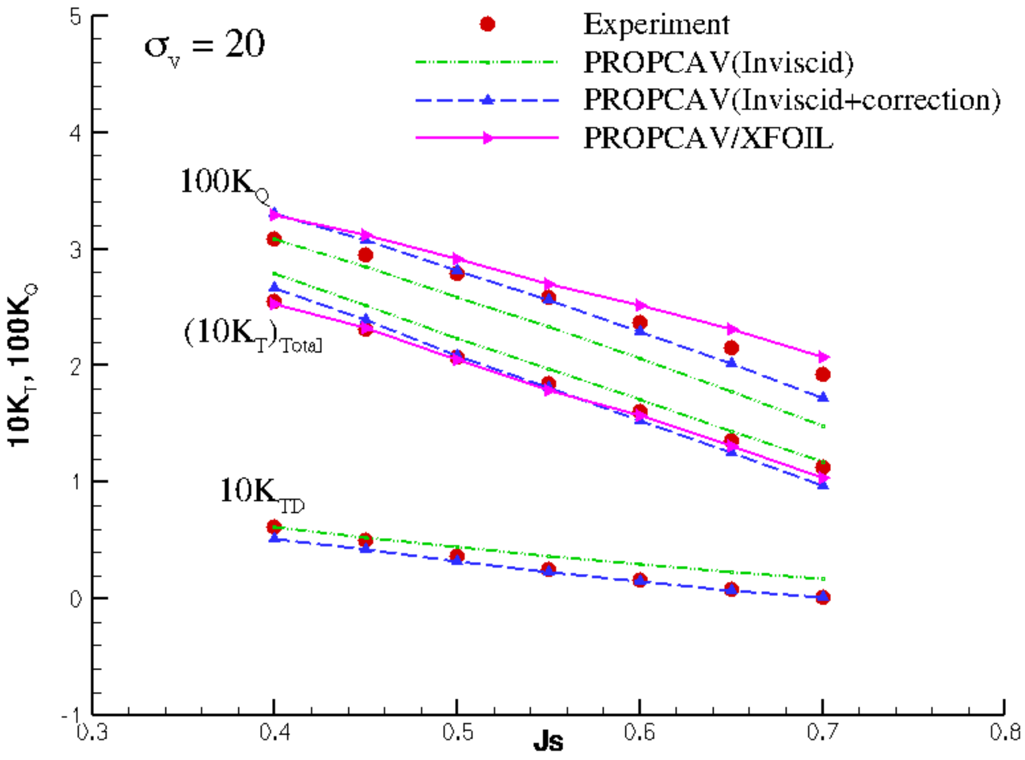

Figure 5.6: Comparison of the wetted blade forces between the present method and the measurements [Dyne 1973]

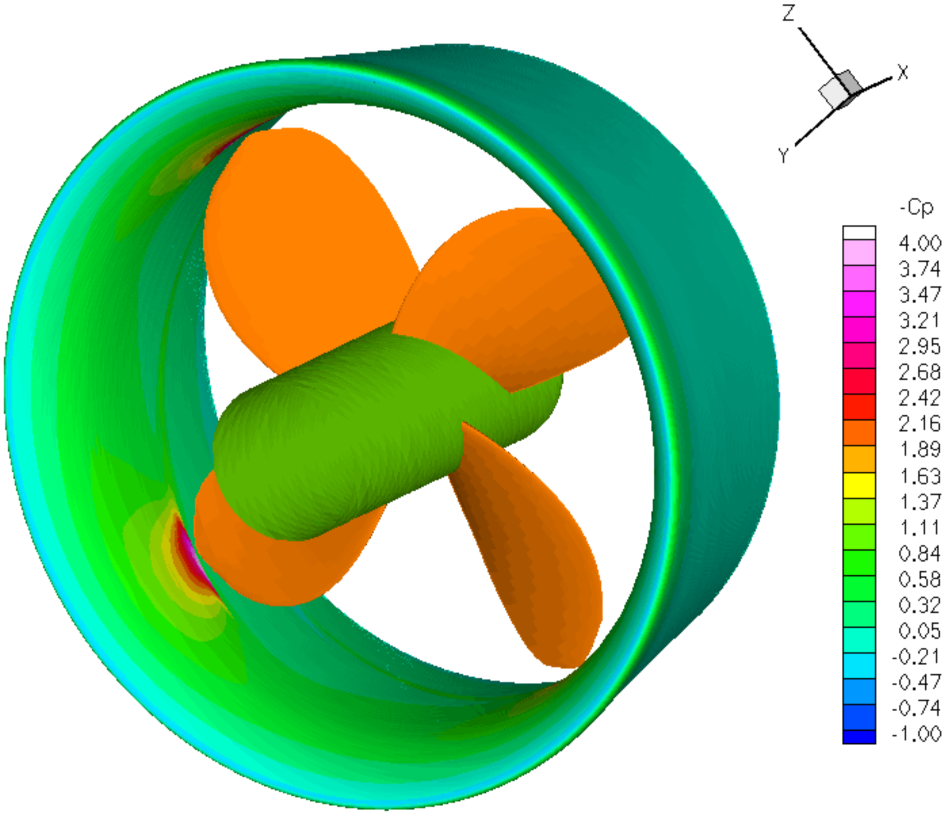

Figure 5.7: Inviscid wetted pressure contours on the DUCT surface at $J_s = 0.5$.

5.3.2 Cavitating Flows

For the cavitating condition, the convergence of the present method is first investigated by looking at the inviscid solutions on the propeller blades and on the duct for $J_s = 0.5$.

Convergence Studies

For the dependence of the present method on number of panels on propeller blades, Figure 5.8 shows the convergence of inviscid cavitating circulation distributions on blade. Noted that the paneling on the blade is varied in both the chord-wise and the span-wise directions. Figure 5.9 and 5.10 present the convergence of inviscid cavity patterns with number of panels on blade in the chord-wise and span-wise directions, respectively. Figure 5.11 presents the convergence of inviscid mean pressure distributions on duct surface, which are calculated by using the circumferentially averaged potentials on the duct. The convergence of the present method is fast and 60×20 panels on the blade is used for other convergence tests.

For the convergence of solutions with the panel size of propeller trailing wake, Figure 5.12 shows the inviscid cavitating circulation distributions on the blade. Figure 5.13 presents the inviscid cavity patterns, and Figure 5.14 shows the mean pressure distributions on the duct. The convergence of the results is pretty good, and $\Delta\theta = 6^o$ is used for the following studies.

For convergence with number of panels on duct in the chord-wise and circumferential directions, Figure 5.15 presents the dependence of cavitating circulation distributions on blade. Figure 5.16 and 5.17 show the convergence of inviscid

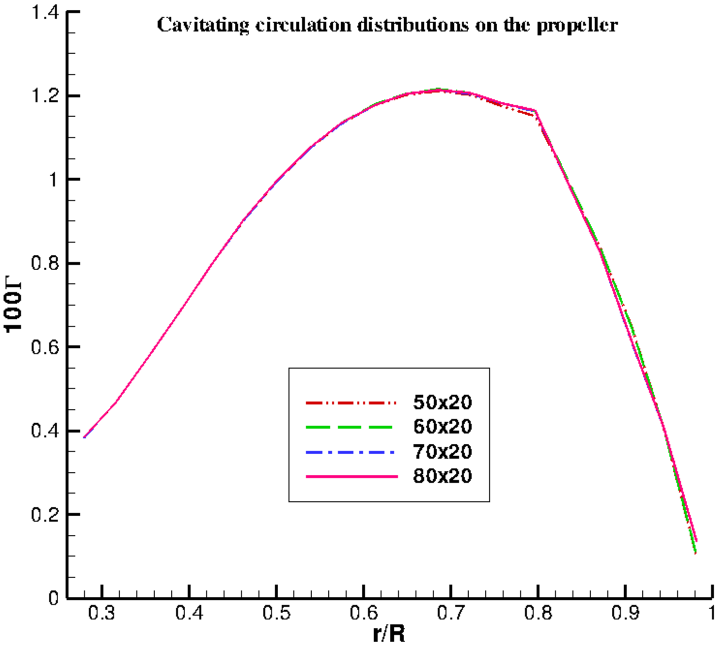

(a) Chord-wise

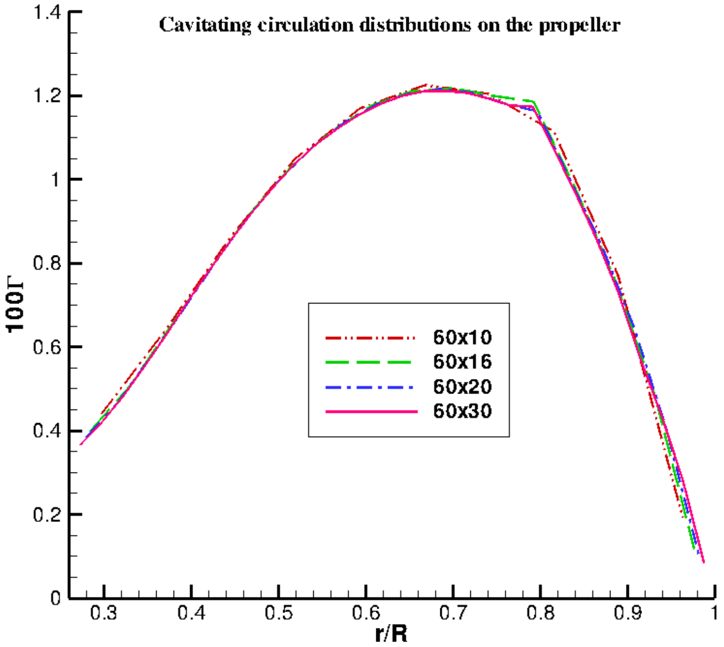

(b) Span-wise

Figure 5.8: Convergence of inviscid cavitating circulation distributions on propeller blade with number of panels on *blade* at $\sigma_v = 5$, $J_s = 0.5$.

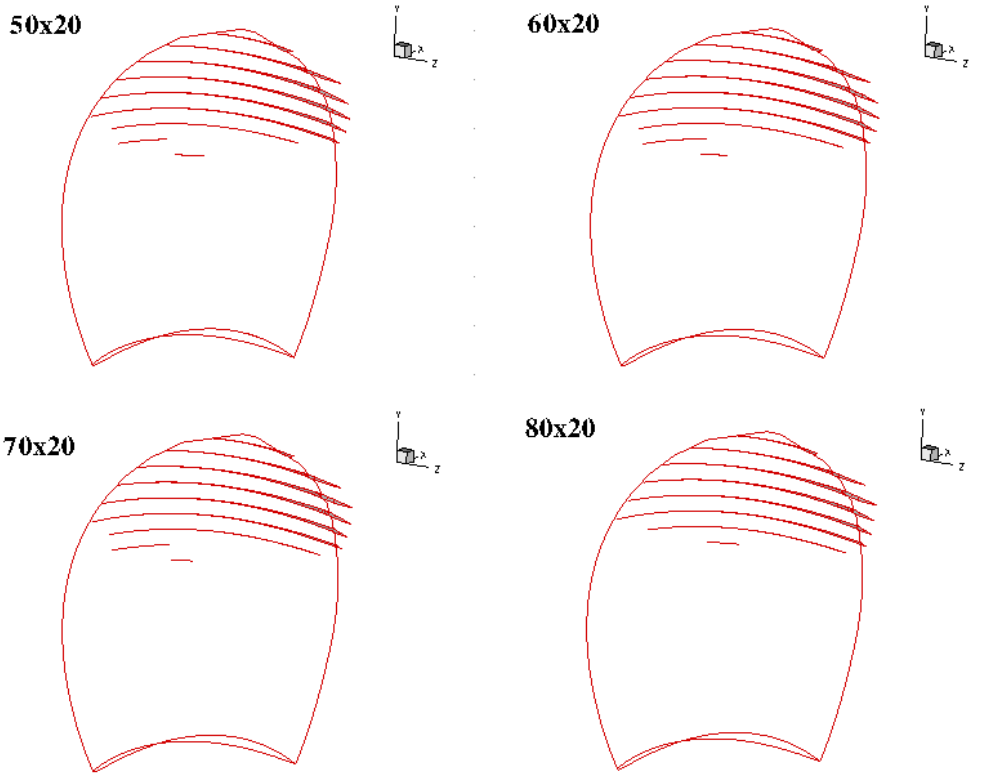

Figure 5.9: Convergence of inviscid cavity patterns with number of panels on chordwise number of panels on *blade* at $\sigma_v = 5$, $J_s = 0.5$.

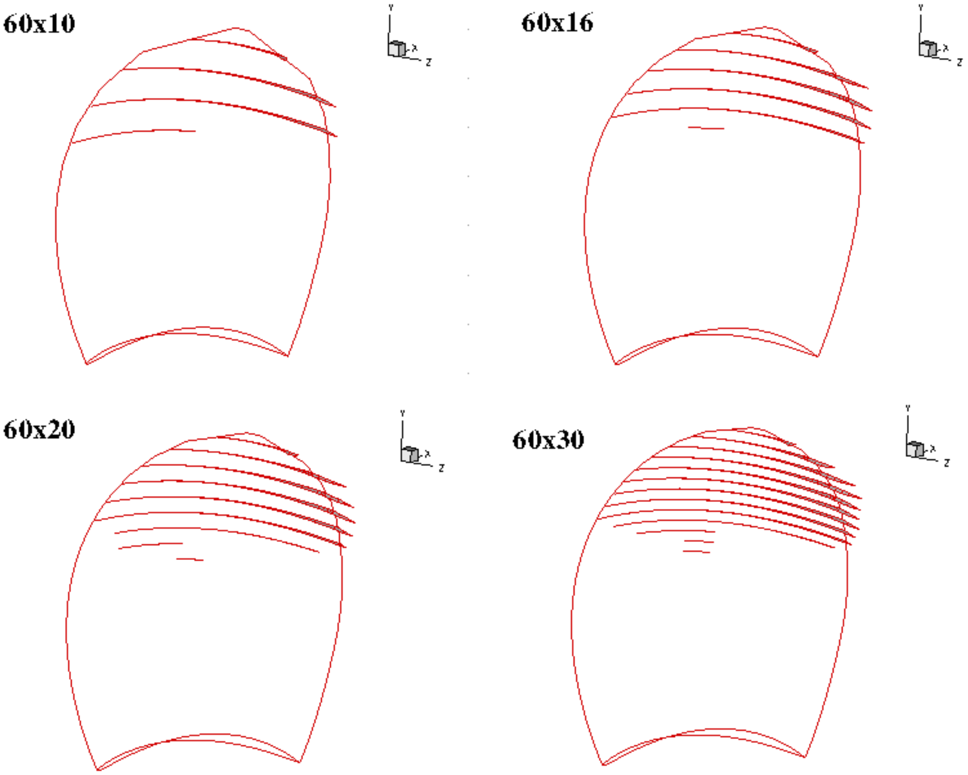

Figure 5.10: Convergence of inviscid cavity patterns with number of panels on span-wise number of panels on *blade* at $\sigma_v = 5$, $J_s = 0.5$.

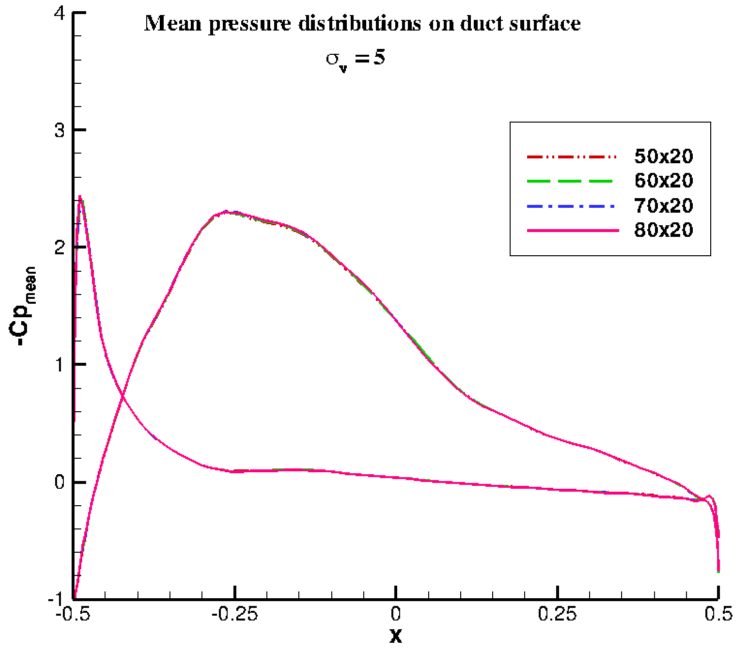

(a) Chord-wise

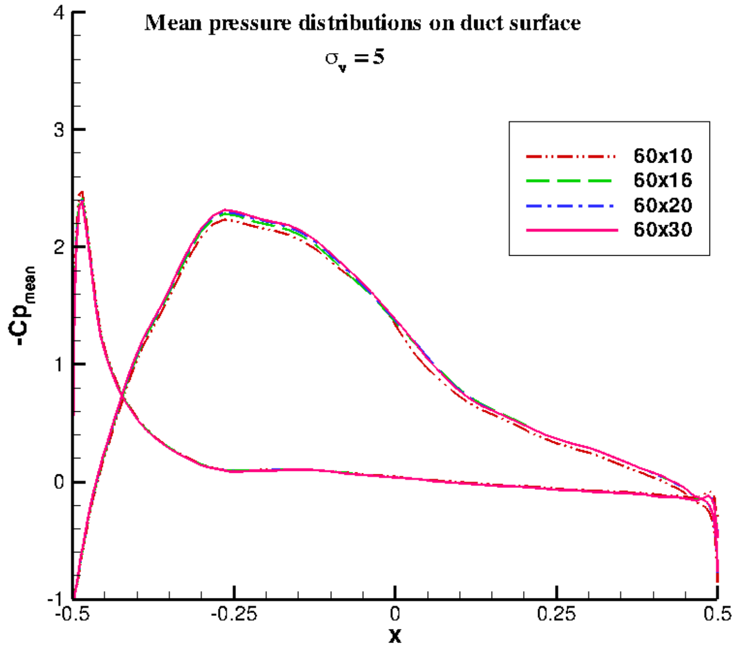

(b) Span-wise

Figure 5.11: Convergence of inviscid mean pressure distributions on duct with number of panels on *blade* at $\sigma_v = 5$, $J_s = 0.5$.

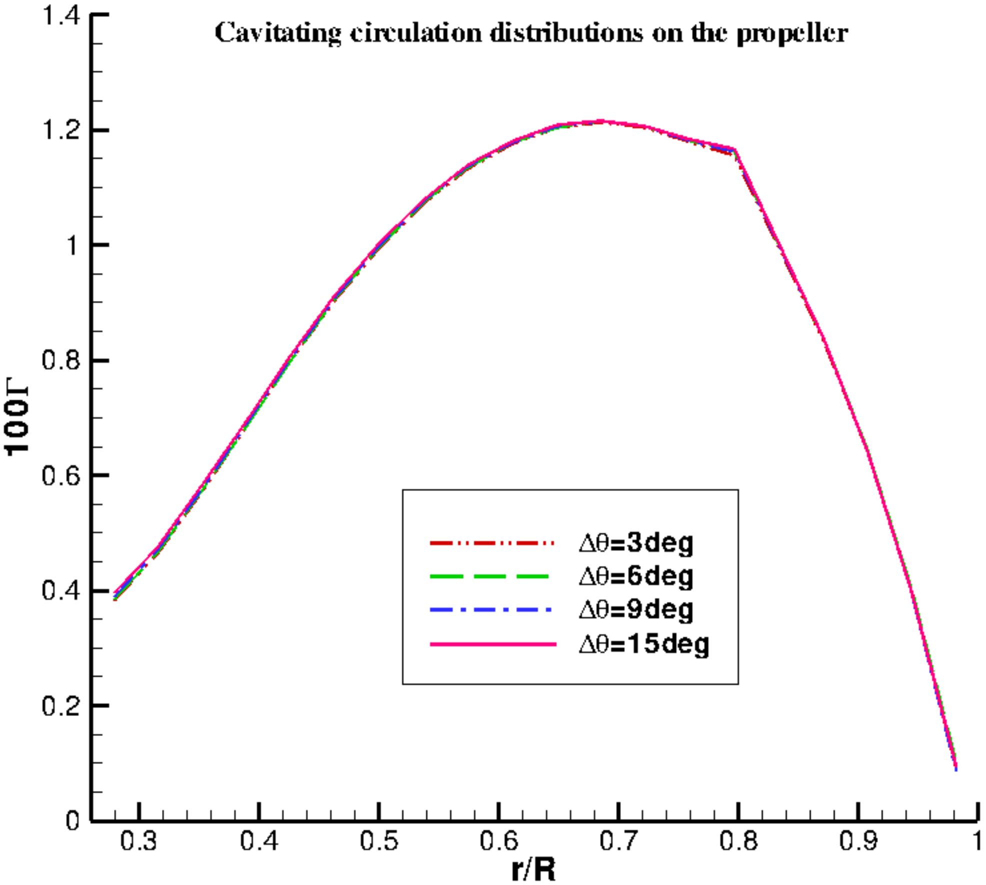

Figure 5.12: Convergence of inviscid cavitating circulation distributions on propeller blade with panel size of trailing wake at $\sigma_v = 5$, $J_s = 0.5$.

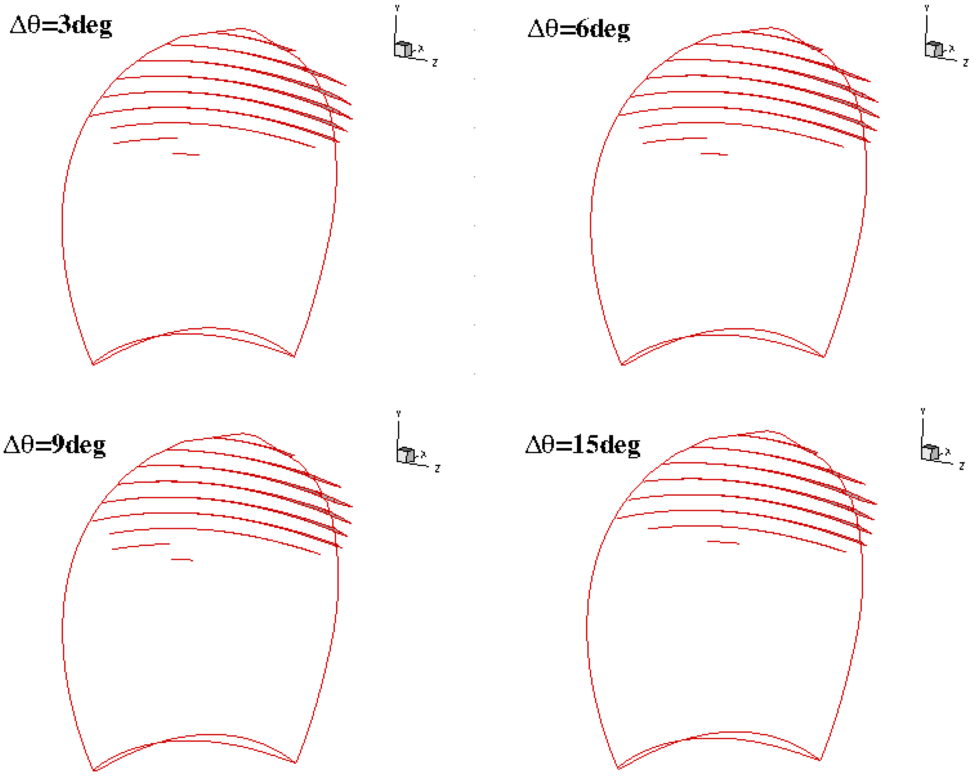

Figure 5.13: Convergence of inviscid cavity patterns with panel size of trailing wake at $\sigma_v = 5$, $J_s = 0.5$.

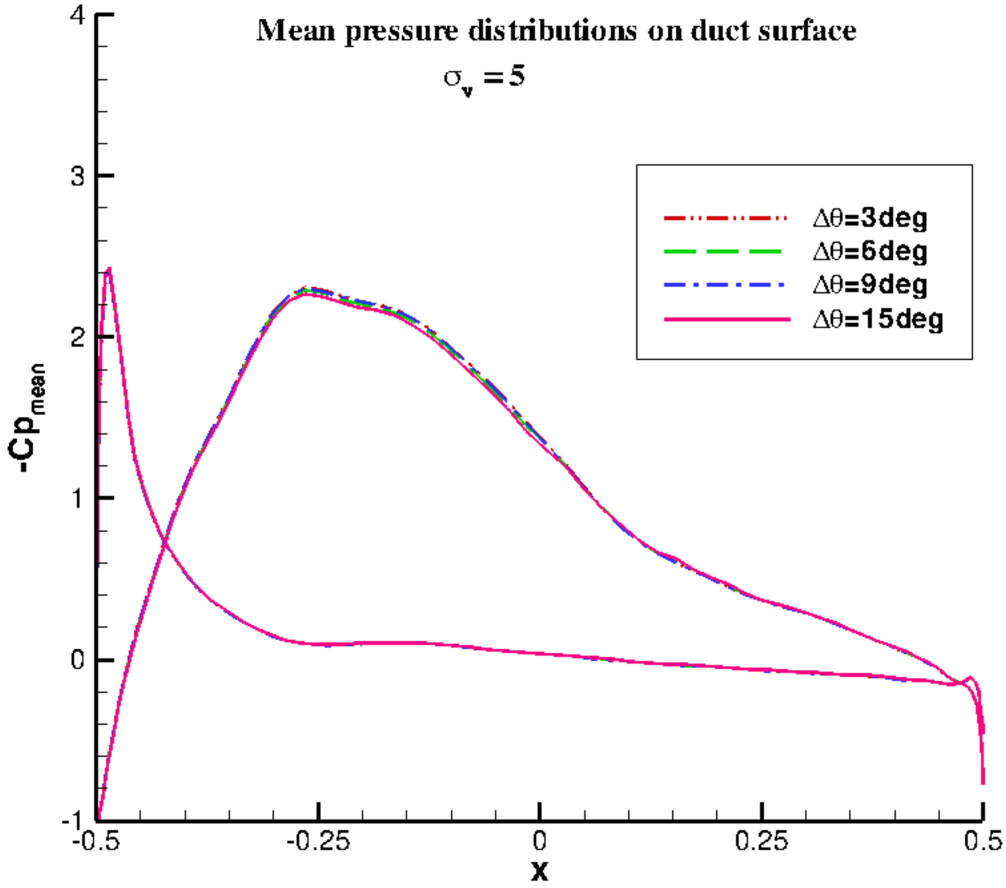

Figure 5.14: Convergence of inviscid mean pressure distributions on duct with panel size of trailing wake at $\sigma_v = 5$, $J_s = 0.5$.

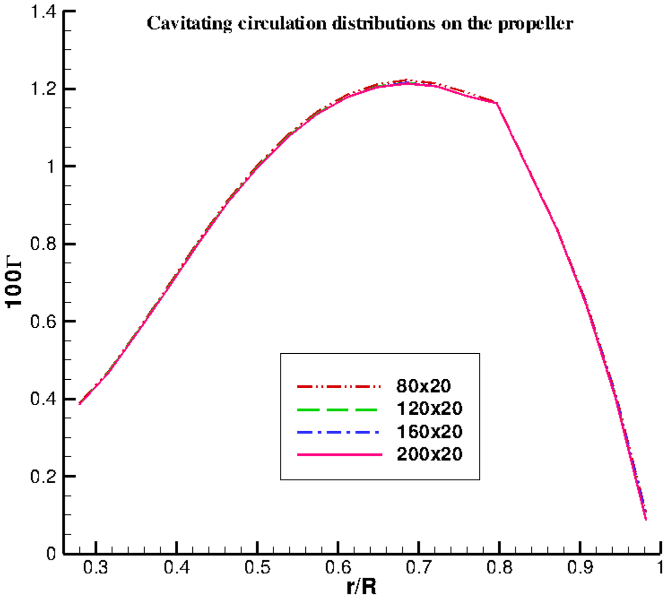

(a) Chord-wise

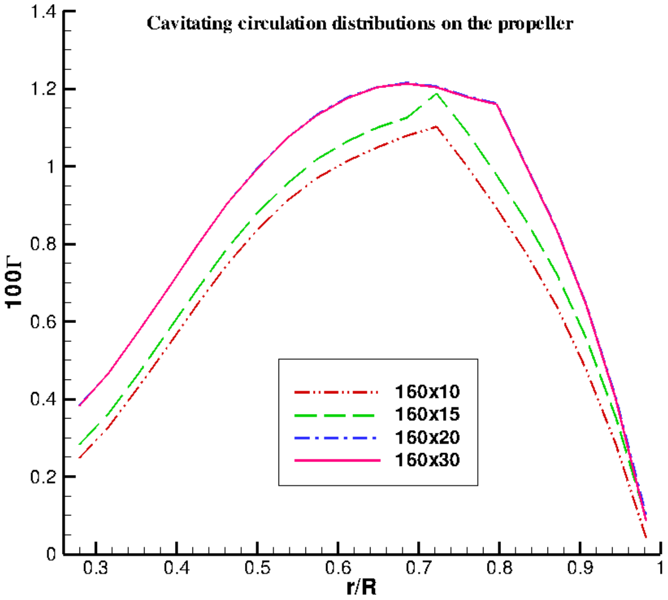

(b) Circumferential (No. of panels between blades)

Figure 5.15: Convergence of inviscid cavitating circulation distributions on propeller blade with number of panels on *duct* at $\sigma_v = 5$, $J_s = 0.5$.

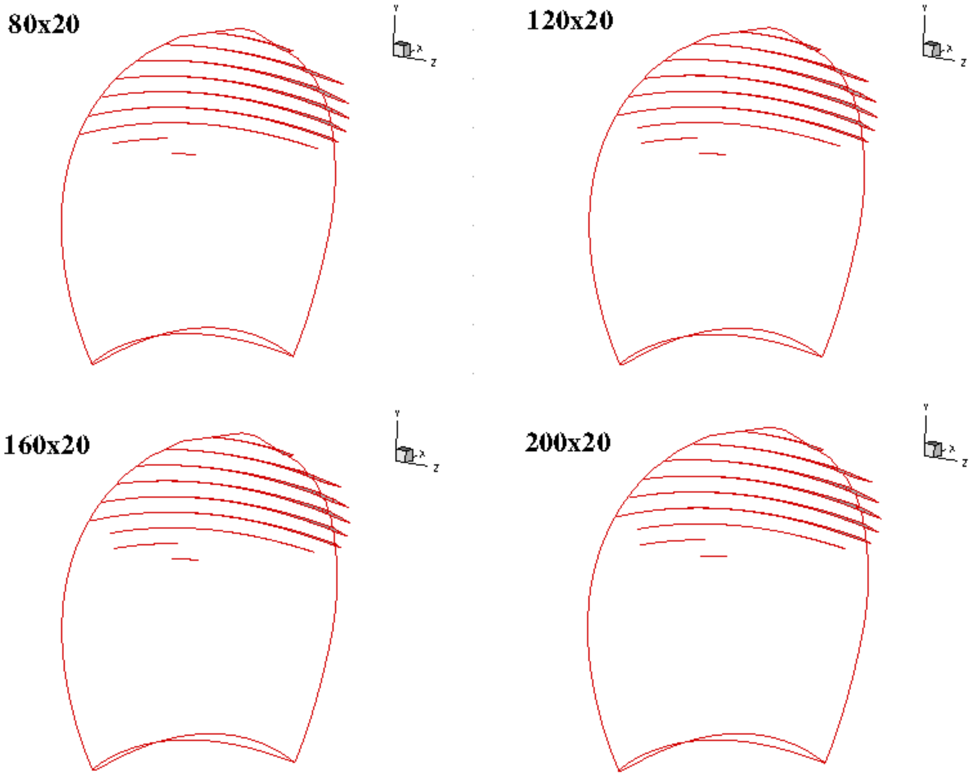

Figure 5.16: Convergence of inviscid cavity patterns with number of panels along Chord-wise direction on *duct* at $\sigma_v = 5$, $J_s = 0.5$.

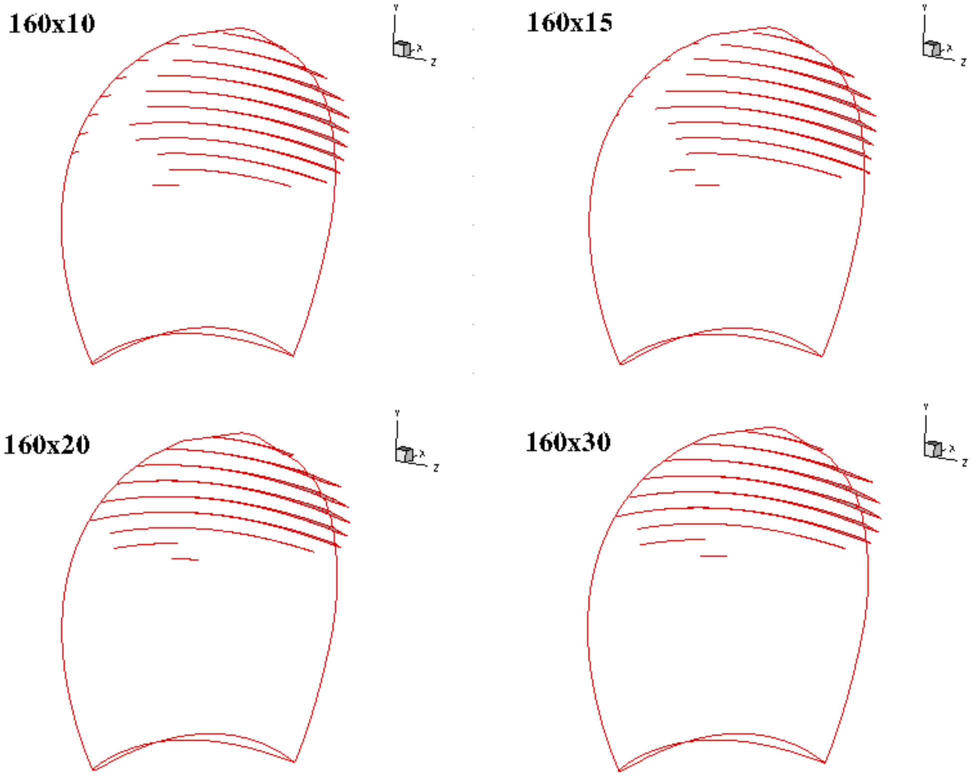

Figure 5.17: Convergence of inviscid cavity patterns with number of panels (between blades) along Circumferential direction on *duct* at $\sigma_v = 5$, $J_s = 0.5$.

cavity patterns. Same as in the wetted case, it requires at least 20 panels in the circumferential direction on duct to achieve convergence.

Results

At $\sigma_v = 5$, the present method predicts that the flows are all cavitating for J_s values varying from 0.4 to 0.7. For the PROPCAV/XFOIL runs, it generally takes about 40.0 minutes to finish both the inviscid and viscous analysis on a cluster with 1 CPU of AMD Opteron (1.6GHz & 2G RAM per CPU).

Figure 5.18 shows the predicted total thrust, torque, and duct thrust forces compared with the measured in experiments at $\sigma_v = 5$. Figure 5.19 shows the predicted inviscid cavity shapes on the propeller blade at $J_s = 0.6, 0.525, 0.45$ and 0.425. Super cavities happen at $J_s = 0.525$. However, from the experimental data, partial cavities are expected at $J_s = 0.525$ and super-cavities happen at a lower advance ratio $J_s = 0.45$. Therefore, the present method predicts that thrust breakdown occurs at a higher J_s than the measurements. For the viscous forces from PROPCAV/XFOIL, the torque forces have a better correlation with the measurement for partial cavitating cases than using empirical corrections, but for super cavitating cases $J_s \geq 0.525$, the flow seem to be greatly affected by the viscous effect. Even though the present method under-predicts the forces at low J_s values, the predicted forces at high J_s values are well compared with the measured. It should be pointed out that, the effects of viscosity on cavity patterns are not evaluated in this work. As discussed in Chapter 3, for a given cavitation number, the extent and size of the cavity including the effects of viscosity will be smaller than the inviscid solution.

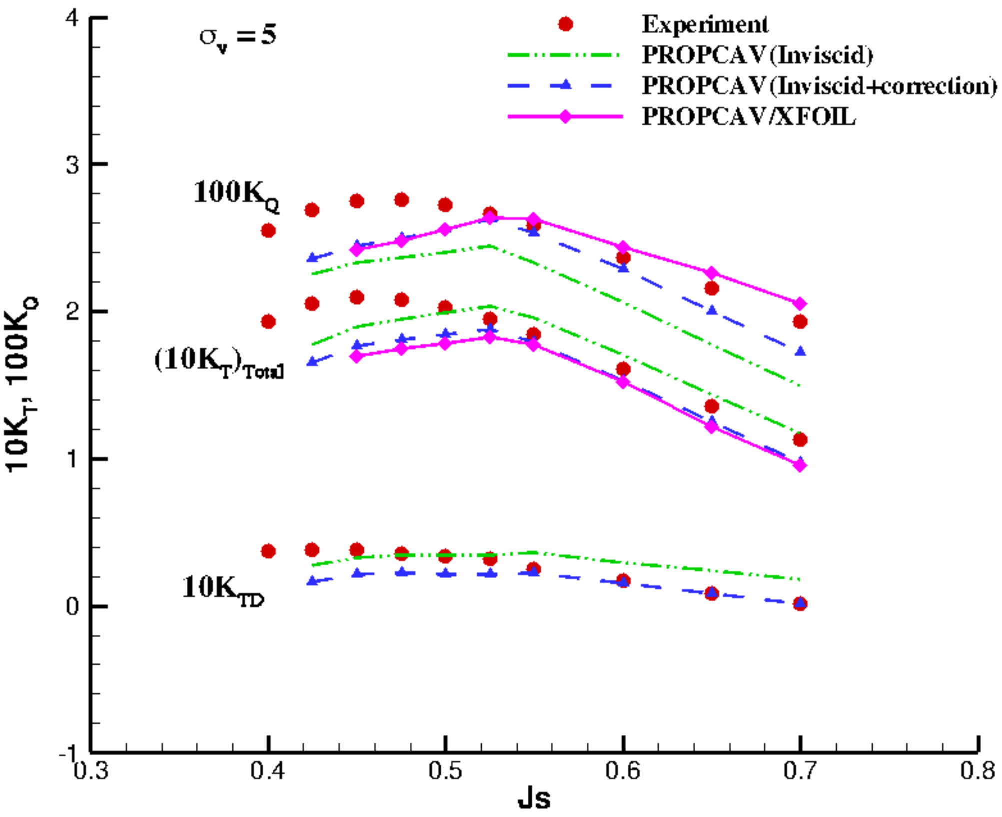

Figure 5.18: Comparison of the cavitating blade forces vs. advance ratio J_s between the present method and the measurements [Dyne 1973], at $\sigma_v = 5$.

Therefore, it is expected that including the effects of viscosity on cavity patterns will improve the prediction of thrust breakdown by the present method.

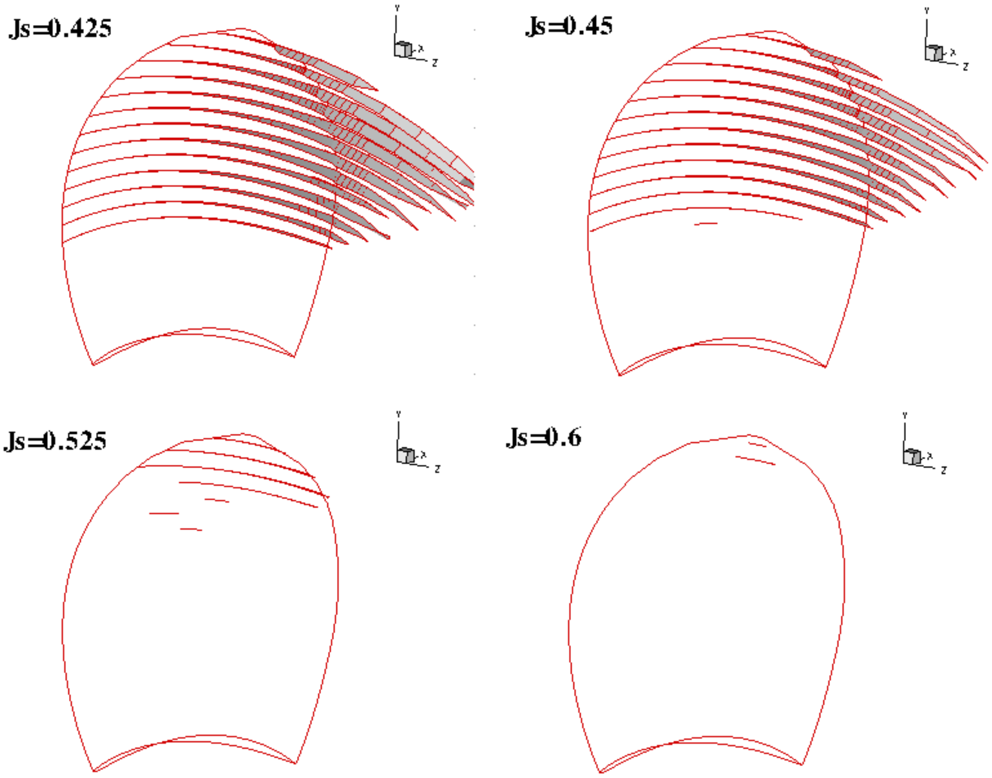

Figure 5.19: Predicted cavity patterns by the present method at $J_s = 0.6, 0.525, 0.45$ and 0.425.

5.4 Summary

The present method PROPCAV/XFOIL was applied to predict the steady wetted and cavitating performance of ducted propellers subject to uniform inflow. The interaction between the propeller and the duct was considered directly with the boundary value problem, and no iterations between the two were needed. Extensive convergence studies on circulation distributions, cavity shapes, and pressure distributions were performed to check grid dependence of the present method. Compared to the inviscid model with empirical viscous corrections, the present viscous/inviscid interaction method improved the prediction of blade forces on the propulsor, and had better correlation with the experimental measurements than using empirical viscous corrections. In addition, it was noted that the present method was able to predict thrust breakdown due to the occurrence of cavitation on blade at low advance ratios, even though the present method predicted the thrust breakdown to happen at higher advance ratios. It is anticipated that, if the effects of viscosity on cavity patterns are included, the correlation of the thrust breakdown between the present method and the measurements will improve.

Chapter 6

Viscous Flow in Water-jets

In this chapter, the viscous/inviscid interaction method (PROPCAV/XFOIL) is extended to predict the performance of wetted and cavitating water-jet propulsors, including the effects of viscosity. The flow field around the water-jet propulsor is solved by using an iterative procedure to include the interactions between rotor and stator in a time-averaged sense. Two approaches are proposed to evaluate the time-averaged effects of each component on the other. Results from the present methods are compared with experimental measurements.

6.1 Introduction

Water-jet propulsors has drawn significant attention from researchers and designers because of the increasing demand of high-speed vessels in naval and commercial application in recent years. Compared to conventional propellers, which tend to experience cavitation and related problems at higher speeds, water-jet propulsors offer several advantages. They have improved maneuverability, and can reduce the possibility of cavity occurrence by controlling the flow inside the casing, and can protect the rotor/stator blades from debris damages. Nevertheless, cavitation is still the most important factor that significantly affect the performance of water-jet propulsors, and can cause a lot of detrimental effects: erosion, noise, and vibrations. Furthermore, as for open and ducted propellers, thrust breakdown due to cavitation is the foremost hydrodynamic issue for water-jet propulsors.

Performance prediction of water-jet propulsors using numerical methods is much more challenging than that of conventional propellers because of the complexity of water-jet geometric configurations and the interactions between the components of water-jet propulsor. At present, our capability to simulate viscous flows around cavitating water-jet propulsors is very limited. Issues concerning the prediction of performance and design of water-jets have been reviewed by Kerwin [Kerwin 2006]. A hybrid design approach proposed by [Kerwin et al. 1997] was applied to the prediction and design of water-jet components [Taylor et al. 1998] and [Kerwin et al. 2006]. In these hybrid methods, the inviscid flow methods (vortex-lattice methods) were applied on the blades to obtain the performance of the rotor/stator; either Reynolds-Averaged Navier-Stokes (RANS) or Euler equations solvers were coupled with the inviscid solver to include the effects of the hull and other appendages, and to analyze the global flow through the water-jet pump. On the other hand, CFD tools (particularly RANS solvers) have been increasingly used to predict flow inside and around the water-jets. [Chun et al. 2002] applied a RANS method to model the full water-jet system in the unsteady sense by using a moving, non-orthogonal body-fitted multi-blocked grid system. The interface boundary between the rotor and the stator was handled with the sliding multi-block technique. Their results were in good correlation with experimental measurements. [Brewton et al. 2006] incorporated periodic boundaries and a mixing plane model into the RANS method, and considered the interaction between the rotor and the stator in the time-averaged sense. Although CFD tools made significant improvements in understanding the detailed flow phenomena, prediction of unsteady cavitating performance of water-jet propulsors still remains a formidable task for CFD tools.

In this study, the present viscous/inviscid interactive method is applied to predict the performance of cavitating water-jet propulsors, including the effect of viscosity. At this stage, only axial flow pumps subject to uniform upstream inflow is addressed, the viscous flow due to the hull or other appendages is ignored. The interactive effects between rotor and stator are considered in a time-averaged sense in a similar way as presented in [Taylor et al. 1998], [Kinnas et al. 2002], [Kerwin et al. 2006], and [Brewton et al. 2006].

6.2 Inviscid Water-jet Model

In this section, the boundary element method (PROPCAV) described in Chapter 2 is extended to predict performance of wetted and cavitating water-jets. The assumptions, governing equations and boundary conditions for solving the problem are summarized.

6.2.1 Assumptions

A typical configuration of water-jet geometry with the related coordinate systems is depicted in Figure 6.1. (x_s, y_s, z_s) denotes the ship fixed coordinate system, and (x, y, z) is the blade fixed coordinate system. The following assumptions are made:

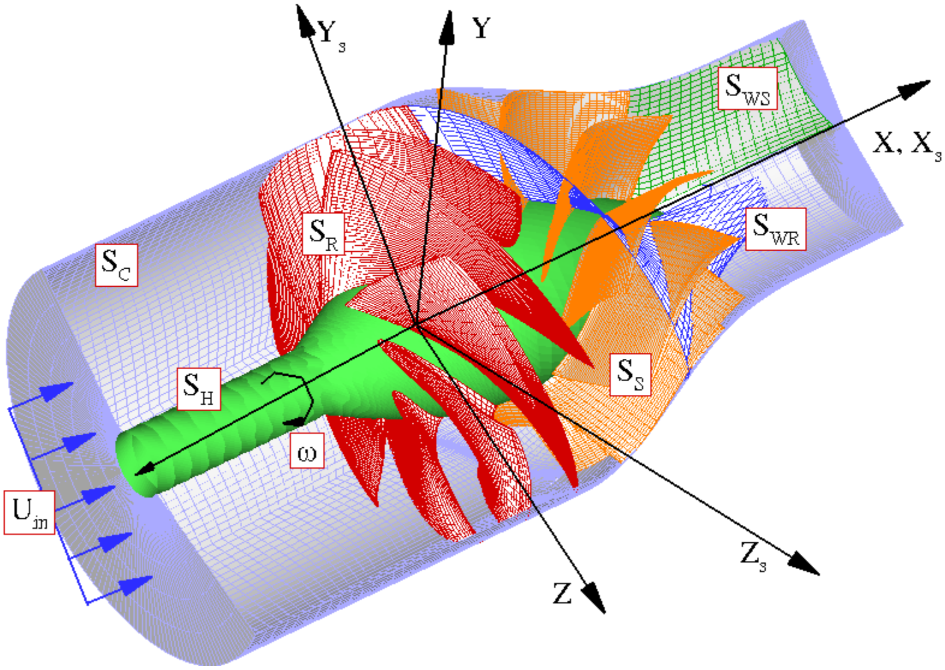

Figure 6.1: Rotor- and Stator-Fixed Coordinate systems and paneled geometry of water-jet components.

- The inflow at the water-jet inlet $\vec{U}_{in}$, which is defined in the ship fixed coordinate system, is assumed to be uniform.

- The water-jet rotor rotates with a constant angular velocity, $\vec{\omega}$.

- Stator does not rotate and is fixed in the (x, y, z) coordinate system.

- Inflow velocity in the blade fixed coordinate system V_{in}:

  $$\vec{q}_{in}(x, y, z, t) = \vec{U}_{in}(x, r, \theta) \qquad \text{for stator,}$$
  $$\vec{q}_{in}(x, y, z, t) = \vec{U}_{in}(x, r, \theta' - \omega t) - \vec{\omega} \times \vec{x} \qquad \text{for rotor,}$$

  where $r = \sqrt{(y^2 + z^2)}$, $\theta' = \tan^{-1}(z/y)$, and $\vec{x} = (x, y, z)$.

- Flow is assumed to be inviscid, incompressible and irrotational.

  $$\vec{q}(x, y, z, t) = \vec{q}_{in}(x, y, z, t) + \nabla\phi(x, y, z, t)$$

  where $\vec{q}(x, y, z, t)$ is the total velocity at any point, (x, y, z), inside the flow domain. $\nabla\phi(x, y, z, t)$ is the perturbation velocity. ϕ is the perturbation potential which satisfies the Laplace's equation $\nabla^2\phi = 0$.

6.2.2 Governing Equations

The perturbation potential, $\phi(x, y, z)$, at any point $p(x, y, z)$ located either on the wetted rotor/stator blades and hub surface, $S_R \cup S_S \cup S_H$, and the casing surface, S_C, or on the cavitating surfaces on rotor/stator, $S_{RC} \cup S_{SC}$, has to satisfy the Green's third identity Equation 6.1. It should be pointed out that ϕ should also be a function of time, since the interactions between the rotational and stationary components of water-jet are unsteady in nature. However, numerical simulation of the interactions between rotor and stator in a fully unsteady manner is very complicated and computational expensive. At this stage, the problem will be solved in a time-averaged sense.

$$\begin{aligned} 2\pi\phi(\vec{x}) &= \int_{S_R+S_{RC}} \left[\phi_q(\vec{x})\frac{\partial G(p;q)}{\partial n_q} - G(p;q)\frac{\partial \phi_q(\vec{x})}{\partial n_q}\right] ds \\ &+ \int_{S_{RW}} \Delta\phi_{RW}(\vec{x})\frac{\partial G(p;q)}{\partial n_q} ds \\ &+ \int_{S_S+S_{SC}} \left[\phi_q(\vec{x})\frac{\partial G(p;q)}{\partial n_q} - G(p;q)\frac{\partial \phi_q(\vec{x})}{\partial n_q}\right] ds \\ &+ \int_{S_{SW}} \Delta\phi_{SW}(\vec{x})\frac{\partial G(p;q)}{\partial n_q} ds \\ &+ \int_{S_C} \left[\phi_q(\vec{x})\frac{\partial G(p;q)}{\partial n_q} - G(p;q)\frac{\partial \phi_q(\vec{x})}{\partial n_q}\right] ds \qquad (6.1) \end{aligned}$$

where the subscripts, q and p, correspond to the variable point and the field point, respectively. $G(p;q) = 1/R(p;q)$ is the Green function, where $R(p;q)$ is the distance between the field point p and the variable point q. $\vec{n}_q$ is the unit normal vector pointing into the flow field. $\Delta\phi_{RW}$ and $\Delta\phi_{SW}$ are the potential jump in the trailing wake sheets shedding from either the rotor or the stator trailing edge, respectively. S_{RC} and S_{SC} are the cavity surfaces on the rotor and on the stator.

Figure 6.2 shows the schematic for the complete rotor and stator problem. Figure 6.3 and Figure 6.4 show the schematics for the rotor problem and for the stator problem, respectively. The flow field inside the water-jet pump is solved in an iterative manner by solving the rotor and stator problems separately and by

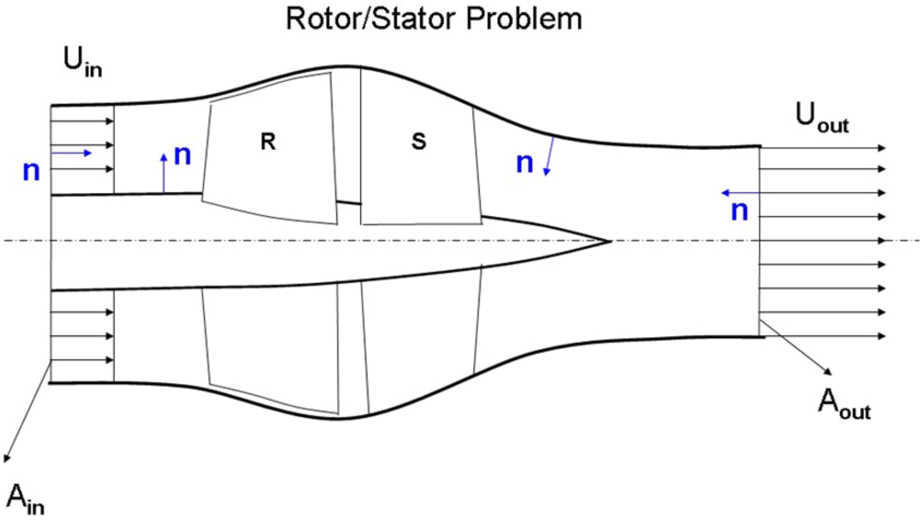

Figure 6.2: Schematic for the combined rotor/stator problem, taken from [Kinnas et al. 2007b].

considering the time-averaged effect of one device on the other. Two approaches are developed to evaluate the interactive effects between rotor and stator. One approach is to use the circumferentially averaged *induced potentials* [Kinnas et al. 2007b], and the other one is to use circumferentially averaged *induced velocities*. For both approaches, the rotor is solved with respect to the rotating coordinate system and the stator is solved with respect to the ship fixed coordinate system.

6.2.3 The Induced Potential Approach

In this approach, the interactive effects of each component on the other are evaluated by using circumferentially averaged induced potentials. Equations 6.2 and 6.4 give the integral equations for the rotor and stator problems, respectively.

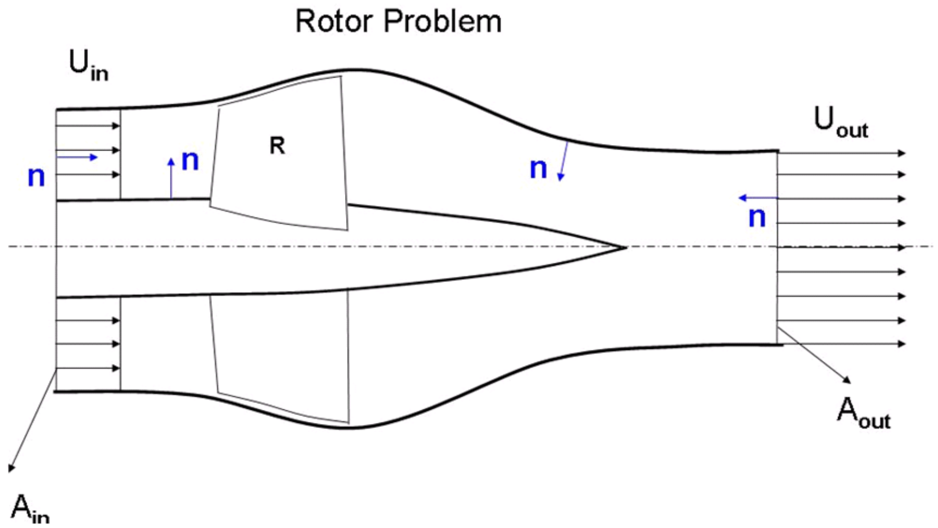

Figure 6.3: Schematic for the rotor problem, taken from [Kinnas et al. 2007b].

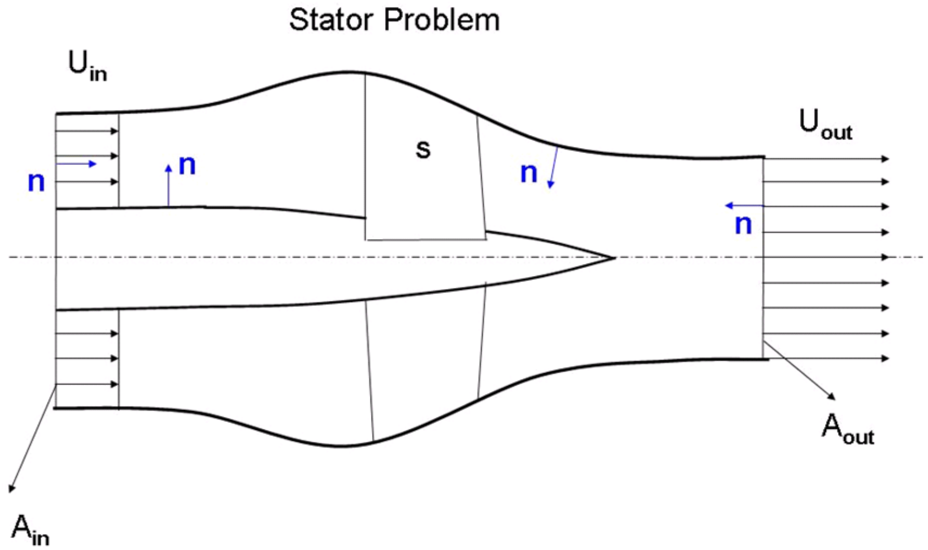

Figure 6.4: Schematic for the stator problem, taken from [Kinnas et al. 2007b].

The induced potentials on the other component are calculated using the integral equations for $\phi_{RS}(\vec{x})$ and $\phi_{SR}(\vec{x})$, and then circumferentially averaged to apply to the control points.

The Rotor Problem:

Equation 6.2 gives the integral equation for the rotor problem in the induced potential approach,

$$\begin{aligned} 2\pi\phi(\vec{x}) &= \int_{S_R+S_{RC}} \left[\phi_q(\vec{x})\frac{\partial G(p;q)}{\partial n_q} - G(p;q)\frac{\partial \phi_q(\vec{x})}{\partial n_q}\right] ds \\ &+ \int_{S_{RW}} \Delta\phi_{RW}(\vec{x})\frac{\partial G(p;q)}{\partial n_q} ds \\ &+ \int_{S_C} \left[\phi_q(\vec{x})\frac{\partial G(p;q)}{\partial n_q} - G(p;q)\frac{\partial \phi_q(\vec{x})}{\partial n_q}\right] ds \\ &+ 4\pi\phi_{RS}(\vec{x}) \end{aligned} \tag{6.2}$$

where S_R denotes the rotor surface, and S_{RC} denotes the rotor cavity. S_{RW} is the rotor wake. S_C is the casing surface. $\Delta\phi_{RW}$ is the potential jump across the rotor wake. $\phi_{RS}(\vec{x})$ is the circumferentially averaged values of the induced potentials on rotor, hub and water-jet casing due to stator, calculated by the following integral equation:

$$\begin{aligned} 4\pi\phi_{RS}(\vec{x}) &= \int_{S_S+S_{SC}} \left[\phi_q(\vec{x})\frac{\partial G(p;q)}{\partial n_q} - G(p;q)\frac{\partial \phi_q(\vec{x})}{\partial n_q}\right] ds \\ &+ \int_{S_{SW}} \Delta\phi_{SW}(\vec{x})\frac{\partial G(p;q)}{\partial n_q} ds \end{aligned} \tag{6.3}$$

where S_S denotes the stator surface, and S_{SC} denotes the stator cavity. S_{SW} is the stator wake. $\Delta\phi_{SW}$ is the potential jump across the stator wake.

The Stator Problem:

Similar to the rotor problem, the integral equation for the stator problem in the induced potential approach can be written as,

$$\begin{aligned}
2\pi\phi(\vec{x}) &= \int_{S_S+S_{SC}} \left[\phi_q(\vec{x})\frac{\partial G(p;q)}{\partial n_q} - G(p;q)\frac{\partial \phi_q(\vec{x})}{\partial n_q}\right] ds \\
&+ \int_{S_{SW}} \Delta\phi_{SW}(\vec{x})\frac{\partial G(p;q)}{\partial n_q} ds \\
&+ \int_{S_C} \left[\phi_q(\vec{x})\frac{\partial G(p;q)}{\partial n_q} - G(p;q)\frac{\partial \phi_q(\vec{x})}{\partial n_q}\right] ds \\
&+ 4\pi\phi_{SR}(\vec{x}) \qquad (6.4)
\end{aligned}$$

where $\phi_{SR}(\vec{x})$ is the circumferentially averaged values of the induced potentials on stator, hub and water-jet casing due to rotor, calculated by the following equation:

$$\begin{aligned}
4\pi\phi_{SR}(x,y,z) &= \int_{S_R+S_{RC}} \left[\phi_q(\vec{x})\frac{\partial G(p;q)}{\partial n_q} - G(p;q)\frac{\partial \phi_q(\vec{x})}{\partial n_q}\right] ds \\
&+ \int_{S_{RW}} \Delta\phi_{RW}(\vec{x})\frac{\partial G(p;q)}{\partial n_q} ds \qquad (6.5)
\end{aligned}$$

It should be pointed out that, when taking the circumferentially averaged mean of induced potentials, changes of the induced swirl (tangential) velocity will not be taken into account. In the case of the stator problem, the swirl velocities induced by the rotor on the stator (assumed to be post-swirl) have to be evaluated and included, as a velocity term, in the kinematic boundary condition on the stator blades. Therefore, the kinematic boundary condition on the stator blades must be adjusted as follows:

$$\left.\frac{\partial \phi}{\partial n}\right|_{stator} = -\left(\vec{q}_{in} + \vec{u}_{tan,SR}\right)\cdot\vec{n} \qquad (6.6)$$

where $\vec{u}_{tan,SR}$ is the tangential (swirl) velocity induced by the rotor on the stator control points. In the case of the rotor problem, this adjustment is not required for the kinematic boundary condition on the rotor, since the stator does not induce any swirl upstream of it.

Evaluation of Circumferentially Averaged $\vec{u}_{tan,SR}$

Figure 6.5 shows a sketch of the rotor and the rotor wake. According to Stokes' theorem, the circumferentially averaged tangential velocity $\vec{u}_{tan,SR}$ at any point in the rotor wake can be calculated using the following formula.

$$\vec{u}_{tan,SR} = \frac{\Gamma \times NBLADE}{2\pi R} \tag{6.7}$$

where Γ is the strength of the vortex ring at certain radius, and can be interpolated from the solution of the rotor problem. $NBLADE$ is the number of blades of the rotor. R is the radius to the rotor axis.

For the stator problem, the tangential velocities are first evaluated using Equation 6.7 at the centroids of the rotor wake, and then interpolated to the stator control points.

6.2.4 The Induced Velocity Approach

In the induced velocity approach, the interactive effects between the rotor and the stator are evaluated by using circumferentially averaged induced velocities. This section summarizes the integral equations for the rotor and stator problems, and the calculation of the circumferentially averaged induced velocities.

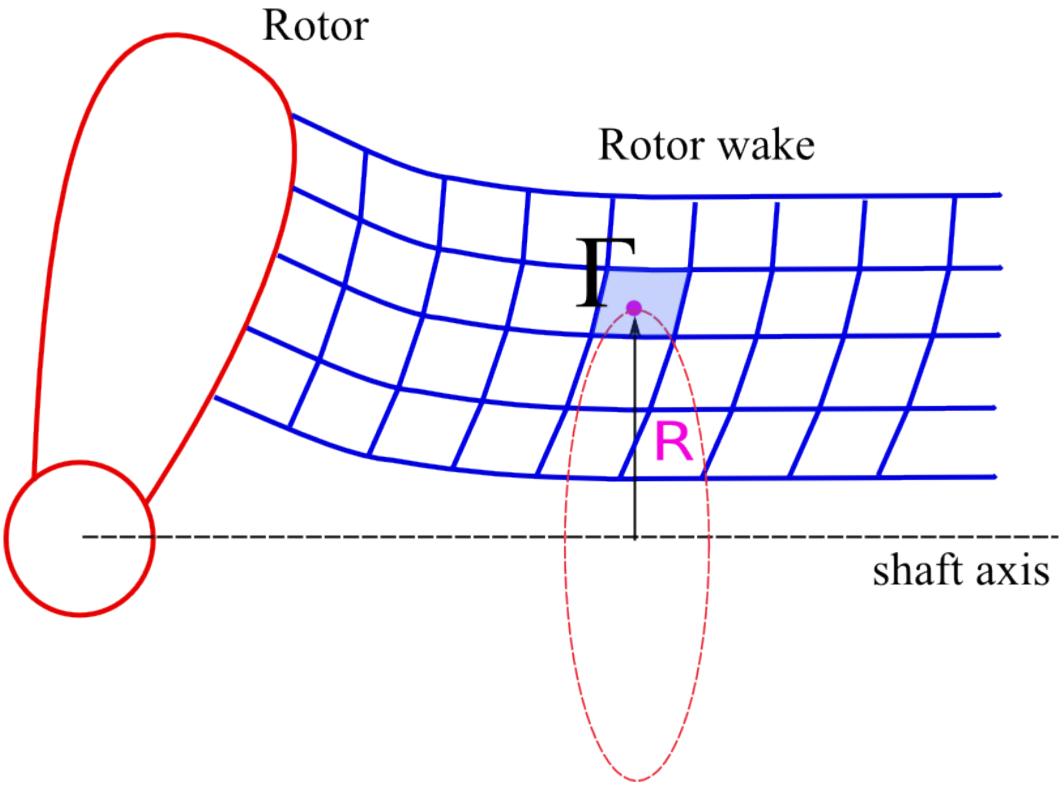

Figure 6.5: Sketch showing the rotor and rotor wake, for the evaluation (using Stokes' theorem) of the circumferentially averaged tangential velocity at any point in the rotor wake.

The Rotor Problem:

Equation 6.8 is the integral equation for the rotor problem using the induced velocity approach,

$$\begin{aligned}
2\pi\phi(\vec{x}) &= \int_{S_R+S_{RC}} \left[\phi_q(\vec{x})\frac{\partial G(p;q)}{\partial n_q} - G(p;q)\frac{\partial \phi_q(\vec{x})}{\partial n_q}\right] ds \\
&+ \int_{S_{RW}} \Delta\phi_{RW}(\vec{x})\frac{\partial G(p;q)}{\partial n_q} ds \\
&+ \int_{S_C} \left[\phi_q(\vec{x})\frac{\partial G(p;q)}{\partial n_q} - G(p;q)\frac{\partial \phi_q(\vec{x})}{\partial n_q}\right] ds \qquad (6.8)
\end{aligned}$$

where the source strength $\partial\phi/\partial n$ is modified as,

$$\frac{\partial \phi}{\partial n} = -\left(\vec{q}_{in}(x,y,z,t) + \vec{u}_{RS}\right)\cdot\vec{n}$$

$\vec{u}_{RS}$ is the circumferentially averaged induced velocities on rotor, hub and casing surfaces by the stator, calculated as follows:

$$\begin{aligned}
4\pi\vec{u}_{RS} &= \int_{S_S+S_{SC}} \left[\phi_q(\vec{x})\nabla\left(\frac{\partial G(p;q)}{\partial n_q}\right) - \nabla G(p;q)\frac{\partial \phi_q(\vec{x})}{\partial n_q}\right] ds \\
&+ \int_{S_{SW}} \Delta\phi_{SW}(\vec{x})\nabla\left(\frac{\partial G(p;q)}{\partial n_q}\right) ds \qquad (6.9)
\end{aligned}$$

$\nabla\left(\partial G/\partial n\right)$ and ∇G can be evaluated by using the RPAN routine, which calculates the induced potentials and velocities due to unit strength sources and normal dipoles over a quadrilateral panel [Newman 1986].

The Stator Problem:

The integral equation for the stator problem is,

$$\begin{aligned}
2\pi\phi(\vec{x}) &= \int_{S_S+S_{SC}} \left[\phi_q(\vec{x})\frac{\partial G(p;q)}{\partial n_q} - G(p;q)\frac{\partial \phi_q(\vec{x})}{\partial n_q}\right] ds \\
&+ \int_{S_{SW}} \Delta\phi_{SW}(\vec{x})\frac{\partial G(p;q)}{\partial n_q} ds \\
&+ \int_{S_C} \left[\phi_q(\vec{x})\frac{\partial G(p;q)}{\partial n_q} - G(p;q)\frac{\partial \phi_q(\vec{x})}{\partial n_q}\right] ds \qquad (6.10)
\end{aligned}$$

where

$$\frac{\partial \phi}{\partial n} = -\left(\vec{q}_{in}(x,y,z,t) + \vec{u}_{SR}\right)\cdot\vec{n}$$

$\vec{u}_{SR}$ is the circumferentially averaged induced velocities on stator, hub and casing surfaces by the rotor, calculated as follows:

$$\begin{aligned}
4\pi\vec{u}_{SR} &= \int_{S_R+S_{RC}} \left[\phi_q(\vec{x})\nabla\left(\frac{\partial G(p;q)}{\partial n_q}\right) - \nabla G(p;q)\frac{\partial \phi_q(\vec{x})}{\partial n_q}\right] ds \\
&+ \int_{S_{RW}} \Delta\phi_{RW}(\vec{x})\nabla\left(\frac{\partial G(p;q)}{\partial n_q}\right) ds \qquad (6.11)
\end{aligned}$$

It should be noticed that the swirl velocity $\vec{u}_{tan,SR}$ in Equation 6.7 can also be evaluated by using Equation 6.11 and then circumferentially averaged with respect to the angular position.

6.2.5 Boundary Conditions

The kinematic and dynamic boundary conditions applied on the casing, hub, rotor and stator surfaces are the same as those detailed in Chapter 2. There are slight differences between the rotor and stator problems while implementing the dynamic boundary condition on cavity surface.

The dynamic boundary condition on cavity surface requires that the pressure on the cavity surface is constant and equal to the cavitating pressure, p_v. After applying the Bernoulli's equation, the total velocity, $\vec{q}_t$, on the rotor or stator cavity surface can be derived as follows:

$$|\vec{q}_t|^2 = \begin{cases} n^2 D^2 \sigma_n + |\vec{q}_{in}|^2 + \omega^2 r^2 - 2gy_s - 2\dfrac{\partial \phi}{\partial t} & \text{for rotor} \\ |\vec{q}_{in}|^2 - 2gy_s - 2\dfrac{\partial \phi}{\partial t} & \text{for stator} \end{cases} \tag{6.12}$$

where r is the distance from the axis of rotation. g and y_s are the gravitation constant and the vertical distance from the horizontal plane through the axis of rotation. n and D are the blade rotational frequency and the propeller diameter, respectively. The cavitation number, σ_n, for the rotor and stator problem is defined as follows:

$$\sigma_n = \begin{cases} \dfrac{P_o - P_v}{0.5\rho n^2 D^2} & \text{for rotor} \\ \\ \dfrac{P_o - P_v}{0.5\rho U_{in}^2} & \text{for stator} \end{cases} \tag{6.13}$$

P_o is the far upstream pressure on the shaft axis, P_v is the vapor pressure of water, and ρ is the water density.

Boundary Conditions at Water-jet Inlet and Outlet

Unlike the open or ducted propeller located in unbounded flow domain, the rotor/stator is now operating inside a casing, and the water-jet problem is actually an internal boundary value problem. Boundary conditions at the water-jet inlet and outlet are required in order to uniquely determine the solution.

1. At the water-jet inlet, the flow is assumed to be equal to the inflow.

   $$\left.\frac{\partial \phi}{\partial n}\right|_{in} = 0$$

   For internal boundary value problems, to avoid singular matrix in the left hand-side of the resulted system equation, ϕ is assumed to be zero everywhere at the inlet of the water-jet.

2. The flow at the water-jet outlet has to satisfy the mass conservation,

   $$\left.\frac{\partial \phi}{\partial n}\right|_{out} = U_{in} - U_{out}$$

   thus, the flow velocities at the outlet is,

   $$U_{in} \cdot A_{in} = U_{out} \cdot A_{out} \qquad \text{, or} \qquad U_{out} = U_{in} \cdot \frac{A_{in}}{A_{out}}$$

   where U_{in} is the inflow velocity. A_{in} and A_{out} are the water-jet inlet and outlet area, respectively.

6.2.6 Interaction between Rotor and Stator

The interactive effects between the water-jet rotor and stator are taken into account based on an iterative procedure by using the circumferentially averaged induced potentials and/or induced velocities. The problems for both components iterate until the forces converge to a certain criterion. This section presents the algorithm used to calculate the circumferentially averaged effects between the components. Both the induce potential approach and the induced velocity approach use the same averaging algorithm. As an example, the calculation of the circumferentially averaged induced potentials in the case of stator problem is explained.

As shown in Figure 6.6, the induced potentials on the stator control points induced by each panel on the rotor key blade are first calculated using Equation 6.5 and then circumferentially averaged through the following expression:

$$\phi_{SR}^{1} = \frac{\sum_{i=1}^{i=N} \phi_i^1}{N} \tag{6.14}$$

where N is the total number of equally spaced elements over a full circle. The subscript 1 indicates one panel on the rotor key blade.

It should be clarified that the circumferentially averaged induced potentials due to the rotor wake are first evaluated at the control points of the rotor wake using the same method as in Figure 6.6, and then interpolated to the control points of the stator. Figure 6.7 shows the sample plot of induced potentials ϕ_i at one point (in the rotor wake) by the rotor and its wake with respect to the index no. of the equally spaced elements over a full circle. The averaged induced potential $\bar{\phi}_{ind}$ by the rotor and rotor wake is also plotted.

6.3 Viscous Water-jet Model

The emphasis of this study is placed on the viscous flow inherent with the water-jet rotor and stator blades. The viscous boundary layer flow due to the hull, casing and other appendages is beyond the scope of this dissertation. In this section, the inviscid water-jet model (PROPCAV) described above is coupled with the 2-D integral boundary layer analysis (XFOIL) to investigate the effects of viscosity on forces and cavity patterns.

The boundary layer flow is assumed to be two dimensional along strips of

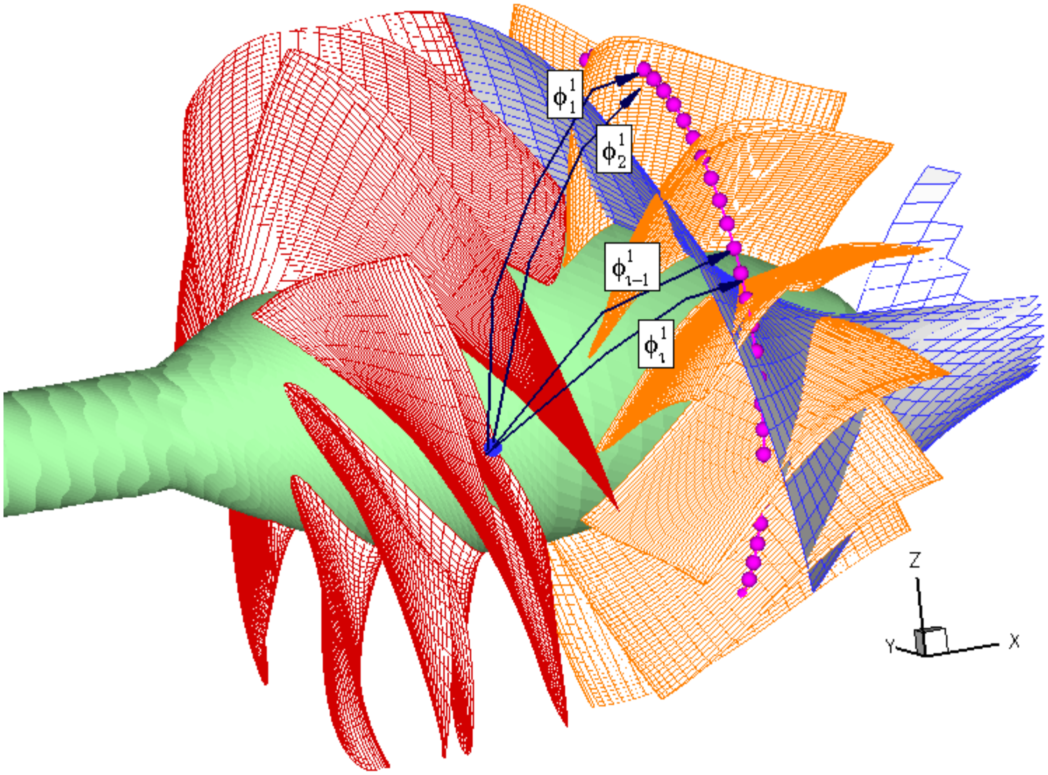

Figure 6.6: The inclusion of the effect of rotor into the stator control points.

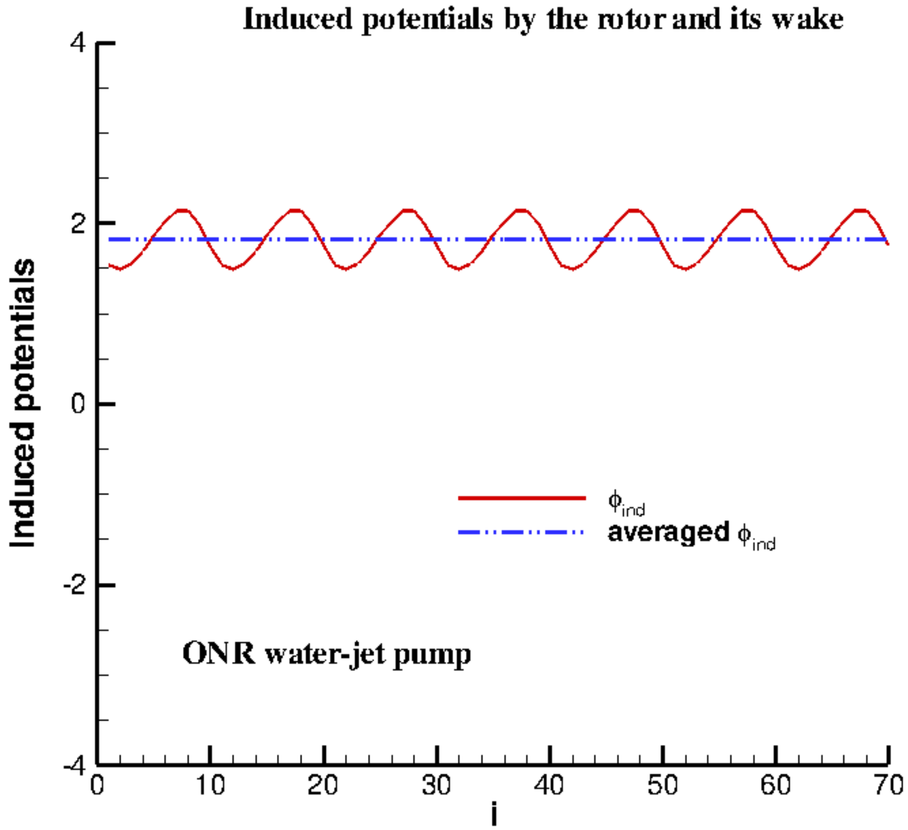

Figure 6.7: Sample plot of induced potentials ϕ_i at one point in the rotor wake vs. index no. of the equally spaced elements over a full circle. The averaged induced potential $\bar{\phi}_{ind}$ by the rotor and rotor wake is also plotted.

the water-jet rotor/stator blades. For rotors and stators, these strips are assumed to follow the inner surface of the casing or the outer surface of the hub, instead of using constant radius strips. The strengths of the blowing sources, which represent the effects of boundary layer displacement thickness, are solved along the strip wise direction. For the cavitating problem, the boundary layers are allowed to develop over the cavity surfaces by forcing the friction coefficient to zero on top of the cavity. The complex two-phase flow near the cavity surface is ignored, and the fluid/vapor interface is treated as constant pressure, free streamline.

For water-jet flows, the viscous boundary layer analysis and the coupling algorithm between the inviscid and viscous models are the same as that described in Chapter 2. As an example, the governing equation for the viscous flow in the case of rotor problem using the induced potential approach is given below. When including the effects of the blowing sources, the Greens formulation, Equation 6.2, can be written as follows :

$$\begin{aligned}
2\pi\phi(\vec{x}) &= \int_{S_R+S_{RC}} \left[\phi_q(\vec{x})\frac{\partial G(p;q)}{\partial n_q} - G(p;q)\frac{\partial \phi_q(\vec{x})}{\partial n_q}\right] ds \\
&+ \int_{S_{RW}} \Delta\phi_{RW}(\vec{x})\frac{\partial G(p;q)}{\partial n_q} ds \\
&+ \int_{S_C} \left[\phi_q(\vec{x})\frac{\partial G(p;q)}{\partial n_q} - G(p;q)\frac{\partial \phi_q(\vec{x})}{\partial n_q}\right] ds \\
&+ 4\pi\phi_{RS}(x,y,z) \\
&- \int_{S_R+S_{RC}+S_{RW}} \hat{\sigma}(p;q)\frac{\partial \phi_q(\vec{x})}{\partial n_q} ds \qquad (6.15)
\end{aligned}$$

where $\hat{\sigma}$ is the strength of the blowing source defined as:

$$\hat{\sigma} = \frac{d\left(U_e\delta^*\right)}{ds}$$

U_e is the edge velocity along the boundary layer and δ^* is the displacement boundary layer thickness.

6.4 Numerical Results

This study focuses on the an axial water-jet pump (ONR-AWJ1[1]), which is currently being tested at Johns Hopkins University with support by the Office of Naval Research (ONR). The rotor is 7-bladed, and the stator is 11-bladed, as shown in Figure 6.8. Figure 6.9 and 6.10 show the representative panel arrangements on the various components of the ONR-AWJ1 water-jet pump. The panels for the rotor or the stator problems are aligned with the geometry at the tip of the rotor or the stator blades, respectively. Figure 6.11 shows the detailed panel arrangements at the junctions of the blades with the hub or the casing.

In this work, the tip gap between the rotor (or stator) tip and the casing surface is assumed to be equal to zero, even though the actual gap is usually less than 1%. As shown in [Kerwin 2006], where the orifice equation was implemented in the case of a wing close to a wall, for a gap of 1% the results with zero gap were much closer to those from the inviscid theory with the orifice equation implemented, than to those from inviscid theory where the actual gap was used.

In the following sections, the present method is applied to the ONR-AWJ1 water-jet pump. Systematic convergence studies are presented for the casing casing, rotor-only and stator-only problems. The proposed iterative methods for the

---

[1] Private contact with Mr. Thad Michael at Naval Surface Warfare Center Carderock Division, USA

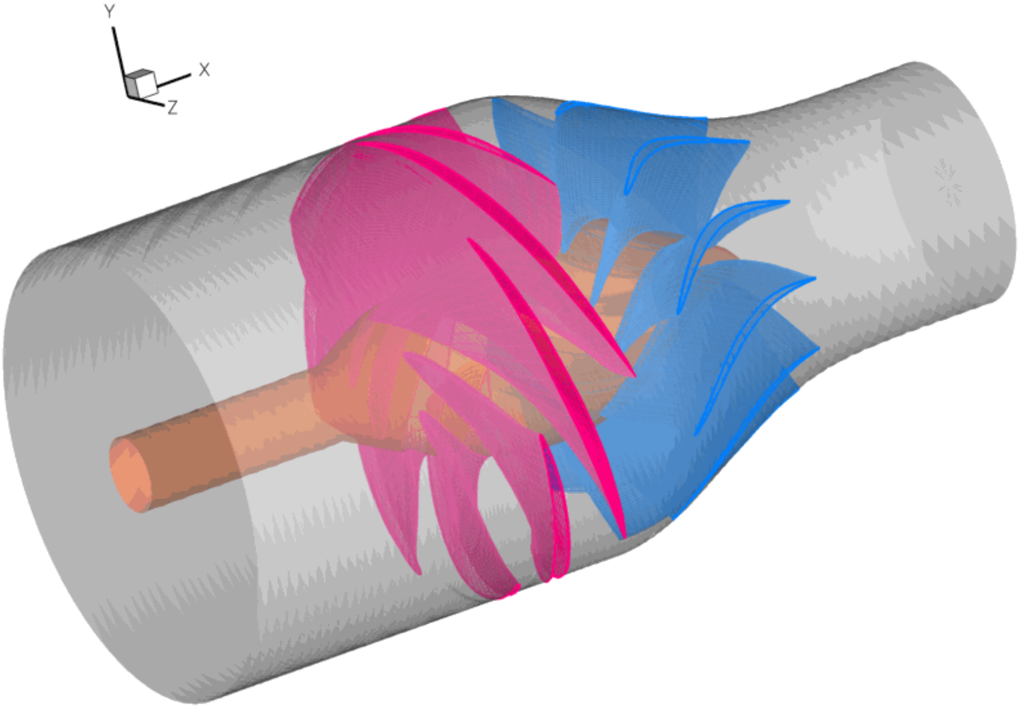

Figure 6.8: Paneled geometry of the ONR-AWJ1 water-jet pump with a 7-blade rotor and an 11-blade stator, viewed from upstream.

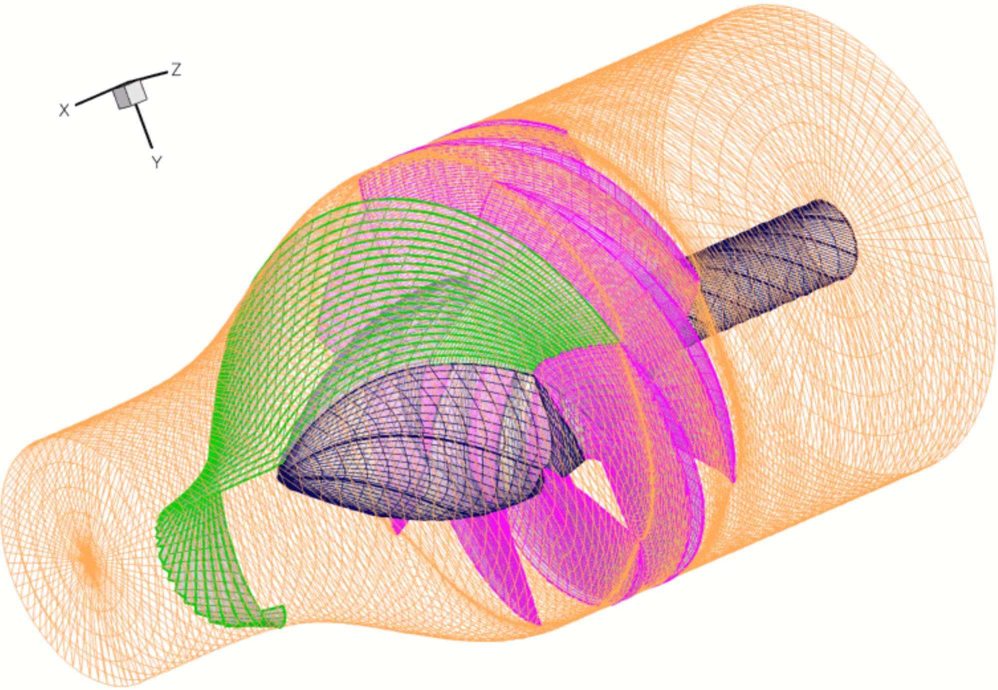

Figure 6.9: Paneled geometry of the ONR-AWJ1 water-jet pump for the rotor problem (the trailing wake of one blade is also shown), viewed from down stream.

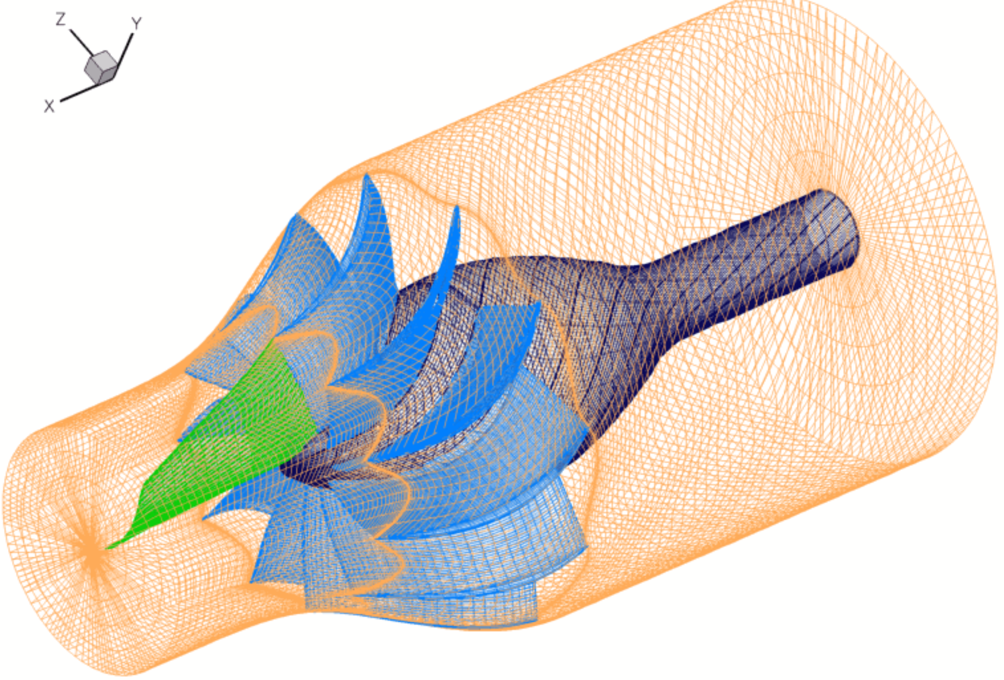

Figure 6.10: Paneled geometry of the ONR-AWJ1 water-jet pump for the stator problem (the trailing wake of one blade is also shown), viewed from down stream.

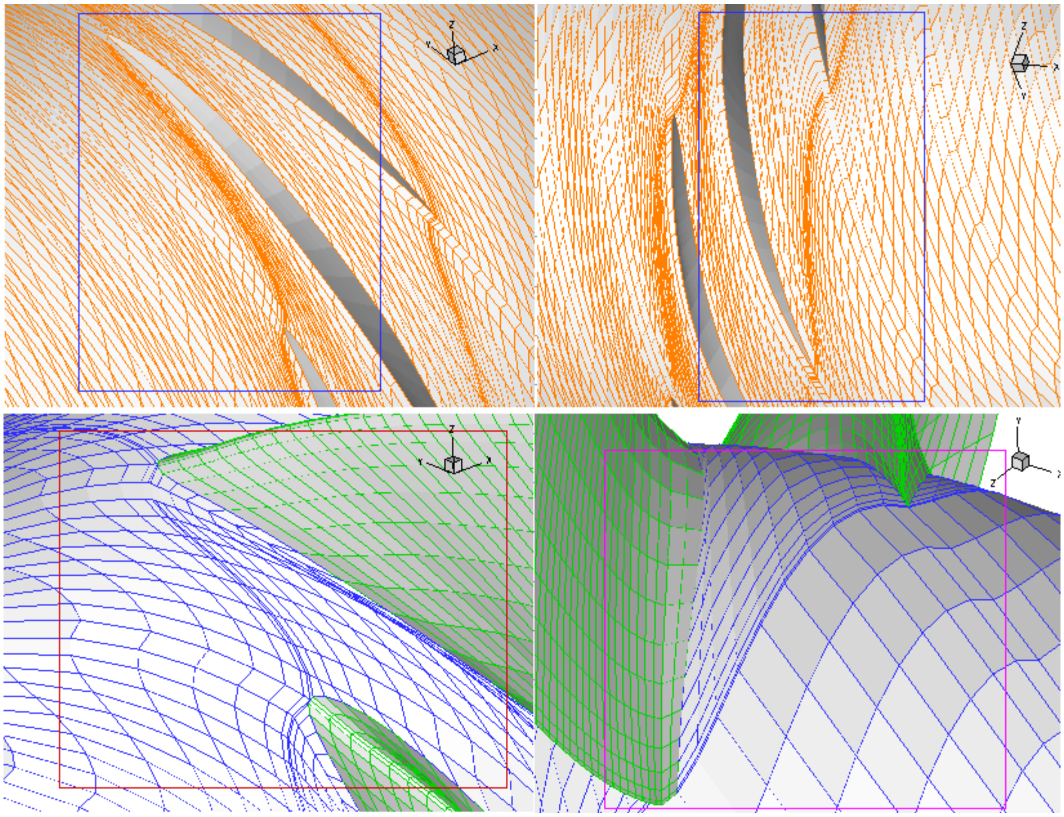

Figure 6.11: Details of paneling: on the casing at the blade leading edge (top left), on the casing at the blade trailing edge (top right), on the hub at the blade leading edge (bottom left), and on the hub at the blade trailing edge (bottom right).

rotor/stator interaction analysis by using the induced potential and velocity approaches are compared. Numerical results from the present method are compared with the with the experimental measurements at the Johns Hopkins University.

6.4.1 Bare Casing

This section presents the studies of flow inside the bare casing of the ONR-AWJ1 water-jet pump. Equation 6.16 gives the governing equation for bare casing problem,

$$2\pi\phi(\vec{x}) = \int_{S_C} \left[\phi_q(\vec{x}) \frac{\partial G(p;q)}{\partial n_q} - G(p;q) \frac{\partial \phi_q(\vec{x})}{\partial n_q} \right] ds \tag{6.16}$$

where S_C denotes the casing surface.

Convergence Test

As shown in Figure 6.12, mesh on the casing is aligned with four different pitch angles, $90^o, 60^o, 45^o$ and 30^o, to obtain different discretization. Only for the case of pitch angle= 90^o, the panel on the casing is planar. With the decrease of the pitch angle, the panel on the casing become more distorted. Figure 6.13 shows a sample discretization on one quarter of the casing for pitch angle $= 90^o$, and Figure 6.14 shows that for pitch angle $= 30^o$. It should be pointed out that, when evaluating the influence coefficients in the case of pitch angle $< 90^o$, the control point of each panel is moved to a new location where it has the same radius as that of the control point for planar panel (pitch angle= 90^o), according to the scheme presented by [Kerwin et al. 1987].

Figures 6.15 and 6.16 present the dependence of inviscid wetted potentials

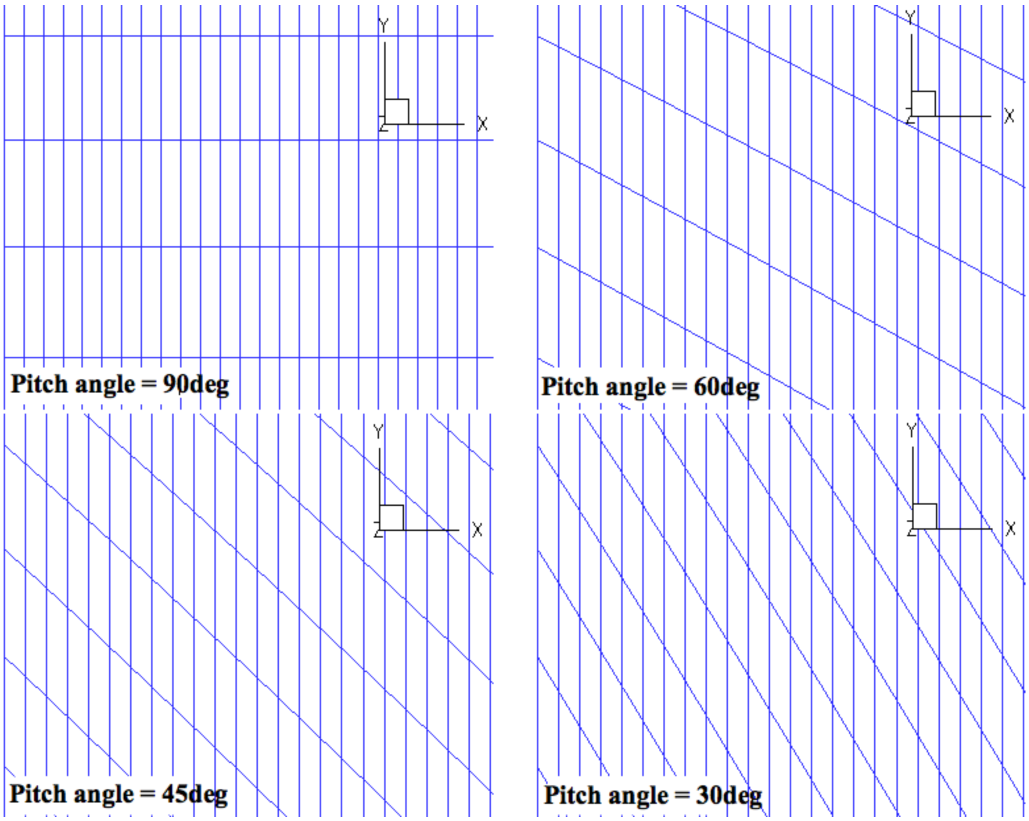

Figure 6.12: Different types of discretization on ONR-AWJ1 casing.

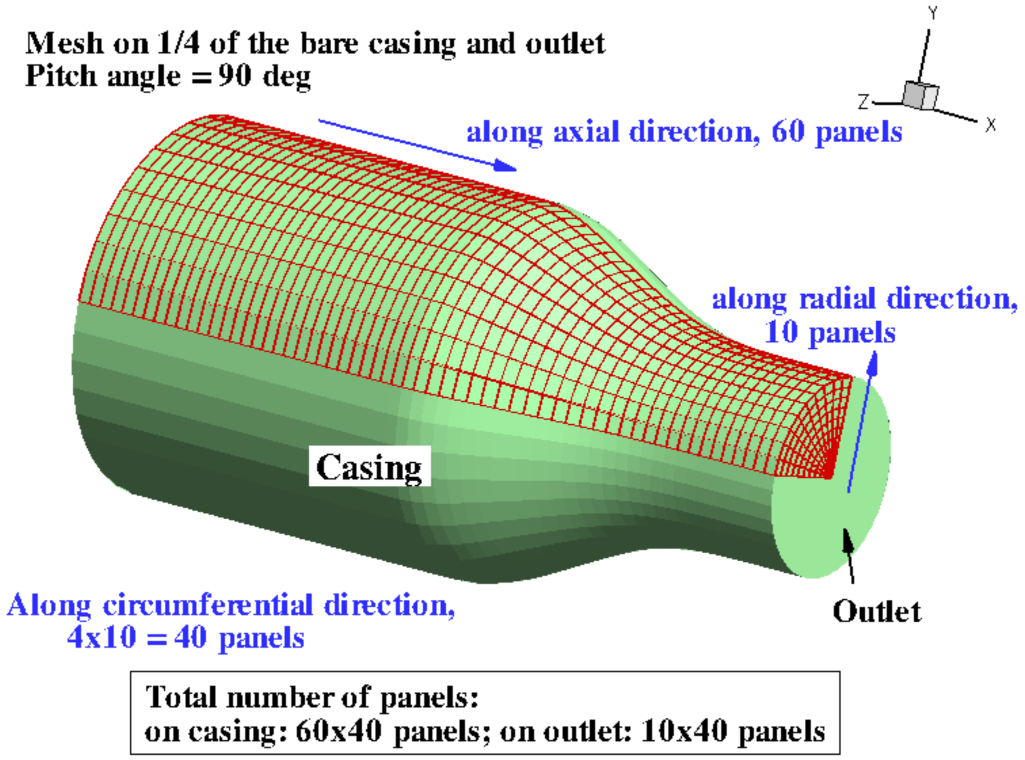

Figure 6.13: Sample discretization on ONR-AWJ1 casing. Total no. of panels on casing is 60×40 panels, and on outlet is 10×40 panels. Pitch angle = 90^o.

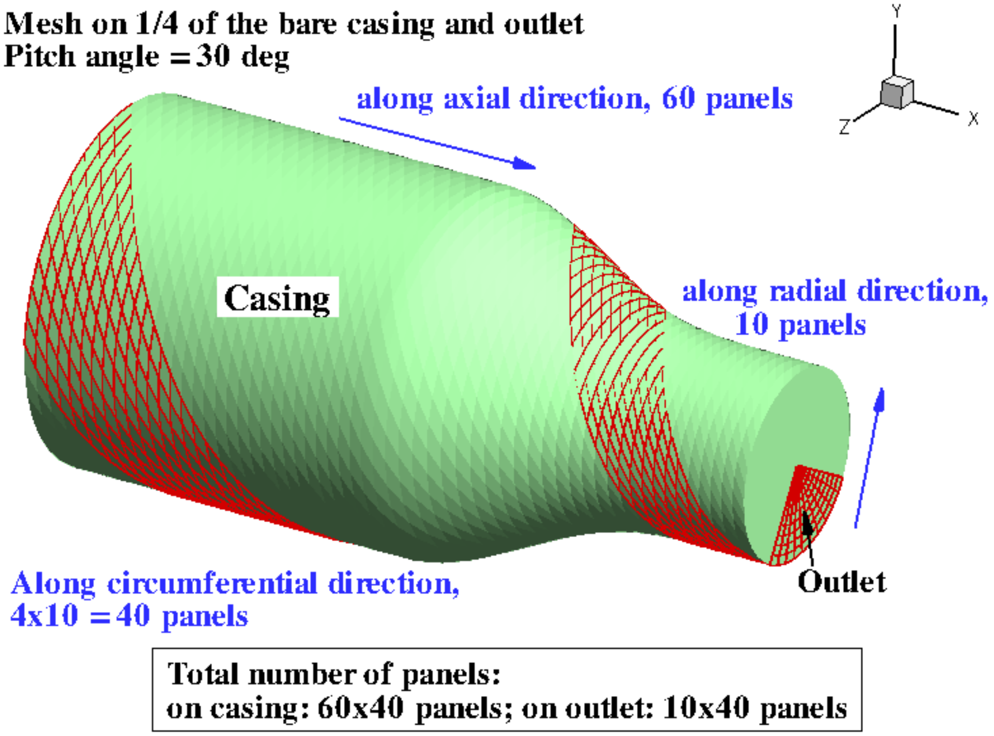

Figure 6.14: Sample discretization on ONR-AWJ1 casing. Total no. of panels on casing is 60×40 panels, and on outlet is 10×40 panels. Pitch angle = 30^o.

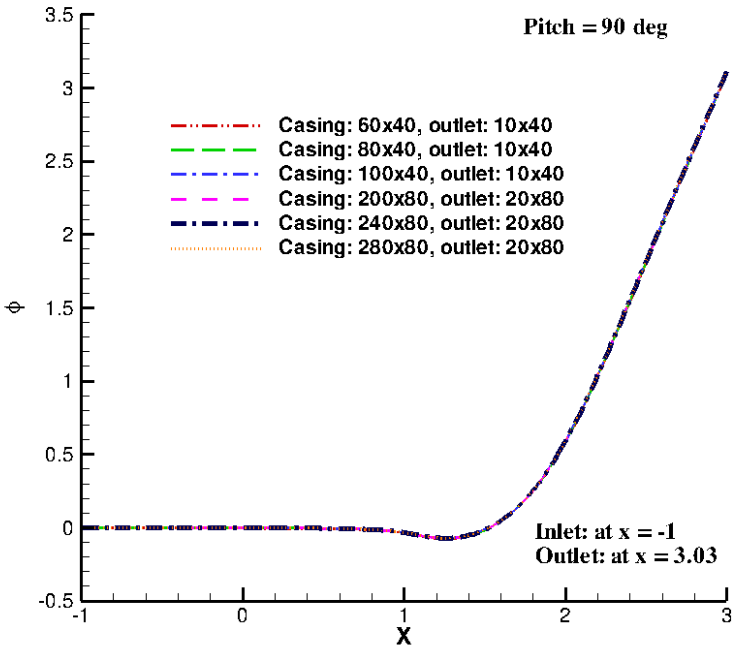

(a) Pitch angle=90^o

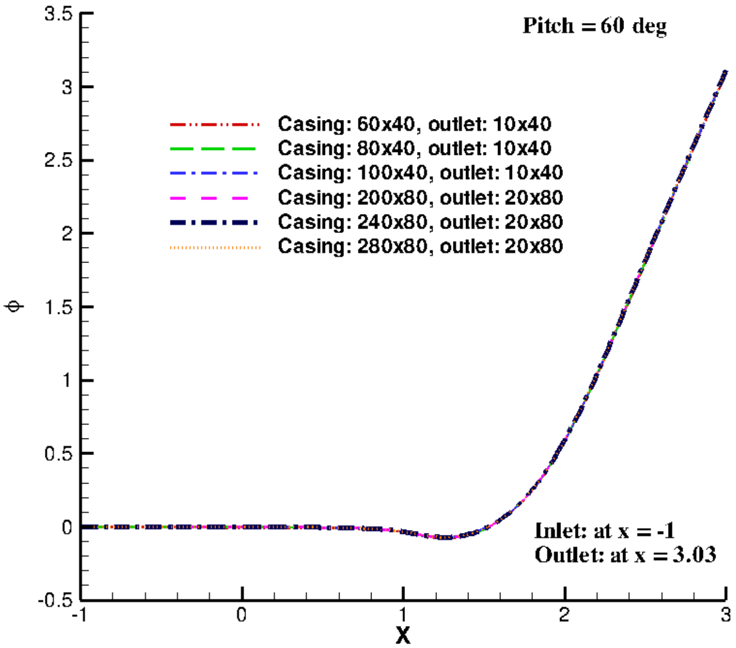

(b) Pitch angle=60^o

Figure 6.15: Convergence of inviscid wetted potentials on casing with number of panels on casing and outlet. Bare casing, pitch angle = 90 & 60 deg.

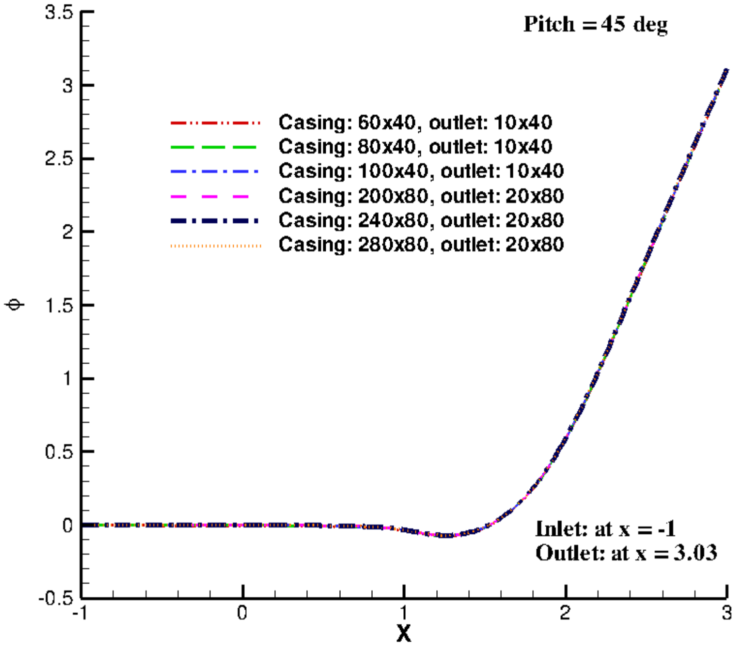

(a) Pitch angle=45^o

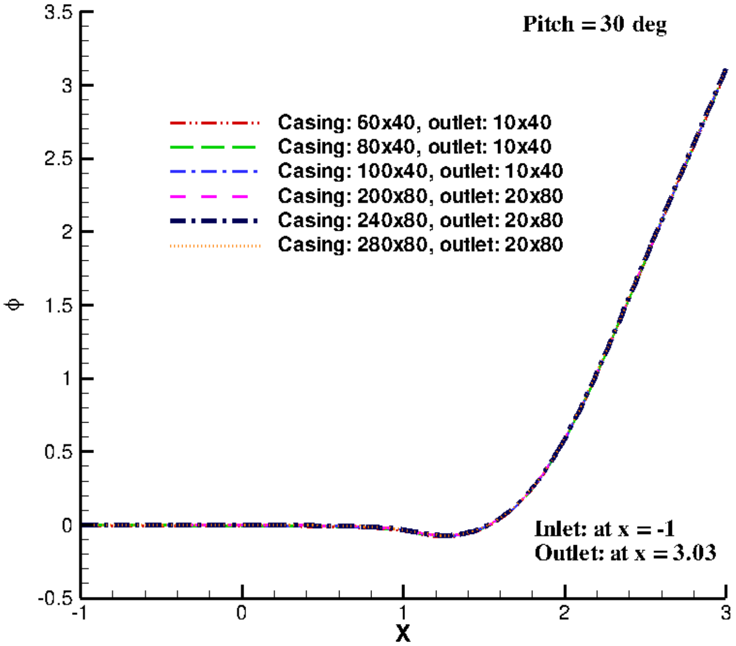

(b) Pitch angle=30^o

Figure 6.16: Convergence of inviscid wetted potentials on casing with number of panels on casing and outlet. Bare casing, pitch angle = 45 & 30 deg.

on casing with number of panels on casing and outlet, for the four types of discretization. The legend, *Casing:* 60×40, indicates that 60 panels is used along the axial direction, and 40 panels is used in the circumferential direction (of a full circle) of the casing, as shown in Figure 6.13. Similarly, *outlet:* 10×40, indicates that 10 panels is used along the radial direction, and 40 panels is used in the circumferential direction of the outlet. The results are all overlapped with each other and independent of number of panels on the casing and outlet.

Verification Test

To check the accuracy of calculated induced potentials and induced velocities, the following verification tests are performed. The induced potentials, ϕ_{ind}, and the induced velocities, $\vec{u}_{ind}$, on the body can be evaluated through Equations (6.17) and (6.18) by using the solved dipole strengths and known source strengths. The calculated ϕ_{ind} on the casing should be exactly the same as the solved ϕ, and $\left(\frac{\partial \phi}{\partial n}\right)_{evaluated} = \vec{u}_{ind} \cdot \vec{n}$ should be equal to the known source strength $\left(\frac{\partial \phi}{\partial n}\right)_{given} = -\vec{U}_{in} \cdot \vec{n}$ on the casing surface.

$$2\pi\phi_{ind} = \int_{S_C} \left[\phi_q(\vec{x}) \frac{\partial G(p;q)}{\partial n_q} - G(p;q) \frac{\partial \phi_q(\vec{x})}{\partial n_q} \right] ds \tag{6.17}$$

$$4\pi\vec{u}_{ind} \quad = \quad \int_{S_C} \left[\phi_q(\vec{x}) \nabla \left(\frac{\partial G(p;q)}{\partial n_q} \right) - \nabla G(p;q) \frac{\partial \phi_q(\vec{x})}{\partial n_q} \right] ds \tag{6.18}$$

Figures 6.17 and 6.18 show the comparisons of the calculated ϕ_{ind} with the solution ϕ for all 4 types of meshing on casing. The comparisons between the two

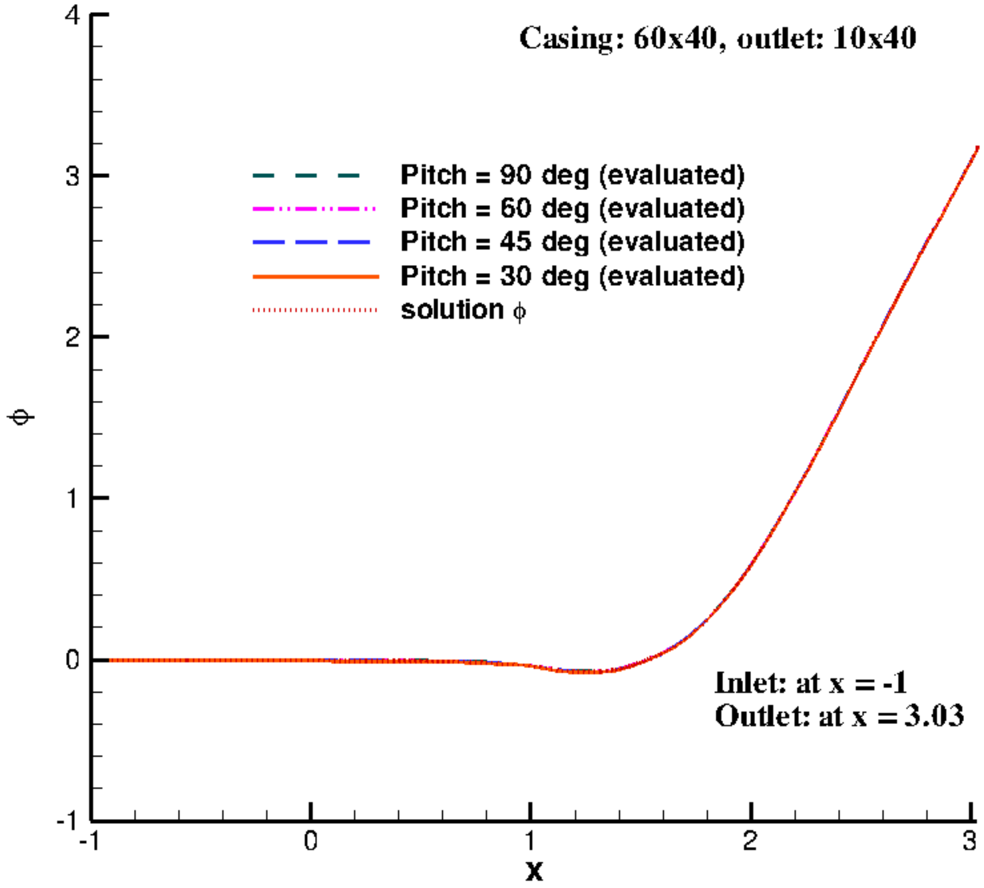

Figure 6.17: Comparison of calculated ϕ_{ind} with the solution ϕ on bare casing. Total no. of panels on casing: 60×40, outlet: 10×40.

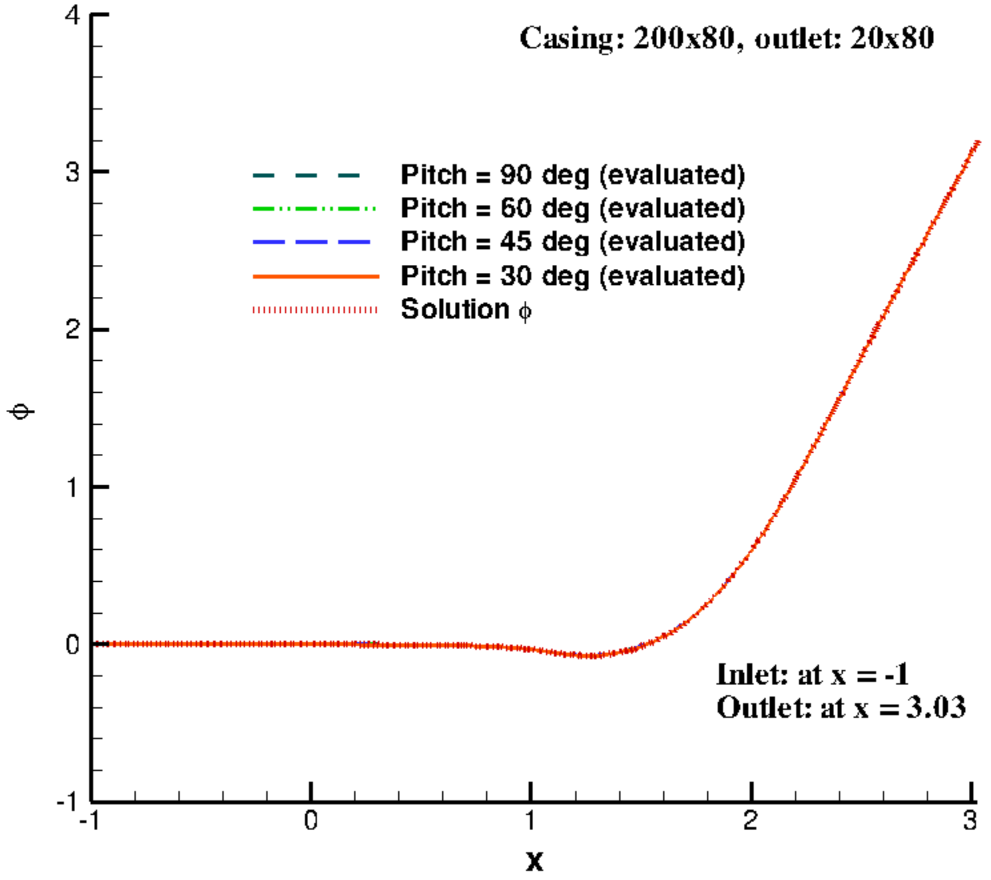

Figure 6.18: Comparison of calculated ϕ_{ind} with the solution ϕ on bare casing. Total no. of panels on casing: 200×80, outlet: 20×80.

are very good, and the discretization on casing also does not affect the calculations. It indicates that the present algorithm can calculate the correct induced potentials.

Figure 6.19 shows the comparisons of the evaluated $\left(\frac{\partial\phi}{\partial n}\right)_{evaluated}$ with the given source strength $\left(\frac{\partial\phi}{\partial n}\right)_{given}$ in the boundary conditions. The comparisons are good for large pitch angles, but with large discrepancies for small pitch angles. By applying more panels on the casing and outlet, the comparisons can be improved a lot for large pitch angles but not much for small ones, as shown in Figure 6.20. The reason for the discrepancies is that the induced velocities at control points of distorted panels due to sources or dipoles on the other distorted (non-planar) panels are not correctly calculated.

6.4.2 Rotor Only Calculations

In this section, in the case of only having rotor inside the casing, grid dependence studies and verification tests of induced potentials, ϕ_{ind}, and induced velocities, $\vec{u}_{ind}$, are first conducted using the inviscid water-jet model for $J_s = 0.49$. Next, the viscous wetted flow results for rotor only case at different advance ratios by the present method are presented.

Convergence study

Figure 6.21 presents the dependence of inviscid wetted circulation distributions on rotor blade, at $J_s = 0.49$ with number of panels on the casing and water-jet outlet. The circulation Γ is defined as $\Gamma = \Delta\phi_{TE}/2\pi R\sqrt{V_s^2 + (0.7n\pi D)^2}$, where $\Delta\phi_{TE}$ is the potential jump at the trailing edge of the rotor blade at each radius, V_s

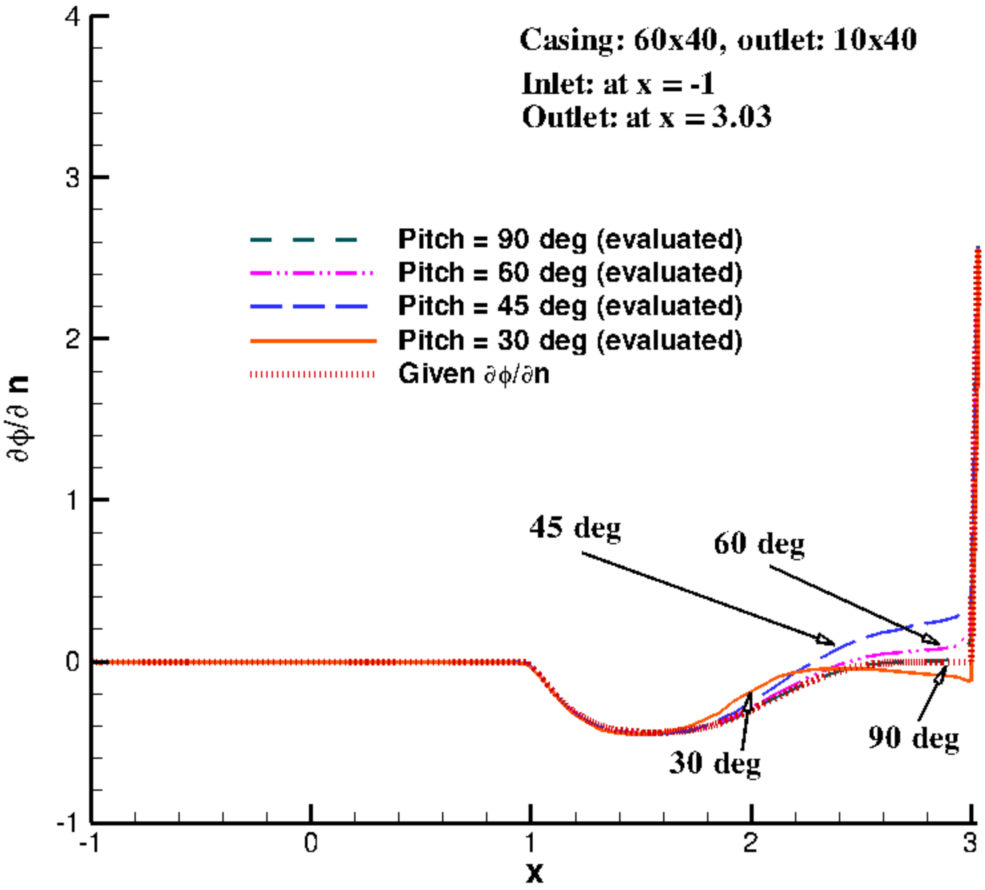

Figure 6.19: Comparison of calculated $\left(\frac{\partial\phi}{\partial n}\right)_{evaluated}$ with the known source strength $\left(\frac{\partial\phi}{\partial n}\right)_{given}$ on bare casing. Total no. of panels on casing: 60×40, outlet: 10×40.

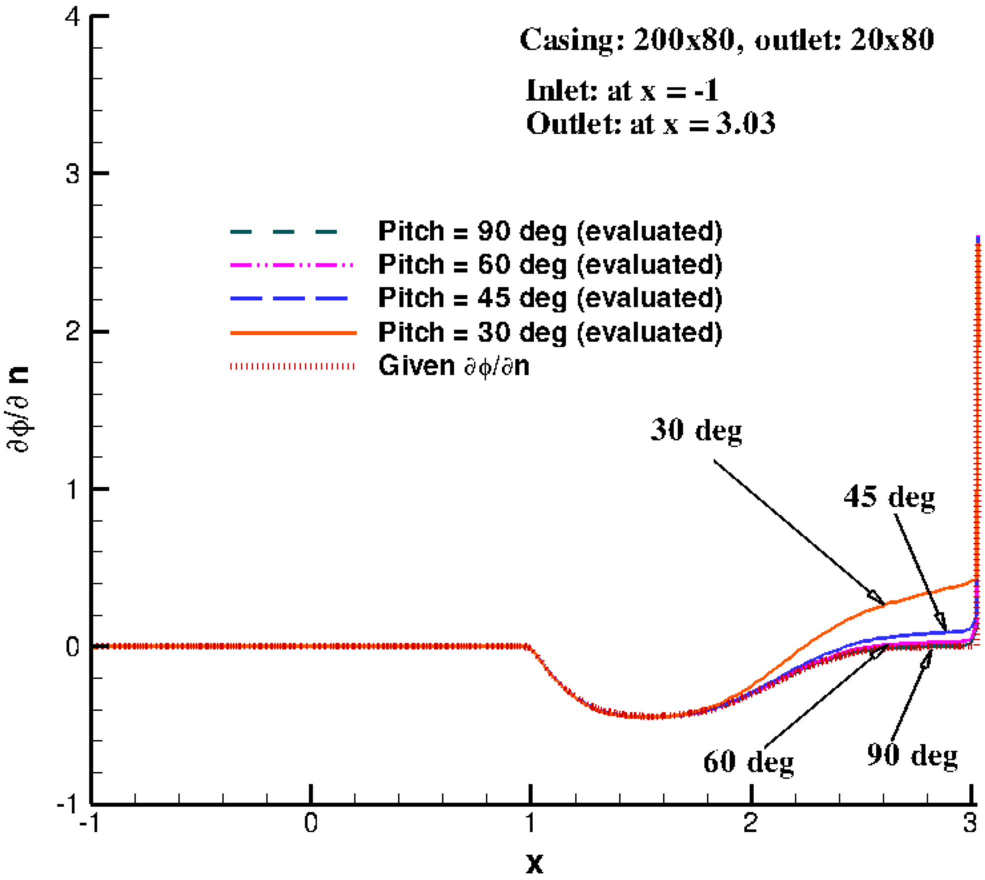

Figure 6.20: Comparison of calculated $\left(\frac{\partial\phi}{\partial n}\right)_{evaluated}$ with the known source strength $\left(\frac{\partial\phi}{\partial n}\right)_{given}$ on bare casing. Total no. of panels on casing: 200×80, outlet: 20×80.

is the ship speed and n is the propeller rotational frequency. The legend, *Casing:* 120×70, indicates that 120 panels is used along the axial direction, and 70 panels is used in the circumferential direction (of a full circle) of the casing. As shown in Figure 6.22, for a 7-bladed rotor, 10 panels is used along the circumferential direction between two adjacent blade rows, and there are totally $7 \times 10 = 70$ panels along the full circle. It should be pointed out that 10 panels reaches the maximum number of panels that can be used between two adjacent blade rows to obtain smooth mesh on the casing. Similarly, *Outlet:* 10×70 indicates that 10 panels is used in the radial direction, and 70 panels is used in the circumferential direction (of a full circle) of the water-jet outlet. As shown in Figure 6.21, at least 200 panels along the axial direction of the casing is required to achieve converged results. Number of panels on the outlet has little affect on the convergence of the results.

Figure 6.23 presents the dependence of inviscid wetted circulation distributions on blade with number of panels on rotor blade in the chord-wise and span-wise directions. The legend, *On rotor:* 60×10, indicates that 60 panels is used in the chord-wise direction and 10 panels in the span-wise direction of the rotor. The circulations are independent of the number of panels used on the blade.

Figure 6.24 shows the convergence of inviscid wetted circulation distributions with the panel size of the rotor trailing wake. Five different angle increments, $\Delta\theta = 2^o, 4^o, 6^o, 8^o$ and 10^o for the wake geometry are used. The convergence of the results is very good and not affected by the wake angle increments.

In addition, the effects of casing length on the convergence of the method are investigated. Figure 6.25 shows the convergence of inviscid wetted circulation

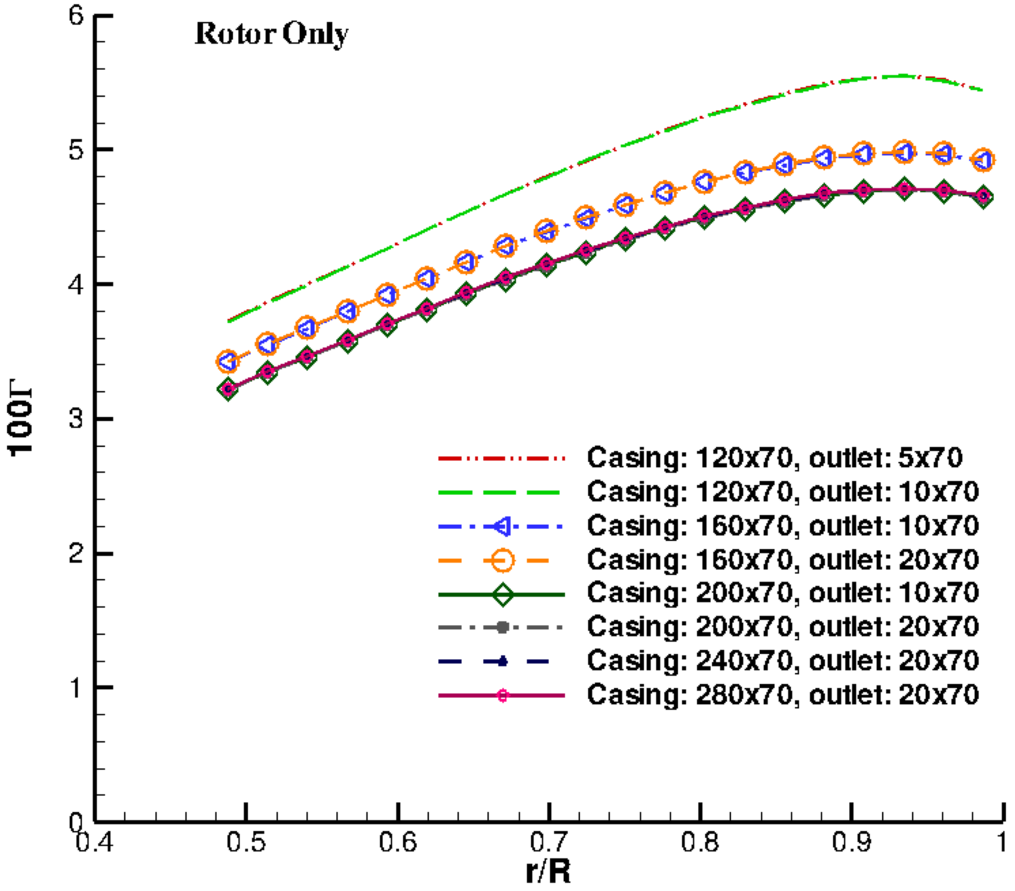

Figure 6.21: Convergence of inviscid wetted circulation distributions on ONR-AWJ1 rotor with number of panels on the casing and outlet. Rotor only, $J_s = 0.49$.

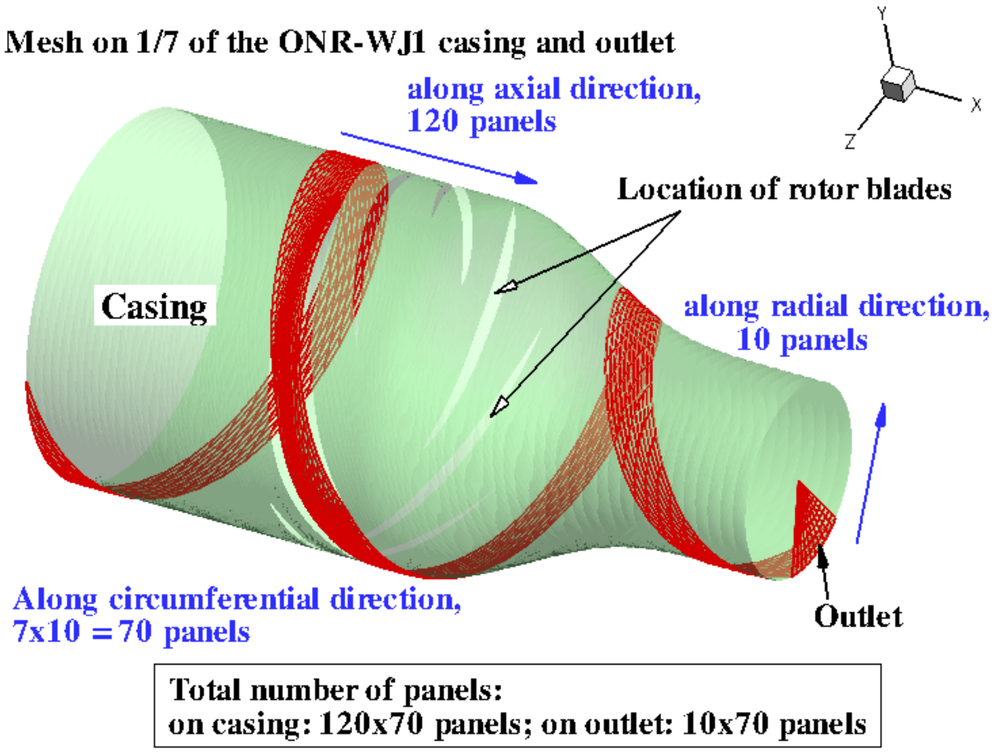

Figure 6.22: Sample discretization on the casing. Total no. of panels on casing is 120×70 panels, and on outlet 10×70 panels. ONR-AWJ1 water-jet pump. Rotor Only Case.

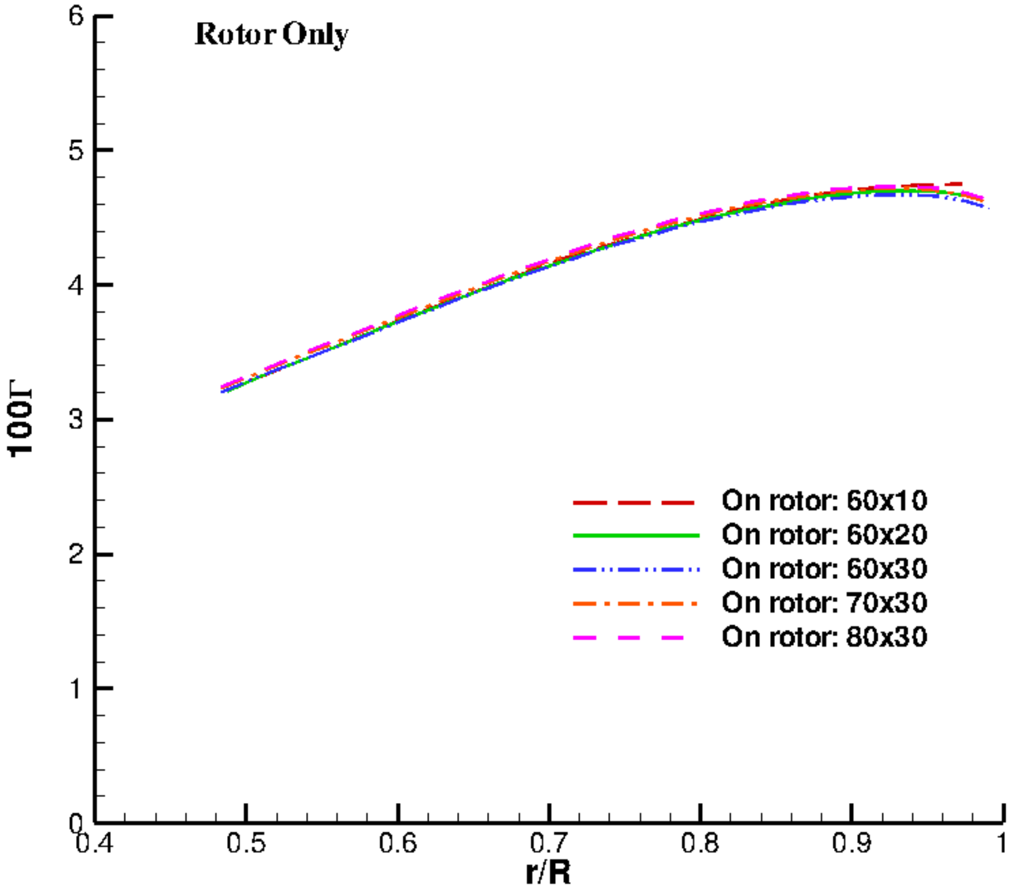

Figure 6.23: Convergence of inviscid wetted circulation distributions on ONR-AWJ1 rotor with number of panels on the rotor blade. Rotor only, $J_s = 0.49$.

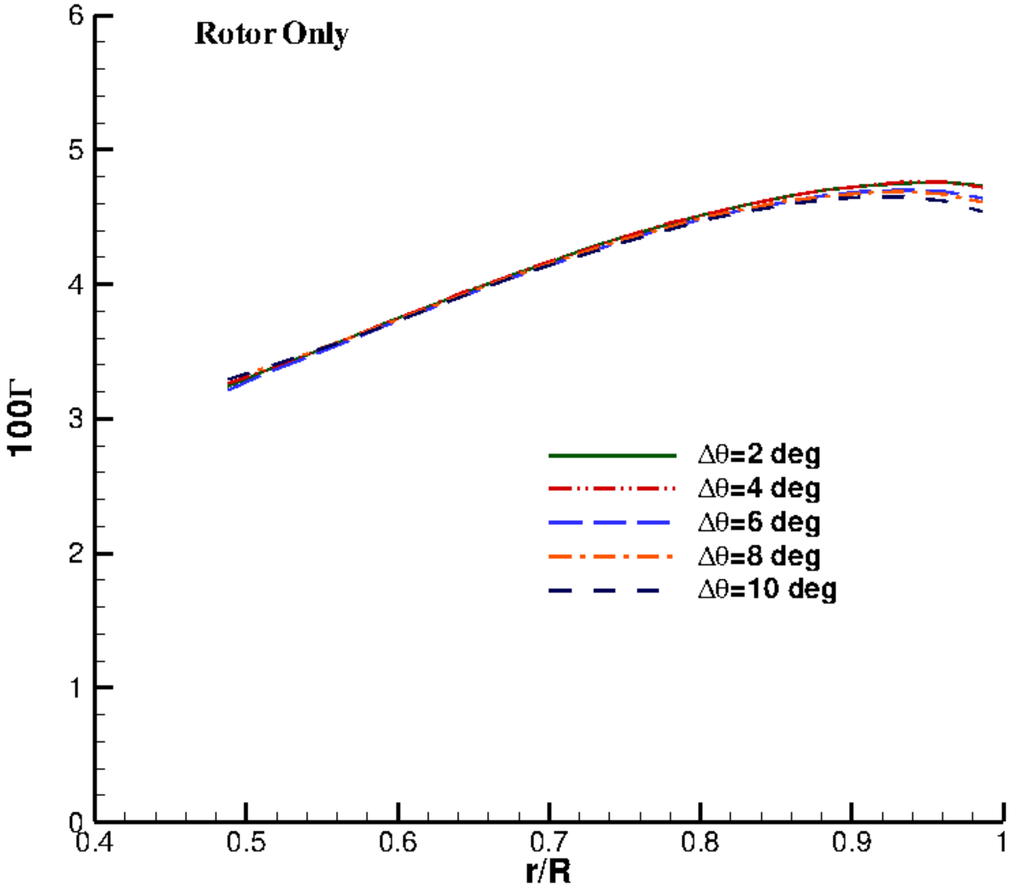

Figure 6.24: Convergence of inviscid wetted circulation distributions on ONR-AWJ1 rotor with panel size of the rotor trailing wake. Rotor only, $J_s = 0.49$.

distributions on rotor blade with the length of the casing. The legend, Original Casing: [-1, 3], indicates that the ONR-AWJ1 casing starts at $x = -1$ and ends at $x = 3$. The legend, Extended Casing: [-2, 4], indicates that the casing is extended from $x = -2$ to $x = 4$. Figure 6.26 shows the original casing and one of the extended casing geometries. The length of the casing has almost no effects on the circulation distributions.

Verification Test

Similar verification tests as for the casing only case are carried out to check the accuracy of calculated induced potentials and induced velocities for the rotor-only case. Induced potentials are evaluated by using Equations (6.2) and (6.3), and induced velocities are calculated by using Equations (6.8) and (6.9). The evaluated ϕ on the rotor, hub, and casing should be exactly the same as the solution ϕ, and $\left(\frac{\partial \phi}{\partial n}\right)_{evaluated} = \vec{u}_{ind} \cdot \vec{n}$ should be equal to the given source strength $\left(\frac{\partial \phi}{\partial n}\right)_{given}$ on the rotor, hub, and casing surface.

Figure 6.27 shows the index direction of panels on the rotor. Figure 6.28 compares the evaluated ϕ and the solution ϕ at each panel on the rotor. The differences between the two, PHIDIF, are also plotted in the figure. PHIDIF is calculated by the following equation,

$$\text{PHIDIF} = \frac{|\phi_{evaluated} - \phi_{solution}|}{|\phi_{solution}|_{max}} \tag{6.19}$$

where $|\phi_{solution}|_{max}$ is the maximum absolute value of the solution ϕ. Figure 6.29 and Figure 6.31 show the index direction of panels on the hub and casing, respec-

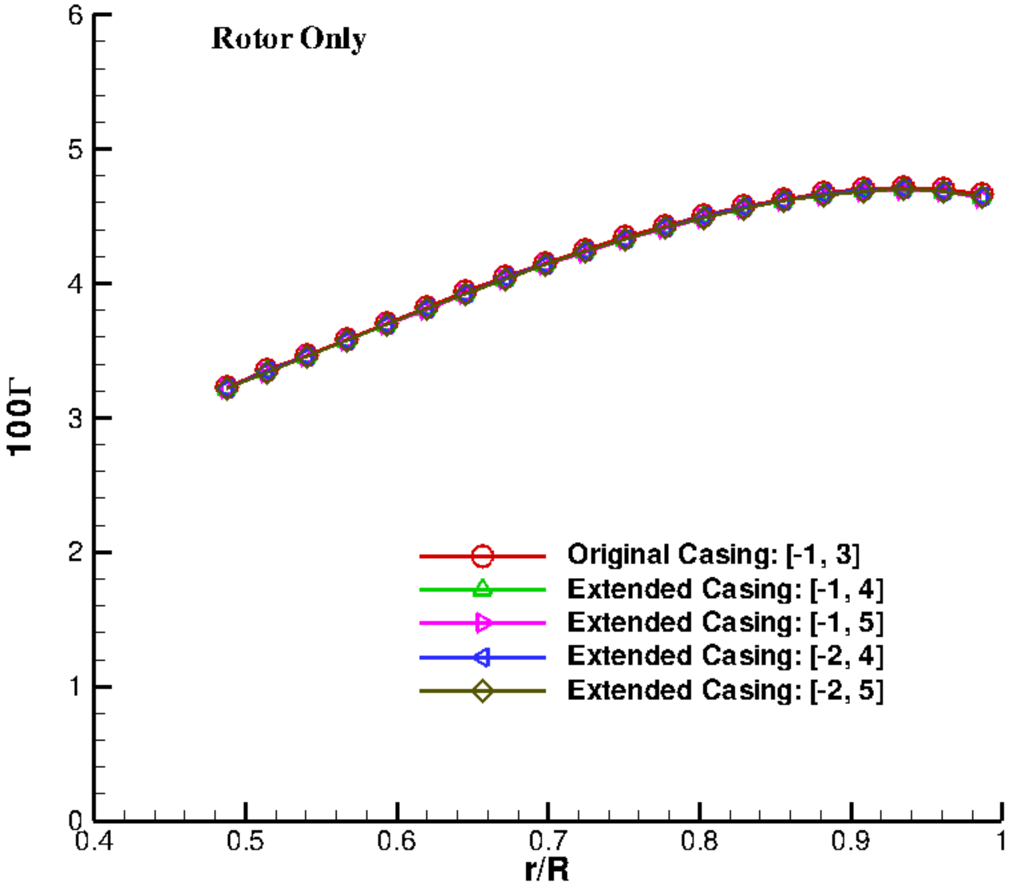

Figure 6.25: Convergence of inviscid wetted circulation distributions on ONR-AWJ1 rotor with the length of casing. Rotor only, $J_s = 0.49$.

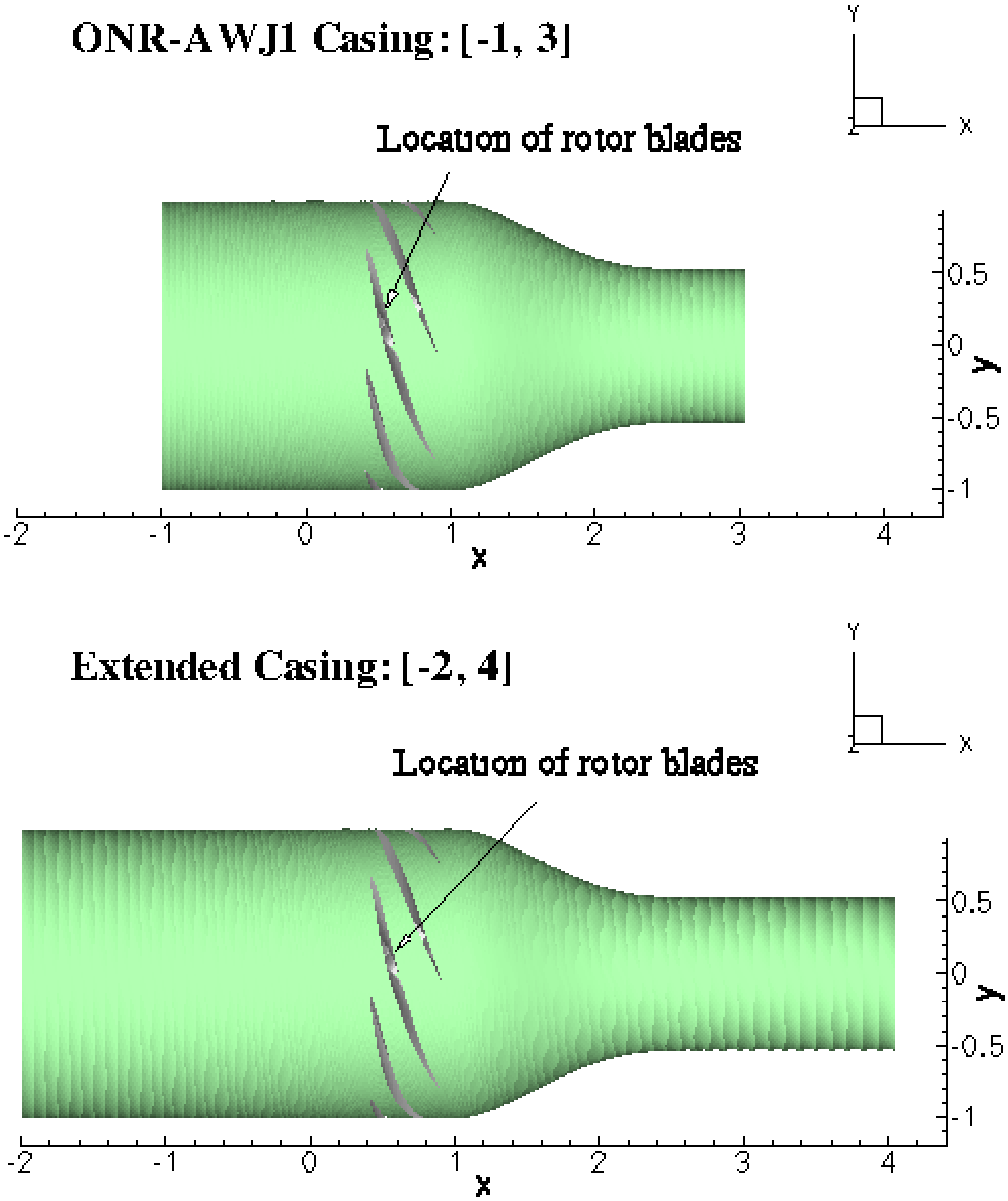

Figure 6.26: The ONR-AWJ1 casing vs. one extended casing.

tively. Figure 6.30 and 6.32 show the comparisons of evaluated ϕ and the solution ϕ on the hub and on the casing. All the comparisons are very good, and the induced potentials are evaluated accurately.

Figure 6.33 compares the evaluated $\left(\frac{\partial\phi}{\partial n}\right)_{evaluated}$ and the given source strength $\left(\frac{\partial\phi}{\partial n}\right)_{given}$ on the rotor. The differences between the two, DPDNDIF, are also plotted. DPDNDIF is calculated by the following equation,

$$\text{DPDNDIF} = \frac{\left|\left(\frac{\partial\phi}{\partial n}\right)_{evaluated} - \left(\frac{\partial\phi}{\partial n}\right)_{given}\right|}{\left|\left(\frac{\partial\phi}{\partial n}\right)_{given}\right|_{max}} \tag{6.20}$$

where $\left|\left(\frac{\partial\phi}{\partial n}\right)_{given}\right|_{max}$ is the maximum absolute value of the given $\left(\frac{\partial\phi}{\partial n}\right)_{given}$. The comparisons are good so that the present method can accurately evaluated the induced velocities on the rotor. However, the comparisons of $\left(\frac{\partial\phi}{\partial n}\right)_{evaluated}$ and the known source strength $\left(\frac{\partial\phi}{\partial n}\right)_{given}$ on the hub and casing surfaces are very bad, as shown in Figure 6.34 and Figure 6.35. So, the calculated induced velocities on the hub and casing are not correctly evaluated. The reason for the large discrepancies is most probably because that the panels on the hub and casing surfaces are mostly distorted, and the induced velocities at the control point of a distorted panel due to singularities on the other distorted panels can not be calculated correctly by using the RPAN routine.

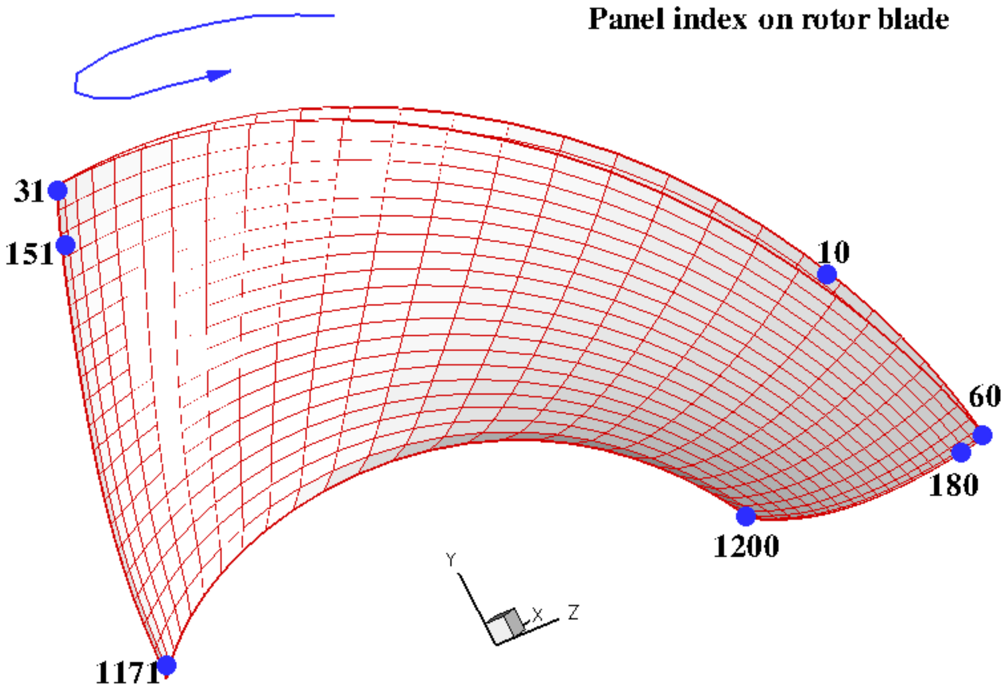

Figure 6.27: Panel index on the ONR-AWJ1 rotor key blade. Rotor only case.

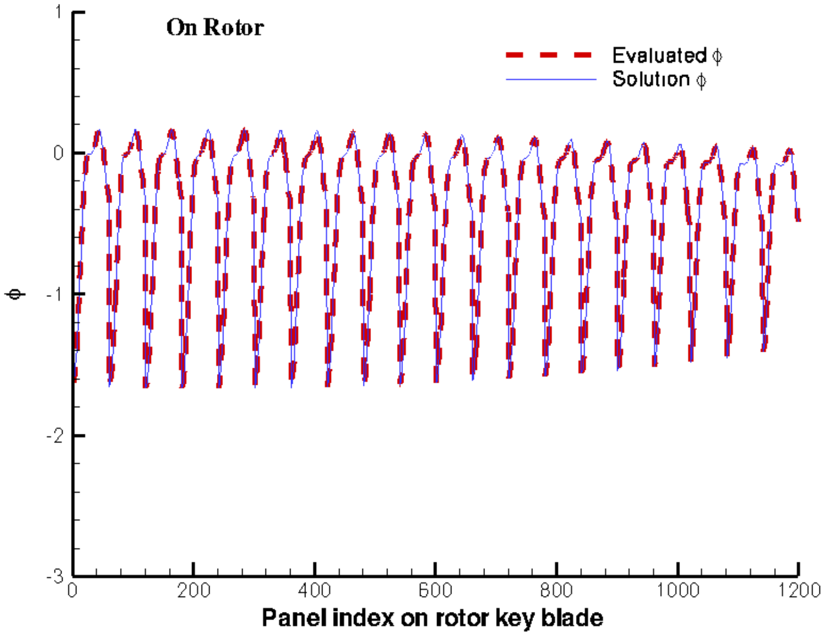

(a) Comparison of ϕ at each panel on the rotor

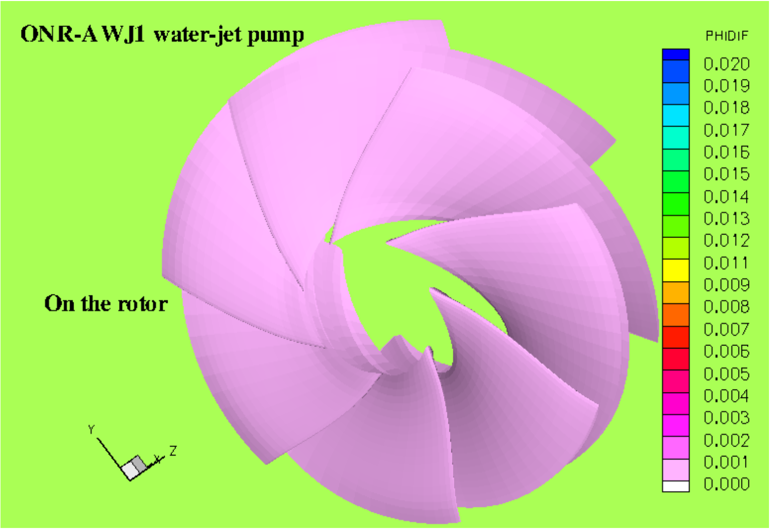

(b) Differences $\dfrac{|\phi_{evaluated} - \phi_{solution}|}{|\phi_{solution}|_{max}}$ on the rotor

Figure 6.28: Comparison of the evaluated ϕ and the solution ϕ at each panel on the ONR-AWJ1 rotor. Rotor only case.

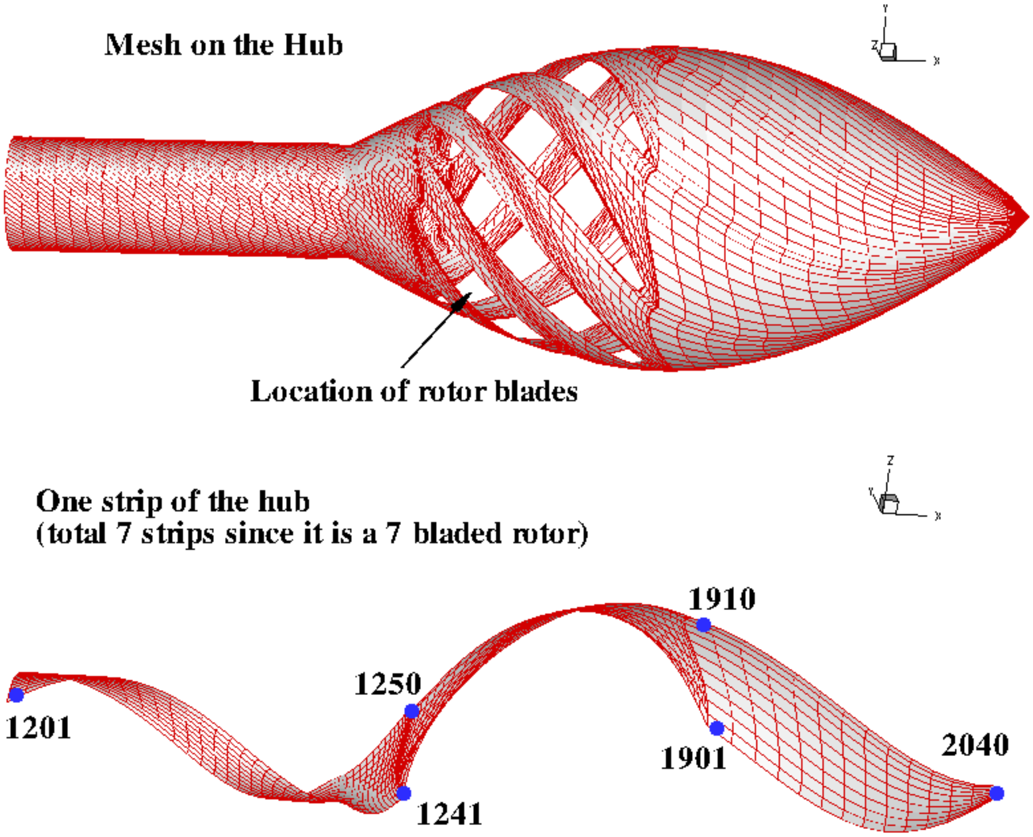

Figure 6.29: Panel index on the ONR-AWJ1 hub surface. Rotor only case.

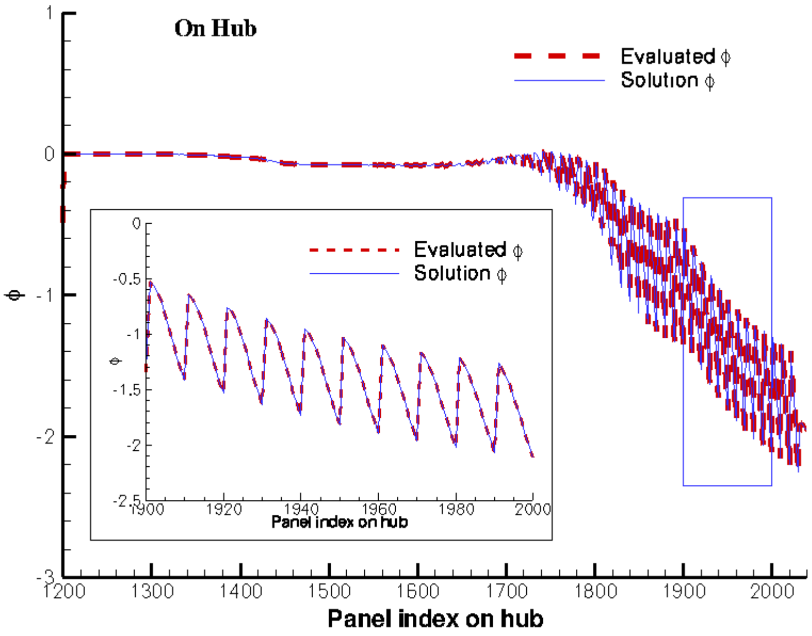

(a) Comparison of ϕ at each panel on the hub

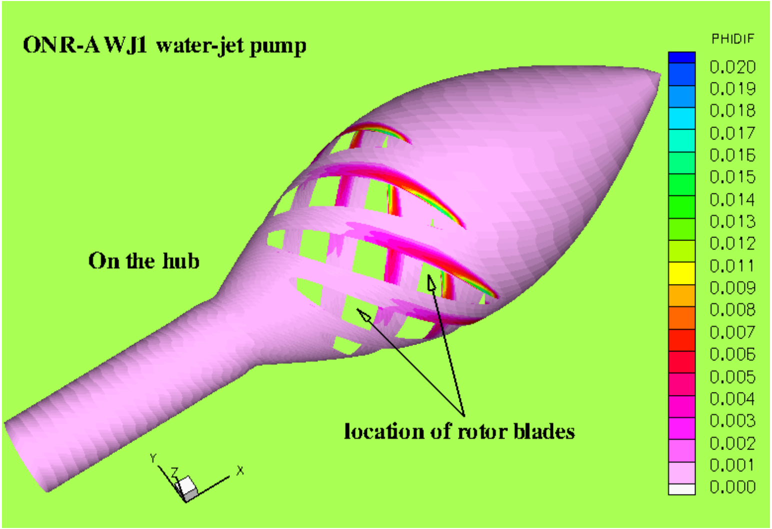

(b) Differences $\dfrac{|\phi_{evaluated} - \phi_{solution}|}{|\phi_{solution}|_{max}}$ on the hub

Figure 6.30: Comparison of the evaluated ϕ and the solution ϕ at each panel on the ONR-AWJ1 hub. Rotor only case.

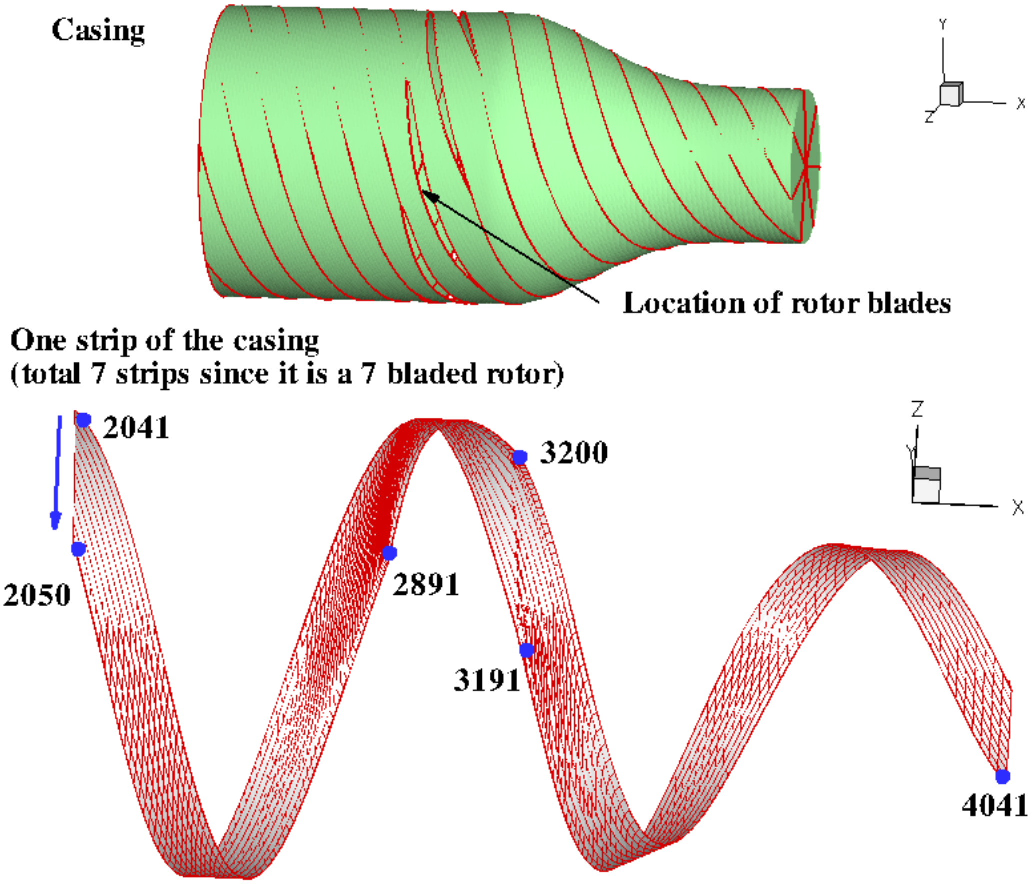

Figure 6.31: Panel index on the ONR-AWJ1 casing surface. Rotor only case.

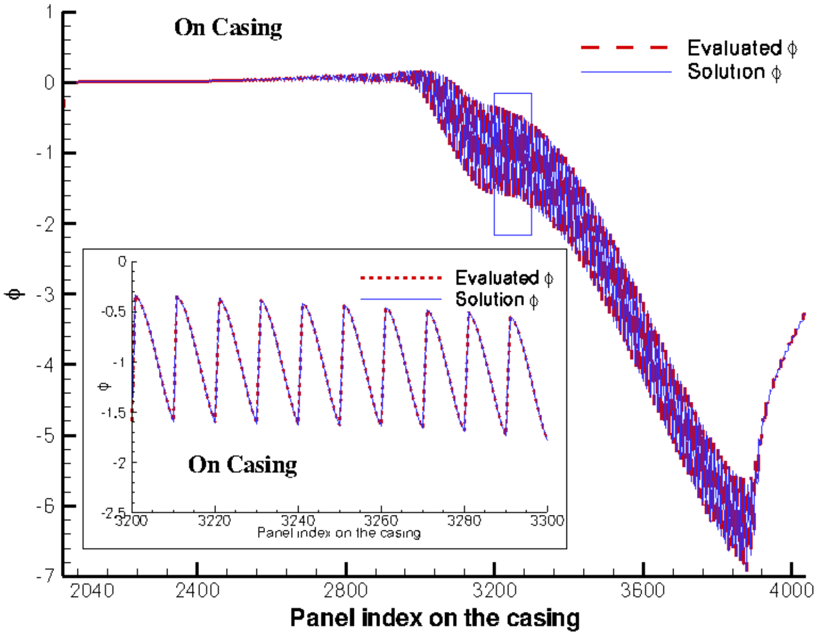

(a) Comparison of ϕ at each panel on the casing

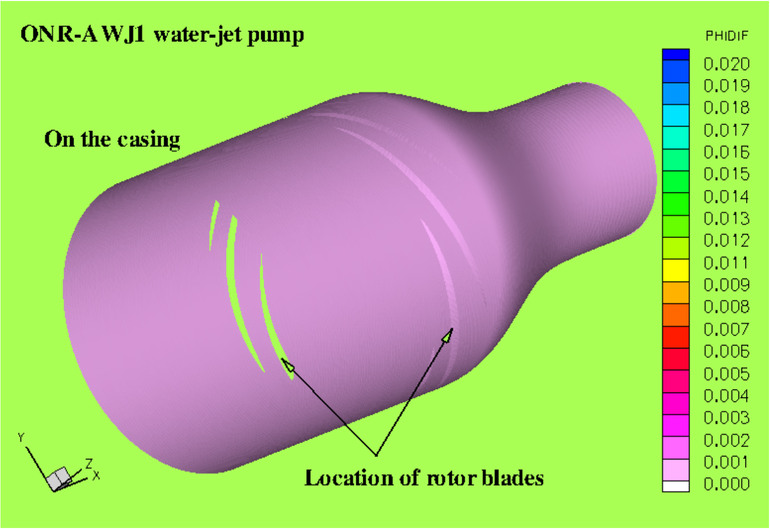

(b) Differences $\dfrac{|\phi_{evaluated} - \phi_{solution}|}{|\phi_{solution}|_{max}}$ on the casing

Figure 6.32: Comparison of the evaluated ϕ and the solution ϕ at each panel on the ONR-AWJ1 casing. Rotor only case.

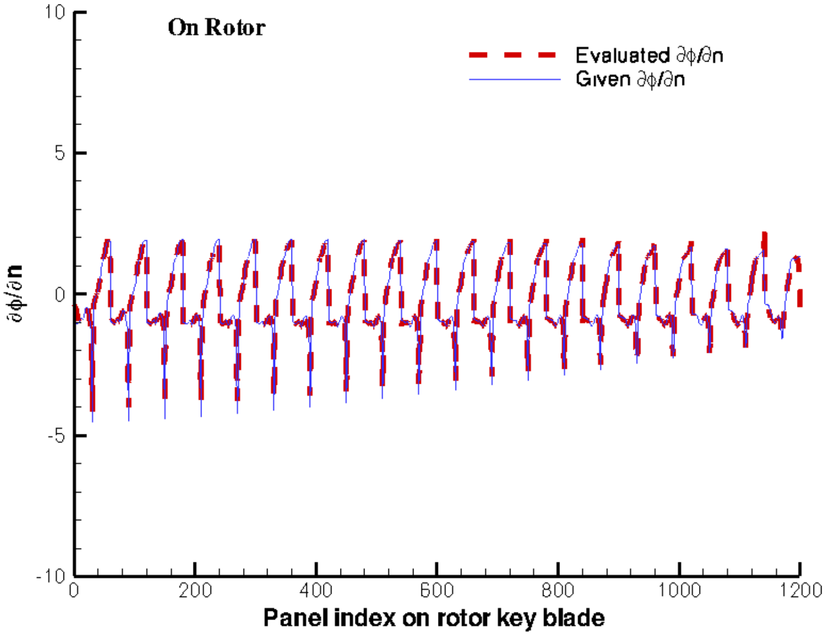

(a) Comparison of $\partial\phi/\partial n$ at each panel on the rotor

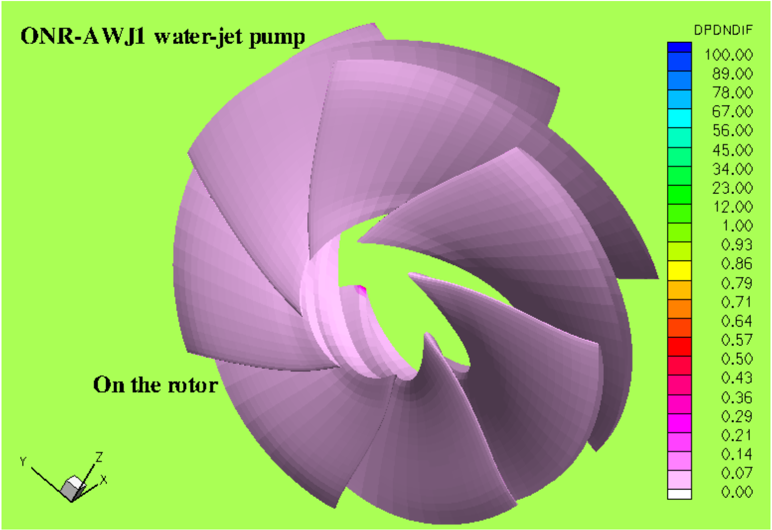

(b) Differences $\dfrac{|\partial\phi/\partial n_{evaluated} - \partial\phi/\partial n_{given}|}{|\partial\phi/\partial n_{given}|_{max}}$ on the rotor

Figure 6.33: Comparison of the $\left(\frac{\partial\phi}{\partial n}\right)_{evaluated}$ and the known source strength $\left(\frac{\partial\phi}{\partial n}\right)_{given}$ on the ONR-AWJ1 rotor. Rotor only case.

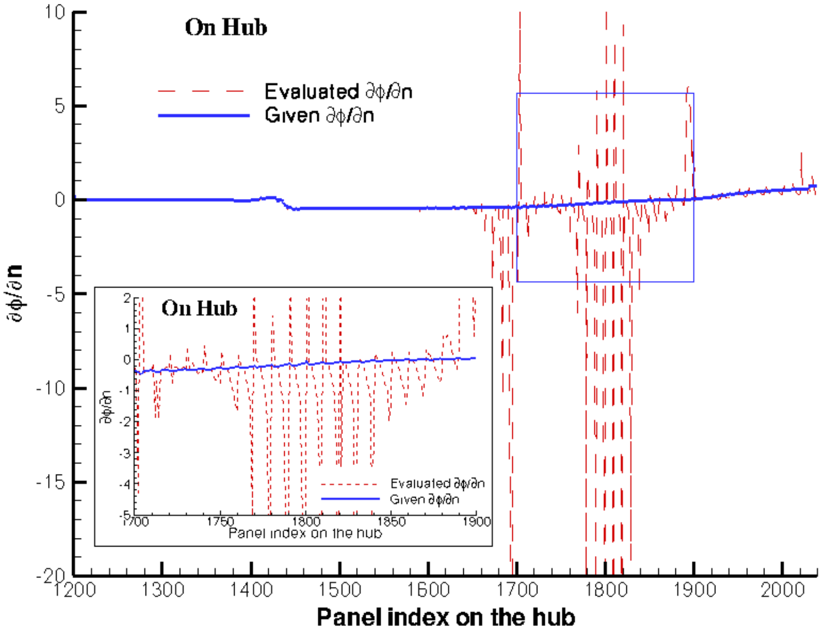

(a) Comparison of $\partial\phi/\partial n$ at each panel on the hub

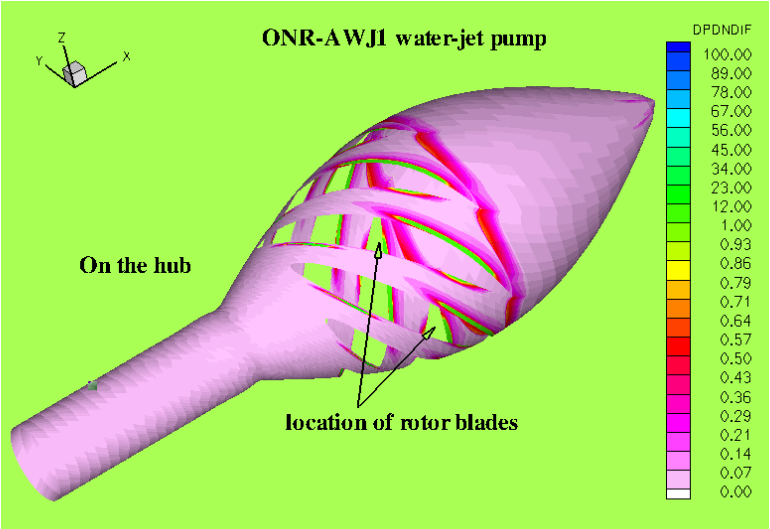

(b) Differences $\dfrac{|\partial\phi/\partial n_{evaluated} - \partial\phi/\partial n_{given}|}{|\partial\phi/\partial n_{given}|_{max}}$ on the hub

Figure 6.34: Comparison of the $\left(\frac{\partial\phi}{\partial n}\right)_{evaluated}$ and the known source strength $\left(\frac{\partial\phi}{\partial n}\right)_{given}$ on the ONR-AWJ1 hub. Rotor only case.

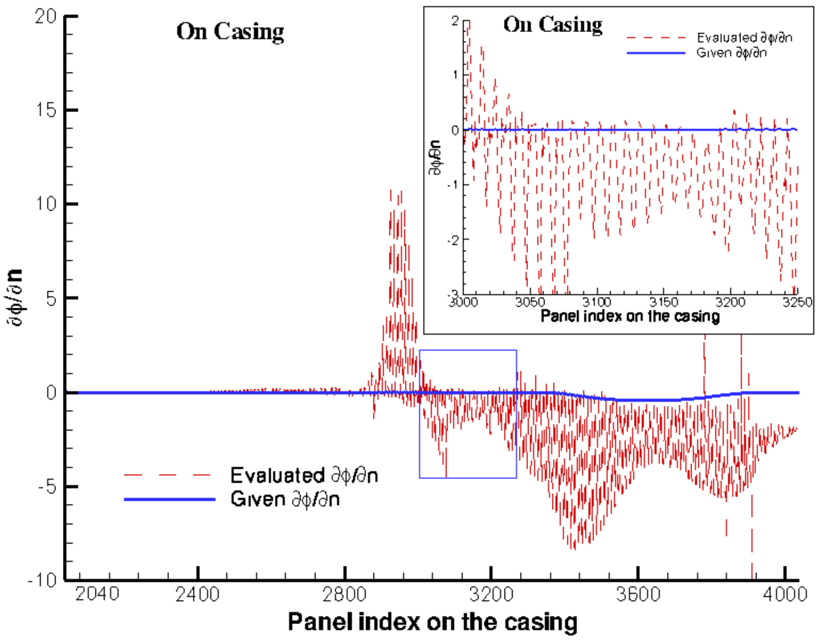

(a) Comparison of $\partial\phi/\partial n$ at each panel on the casing

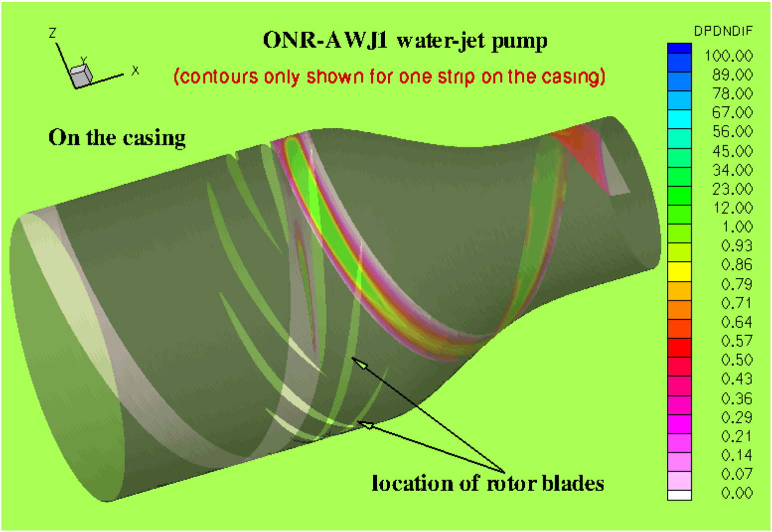

(b) Differences $\dfrac{|\partial\phi/\partial n_{evaluated} - \partial\phi/\partial n_{given}|}{|\partial\phi/\partial n_{given}|_{max}}$ on the casing

Figure 6.35: Comparison of the $\left(\frac{\partial\phi}{\partial n}\right)_{evaluated}$ and the known source strength $\left(\frac{\partial\phi}{\partial n}\right)_{given}$ on the ONR-AWJ1 casing. Rotor only case.

Table 6.1: Reynolds numbers at different J_s values, ONR-AWJ1 water-jet pump.

J_s	Reynolds number Re_D
0.3707	5.74e+5
0.4162	6.44e+5
0.4908	7.60e+5
0.5262	8.15e+5

Viscous Wetted Solution

The rotor diameter is 12.0 inches. The flow Reynolds number and the advance ratios are listed in Table 6.1. The rotational speed for the rotor at all J_s values is the same, and $n = 1000$ rpm. A turbulence level of 1% and free transition condition on both the suction and pressure sides of the rotor blade are tested for the viscous run. It generally takes about 40.0 minutes to finish both the inviscid and viscous analysis on a cluster with 1 CPU of AMD Opteron (1.6GHz & 2G RAM per CPU).

Figure 6.36 and 6.37 show the predicted blade forces on the rotor using the viscous/inviscid interaction method (PROPCAV/XFOIL) and comparisons with the measurements. As expected, the torque forces on the rotor without considering the stator effect are very close to the measurements, where the interactions between the components were included. The effect of viscosity is not significant in this case, and the predicted torque forces by PROPCAV/XFOIL are slightly higher than those by using empirical viscous corrections.

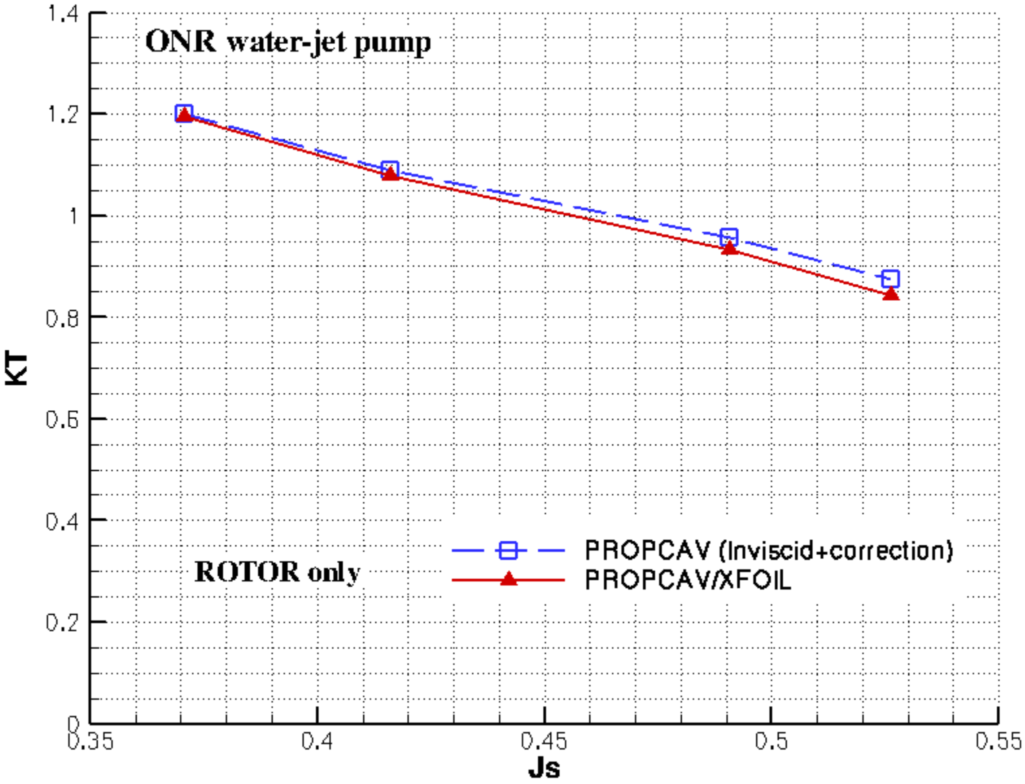

Figure 6.36: The predicted rotor thrust coefficients (wetted) for the ONR-AWJ1 water-jet pump at different J_s values.

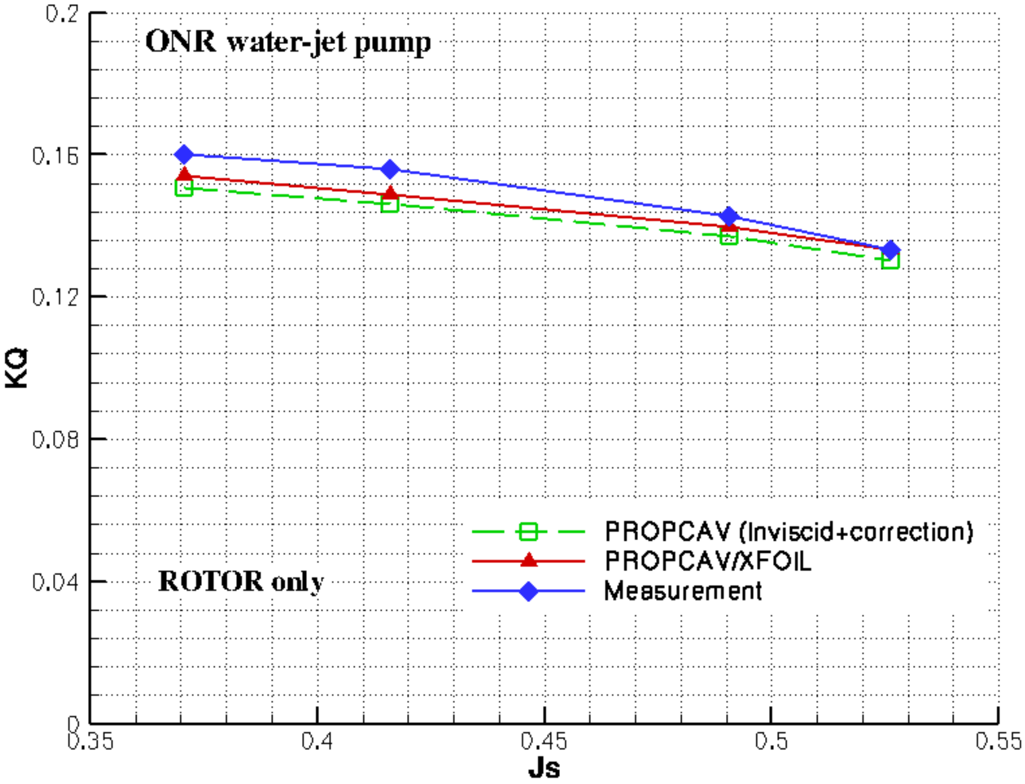

Figure 6.37: Comparison of the measured and predicted rotor torque coefficients (wetted) for the ONR-AWJ1 water-jet pump at different J_s values.

Inviscid Cavitating Solution

In the case of cavitation, the pressure on the cavity should be equal to the vapor pressure. According to the definition of the cavitation number for the rotor, the following equation is valid on the cavity:

$$-C_p = \sigma_n \tag{6.21}$$

An inviscid cavitating run is tested for the ONR-AWJ1 rotor without considering the rotor/stator interaction at $J_s = 0.49$ and $\sigma_n = 0.56$. Figure 6.38 and 6.39 compare the wetted and cavitating pressure distributions at different sections along the span of the rotor blades. Please note that the cavitating pressure distributions are such that $-C_p = \sigma_n$ on the cavity and $-C_p < \sigma_n$ elsewhere on the blade.

Figure 6.40 and 6.41 show the predicted cavity patterns and the cavitating pressure contours on both sides of the rotor blades. It is shown that mid-chord cavities are predicted on the back side, and there are no cavities on the face side of the rotor.

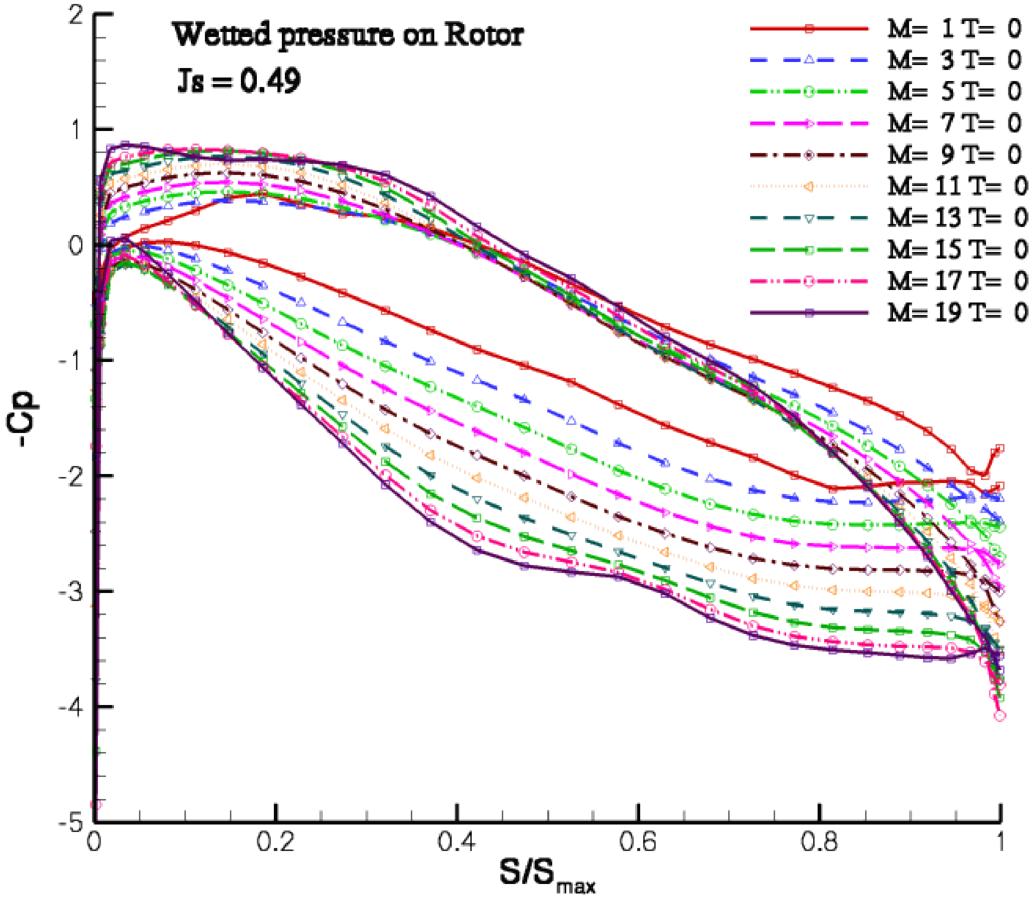

Figure 6.38: The predicted inviscid wetted pressure distributions on the ONR-AWJ1 rotor without considering the rotor/stator interaction at $J_s = 0.49$.

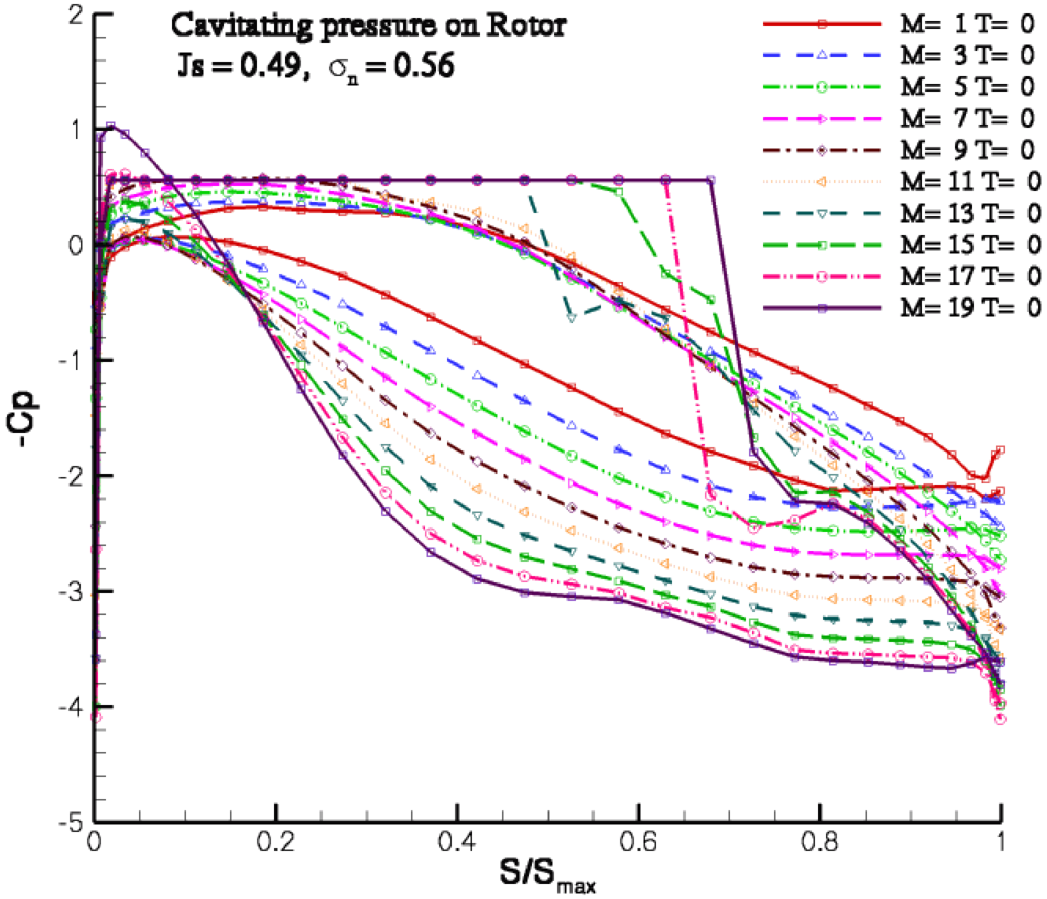

Figure 6.39: The predicted inviscid cavitating pressure distributions on the ONR-AWJ1 rotor without considering the rotor/stator interaction at $\sigma_n = 0.56$, $J_s = 0.49$.

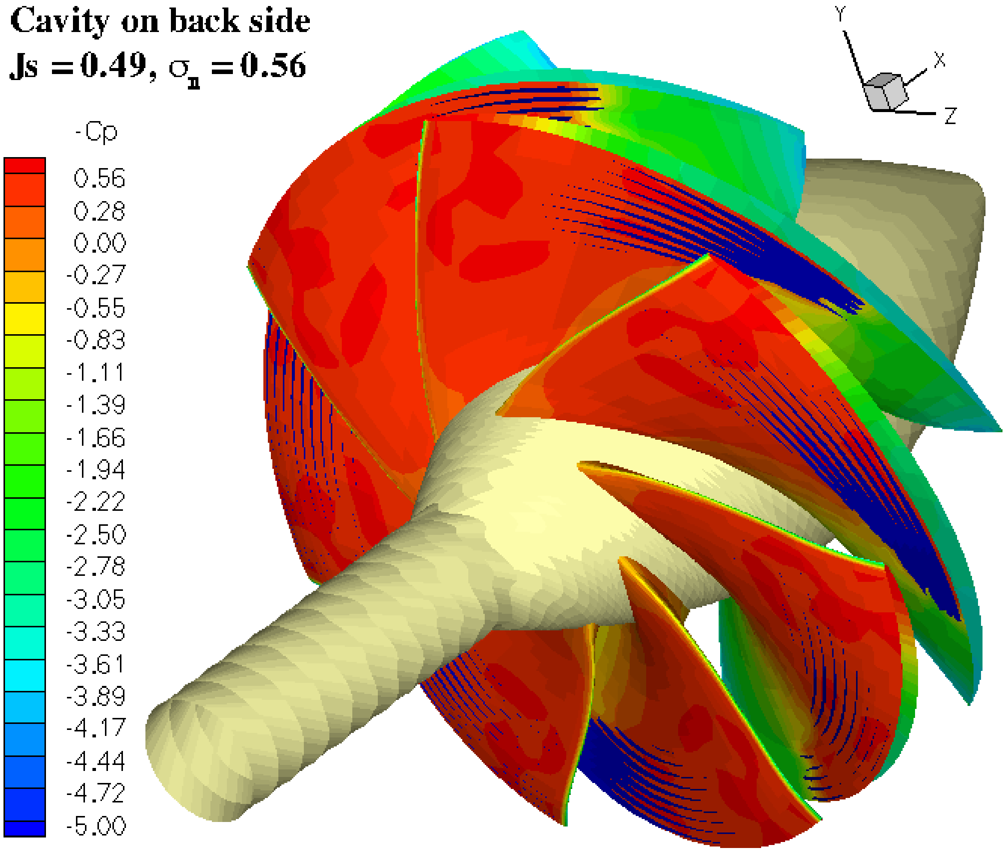

Figure 6.40: The predicted inviscid cavity patterns on the the back side of the ONR-AWJ1 rotor without considering the rotor/stator interaction at $\sigma_n = 0.56$, $J_s = 0.49$.

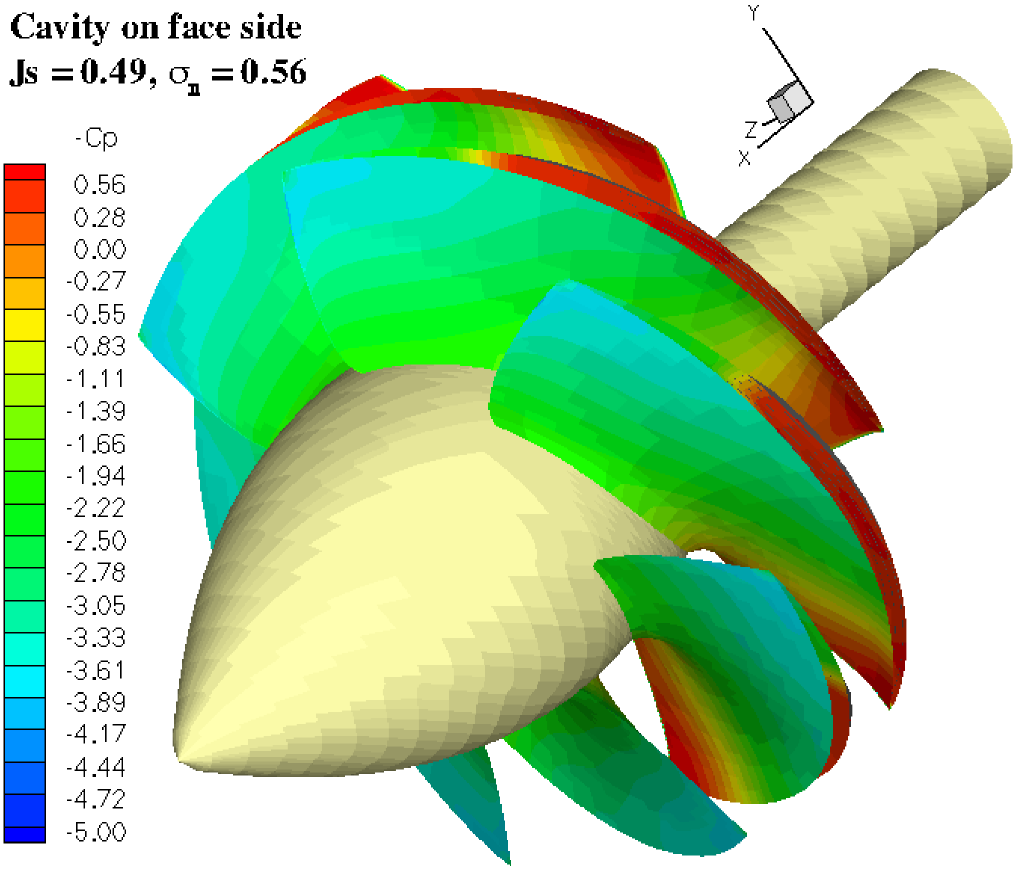

Figure 6.41: The predicted inviscid cavity patterns on the face side of the ONR-AWJ1 rotor without considering the rotor/stator interaction at $\sigma_n = 0.56$, $J_s = 0.49$.

6.4.3 Stator Only Calculations

This section presents the grid dependence studies in the case of having only the ONR-AWJ1 stator inside the casing, by using the inviscid water-jet model for $J_s = 0.49$.

Convergence Study

Figure 6.42 shows the sample discretization on the casing and outlet for the stator only case. There are totally 120×110 panels on the casing, and 10×110 panels on the outlet of the ONR-AWJ1 water-jet pump. Figure 6.43 presents the dependence of inviscid wetted circulation distributions on stator blade with number of panels on the casing and water-jet outlet. The circulation Γ_S is defined as $\Gamma_S = \Delta\phi_{TE}/2\pi R V_s$, where $\Delta\phi_{TE}$ is the potential jump at the trailing edge of the stator blade at each radius, and V_s is the ship speed. The convergence of the results is very fast and not affected by the number of panels on the casing and water-jet outlet.

Figure 6.44 shows the convergence of inviscid wetted circulation distributions with the panel size of stator trailing wake. The circulations on the stator are independent of the panel size of the trailing wake.

6.4.4 Rotor/Stator Interaction

In this section, the effects of one component on the other are investigated by using the induced potential approach and the induced velocity approach. Results from both approached are presented and compared with experimental measurements.

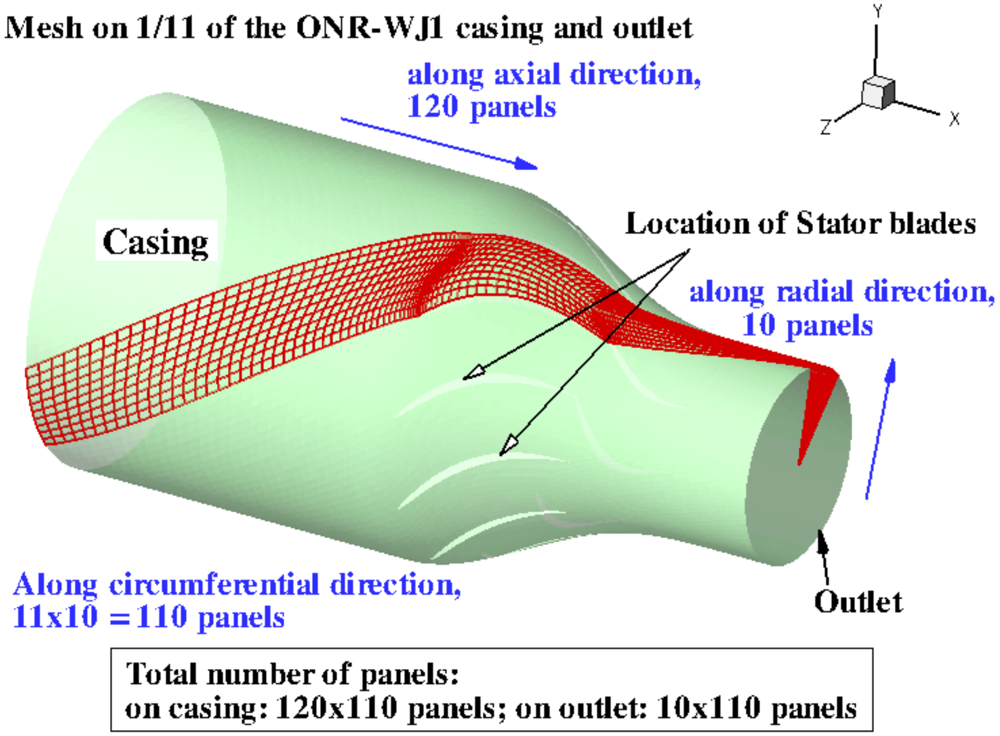

Figure 6.42: Sample discretization on the casing. Total no. of panels on casing is 120×110 panels, and on outlet 10×110 panels. ONR-AWJ1 water-jet pump. Stator Only Case.

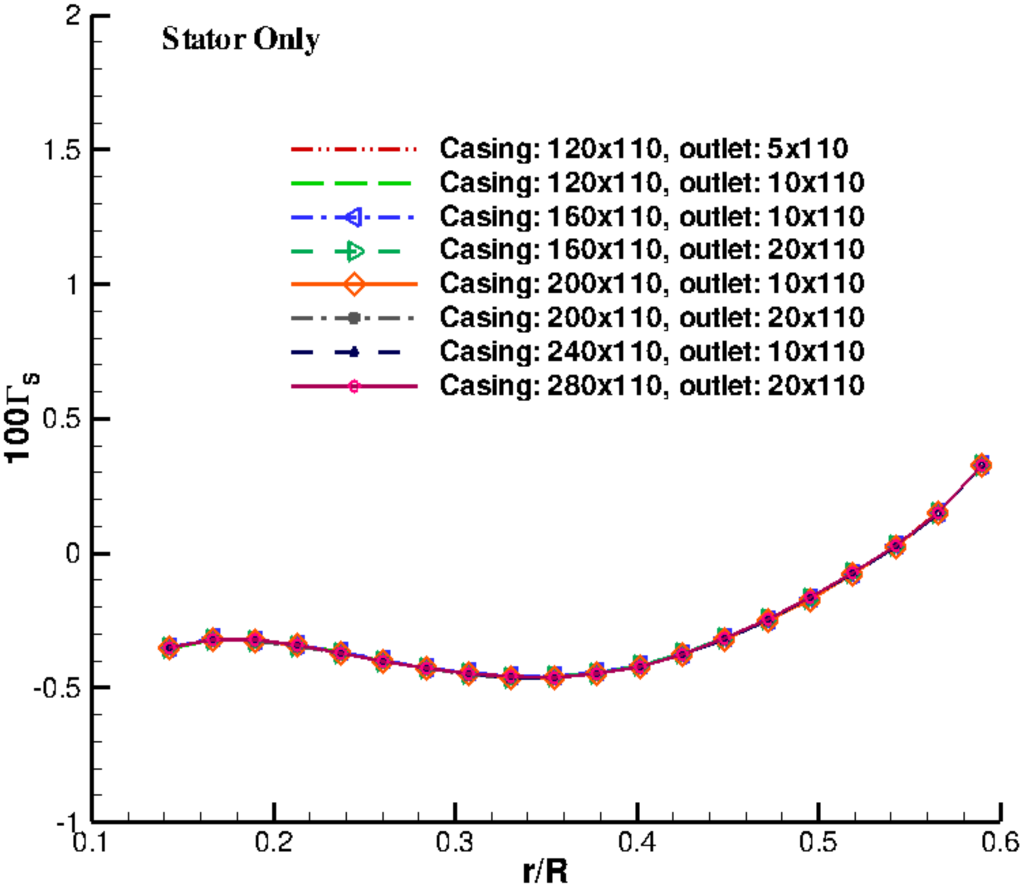

Figure 6.43: Convergence of inviscid wetted circulation distributions on ONR-AWJ1 stator with number of panels on the casing and outlet. Stator only, $J_s = 0.49$.

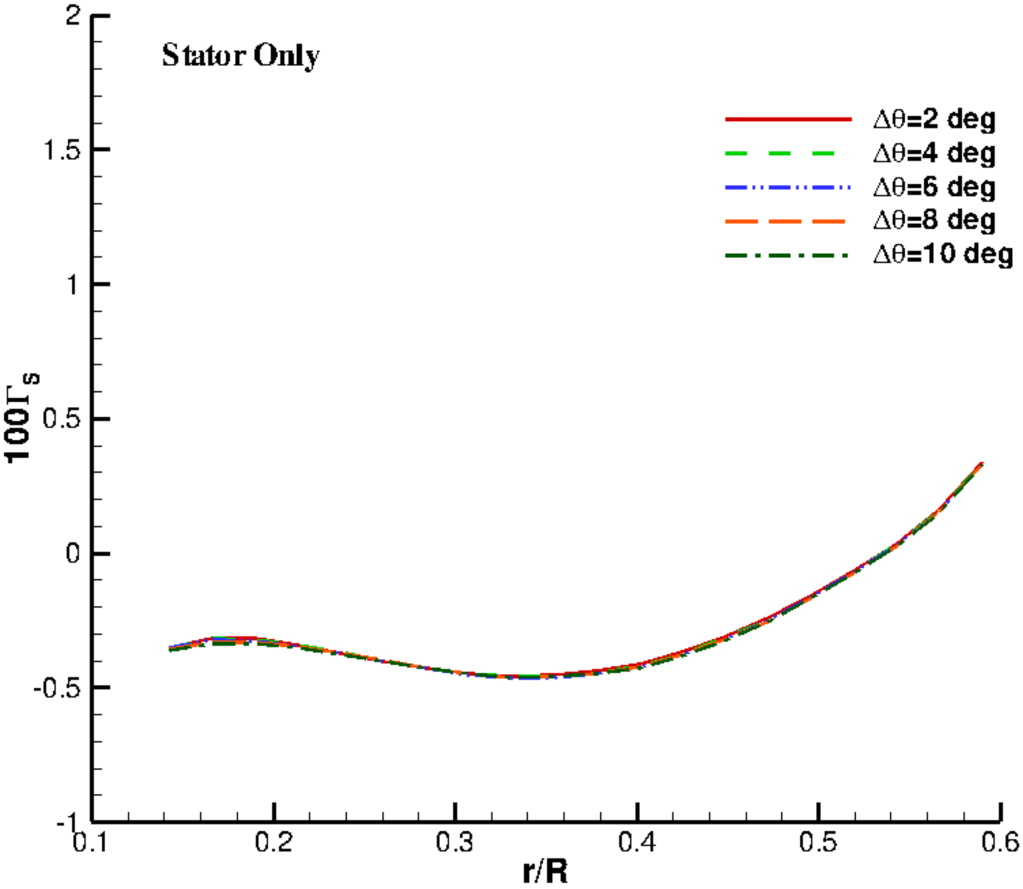

Figure 6.44: Convergence of inviscid wetted circulation distributions on ONR-AWJ1 stator with panel size of stator trailing wake. Stator only, $J_s = 0.49$.

Validation of Circumferentially Averaged $\vec{u}_{tan,SR}$

In the induced potential approach, the circumferentially averaged induced tangential velocities $\vec{u}_{tan,SR}$ are calculated by using Equation (6.7). In order to validate this method, after performing the rotor only run, $\vec{u}_{tan,SR}$ calculated by using Equation (6.7) are compared with those calculated by the integral equation (6.11) using the RPAN routine [Newman 1986]. RPAN evaluates the induced velocities by a unit strength source or dipole (planar) panel. Figure 6.45 shows the comparison of the circumferentially averaged $\vec{u}_{tan,SR}$ by using Equation (6.7) and by using Equation (6.11). In both calculations, the circumferentially averaged induced velocities by the rotor are first evaluated at the centroids of the rotor wake, and then interpolated to the control points on the stator blade. The results by the two methods agree well with each other. The advantage of using Equation (6.7) than the direct evaluation through RPAN is that it can save the cost of computational time.

Results from the Induced Potential Approach

For the induced potential approach, Figure 6.46 and 6.47 show the convergence of wetted circulation distributions on the rotor and on the stator with respect to number of iterations (between rotor and stator) for the ONR-AWJ1 water-jet pump at $J_s = 0.49$, respectively. The results of the $0th$ iteration in the figures correspond to the rotor or the stator solution without including the interaction between the two. Note that the iterative process converges very quickly, within the $2nd$ iteration in this case. The total run time after all iterations is about 3.5 hours on a cluster with 1 CPU of AMD Opteron (1.6GHz & 2G RAM per CPU). Please note that, al-

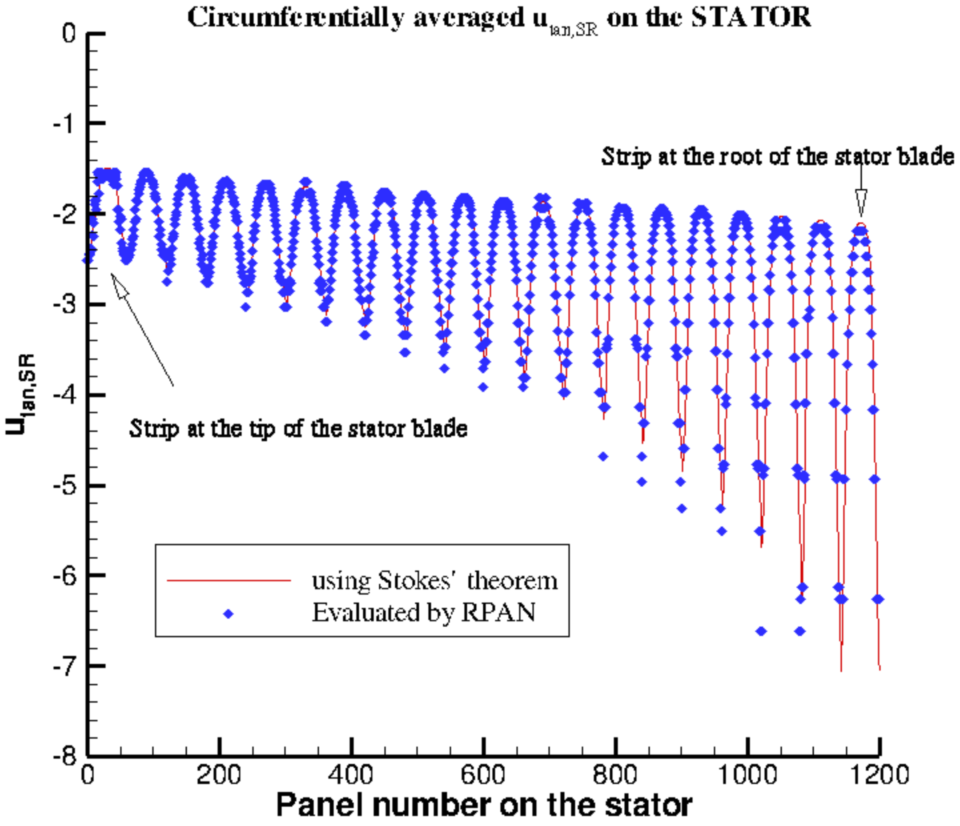

Figure 6.45: Comparison of the circumferentially averaged $\vec{u}_{tan,SR}$ on the stator induced by the rotor and rotor wake evaluated by Equation 6.7 and evaluated through RPAN. ONR-AWJ1 water-jet pump.

though induced potentials have periodicity in the circumferential direction, the total number of equally spaced elements over a full circle NNN is used here for the convenience of checking periodicity. For the stator problem, $NNN = 10 \times 7 = 70$ was used to evaluated the effect of rotor on stator. Similarly, for the rotor problem, $NNN = 10 \times 11 = 110$ was used to evaluated the effect of stator on rotor.

Figure 6.48 shows the convergence of the predicted rotor forces with respect to the total number of points used for time averaging. The results are almost overlapped with each other, and not affected by the total number of points used.

Figure 6.49 compares the contours of the predicted wetted pressures on the rotor before and after including the interaction between rotor and stator.

The above calculations using the induced potential approach show that, as expected, the stator does not affect much of the loadings on the rotor and the presence of rotor increases the loadings on the stator significantly. Figure 6.50 compares the predicted wetted thrust forces on the rotor including the interaction with the stator using the two approaches. The wetted thrust forces for rotor-only case is also presented in the figure.

Figure 6.51 compares the predicted torque forces on rotor without and with the interaction with the stator, and with the measurements at the Johns Hopkins University. The reason for the small discrepancies in the torque is most probably because of the assumption that the gap size at the rotor tip is zero even though the actual gap is 0.5% of the rotor radius. Thus, the effects of the viscous gap flow and of the associated tip gap vortex on the solution were not accounted for properly.

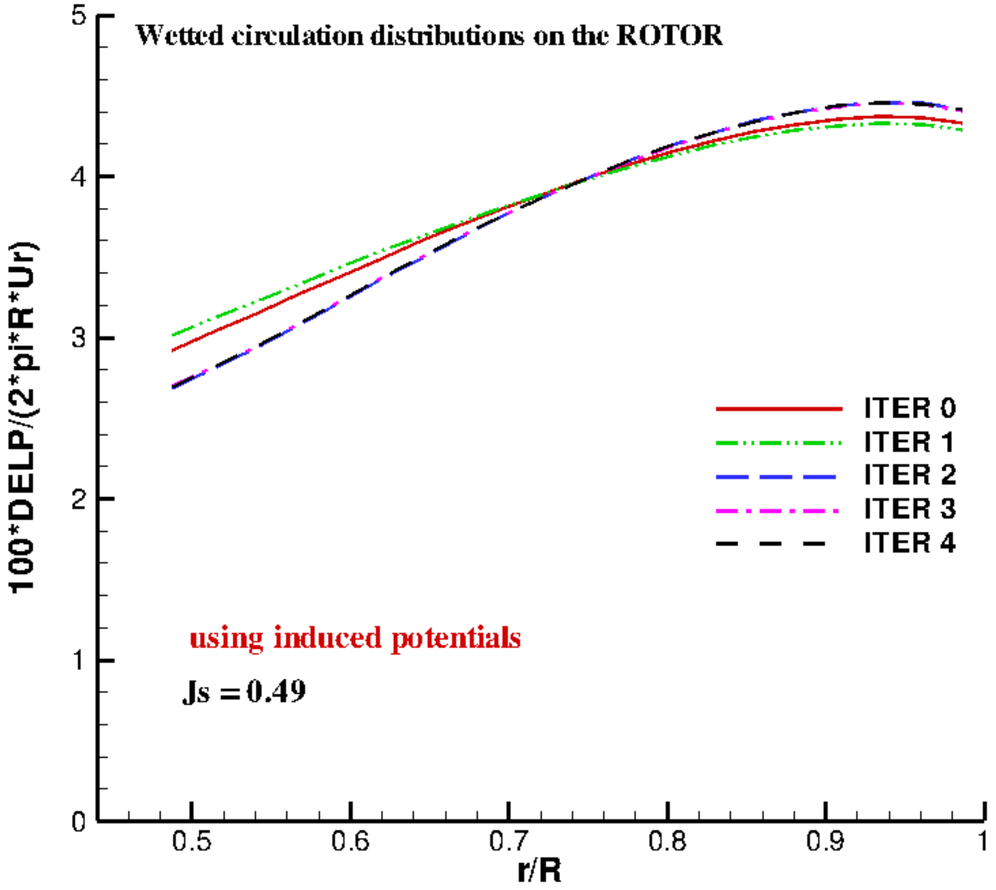

Figure 6.46: Convergence of wetted circulation distribution on ROTOR with number of iterations for ONR-AWJ1 water-jet pump at $J_s = 0.49$, *induced potential approach*. (The $0th$ iteration corresponds to the rotor solution without the stator.)

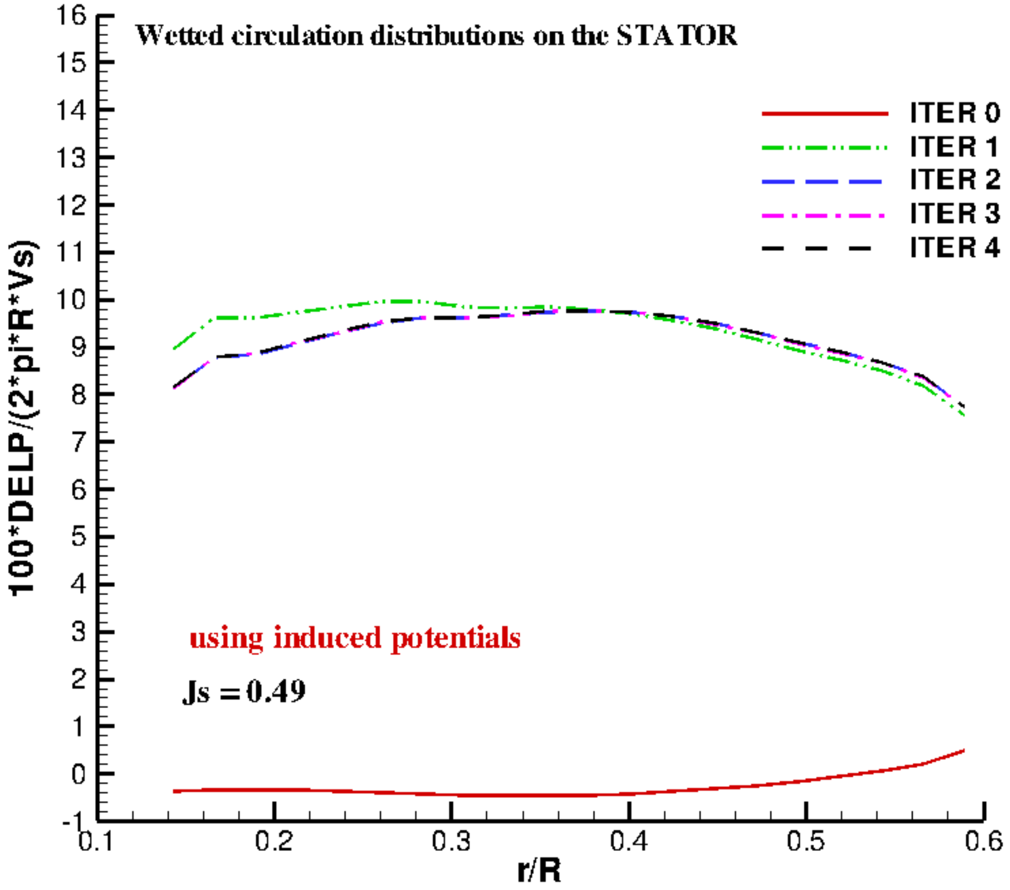

Figure 6.47: Convergence of wetted circulation distribution on STATOR with number of iterations for ONR-AWJ1 water-jet pump at $J_s = 0.49$, *induced potential approach*. (The $0th$ iteration corresponds to the stator solution without the rotor.)

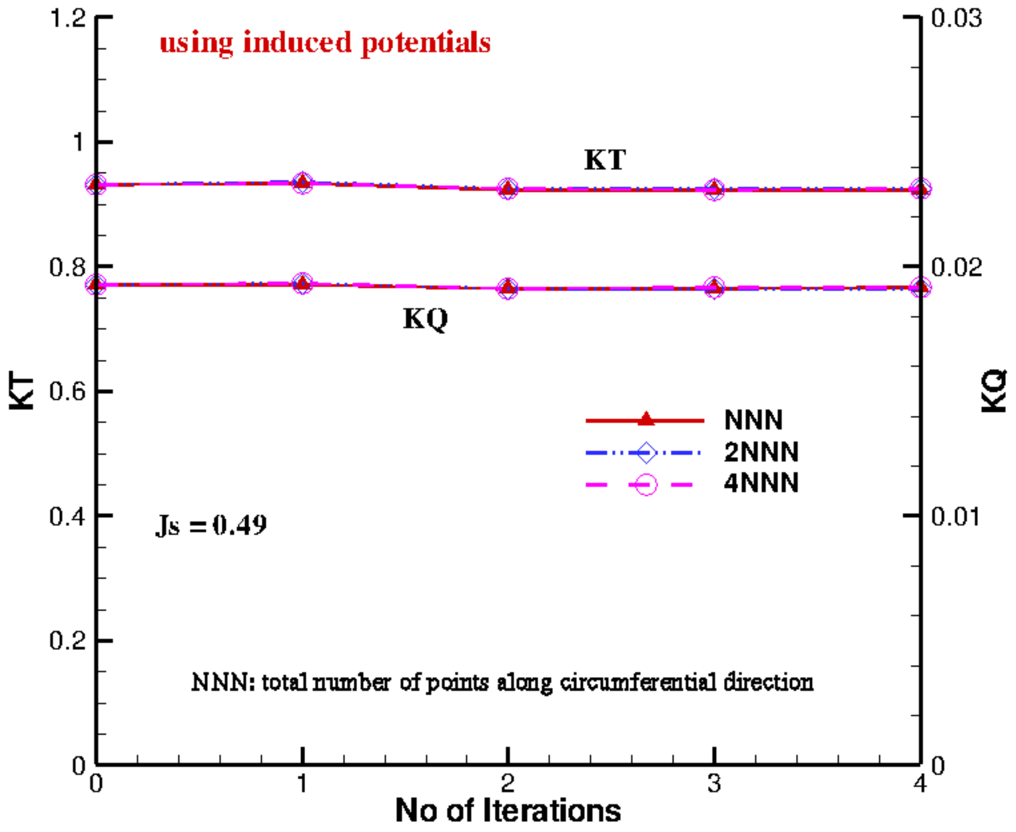

Figure 6.48: Convergence of rotor thrust and torque (wetted) with total number of points used for time averaging, ONR-AWJ1 water-jet pump, $J_s = 0.49$, *induced potential approach*. (The $0th$ iteration corresponds to the stator solution without the rotor.)

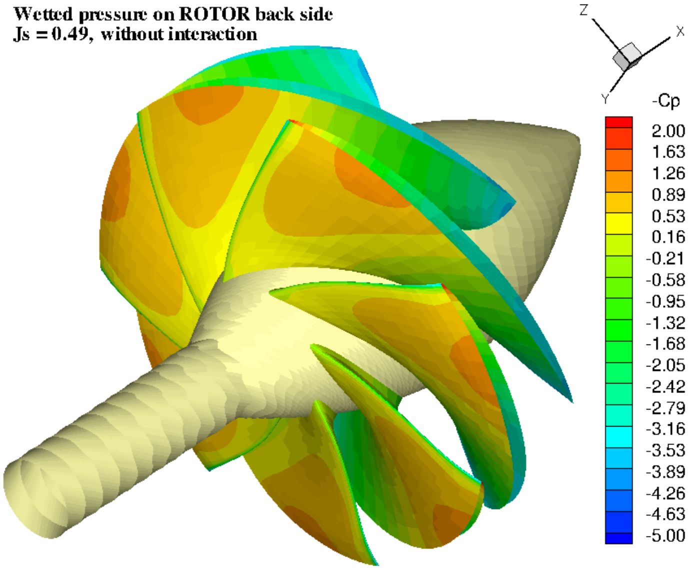

(a) Rotor Only

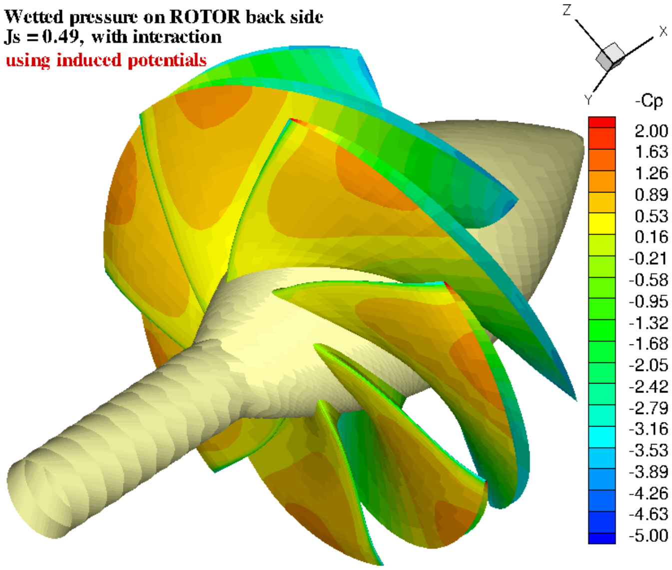

(b) Rotor/Stator Interaction

Figure 6.49: Comparison of wetted pressure contours on the suction (back) side of the rotor blades, WITHOUT and WITH interaction with stator; *induced potential approach*, ONR-AWJ1 water-jet pump, $J_s = 0.49$.

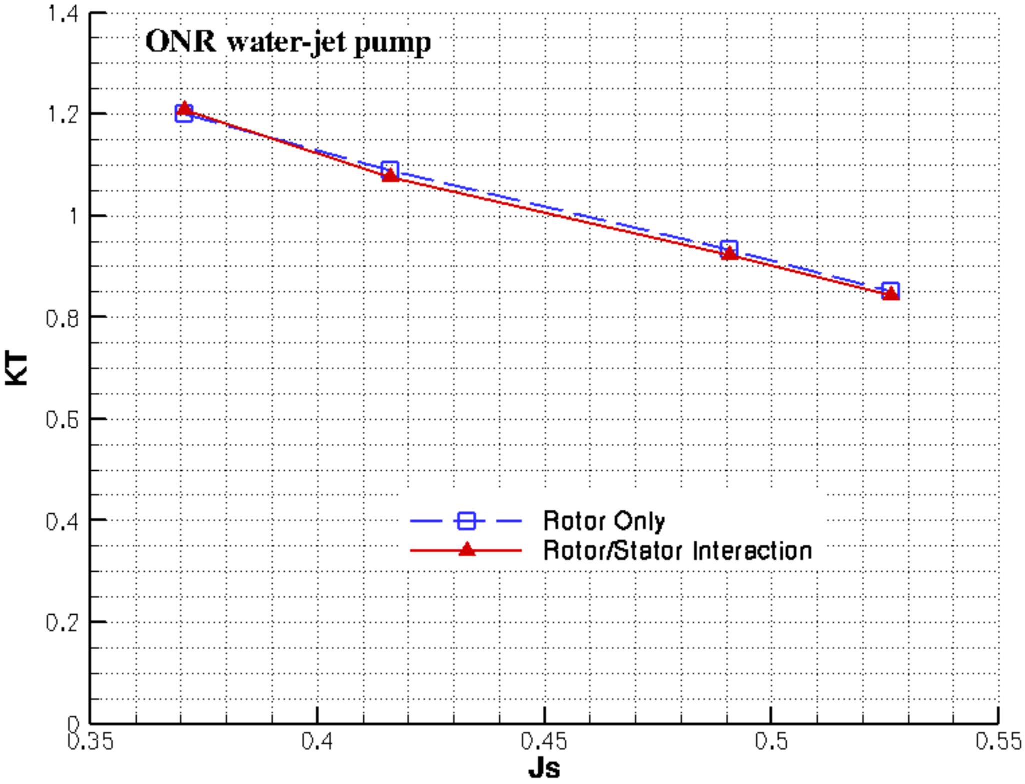

Figure 6.50: Predicted thrust forces on the rotor by using both induced potential approach at different J_s values for the ONR-AWJ1 water-jet pump.

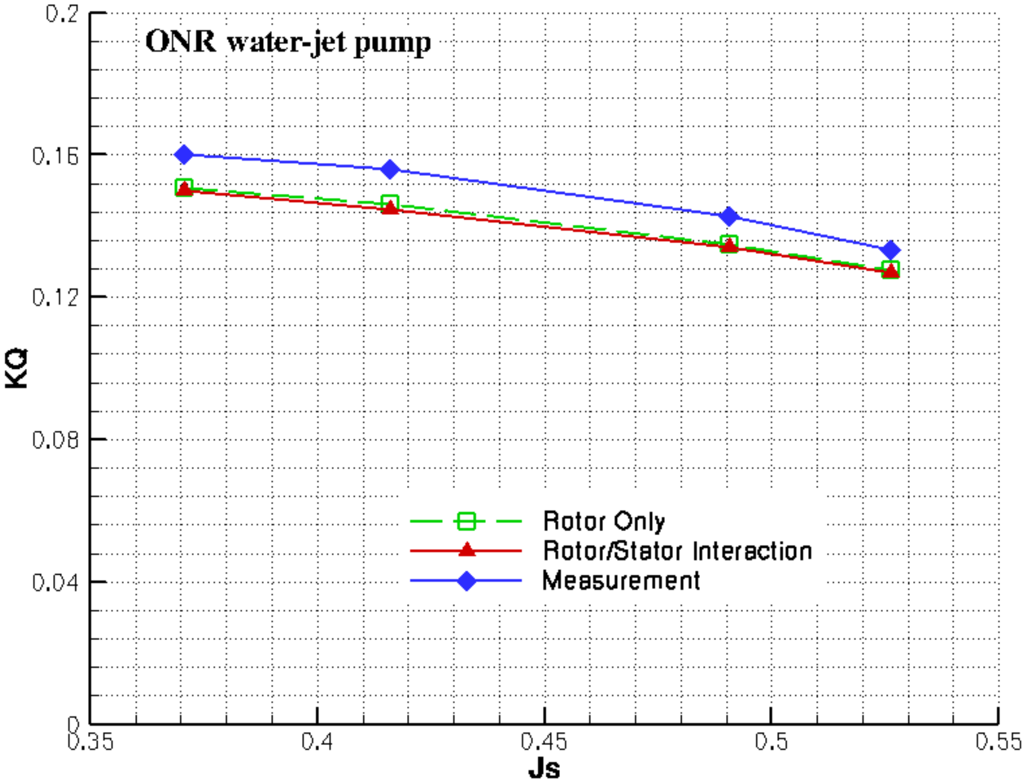

Figure 6.51: Comparison of the predicted torque forces on the rotor by using induced potential approach at different J_s values with the measured, ONR-AWJ1 water-jet pump.

6.5 Summary

A viscous/inviscid interaction method was extended to predict the cavitating performance of water-jet pumps subject to uniform inflow, including the effects of viscosity. The interaction between the rotor and the stator was evaluated in an iterative manner, by considering the circumferentially averaged effects of one on the other. The effect of viscosity was evaluated by coupling PROPCAV with XFOIL.

The presented predictions of the torque on ONR-AWJ1 water-jet pump were found to be less than 5% lower than those measured. The slight discrepancy between the predictions and the measurements might be attributed to the effects of the viscous gap flow on the rotor performance. The effects of the viscous tip gap on water-jet rotors can be considered by applying the orifice equation approach [Kerwin et al. 1987], as was recently implemented in the case of ducted propellers [Kinnas et al. 2004], as well as by tracking the tip gap vortex and its effect on the blade loading by applying the method presented in [Gu 2006].

Chapter 7

Conclusions

7.1 Conclusions

In conclusion, an accurate and efficient viscous/inviscid interaction method has been developed to predict the effects of viscosity on the performance of wetted and cavitating propulsors, by strongly coupling an existing boundary element method with a 2-D integral boundary layer analysis code. In the past, the solutions of the boundary layer flow on propulsor blades were not evaluated, and the effects of viscosity were approximated by applying empirical corrections to the inviscid solution.

Contributions of the present work include:

- Prediction of the effects of viscosity on wetted and cavitating single/multi-component propulsor flows (external flow problems). In previous methods for predicting propulsor flows, viscous pressures on the propulsor blades were not evaluated and the viscous forces were calculated by using the viscous pitch correction and a constant friction coefficient all over the blade. In the present viscous/inviscid interaction method, the wall transpiration model was used to couple the external inviscid flow and the inner boundary layer flows based on the strip theory assumption. The cavity surface was treated as a constant pressure free-streamline, and the cavitating velocities were evaluated on the blade surface underneath the cavity. The friction coefficient on the cavity was forced to be zero for the boundary layer analysis. The thrust/lift forces and the torque/drag forces were calculated by integrating the viscous pressures on blades and by evaluating the sectional drag coefficient at each strip. The present method was validated extensively in the case of 2-D and 3-D hydrofoils, bare duct, open and ducted propellers. The present method was found to require a small fraction of the computational effort required by RANS solvers. The results from the present method were found to have better correlation with experimental measurements than those using empirical viscous corrections.

- Development of the modeling of the inviscid flow and its coupling with a boundary layer solver (XFOIL) inside a water-jet pump (internal problem), by using an *induced potential approach* and an *induced velocity approach* to evaluate the effects of one component on the other. The time averaged flow was addressed. Systematic grid dependence and verification studies were conducted in the case of bare casing, rotor-only, and stator only problems. The method converged very fast with iterations between the rotor and stator, and the results had little dependence on space discretization. The induced potentials calculated by the present method were accurate, however, the calculated induced velocities were inaccurate because the RPAN routine had limitations in evaluating induced velocities due to singularities on distorted (non-planar) panels. Results considering the interactive effects between the components by using the *induced potential approach* were validated with the experimental measurements, and the torque forces on the rotor agreed well with the measured. The effect of the stator on the rotor performance was found to be small. The coupling of the inviscid model and the viscous boundary layer analysis was applied on the water-jet rotor or stator blade by using the proposed coupling algorithm as for the external problems. Results for rotor-only problem were presented and found to have good correlation with experimental measurements.

7.2 Discussion and Recommendations

Even though the present method predicts accurate pressure distributions and blade forces on the propulsor blades, additional research as stated next may be conducted to improve the present method.

- Prediction of viscous cavity: The cavity patterns including the effects of viscosity can be determined based on an iterative procedure by updating the boundary layer “blowing” sources in the modified Green’s formulation Equation (2.13) until the viscous cavity shape converges. This will require an extension of the method presented in Chapter 3 to 3-D cavitating flows.
- Cavity detachment search: According to previous studies [Arakeri and Acosta 1973; Arakeri 1975; Franc and Michel 1985], viscosity plays an important role in the detachment of cavities. Franc & Michael found that the cavity detachment should occur downstream of laminar separation where the bound-

ary layer shape factor $H = 4$ [Franc and Michel 1985]. The viscous/inviscid interaction method makes it possible to include the effect of viscosity on cavity detachment search in numerical predictions by using an iterative method. Moreover, this iterative method can also be applied to detect the setup of the leading edge vortices at low advance ratios by using a criterion similar to that of [Greeley 1982].

- Detailed validations of the water-jet modeling: Systematic correlations of the predictions with the detailed measurements on the ONR-AWJ1 water-jet pump [1] of velocity and pressure in the flow field, and the head-rise (rise in total pressure head) from the inlet to the outlet section, are suggested for validation of the present water-jet model. In the case of cavitating water-jets, the correlation between the predicted and the observed cavity plan-forms on rotor andor stator blades, and rotor thrust and torque breakdown due to cavitation should be carried out. Performance of unsteady cavitating water-jets, such as in the case of non-axisymmetric inflows, can also be predicted by evaluating the 3-D (time-averaged or unsteady) effective wake to the rotor or stator blades via coupling with a method (*e.g.* a RANS solver) which solves for the global flow inside the water-jet including at least the inlet, the outlet, as well as a part of the hull in the vicinity of the water-jet.

Other recommendations for further research:

---

[1] Planned to be performed at Johns Hopkins University.

- Including the cross flow: The present method ignores the boundary layer flows in the cross flow direction, which can result in inaccurate prediction of pressures when the local flow is very complicated, *e.g.* the flow at the root of an open propeller. Coupling of the 3-D boundary element method with 3-D boundary layer equations is suggested for the performance predictions of propulsor flows by using a improved model of Milewski [Milewski 1997a].

- Including the tip gap model: The viscous flow within the small gap region (between the propeller tip and the casing/duct inner surface) is not considered in the present method. According to previous work [Kerwin et al. 1987; Hughes 1997; Moon et al. 2002; Brewer et al. 2003; Gu 2006], the viscous gap flow increases the loading near blade tip as the gap size becomes smaller. A gap model by using the orifice equation model proposed by [Kerwin et al. 1987] or by using a tip leakage vortex model [Kinnas et al. 2005a; Gu 2006] is suggested to be implemented in the present method. The tip gap model can be verified and validated with experimental measurements or other methods, such as FLUENT and U^2NCLE.

- Treatment of non-zero trailing edge: In recent years, there has been an increasing number of propellers which are designed with a non-zero thickness trailing edge. Some of them are super cavitating or surface piecing propellers, while the others are traditional fully submerged propellers. There are two methods often used in the treatment of finite thickness trailing edge using inviscid solvers. The first one is by forcing the finite thickness at the trailing edge to be zero. This is not a proper way because some physics, especially the separation phenomena behind the finite trailing edge, will be left out. The other method is to assume a separated zone behind the finite thickness trailing edge, with a prescribed pressure value over the separated zone (*i.e.* equal to vapor pressure for cavitating flow). This method worked successfully in cavitating flows, but not well in wetted flows because the pressure over the separation zone is not known. The present viscous/inviscid interaction method can be used to evaluate the pressure distribution over the separated zone at the finite trailing edge using an iterative method.

- Experimental uncertainty: It was noted that, in correlation with the experiments, the uncertainties of the experimental data are not available in the related literature. The experimental uncertainties can be caused by limited accuracy of the measuring apparatus, and/or by limitation of simplification of the measurement procedure, and/or by changes of the environment, such as temperature. It is suggested that the margin of experimental error should be clarified in the publications.

Appendices

Appendix A

Boundary Layer Empirical Closure Relations

This appendix presents the empirical closure formulae used for the 2-D integral boundary layer analysis (XFOIL) [Drela and Giles 1987; Drela 1989]. The formulae here are specialized for incompressible flow. The fluid density ρ is constant and the Mach number Me is equal to zero.

Functional Dependencies

$$H^* = H^*(H_k, M_e, Re_\theta), \quad H^{**} = H^{**}(H_k, M_e) \tag{A.1}$$

$$C_f = C_f(H_k, M_e, Re_\theta), \quad C_D = C_D(H_k, M_e, Re_\theta) \tag{A.2}$$

Kinematic Shape Parameter

$$H_k = \frac{H - 0.290 M_e^2}{1 + 0.113 M_e^2} = H \tag{A.3}$$

Density Shape Parameter

$$H^{**} = \left(\frac{0.064}{H_k - 0.8} + 0.251 \right) M_e^2 = 0 \tag{A.4}$$

Kinetic Energy Shape Parameter

laminar

$$\begin{aligned} H^* &= 1.515 + 0.076 \frac{(4 - H_k)^2}{H_k}, \quad H_k < 4 \\ &= 1.515 + 0.040 \frac{(H_k - 4)^2}{H_k}, \quad H_k > 4 \end{aligned} \tag{A.5}$$

turbulent

$$\begin{aligned} H^* &= 1.505 + \frac{4}{Re_\theta} + \left(0.165 - \frac{1.6}{Re_\theta^{1/2}}\right)\frac{(H_0 - H_k)^{1.6}}{H_k}, \;\; H_k < H_0 \\ &= 1.505 + \frac{4}{Re_\theta} \\ &\quad + (H_k - H_0)^2 \left[\frac{0.04}{H_k} + \frac{0.007 \log Re_\theta}{\left(H_k - H_0 + \frac{4}{\log Re_\theta}\right)^2}\right], \;\; H_k > H_0 \end{aligned} \tag{A.6}$$

where

$$\begin{aligned} H_0 &= 4, & Re_\theta < 400 \\ &= 3 + \frac{400}{Re_\theta}, & Re_\theta > 400 \end{aligned}$$

Boundary Layer Thickness

$$\delta = \left(3.15 + \frac{1.72}{H_k - 1}\right)\theta + \delta^* \tag{A.7}$$

Equilibrium Shear Stress Coefficient

$$C_{\tau EQ} = H^* \frac{0.015}{1 - U_s} \frac{(H_k - 1)^3}{H_k^2 H} \tag{A.8}$$

where

$$U_s = \frac{H^*}{2}\left(1 - \frac{4}{3}\frac{H_k - 1}{H}\right) \tag{A.9}$$

Skin Friction Coefficient

laminar

$$\begin{aligned} \frac{C_f}{2} &= \frac{1}{Re_\theta}\left[-0.067 + 0.01977\frac{(7.4 - H_k)^2}{H_k - 1}\right], \;\; H_k < 7.4 \\ &= \frac{1}{Re_\theta}\left[-0.067 + 0.022\left(1 - \frac{1.4}{H_k - 6}\right)^2\right], \;\; H_k > 7.4 \end{aligned} \tag{A.10}$$

turbulent

$$\begin{aligned} C_f &= 0.3e^{-1.33H_k}\left[\log_{10}\left(\frac{Re_\theta}{F_c}\right)\right]^{-1.74-0.31H_k} \\ &+ 0.00011\left[\tanh\left(4-\frac{H_k}{0.875}\right)-1\right] \end{aligned} \tag{A.11}$$

Turbulent velocity profile

$$\begin{aligned} \frac{U}{U_e} &= \frac{U_\tau}{U_e}\frac{s}{0.09}\arctan(0.09y^+) \\ &+ \left(1-\frac{U_\tau}{U_e}\frac{s\pi}{0.18}\right)\tanh^{1/2}[a(\eta/\theta)^b] \end{aligned} \tag{A.12}$$

where $\frac{U_\tau}{U_e} = |\frac{C_f}{2}|^{1/2}$, $s = \frac{C_f}{|C_f|}$, $y^+ = \frac{U_\tau}{\mu_e/\rho_e}\eta$.

Dissipation Coefficient

laminar

$$\begin{aligned} C_D &= \frac{Re_\theta H^*}{2}\left[0.207+0.00205(4-H_k)^{5.5}\right], \quad H_k < 4 \\ &= \frac{Re_\theta H^*}{2}\left[0.207-0.003\frac{(H_k-4)^2}{1+0.02(H_k-4)^2}\right], \quad H_k > 4 \end{aligned} \tag{A.13}$$

turbulent

$$C_D = \frac{C_f}{2}U_s + C_\tau(1-U_s) \tag{A.14}$$

Appendix B

Edge Velocity Equation

This appendix presents the derivation of the discrete form of the boundary layer edge velocity Equation (2.14) for the present viscous-inviscid interaction method, based on the work by [Milewski 1997a].

From [Milewski 1997a], the perturbation potential including the viscosity effects can be decomposed into an inviscid part and a viscous correction part:

$$\phi = \phi^{(I)} + \phi^{(V)} \tag{B.1}$$

where the inviscid component, $\phi^{(I)}$, is given by the solution of Equation (2.4), and the viscous correction, $\phi^{(V)}$, is a function of the ”blowing” source strengths.

The discrete form of Equation (B.1) for any point on the body or in the wake is:

$$\phi_i = \phi_i^{(I)} + \sum_{l=1}^{Ntot} H_{il}\sigma_l^v \qquad i = 1, \ldots, Ntot \tag{B.2}$$

where $Ntot$ is the total number of panels on the body and wake surfaces. The ”blowing” source strength is defined as $\sigma_l^v = (\nabla s \cdot \mathbf{m})_l$, where **m** denotes the mass defect terms along the stripwise direction ξ and spanwise direction η in the blade local coordinate system.

The edge velocities for any point on the body or in the wake is expressed as:

$$\mathbf{U}_{ei} = \mathbf{U}_{ei}^{(I)} + \sum_{l=1}^{Ntot} G_{il}\sigma_l^v \tag{B.3}$$

Where $\mathbf{U}_{ei}$ denotes the edge velocities along ξ and η directions, $G = \nabla sH = (\frac{\partial H}{\partial \xi}, \frac{\partial H}{\partial \eta})$.

In terms of mass defect, Equation (B.3) can be written as:

$$\begin{aligned} U_{ei}^{\xi} &= U_{ei}^{\xi(I)} + \sum_{l=1}^{Nnodes} E_{il}^{\xi}(m_\xi)_l + \sum_{l=1}^{Nnodes} F_{il}^{\xi}(m_\eta)_l \\ U_{ei}^{\eta} &= U_{ei}^{\eta(I)} + \sum_{l=1}^{Nnodes} E_{il}^{\eta}(m_\xi)_l + \sum_{l=1}^{Nnodes} F_{il}^{\eta}(m_\eta)_l \end{aligned} \tag{B.4}$$

where $Nnodes$ is the total number of panel nodes on the body and in the wake. As in [Milewski 1997a], $E_{il} = (E_{il}^{\xi}, E_{il}^{\eta})$ are the induced velocity components at node i due to a unit mass defect in the ξ direction at node l; and $F = (F_{il}^{\xi}, F_{il}^{\eta})$ are the induced velocity components at node i due to a unit mass defect in the η direction at node l.

As discussed in Chapter 2, if the boundary layer is assumed to be developed only along the blade strips, and the cross flow over the propulsor blades is ignored. Therefore, Equation (B.4) can be simplified as the following,

$$U_{ei}^{\xi} = U_{ei}^{\xi(I)} + \sum_{l=1}^{Nnodes} E_{il}^{\xi}(m_\xi)_l \tag{B.5}$$

$$U_{ei}^{\eta} = 0 \tag{B.6}$$

Equation (B.5) corresponds to the discrete form of Equation (2.14), and E^{ξ} corresponds to the geometry dependent operator $\Im$.

Appendix C

Evaluation of Influence Coefficients

This appendix presents the evaluation of influence coefficients for 2-D and 3-D external and internal problems.

1. **Green's Function**

$$G = \frac{1}{2\pi} \ln r \qquad \text{for 2-D probem}$$

$$G = -\frac{1}{4\pi}\frac{1}{r} \qquad \text{for 3-D problem}$$

where r is the distance between the field point and variable point.

2. **2-D Influence Coefficients**

$$\text{Dipole:} \qquad D_{ij} = \frac{1}{2\pi} \int \frac{\partial(\ln r)}{\partial n} dS$$

$$\text{Source:} \qquad S_{ij} = \frac{1}{2\pi} \int \ln r dS$$

3. **3-D Influence Coefficients**

$$\text{Dipole:} \qquad D_{ij} = -\frac{1}{4\pi} \int \frac{\partial(1/r)}{\partial n} dS$$

$$\text{Source:} \qquad S_{ij} = -\frac{1}{4\pi} \int \frac{1}{r} dS$$

4. Calculation of 2-D Dipole Influence Coefficients

External Problem

$$D_{ji} = \frac{\omega_{ji}}{2\pi}$$

$$D_{ii} = \frac{1}{2}, \qquad \sum_{i \neq j} D_{ji} = \frac{1}{2}$$

j denotes the "jth" field point, and i denotes the "ith" panel.

$$\sum_{i} D_{ji} = 1$$

Internal Problem

$$D_{ji} = -\frac{\omega_{ji}}{2\pi}$$

$$D_{ii} = \frac{1}{2}, \qquad \sum_{i \neq j} D_{ji} = \frac{1}{2}$$

$$\sum_{i} D_{ji} = 0$$

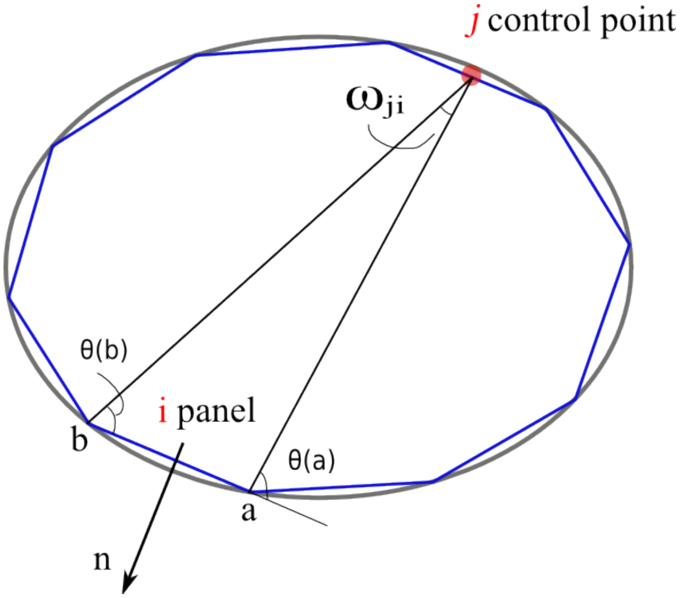

(a) external problem

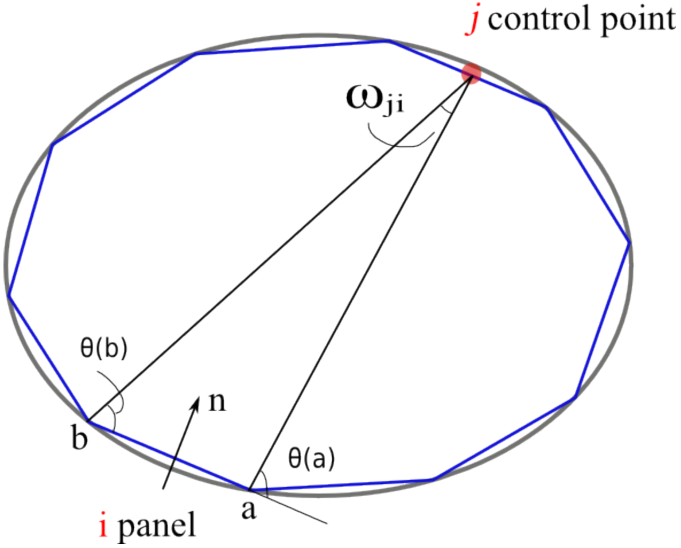

(b) internal problem

Figure C.1: Calculation of the dipole influence coefficients for 2-D external and internal problems.

Bibliography

Abdel-Maksoud, M. and Heinke, H. J. (2002). Scale effects on ducted propellers. In *Twenty-Fourth ONR Symposium on Naval Hydrodynamics*, Fukuoka, Japan.

Arakeri, V. H. (1975). Viscous effects on the position of cavitation separation from smooth bodies. *Journal of Fluid Mechanics*, vol 68(No. 4):779–799.

Arakeri, V. H. and Acosta, A. J. (1973). Viscous effect in the inception of cavitation on axisymmetric bodies. *Journal of Fluids Engineering*, vol 95(No. 4):519–527.

Bal, S. and Kinnas, S. A. (2003). A numerical wave tank for cavitating hydrofoils. *Journal of Computational Mechanics*, vol 32(5-6).

Black, S. D. (1997). *Integrated Lifting-Surface/Navier-Stokes Design and Analysis Methods for Marine Propulsors*. PhD thesis, Department of Ocean Engineering, MIT.

Brebbia, C. A. and Dominguez, J. (1989). *Boundary Elements An Introductory Course*. Computational Mechanics Publications-Mc Graw-Hill Inc., New York.

Breslin, J., Van Houten, R., Kerwin, J., and C.-A., J. (1982). Theoretical and experimental propeller-induced hull pressures arising from intermittent blade cavitation, loading, and thickness. *Transactions SNAME*, vol 90.

Brewer, W. H. and Kinnas, S. A. (1996). CAV2DBL(cavitating 2-dimensional with boundary layer) user's manual(version 1.0). Technical report, Department of Ocean Engineering,MIT.

Brewer, W. H. and Kinnas, S. A. (1997). Experiment and viscous flow analysis on a partially cavitating hydrofoil. *Journal of Ship Research*, vol 41(3):161–171.

Brewer, W. H., Marcum, D. L., Jessup, S. D., Chesnakes, C., Hyames, D. G., and Sreenivas, K. (2003). An unstructured rans study of tip-leakage vortex cavitation inception. In *ASME Fluids Engineering Division Summer Meeting*, Honolulu, HI.

Brewton, S., Gowing, S., and Gorski, S. (2006). Performance predictions of a water-jet rotor and rotor/stator combination using rans calculations. In *Twenty Sixth ONR Symposium on Naval Hydrodynamics*, Rome, Italy.

Brockett, T. (1966). Minimum pressure envelopes for modified naca-66 sections with naca a=0.8 camber and buships type i and type ii sections. Technical Report 1780, DTNSRDC Report.

Catherall, D. and Mangler, K. W. (1966). The integration of the two-dimensional laminar boundary-layer equations past the point of vanishing skin friction. *Journal of Fluid Mechanics*, vol 26:163–182.

Chen, B., Stern, F., and Kim, W. (1994). Computation of unsteady viscous marine propulsor blade and wake flow. In *Twentieth ONR Symposium on Naval Hydrodynamics*, University of California, Santa Barbara.

Choi, J.-K. and Kinnas, S. A. (1998). Numerical water tunnel in two and three dimensions. *Journal of Ship Research*, vol 42(2):86–98.

Choi, J.-K. and Kinnas, S. A. (2003). Prediction of unsteady effective wake by an euler solver/vortex-lattice coupled method. *Journal of Ship Research*, vol 47(2):131–144.

Chorin, A. J. (1967). A numerical method for solving incompressible viscous flow problems. *Journal of Computational Physics*, vol 2:12–26.

Chorin, A. J. (1973). Numerical study of slightly viscous flow. *Journal of Fluid Mechanics*, vol 57:785–796.

Chun, H. H., Park, W. G., and June, J. G. (2002). Experimental and cfd analysis for rotor-stator interaction of a water-jet pump. In *Twenty fourth ONR Symposium on Naval Hydrodynamics*, Fukuoka, Japan.

Coenen, E. G. M. (2001). *Viscous-Inviscid Interaction with the Quasi-Simultaneous Method for 2D and 3D Aerodynamic Flow*. PhD thesis, University of Groningen.

Coney, W. B. (1989). Some notes on the calculation of viscous effects on lift. Technical Report 89-8, Department of Ocean Engineering, MIT.

Cousteix, J. (1986). Three dimensional and unsteady boundary layer computations. *Annual Review of Fluid Mechanics*, vol 18:173–196.

Cousteix, J. and Houdeville, R. (1981). Singularities in three dimensional and turbulent boundary layer calculations and separation phenomena. *AIAA J.*, vol 19(8):976–985.

Drela, M. (1985). *Two-dimensional Transonic Aerodynamic Design and Analysis Using the Euler Equations*. PhD thesis, Department of Aeronautics and Astronautics, MIT.

Drela, M. (1989). XFOIL: An analysis and design system for low Reynolds number airfoils. In *Lecture Notes in Engineering (Volume 54, Low Reynolds Number Aerodynamics)*, New York. Springer-Verlag.

Drela, M. and Giles, M. B. (1987). Viscous-inviscid analysis of transonic and low reynolds number flows. *AIAA J.*, vol 25:1347–1355.

Dyne, G. (1973). Systematic studies of accelerating ducted propellers in axial and incline flows. *Symposium on Ducted Propellers, RINA*, pages 114–124.

Ebert, M. P., Gorski, J. J., and Coleman, R. M. (2003). Viscous flow calculation of waterjet propelled ships. In *8th International Conference on Numerical Ship Hydrodynamics*, Busan, Korea.

Edwards, D. E. and Carter, J. E. (1985). Analysis of three dimensional separated flow with the boundary layer equations. In *AIAA 7th Computational Fluid Dynamics Conference, Cincinnati, OH, Technical Papers (A85-40926 19-34)*, pages 99–107.

Edwards, D. E., Carter, J. E., and Smith, F. T. (1987). Analysis of three dimensional separated flow with the boundary layer equations. *AIAA J.*, vol 25:380–387.

Fairman, R. S. (2000). *Investigation Into The Discrepancies Between Computational Fluid Dynamic Lift Predictions and Experimental Results*. PhD thesis, Department of Ocean Engineering, MIT.

Falcão de Campos, J. A. C. (1983). On the calculation of ducted propeller performance in axisymmetric flows. Technical Report 696, Netherlands Ship Model Basin, Wageningen, The Netherlands.

Fine, N. E. (1988). Computational and experimental investigations of the flow around cavitating hydrofoils. Technical Report No. 88-6, Department of Ocean Engineering, MIT.

Fine, N. E. (1992). *Nonlinear Analysis of Cavitating Propellers in Nonuniform Flow*. PhD thesis, Department of Ocean Engineering, MIT.

Fine, N. E. (1993). Nonlinear analysis of cavitating hydrofoils and propellers (a user's guide to procav and other analysis codes). Technical report, Department of Ocean Engineering, MIT.

Fine, N. E. and Kinnas, S. A. (1993). A boundary element method for the analysis of the flow around 3-d cavitating hydrofoils. *Journal of Ship Research*, vol 37:213–224.

Franc, J. P. and Michel, J. M. (1985). Attached cavitation and the boundary layer: experimental investigation and numerical treatment. *Journal of Fluid Mechanics*, vol 154:63–90.

Gibson, I. S. and Lewis, R. I. (1973). Ducted propeller analysis by surface vorticity and actuator disk theory. In *Proceedings of the Symposium on Ducted Propellers, RINA*, Teddington, England.

Glover, E. J. and Ryan, P. G. (1973). A comparison of the theoretical and experimental performance of a ducted propeller system. In *Symposium on Ducted Propellers*, Teddington, England. The Royal Institution of Naval Architects.

Greeley, D. S. (1982). *Marine Propeller Blade Tip Flows*. PhD thesis, Department of Ocean Engineering, MIT.

Groves, N. C. and Chang, M. S. (1984). A differential method for three dimensional laminar and turbulent boundary layers of rotating blades. In *Fifteenth ONR Symposium on Naval Hydrodynamics*, Hamburg, Germany.

Gu, H. (2006). *Numerical Modeling of Flow around Ducted Propellers*. PhD thesis, Department of Civil, Architectural Environmental Engineering, The University of Texas at Austin.

Hsiao, C.-T. and Chahine, G. L. (2004). Numerical study of cavitation inception due to vortex/vortex interaction in a ducted propeller. In *Twenty-Fifth ONR Symposium on Naval Hydrodynamics*, St. John's, Newfoundland and Labrador, Canada.

Hufford, G. (1992). Viscous flow around marine propellers using boundary layer strip theory. Master's thesis, Department of Aeronautics and Astronautics, MIT.

Hufford, G. S., Drela, M., and Kerwin, J. E. (1994). Viscous flow around marine propellers using boundary-layer strip theory. *Journal of Ship Research*, vol 38(1):52–62.

Hughes, M. J. (1997). Impementation of a special procedure for modeling the tip clearance flow in a panel method for ducted propulsors. In *Propellers/Shafting '97 Symposium*, Virginia Beach, VA. The Society of Naval Architects & Marine Engineers.

Hughes, M. J., Kinnas, S. A., and Kerwin, J. E. (1992). Experimental validation of a ducted propeller analysis method. *Journal of Fluids Engineering*, vol 114(2):214–219.

Jerome, M. H. (1998). Fluid mechanics for sailing vessel design. *Annual Review of Fluid Mechanics*, vol 30:613–653.

Jessup, S. D. (1989). *An experimental investigation of viscous aspects of propeller blade flow*. PhD thesis, The Catholic University of America.

Kerwin, J. E. (2006). Hydrodynamic issues in water-jet design and analysis. In *Twenty Sixth ONR Symposium on Naval Hydrodynamics*, Rome, Italy.

Kerwin, J. E., Keenan, D. P., Black, S. D., and Diggs, J. G. (1994). A coupled viscous/potential flow design method for wake adapted multi-stage, ducted propulsors using generalized geometry. *Transactions SNAME*, vol 102.

Kerwin, J. E., Kinnas, S. A., Lee, J. T., and Shih, W.-Z. (1987). A surface panel method for the analysis of ducted propellers. *Transactions SNAME*, vol 95:93–122.

Kerwin, J. E. and Lee, C. S. (1978). Prediction of steady and unsteady marine propeller performance by numerical lifting surface theory. *Transactions SNAME*, vol 86.

Kerwin, J. E., Michael, T. J., and Neely, S. K. (2006). Improved algorithms for the design/analysis of multi-component complex propulsors. In *11th Propeller/Shafting Symposium, Society of Naval Architects and Marine Engineers*, Williamsburg, Virginia, USA.

Kerwin, J. E., Taylor, T. E., Black, S. D., and McHugh, G. P. (1997). A coupled lifting-surface analysis technique for marine propulsors in steady flow. In *Propellers/Shafting '97 Symposium*, pages 1–15 (Paper No. 20), Virginia Beach, VA. Society of Naval Architects & Marine Engineers.

Kinnas, S. A. (1998). The prediction of unsteady sheet cavitation. In *Third International Symposium on Cavitation*, Grenoble, France.

Kinnas, S. A. (2001a). Lecture 1: Supercavitating 2-d hydrofoils: prediction of performance and design. In *Special Course on Supercavitating Flows*, von Karman Institute, Brussels, Belgium.

Kinnas, S. A. (2001b). Lecture 2: Supercavitating 3-d hydrofoils and propellers:

prediction of performance and design. In *Special Course on Supercavitating Flows*, von Karman Institute, Brussels, Belgium.

Kinnas, S. A., Choi, J.-K., Lee, H. S., and Young, Y. L. (2000). Numerical cavitation tunnel. In *NCT50, International Conference on Propeller Cavitation*, Newcastle upon Tyne, England.

Kinnas, S. A., Choi, J.-K., Lee, H. S., Young, Y. L., Gu, H., Kakar, K., and Natarajan, S. (2002). Prediction of cavitation performance of single or multi-component propulsors and their interaction with the hull. *Transactions SNAME*, vol 110:215–244.

Kinnas, S. A. and Fine, N. E. (1991). Non-Linear Analysis of the Flow Around Partially or Super-Cavitating Hydrofoils by a Potential Based Panel Method. In *Boundary Integral Methods-Theory and Applications, Proceedings of the IABEM-90 Symposium, Rome, Italy, October 15-19, 1990*, pages 289–300, Heidelberg. Springer-Verlag.

Kinnas, S. A. and Fine, N. E. (1992). A nonlinear boundary element method for the analysis of unsteady propeller sheet cavitation. In *Nineteenth ONR Symposium on Naval Hydrodynamics*, pages 717–737.

Kinnas, S. A. and Fine, N. E. (1993a). MIT-PCPAN and MIT-SCPAN User's Manual, Version 1.0 the Analysis of Partially and Super Cavitating Hydrofoils.

Kinnas, S. A. and Fine, N. E. (1993b). A numerical nonlinear analysis of the flow around two- and three-dimensional partially cavitating hydrofoils. *Journal of Fluid Mechanics*, vol 254:151–181.

Kinnas, S. A. and Hsin, C.-Y. (1992). Boundary element method for the analysis of the unsteady flow around extreme propeller geometries. *AIAA Journal*, vol 30:688–696.

Kinnas, S. A., Hsin, C.-Y., and Keenan, D. P. (1991). A potential based panel method for the unsteady flow around open and ducted propellers. In *Eighteenth ONR Symposium on Naval Hydrodynamics (1990)*, pages 667–685, Washigton D.C. National Academy Press.

Kinnas, S. A., Lee, H. S., and Gu, H. (2005a). Numerical modeling of ducted propellers. In *2005 ASME Fluids Engineering Division Summer Meeting and Exhibitions*, Houston, Texas.

Kinnas, S. A., Lee, H. S., Gu, H., and Deng, Y. (2005b). Prediction of performance and design via optimization of ducted propellers subject to non-axisymmetric inflows. *Transactions SNAME*, vol 113:99–121.

Kinnas, S. A., Lee, H. S., Gu, H., and Gupta, A. (2004). Prediction of performance of ducted and podded propellers. In *Twenty-fifth ONR Symposium on Naval Hydrodynamics*, pages 8–13, St. John's, Newfoundland and Labrador, Canada.

Kinnas, S. A., Lee, H. S., Gu, H., and Natarajan, S. (2007a). Prediction of sheet cavitation on a rudder subject to propeller flow. *Journal of Ship Research*, vol 51:65–75.

Kinnas, S. A., Lee, H. S., Michael, T. J., and Sun, H. (2007b). Prediction of cavitating water-jet propulsor performance using a boundary element method. In *9th International Conference on Numerical Ship Hydrodynamics*, Ann Arbor, Michigan, USA.

Kinnas, S. A., Lee, H. S., Mishra, B., He, L., S.-H., R., and B., S. (2006). In *Eleventh Propellers/Shafting Symposium (PROPS). Society of Naval Architects and Marine Engineers*, Williamsburg, Virginia, USA.

Kinnas, S. A., Lee, H. S., and Mueller, A. C. (1998). Prediction of propeller blade sheet and developed tip vortex cavitation. In *Twenty-second ONR Symposium on Naval Hydrodynamics*, pages 182–198, Washington, D.C.

Kinnas, S. A., Lee, H. S., Sun, H., and He, L. (2007c). Performance prediction of single and multi-component propulsors using coupled viscous/inviscid methods. In *Tenth International Symposium on Practical Design of Ships and Other Floating Structures (PRADS)*, Houston, Texas, USA.

Kinnas, S. A., Mishima, S., and Brewer, W. H. (1994). Non-linear analysis of viscous flow around cavitating hydrofoils. In *Twentieth ONR Symposium on Naval Hydrodynamics*, pages 446–465, University of California, Santa Barbara, CA.

Kinnas, S. A., Sun, H., and Lee, H. S. (2003). Numerical analysis of flow around the cavitating cav2003 hydrofoil. In *CAV2003: Fifth International Symposium on Cavitation*, Osaka, Japan.

Konno, A., Wakabayashi, K., Yamaguchi, H., Maeda, M., Ishii, N., Soejima, S., and Kimura, K. (2002). On the mechanism of the bursting phenomena of propeller tip vortex cavitation. *Journal of Marine Science and Technology*, vol 6, No. 4:181–192.

Krishnaswamy, P. (1999). Re-entrant jet and viscous flow modeling for partially cavitating hydrofoils. Technical Report No. 99-3, Ocean Eng. Group, Department of Civil Engineering, UT Austin.

Lazareff, M. and LeBalleur, J. C. (1986). Computation of three dimensional flows by viscous-inviscid interaction using the mzm method. In *AGARD Fluid Dynamics Panel Symposium on Applications of Computational Fluid Dynamics in Aeronautics*. CP-412.

Lee, C. S. (1979). *Prediction of steady and unsteady performance of marine propellers with and without cavitation by numerical lifting surface theory*. PhD thesis, Department of Ocean Engineering, MIT.

Lee, H. S. (2002). *Modeling of Unsteady Wake Alignment and Developed Tip Vortex Cavitation*. PhD thesis, Department of Civil Engineering, The University of Texas at Austin.

Lee, H. S. (2007). PROPCAV-2D user's manual and documentation. Technical report, Department of Civil Engineering, University of Texas at Austin.

Lee, H. S. and Kinnas, S. A. (2004). Application of bem in the prediction of unsteady blade sheet and developed tip vortex cavitation on marine propellers. *Journal of Ship Research*, vol 48(1):15–30.

Lee, H. S. and Kinnas, S. A. (2005a). A bem for the modeling of unsteady propeller sheet cavitation inside a cavitation tunnel. *Journal of Computational Mechanics*, vol 37(1):41–51.

Lee, H. S. and Kinnas, S. A. (2005b). Fully unsteady wake alignment for propellers in non-axisymmetric flows. *Journal of Ship Research*, vol 49(3):176–190.

Lee, H. S. and Kinnas, S. A. (2006). Prediction of cavitating performance of ducted propeller. In *CAV2006: Sixth International Symposium on Cavitation*, Wageningen, The Netherlands.

Lee, H. S., Kinnas, S. A., Gu, H., and Natarajan, S. (2003). Numerical modeling of rudder sheet cavitation including propeller/rudder interaction and the effects of a tunnel. In *CAV2003: Fifth International Symposium on Cavitation*, Osaka, Japan.

Lee, H. S., Sun, H., and Kinnas, S. A. (2004). PROPCAV user's manual and documentation (version 2.1.1). Technical Report 04-1, Department of Civil Engineering, University of Texas at Austin.

Lee, J.-T. (1987). *A potential based panel method for the analysis of marine propellers in steady flow*. PhD thesis, Department of Ocean Engineering, MIT.

Lemonnier, H. and Rowe, A. (1988). Another approach in modeling cavitating flows. *Journal of Fluid Mechanics*, vol 195.

Lighthill, M. J. (1958). On displacement thickness. *Journal of Fluid Mechanics*, vol 4:383–392.

Lock, R. C. and Williams, B. R. (1987). Viscous-inviscid interactions in external aerodynamics. *Prog. Aerospace Sci.*, vol 24:51–171.

Milewski, W. M. (1997a). *Three-dimensional viscous flow computations using the integral boundary integral equations simultaneously coupled with a low order panel method.* PhD thesis, Department of Ocean Engineering, MIT.

Milewski, W. M. (1997b). Three-dimensional viscous flow computations using the integral boundary layer equations simultaneous coupled with a low order panel method. Technical Report No. 97-4, Department of Ocean Engineering, MIT.

Moon, I. S., Kim, K. S., and Lee, C.-S. (2002). Blade tip gap flow model for performance analysis of waterjetpropulsors. In *International Association for Boundary Element Methods*, Austin, TX.

Morgan, W. B. and Caster, E. B. (1965). Prediction of the aerodynamic characteristics of annular airfoils. Technical Report 1830, DTMB.

Morino, L. and Bharadvaj, B. (1985). Two methods for viscous and inviscid free-wake analysis of helicopter rotors. Technical Report CCAD-TR-85-02, Boston University, Center for Computational and Applied Dynamics.

Morino, L. and Kuo, C.-C. (1974). Subsonic Potential Aerodynamic for Complex Configurations : A General Theory. *AIAA Journal*, vol 12(no 2):191–197.

Mughal, B. H. (1992). A calculation method for the three dimensional boundary layer equations in integral form. Master's thesis, Department of Aeronautics and Astronautics, MIT.

Mughal, B. H. (1998). *Integral Methods for Three Dimensional Boundary Layers*. PhD thesis, Department of Aeronautics and Astronautics, MIT.

Newman, J. N. (1986). Distributions of sources and normal dipoles over a quadrilateral panel. *Journal of Engineering Mathematics*, vol 20:113–126.

Nishida, B. and Drela, M. (1995). Fully simultaneous coupling for three dimensional viscous/inviscid flows. In *AIAA 13th Applied Aerodynamics Conference*. 95-1806-CP.

Nishida, B. A. (1996). *Fully Simultaneous Coupling of the Full Potential Equation and the Integral Boundary Layer Equations in Three Dimensions*. PhD thesis, Department of Aeronautics and Astronautics, MIT.

Rhee, S. H., Kawamura, T., and Li, H. Y. (2005). Propeller cavitation study using an unstructured grid based navier-stokes solver. *Journal of Fluids Engineering*, vol 127:986–994.

Salvatore, F. and Esposito, P. G. (2001a). An improved boundary element analysis of cavitating three-dimensional hydrofoils. In *CAV2001: Forth International Symposium on Cavitation*, Pasadena, California, USA.

Salvatore, F. and Esposito, P. G. (2001b). Numerical analysis of cavitating propellers including viscous effects. In *PRADS, Proceedings of 8th Int. Symp. on the Practical Design of Ships and Mobile Offshore Units*, Shanghai, China.

Salvatore, F., Testa, C., and Greco, L. (2003). A viscous/inviscid coupled formulation for unsteady sheet cavitation modelling of marine propellers. In *CAV2003: Fifth International Symposium on Cavitation*, Osaka, Japan.

Sanchez-Caja, A., P., S. T., and Pylkkanen, J. V. (2006). Simulation of incompressible viscous flow around an endplate propeller using a ranse solver. In *Twenty-Six ONR Symposium on Naval Hydrodynamics*, Rome, Italy.

Sanchez-Caja, A., Rautaheimo, P., and Siikonen, T. (2000). Simulation of incompressible viscous flow around a ducted propeller using a rans equation solver. In *Twenty-Third ONR Symposium on Naval Hydrodynamics*, Valde Reuil, France.

Schlichting, H. (1979). *Boundary Layer Theory*. McGraw-Hill, Inc.

Stanier, M. J. (2002). *Numerical prediction of propeller scale effects*. PhD thesis, University of Southampton, United Kingdom.

Stern, F., Kim, H. T., C., P. V., and Chen, H. C. (1986). Computation of viscous flow around propeller-shaft configurations. Technical Report IIHR No 305, Iowa Institute of Hydraulic Research, The University of Iowa.

Stern, F., Kim, H. T., Patel, V. C., and Chen, H. C. (1988). A viscous-flow approach to the computation of propeller- hull interaction. *Journal of Ship Research*, vol 32(4):246–262.

Stern, F., Zhang, D., Chen, B., Kim, H., and Jessup, S. D. (1994). Computation of viscous marine propulsor blade and wake flow. In *Twentieth ONR Symposium on Naval Hydrodynamics*, University of California, Santa Barbara.

Sun, H. and Kinnas, S. A. (2006). Simulation of sheet cavitation on propulsor blades using a viscous/inviscid interactive method. In *CAV2006: Sixth International Symposium on Cavitation*, Wageningen, The Netherlands.

Taylor, T. E., Scherer, J. O., and Kerwin, J. E. (1998). Water-jet pump design and analysis using a coupled lifting-surface and rans procedure. In *In Royal Institution of Naval Architects Conference on Water-jet Propulsion Latest Developments*, Amsterdam, The Netherlands.

Uto, S. (1993). Computation of incompressible viscous flow around a marine propeller. *Journal of Society of Naval Architects of Japan*.

Van Houten, R. (1986). Analysis of ducted propellers in steady flow. Technical Report 4.76-1, Airflow Research and Manufacturing Corp., Watertown, MA.

Veldman, A. E. P. (1981). New, quasi-simultaneous method to calculate interacting boundary layers. *AIAA J.*, vol 19:79–85.

Villeneuve, R. A. (1993). Effects of viscosity on hydrofoil cavitation. Master's thesis, Massachusetts Institute of Technology.

Villeneuve, R. A. and Kinnas, S. A. (1993). An Interactive Boundary Layer/Potential Flow Method for the Analysis of Partially Cavitating Hydrofoils. Submitted for publication.

Warren, C. L., Taylor, T. E., and Kerwin, J. E. (2000). A coupled viscous/potential-flow method for the prediction of propulsor-induced maneuvering forces. In *Propellers/Shafting '00 Symposium*, Virginia Beach, VA. The Society of Naval Architects & Marine Engineers.

Watanabe, T., Kawamura, T., Takekosi, Y., Maeda, M., and Rhee, S. H. (2003). Simulation of steady and unsteady cavitation on a marine propeller using a rans cfd code. In *CAV2003: Fifth International Symposium on Cavitation*, Osaka, Japan.

White, F. M. (1974). *Viscous Fluid Flow*. McGraw-Hill, Inc.

Wigton, L. B. and Holt, M. (1981). Viscous-inviscid interaction in transonic flow. *AIAA-81-1003*, pages 77–89.

Yates, J. E. (1978). Viscous thin airfoil theory and the Kutta condition. In *AIAA 16th Aerospace Sciences Meeting*, Huntsville, Alabama. 78-152.

Young, Y. L. (2002). *Numerical modeling of super-cavitating and surface-piercing propellers*. PhD thesis, Department of Civil Engineering, The University of Texas at Austin.

Young, Y. L. and Kinnas, S. A. (2001). A bem for the prediction of unsteady mid-chord face and/or back propeller cavitation. *Journal of Fluids Engineering*, vol 123:311–319.

Young, Y. L. and Kinnas, S. A. (2003a). Analysis of supercavitating and surface-piercing propeller flows via bem. *Journal of Computational Mechanics*, vol 32(4-6):269–280.

Young, Y. L. and Kinnas, S. A. (2003b). Numerical modeling of super-cavitating propeller flows. *Journal of Ship Research*, vol 47:48–62.

Young, Y. L. and Kinnas, S. A. (2004). Performance prediction of surface-piercing propellers. *Journal of Ship Research*, vol 48:288–304.

Vita

Hong Sun is from Xinxiang City, Henan Province, China. She attended Xinxiang County No. 1 High School in Xinxiang, Henan Province from 1991 to 1994. In the fall of 1994, she entered the Department of Mechanics at Tianjian University, Tianjin, China, where she obtained her Bachelor's degree in Engineering Mechanics in July, 1998 and her Master's degree in Fluid Mechanics in April, 2001. In August 2002, she enrolled at the University of Texas at Austin for her doctoral study in the Ocean Engineering Group of the Department of Civil, Architectural and Environmental Engineering.

Permanent address: Muye District, LvCun 219
Xinxiang City, Henan Province 453700
People's Republic of China

This dissertation was typeset with LaTeX[†] by the author.

[†] LaTeX is a document preparation system developed by Leslie Lamport as a special version of Donald Knuth's TeX Program.